On the multi-scale vibroacoustic behavior of multi-layer core topology systems

Nassardin Guenfoud

N° d'ordre NNT : 2020LYSEC10

THÈSE DE DOCTORAT DE L'UNIVERSITÉ DE LYON

opérée au sein de **l'École Centrale de Lyon**

en co-tutelle avec **KU Leuven**

École Doctorale ED162

Mécanique - Énergétique - Génie Civil - Acoustique

Spécialité : Génie Mécanique

Soutenue publiquement le 20/02/2020, par :

Nassardin GUENFOUD

On the multi-scale vibroacoustic behavior of multi-layer core topology systems

---

Devant le jury composé de :

N. ATALLA, Professeur des Universités, Université de Sherbrooke,	Président du jury
E. MANCONI, Professeur des Universités, Université de Parme,	Rapporteur
F. FRANCO, Maître de Conférence, Université de Naples,	Rapporteur
A-M. ZINE, Maître de Conférence HDR, École Centrale de Lyon,	Examinateur
E. DECKERS, Professeur des Universités, KU Leuven,	Encadrante
O. BAREILLE, Maître de Conférences HDR, École Centrale de Lyon,	Co-Superviseur
W. DESMET, Professeur des Universités, KU Leuven,	Superviseur
M. ICHCHOU, Professeur des Universités, École Centrale de Lyon,	Superviseur


ÉCOLE CENTRALE DE LYON

École Doctorale ED162

Mécanique - Énergétique - Génie Civil - Acoustique

Spécialité : Génie Mécanique


KU LEUVEN

Arenberg Doctoral School

Faculty of Engineering Science - Faculteit Ingenieurswetenschappen

Mechanical Engineering - Werktuigkunde

On the multi-scale vibroacoustic behavior of multi-layer core topology systems

---

by

Nassardin GUENFOUD

in partial fulfillment of the requirements for the degree of

Doctor of Mechanical Engineering

and

Doctor of Engineering Science (PhD): Mechanical Engineering

Supervisors:

Prof. Mohamed ICHCHOU, École Centrale de Lyon

Prof. Wim DESMET, KU Leuven

Co-Supervisor:

Dr. Olivier BAREILLE, École Centrale de Lyon

Acknowledgement

Firstly, I would like to thank Allah, the Most Merciful, the Omniscient for helping me and allowing me to complete successfully my research. As his beloved Prophet Muhammad (peace and blessings be upon him) said: **"Whoever does not thank people has not thanked Allah."**.

This thesis work has been the subject of an intense research during 3 years between Ecole Centrale de Lyon and KU Leuven in the framework of the Viper Project allowing me to highly enrich my knowledge and my expertise. This project has received funding from the European Union's Horizon 2020 research and innovation program under the Marie Sklodowska-Curie grant agreement No. 675441. I would like to gratefully acknowledge everyone involved in the VIPER project, professors and Marie-Curie fellows.

I would like to sincerely express my gratitude to Prof. Mohamed Najib Ichchou and Prof. Wim Desmet for their supervision during my thesis and their continuous support. They relied on me for conducting this research. They guide me and motivate me all the time giving me many advice to fulfil this research project.

Moreover, I would like to also express many thanks to Prof. Olivier Bareille and Prof. Elke Deckers for their help as co-advisors and assessors, their suggestions, reviews and valuable remarks helping me to reach my objectives.

I would like to thank all the members of the jury, Prof. Abdelmalek Zine, Prof. Elisabetta Manconi and Prof. Francesco Franco for their precious reviews to correct my manuscript and to improve my research work.

I would like also to express a special and sincere thank to Giovanni Tufano, Fabrizio Errico, Dr. Christophe Droz, Dr. Pascal Fossat and Benoit Minard for their help, useful discussions and great support during my thesis.

Finally, I thank my fellow labmates in Ecole Centrale de Lyon.

Dedication

I dedicate my dissertation work to my whole family. I would like to warmly thank them for their love, support, prayers and by taking care of me during all my education. I have not enough words to thank my lovely parents for everything they give me and my wife for her support and continuous encouragement.

To my parents,

To my wife,

قُلْ إِنَّ صَلاَتِى وَنُسُكِى وَمَحْيَاىَ وَمَمَاتِى لِلّهِ رَبِّ الْعَالَمِينَ ﴿١٦٢﴾
لاَ شَرِيكَ لَهُ وَبِذَلِكَ أُمِرْتُ وَأَنَاْ أَوَّلُ الْمُسْلِمِينَ ﴿١٦٣﴾

Résumé

Les panneaux sandwichs en nid d'abeille ont fait l'objet d'intenses recherches ces dernières décennies. En effet, outre leurs bonnes performances mécaniques et leur rapport rigidité poids faible, il en résulte une baisse importante des propriétés acoustiques. Ainsi, de nombreux designs sont régulièrement proposés afin de palier à cette problématique. En parallèle, différents modèles sont développés afin de modéliser des structures de plus en plus complexes, en utilisant notamment les propriétés périodiques dans le but d'étudier la propagation des ondes. Cette dernière permet une étude approfondie des paramètres vibro-acoustique de la structure.

Cette thèse se propose d'étudier des panneaux sandwichs dont le cœur est constitué d'un empilement de nids d'abeille. L'empilement est effectué sans peau intermédiaire, ce qui mène à une rupture d'impédance due aux surfaces de contacts entre les couches. De plus, une telle structure permet d'augmenter l'espace de design jusque-là limité par les structures standard composées d'un unique cœur. Il est alors possible d'obtenir de nombreuses configurations sans altérer la masse, grâce notamment à des décalages entre les couches. Un modèle paramétrique est proposé afin de permettre l'extraction d'une cellule unitaire à travers l'épaisseur du panneau et donc d'appliquer les propriétés périodiques.

La modélisation des structures multicouches en nid d'abeille est effectuée via le modèle éléments finis de la cellule unitaire et l'extension d'un modèle existant afin d'obtenir les propriétés en transmission acoustique. L'étude se focalise alors sur les phénomènes de fréquences de transition, de transmission sonore ainsi que les phénomènes de couplage d'ondes et de résonances internes, pour finir avec une optimisation des paramètres géométriques et l'étude de l'influence de ces derniers sur les performances mécaniques et acoustique de la structure.

Bien que les propriétés mécaniques lors d'un chargement en compression orthogonal au plan du nid d'abeille se révèlent diminuées dans le cas des structures multi-coeur, il est possible d'augmenter fortement leurs propriétés en compression dans le plan du coeur. Celles-ci sont étudiées via la comparaison d'une structure multi-couche en nid d'abeille hexagonal avec une structure standard.

Finalement, ces travaux de thèse se terminent par une étude de l'absorption acoustique avec notamment l'ajout de perforations sur les peaux supérieurs de la structure et l'effet

thermo-visqueux qui se produit dans le coeur. En effet, il est possible d'augmenter la dissipation d'énergie de l'onde acoustique en modifiant la géométrie du nid d'abeille de chaque couche, et donc d'agir sur le coefficient d'absorption. Le parallèle est effectué avec les structures poreuses et les paramètres de Jhonson-Champoux-Allard sont calculés pour caractériser l'écoulement du fluide acoustique ainsi que pour alimenter le modèle.
Une forte augmentation de la transmission acoustique est obtenue sur l'ensemble de la plage de fréquence étudiée ainsi qu'une amélioration des performances en absorption. Toutefois, cela entraîne la diminution des propriétés mécanique dont le module de compression ainsi que la rigidité dynamique.

Mots-clés : multicœur en nid d'abeille, vibroacoustique, transmission et absorption acoustique, fréquence de transition, veering, optimisation.

Abstract

In this last decades, honeycomb sandwich panels have been the subject of intensive researches. Indeed, their high mechanical performance combined to a low stiffness to weight ratio result in a reduced acoustic efficiency. Therefore, many designs are usually proposed to overcome this issue. Besides, different methods are developed to model more complex structures using the periodic structure theory to study the wave propagation allowing to investigate the vibroacoustic parameters.

The main purpose of this thesis is to investigate the vibroacoustic multi-scale behavior of multi-layer core topology systems which consist on stacking layers of honeycomb cores leading to an impedance mismatch between layers. In addition, such structures allow to increase the design space up to now limited to standard sandwich panels made of a single honeycomb core. Therefore, it is possible to obtain many configurations keeping the mass constant with simple shifting process between layers. A parametric model is proposed allowing to extract the unit cell through the thickness of the panel and to apply the periodic structure theory.

Modelling multi-layer core topology systems has been performed using the wave finite element method, and an extended method has been proposed to solve the acoustic transmission problem. The study is focused on transition frequencies, the sound transmission loss as well as veering effects and internal resonances, to finally optimize the geometrical parameters and to analyze their influence on the acoustical and mechanical performances of the structure.

Although the out-of-plane compression properties of multi-layer core topology systems are reduced, it is possible to strongly improve the in-plane compression properties. These later are studied by comparing a multi-layer hexagonal core and a standard single hexagonal core.

Finally, using multi-layer core topology systems and a perforated upper skin, it is possible to increase the energy dissipation occurring inside the core and thus, improve the sound absorption coefficient. Therefore, the thermo-viscous effect is considered. The acoustic behavior is similar to porous media and the Johnson-Champoux-Allard parameters are retrieved to characterize the acoustic fluid flow.

An improvement of the sound transmission loss and the sound absorption coefficient is ob-

tained in a broadband frequency and the obtained resonance frequencies can be modified. However, this leads to lower mechanical properties especially the compression modulus and the dynamic rigidity.

Keywords: multi-layer core systems, vibroacoustic, transmission loss and sound absorption coefficient, transition frequency, veering, optimization.

Samenvatting

In deze laatste decennia zijn de sandwichpanelen op honingraatband het onderwerp geweest van intensieve onderzoeken. Hun hoge mechanische prestaties gecombineerd met een lage stijfheid/gewichtsverhouding resulteren in een verminderde akoestische efficiëntie. Daarom worden veel ontwerpen meestal voorgesteld om dit probleem te overwinnen. Daarnaast zijn er verschillende methoden ontwikkeld om complexere structuren te modelleren met behulp van de periodieke structuur theorie om de golf propagatie te bestuderen waardoor de vibroakoestische parameters te onderzoeken.
Het belangrijkste doel van dit proefschrift is het onderzoeken van het vibroakoestische multiscale gedrag van meerlaagse kerntopologiesystemen die bestaan uit stapellagen honingraatkernen die leiden tot een impedantie-mismatch tussen lagen. Bovendien kunnen dergelijke structuren de ontwerpruimte tot nu toe beperken tot standaard sandwichpanelen die van één honingraatkern zijn gemaakt. Daarom is het mogelijk om vele configuraties te verkrijgen die de massa constant houden met eenvoudig verschuivend proces tussen lagen. Er wordt een parametrisch model voorgesteld waarmee de eenheidscel door de dikte van het paneel kan worden geëxtraheerd en de theorie van de periodieke structuur kan worden toegepast.
Het modelleren van meerlaagse kerntopologiesystemen is uitgevoerd met behulp van de Wave eindige element methode, en er is een uitgebreide methode voorgesteld om het akoestische transmissieprobleem op te lossen. De studie is gericht op transitiefrequenties, het verlies van geluidstransmissie, V-effecten en interne resonanties, om uiteindelijk de geometrische parameters te optimaliseren en hun invloed op de akoestische en mechanische prestaties van de structuur te analyseren.
Hoewel de compressie-eigenschappen buiten het vlak van meerlaagse kerntopologiesystemen worden verminderd, is het mogelijk om de compressie-eigenschappen in het vlak sterk te verbeteren. Deze worden later bestudeerd door een meerlaagse zeshoekige kern te vergelijken met een standaard enkele zeshoekige kern.
Ten slotte is het met behulp van meerlaagse kerntopologiesystemen en een geperforeerde bovenhuid mogelijk om de energiedissipatie in de kern te verhogen en zo de geluidsabsorptiecoëfficiënt te verbeteren. Daarom wordt het thermo-viskeuze effect overwogen. Het akoestische gedrag is vergelijkbaar met poreuze media en de parameters Johnson-

Champoux-Allard worden opgehaald om de akoestische vloeistofstroom te karakteriseren. Een verbetering van het geluidverlies en de geluidsabsorptiecoëfficiënt wordt verkregen in een breedbandfrequentie en de verkregen resonantiefrequenties kunnen worden gewijzigd. Dit leidt echter tot lagere mechanische eigenschappen, met name de compressiemodulus en de dynamische stijfheid.

Trefwoorden: Meerlaagse kernsystemen, vibroakoestisch, Transmissieverlies en geluidsabsorptiecoëfficiënt, Overgangsfrequentie, Sluier, Optimalisatie.

Contents

List of Figures

List of Tables

Introduction

Context

Lightweight components are crucial economical and environmental requirements in modern transportation industry. Many solutions have been developed over the past decades, such as honeycomb panels or composite lay-ups exhibiting remarkable stiffness-to-weight ratio, hence guaranteeing the structural integrity of aircraft and many other engineering structures while drastically reducing their overall weight and fuel consumption.

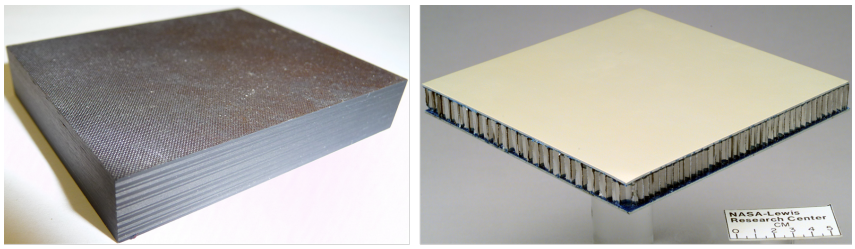

(a) (b)

Figure 1: (a) Composite panel (b) Honeycomb sandwich panel.

Since the well-being of users and passengers has not been considered in the first stage, the consequence has been the raise of unsatisfactory sound acoustic insulation. Moreover, progresses in medicine [1] have shown up the harmful effects of being exposed to a lot of noise. Noisy environments directly affect the health by damaging the hearing and disrupting the organism. For specific fields as aerospace and aeronautics, the noise level is so high that the effect on the structure itself cannot be neglected and should be considered to develop accurate numerical model. During the launch vehicle and lift-off stage, the engine exhaust noise can reach 160 decibels. It leads to high levels of vibration up to damaged structures. In addition, aircrafts are used to carry many stuff without any damages and the generated vibrations are generally the first reason which cause these issues. The frequency range for such environments can be considered as mid-high frequency. Finally, making lightweight structures involve acting on three different aspects: the material used for the structure, the structure's geometry or combining both solutions.

Research objectives

The purpose of this research is to carry out a study on vibroacoustic performance of multi-layer core topology systems (MLCTS). This involves an extension of a proposed model in the literature to analyse the vibroacoustic behavior and then, perform a design optimisation process. Besides, sound absorption properties involving viscous-thermal loss effects are also investigated. Four main objectives are listed as follows:

- Analysis of the vibroacoustic behavior of MLCTS investigating the Sound Transmission Loss (STL) and transition frequencies.
- Optimization and parametric analysis of the core geometry of MLCTS to enhance their vibroacoustic properties.
- Investigation of local dynamic behavior and their impact on the vibroacoustic properties.
- Parametric survey on the influence of the core geometry on the Sound Absorption Coefficient (SAC) and the Sound Transmission Loss (STL).

Thesis outlines

This thesis includes 7 chapters allowing to reach the objectives previously described.

Chapter 1 is dedicated to the literature review on the research topic. It starts with a brief overview of typical structures usually used in the industry such as composites and porous media. Then, sandwich panels are described and followed by the introduction to the periodic structure theory (PST). Afterwards, the definition of the studied indicators is given as well as the review on the existing models to calculated them. In addition, several works consisting on the improvement of vibroacoustic performances are discussed to finally be focused on recent developments about MLCTS in the literature.

Chapter 2 is an introduction to MLCTS and the parametric model that is used for the thesis work is described. Two models are described and a parametric analysis involving multi-layer rectangular core systems (MLRCS) is performed on the transition frequency and the STL.

Chapter 3 is devoted to the investigation of the veering effect and internal resonances occurring in MLCTS, and their ability to improve the STL for a specific frequency.

Chapter 4 is focused on an optimisation process used to retrieve the best core geometry to improve the STL in a broadband frequency, as well as a parametric survey on the

influence of the geometrical parameters defined in the parametric model on the STL and mechanical properties including the static compression and shear modulus.

Chapter 5 is mainly about the ability of MLCTS to enhance both the STL and SAC at low frequencies and for a broadband frequency under normal incidence acoustic waves by adding the viscous-thermal effect occurring inside the stacked cores.

Chapter 6 investigates the in-plane compression properties between a standard single hexagonal core and a multi-layer hexagonal core.

Chapter 7 formulates the conclusions and perspectives of the thesis works.

Chapter 1

State of the Art

Contents

1.1 Design overview

Many sort of designs were developed in the literature to enhance mechanical and acoustical properties of lightweight structures. They have been introduced including more complex geometry which have led to the improvement of models to accurately estimate their properties. Those structures combine many concepts such as composites, sandwich panels, porous media, resonators, periodic structures and so on. It is thus relevant to show the evolution of such designs to finally introduce those studied in this thesis.

1.1.1 Composite structures

Composite assemblies have been the subject of intense researches. They consist of mixing different materials to obtain better properties compared to simple panels. These structures have come up to overcome the mechanical performances limitations of simple panels [2]. Laminates are specific composite structures made by stacking layers of several or the same material with different or same orientations of fibers for each layer (specified by the angle θ in Fig. 1.1). This allows to change their properties in specific directions, having isotropic, orthotropic or anisotropic structures (Fig. 1.1).

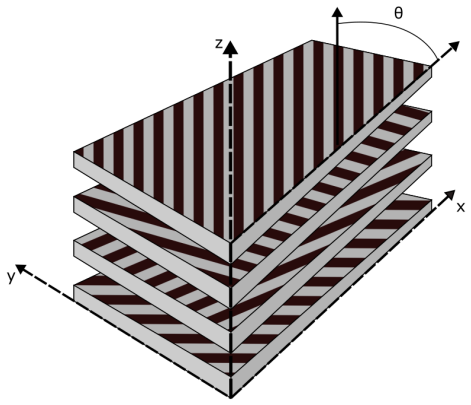

Figure 1.1: Schematic representation of a laminate.

All fibers, materials and layers are stuck together using resins and thin adhesive films. Composite structures lead to high stiffness to weight ratio with better mechanical properties than simple panels made of steel or aluminum. In addition, controlling the orientation gives the opportunity to optimize the strength for specific directions other than loading directions.

Basically, the Classical Laminate Theory (CLT) [2] is used to obtain all required properties of the structure to retrieve the stress-strain relations to finally have the homogenized structure with the Young and Shear Modulus and the poisson ratio in each direction. Extensions of this method were also investigated using higher order deformations theory to better capture the transverse shear effect between layers [3].

In terms of acoustic properties, analytic formulations are developed based on plates theory using homogeneous properties of the composite structure [4]. These methods have the benefit to be simple to implement in finite element softwares. Nevertheless, the modelling process is based on analytic approaches and remains limited as soon as the complexity of the studied structure increases. Experimental analysis of composite structures induce adding more parameters to know in the study (orientation, non-homogeneity and so on) to interpret all the results as shown by Pendleton et al. [5]. Besides, this type of models were used to recover the properties of 3D printed structures and to obtain better correspondence compared to isotropic models since the principle of the 3D printing is to build panels layers by layers authors [6, 7, 8].
Optimization processes were also carried out to find out the best staking sequences to shift the first natural frequency to a higher frequency [9, 10, 11]. Composite structures have many functionalities which can be enhanced to be used in many industrial applications as explained by Gibson et al. [12]. In the military domain, they are widely used to carry weight more easily and due to their better mechanical performances [13] and low mass for transportation. Carbon fiber, epoxy and PWC are the most used materials to make composite panels. However, the acoustic radiations of composite structures are still not negligible as well as poor acoustic insulation performances. Moreover, the manufacturing process and the cost of materials remain high and require very well-controlled production steps.

1.1.2 Porous media

Alternative solutions have been developed to overcome the acoustic issues by introducing porous media. This material is made of a skeleton containing interconnected cavities called pores filled with liquid, a specific gas or air. There are 3 main categories of skeleton which can be listed as fibrous, granular or solid structures as illustrated in Fig. 1.2. Due to the thermal-viscous effect within the cavities, porous media creates energy dissipation inside the pores leading to a high improvement of sound properties especially the Sound Absorption Coefficient (SAC) and high damped structures as well. Moreover, it is possible to stack layers of several porous media (sound packages) to enhance the SAC with lower weight.
Besides, poroelastic media was firstly described by Biot [17, 18] introducing the well-known Biot's theory and then followed by more complex formulations [19]. Allard [20] explained all the physics related to sound propagation in porous media by describing the transfer matrix method concept (TMM), which was firstly explained by Brouard et al [21] allowing to calculate the sound properties for structures made of several layers. The TMM is particularly appreciated in the acoustic engineering due to their fast implementation. A porous media is then characterized by a matrix using up to 9 geometrical and physical

Figure 1.2: Porous media made of (a) fibrous [14], (b) granular [15] and (c) foam [16] materials.

parameters based on Biot's theory. Besides, wave propagation in porous media have been also studied by Serra et al. [22, 23] taking boundary conditions into account.
Empirical methods were also explored by Delany et al. [24] and extended by Miki et al. [25, 26]. They describe in a empirical way the complexity of porous media using experimental characterizations and investigate the effect of these parameters on sound properties. Since many physical parameters need to be retrieved, several methods were developed to characterize some specific parameters related to porous media by analytical [27] and experimental approaches, direct [28] or inverse methods [29, 30]. All these processes and the number of parameters to determine can be complicated to set up. Nevertheless, the high efficiency of the acoustic absorption in addition to their low weight gives an important interest for automotive industry widely used for acoustic treatments and sound packages using melamine, metallic foams [16], fibers [31] or granular [15] adding perforations [32, 33] and inclusions [34] or stacking layers of foams [31, 35, 36, 37].
Concerning the manufacturing process, it is difficult to maintain uniform parameters inside porous media (porosity, density, viscous length, ...) and many uncertainties and issues result from the process. In addition, cutting or reshaping porous medias is not an easy task. Finally, the poor mechanical properties of such structures led the industry to tackle this issue by making sandwich panels combining the high mechanical performances of laminate structures and standard panels, with the acoustic efficiency of a core media located in between.

1.1.3 Sandwich structures

Sandwich panels are defined as structures made of a thick core surrounded by two thin face-sheets as shown in Fig. 1.3 with most of times, stiff skins and soft cores. They can be firstly separated in 4 categories depending on the core design [38]: foams (a), truss (b), honeycombs (c) (rectangular, hexagonal, auxetic, ...) and web core (d) (also called

corrugated core) as illustrated in Fig. 1.3.

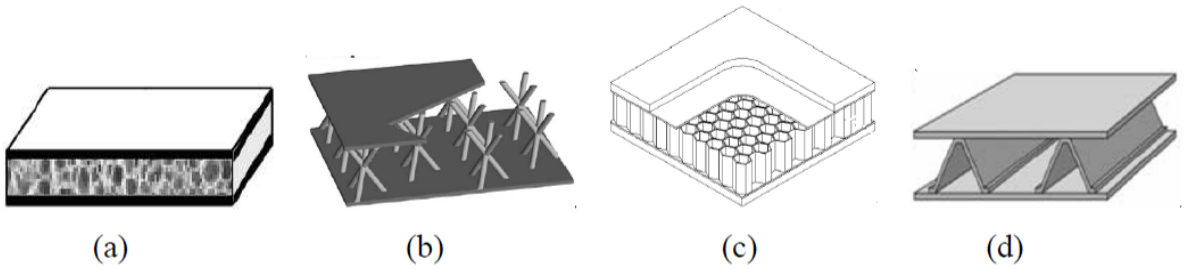

Figure 1.3: Sandwich panels with (a) foam core, (b) truss core, (c) honeycomb core and (d) web core [39].

Those type of designs are compared by Arunkumar et al. [40]. The first configuration enhances the acoustic efficiency adding damping in the structure whereas the second increases significantly the stiffness to weight ratio but in contrast reducing the acoustic performances. In terms of mechanical properties, the core rigidity enhances the tensile and compression modulus of the whole structure and the core geometry can lead to an anisotropic material. Finally, the last two configurations are mainly used for building constructions. Sandwich panels are often considered as periodic structures consisting on repeating an representative elementary volume (REV) in one, two or three dimensions, also called unit cell. Under wave excitation and at some specific frequencies, it will make occur specific characteristics. This topic have been greatly studied in these last decades especially for aerospace industry. Before, Barton et al. [41] and Grosveld et al. [42] showed how honeycomb panels mixed with sound packages including acoustic blankets used on the fuselage improve the sound insulation under in-situ measurements.
The transmission loss modelling of sandwich panels has been fully studied by Dym et al. [43, 44] to then optimize their design for better acoustic efficiency [45]. Analytical formulations were developed by Moore et al. [46] considering isotropic and orthotropic cores. In 2003, Buannic et al. [47] proposes a method to homogenize corrugated core sandwich panels but neglecting transverse shear effects. The same method has been performed by Catapano et al. [48] for honeycomb cores and then used to provide a finite element model (FEM) to do an optimization to obtain better mechanical properties [49]. In 2015, Malek and Gibson [50] studied more specifically hexagonal honeycomb cores with double thickness cell walls as it is generally manufactured in the aerospace industry. Besides, it is also possible to characterize these structures with experimental measurements or numerical analysis to retrieve the elastic modulus [51], the shear modulus [52] or the bending stiffness [53]. Other approaches based on analytical and transfer matrix formulation have been developed to predict wave propagation in sandwich structures [54, 55]. However, such models are limited to standard structures made of a single core and with specific core designs (hexagonal, auxetic, ...). Therefore, the Wave finite element

method (WFEM) using the Periodic Structure Theory (PST) released to be capable to model periodic structures involving more complex core designs (Section 1.2). Recently, an interesting review was proposed by Hussein et al. [56] about the dynamic of phononic materials including periodic structures.

1.2 The Periodic Structure Theory (PST)

The PST was firstly described by Mead et al. [57] using the well-known Bloch Floquet Theorem developed by Brillouin [58]. This concept gives the opportunity to study the wave propagation in periodic structures introducing propagation constants. Therefore, it is possible to obtain the dispersion curve as well as wave propagation speeds which are then used to retrieve the vibroacoustic properties of the structure. The static and dynamic analysis is then restricted to the unit cell and simplify the resolution. This theory was implemented in finite element sofwares to provide the so called WFEM which is nowadays widespread and applied on 1D and 2D periodic structures. Such a method involves modelling and meshing only the unit cell instead of the whole panel reducing drastically the computational cost. In the following section, the 1D and 2D formulation of the WFEM are described.

1.2.1 Wave finite element: 1D formulation

The unit cell of a 1D periodic structure is schematically depicted in Fig. 1.4 with a length d.

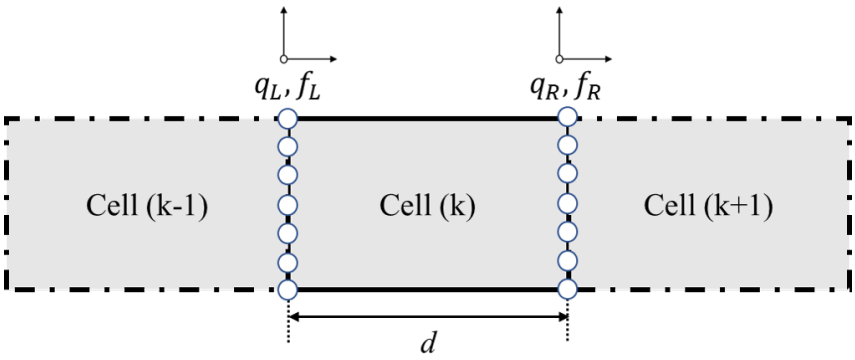

Figure 1.4: Unit cell of a 1D periodic structure with subdivision of the degrees of freedom (dofs).

The 1D formulation for waveguides using a FEM was proposed by Mace and Duhamel [59, 60]. The dynamic equation of the unit cell yields to:

$$\begin{pmatrix} F_L \\ F_R \end{pmatrix} = \begin{pmatrix} D_{LL} & D_{LR} \\ D_{RL} & D_{RR} \end{pmatrix} \begin{pmatrix} u_L \\ u_R \end{pmatrix} \tag{1.1}$$

where u_L, u_R, F_L and F_R denote the displacement on the left and right and the forces applied to the left and right side of the unit cell, respectively. The dynamic stiffness matrix ($\mathbf{D}$) of the unit cell is defined by the stiffness ($\mathbf{K}$) and mass ($\mathbf{M}$) matrix extracted from commercial finite element softwares and the structural damping is taken into account within the damping loss factor η leading to:

$$\mathbf{D} = (\mathbf{K} + i\eta\mathbf{K}) - \omega^2\mathbf{M}. \tag{1.2}$$

The Floquet-Bloch theorem applied to the displacements and forces vectors leads to:

$$u_R = u_L\lambda \quad F_R = -F_L\lambda \tag{1.3}$$

in which λ is defined as the propagation constant defined as :

$$\lambda = \exp(ikd) \tag{1.4}$$

where d is depicted Fig. 1.4. The complex wavenumber k of the infinite periodic structure is finally retrieved by solving the quadratic eigenvalue problem :

$$(\lambda^2\mathbf{D}_{RL} + \lambda(\mathbf{D}_{RR} + \mathbf{D}_{LL}) + \mathbf{D}_{LR})u_L = 0 \tag{1.5}$$

This equation depends on the frequency and values of ω are imposed real. In order to consider only propagating waves without attenuation, the wavenumber k is real. Indeed, the imaginary part represents the attenuation of the waves leading to a spatial decaying amplitude. Therefore, a filtering process should be applied to consider only propagating solutions. The chosen criterion [60] yields to:

$$\mathrm{Im}(k) = \varepsilon\,\mathrm{Re}(k) \tag{1.6}$$

with ε which should be evaluated depending of the considered structure (composite, damped,...).

1.2.2 Wave finite element: 2D formulation

The unit cell of a 2D periodic structure is schematically depicted in Fig. 1.5 and can be separated in 9 different regions of dofs associated with the nodes at these locations as follows: edge corners (u_1, u_2, u_3, u_4), left, right, after and forward surface (u_L, u_R, u_A, u_F) and the internal region (u_I). The vector of dofs related to the displacement $\mathbf{U}$ is then partitioned as follows:

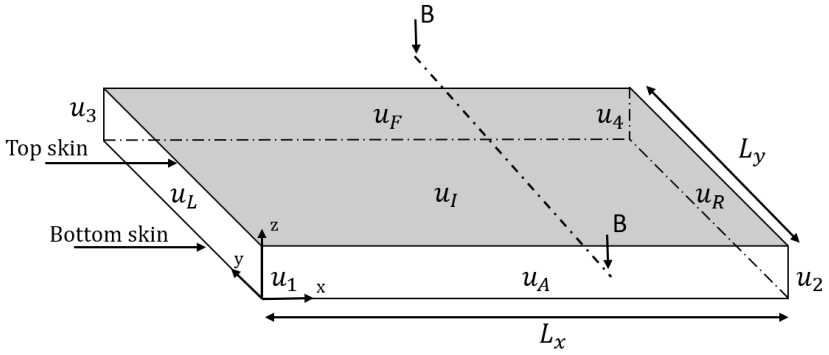

Figure 1.5: Unit cell of a 2D periodic structure with subdivisions of the dofs.

$$\mathbf{U} = [u_1 \;\; u_2 \;\; u_3 \;\; u_4 \;\; u_L \;\; u_R \;\; u_A \;\; u_F \;\; u_I]. \tag{1.7}$$

For complex unit cells, the number of dofs may remain high. Many methods of model order reduction (MOR) have been developed for such problems and the most commonly used one is the Component Modal Synthesis (CMS) [61]. It is an extension of the Craig Bampton approach [62]. The principle is to describe the global response of the structure by different modes of local substructures. In the WFEM context, the CMS is applied to the internal dofs u_I as defined in Fig. 1.5. Besides, the MOR developed by Droz et al. [63, 64] uses a wave basis approach based on a reduced set of wave-shapes. Recently, Boukadia et al. [65] proposes a MOR to fastly compute dispersion curves. They can be combined with the CMS to drastically reduce the computational cost and lead to a reduced dynamic stiffness matrix $\tilde{\mathbf{D}}$ after the dynamic condensation. The strategy to apply these MOR was fully discussed in the paper of Zergoune et al. [66]. The next step is to apply the Bloch's theorem at boundaries which gives the following relations:

$$u_2 = u_1\lambda_x \quad u_3 = u_1\lambda_y \quad u_4 = u_1\lambda_x\lambda_y \quad u_R = u_L\lambda_x \quad u_F = u_A\lambda_y, \tag{1.8}$$

with,

$$\lambda_x = \exp(-i\mu_x) \quad \lambda_y = \exp(-i\mu_y) \quad \mu_x = k_x L_x \quad \mu_y = k_y L_y, \tag{1.9}$$

in which k_x and k_y are the wavenumbers along the x and y direction. The direction x and y correspond to in-plane directions as illustrated in Fig. 1.5. In terms of modelling, these relations Eq. (1.8) imply that the same number of nodes should be used at associated boundaries while there is no constraint on the internal nodes of the unit cell. The PST [67] is then used to compute the propagation constants λ_x, λ_y and eigenvectors Ψ from the spectral equation:

$$\Lambda^{\mathrm{T}}(\lambda_x, \lambda_y) \cdot \tilde{\mathbf{D}} \cdot \Lambda(\lambda_x, \lambda_y) \; \Psi = (0), \tag{1.10}$$

where Λ^{T} is defined by:

$$\Lambda^{\mathrm{T}} = \begin{pmatrix} \mathrm{I} & \lambda_x \mathrm{I} & \lambda_y \mathrm{I} & \lambda_x\lambda_y \mathrm{I} & 0 & 0 & 0 & 0 \\ 0 & 0 & 0 & 0 & \mathrm{I} & \lambda_x \mathrm{I} & 0 & 0 \\ 0 & 0 & 0 & 0 & 0 & 0 & \mathrm{I} & \lambda_y \mathrm{I}. \end{pmatrix} \tag{1.11}$$

The solution of the quadratic eigenvalue problem (Eq. (1.10)) at a given frequency ω is called a direct solution and allows an estimation of the complex frequency-dependent propagation constants and eigenvectors. One of the value of the pair (λ_x, λ_y) has to be 0 to solve the equation and to calculate the wavenumber k in a specific direction x or y. Dispersion curves are then obtained and give the opportunity to calculate the transition frequency of the sandwich panel or in certain cases, simplify the calculation of the Sound Transmission Loss (STL). Finally, it can be mention that such methods can be extended to poroelastic structures [22, 23] or curved panels [68].

1.3 Vibroacoustic indicators

In the following section, the STL, the SAC and the transition frequency are described. The expression of the STL and the SAC are given considering the transmission problem of a simple panel. Then, transition frequencies are illustrated with the dispersion curves of the flexural waves of a random standard sandwich panel made of a rectangular core to highlight the complex dynamic behavior occurring. The manufacturing process of MLCTS can be well-controlled using an industrial 3D printer compared to the process consisting on adding adhesive layers between honeycomb layers. Moreover, the industrial 3D printer available in the laboratory is a Fortus 450. Therefore, those indicators are illustrated using a standard sandwich panel made of a rectangular core with an elastic modulus $E = 1,8 \cdot 10^9$ Pa, a density $\rho = 985$ kg/m^3 and the poisson ratio $\nu = 0,35$ corresponding to the characteristic of the thermoplastic polymer called Acrylonitrile Butadiene Styrene (ABS). This material is used by industrial 3D printers. The skins are made of aluminium with $E = 72 \cdot 10^9$ Pa, $\rho = 2800$ kg/m^3 and $\nu = 0,33$. The global hysteretic damping η is evaluated to be 2 %. The geometrical parameters of the unit cell are : $L_x = 12$ mm, $L_y = 12$ mm, $t_s = 1$ mm the thickness of the skin, $t_c = 1$ mm the thickness of the core and $H = 9$ mm which is the height of the core.

1.3.1 The transition frequency

The transition frequency is a vibroacoustic indicator widely used in aerospace industry. Two different transition frequencies are currently defined in the literature [69]: the first corresponds to the frequency where the dynamic behavior of the sandwich panel switches from bending to shear motion while the second transition frequency occurs when the

bending behavior is located in skins. Typically, both transition frequencies define four main regions separating four main dynamic behaviors of a sandwich panel observed using flexural waves [70]. They are illustrated in Fig. 1.6 and delimited according to the elastic strain energy storage either in the core or the skins of the sandwich panel. The results are shown representing the flexural waves in both directions x and y due to the orthotropy of the structure. In addition, the intersection between the flexural and the acoustic wavenumber (k_0) corresponds to the critical frequency of the structure in which the STL drops. However, due to the orthotropy of the sandwich panel, two critical frequencies are obtained. Therefore, the STL is expected to be drastically reduced between f_{cx} and f_{cy}. Wavemode shapes were captured using in-house softwares. Different zones can be defined as follows:

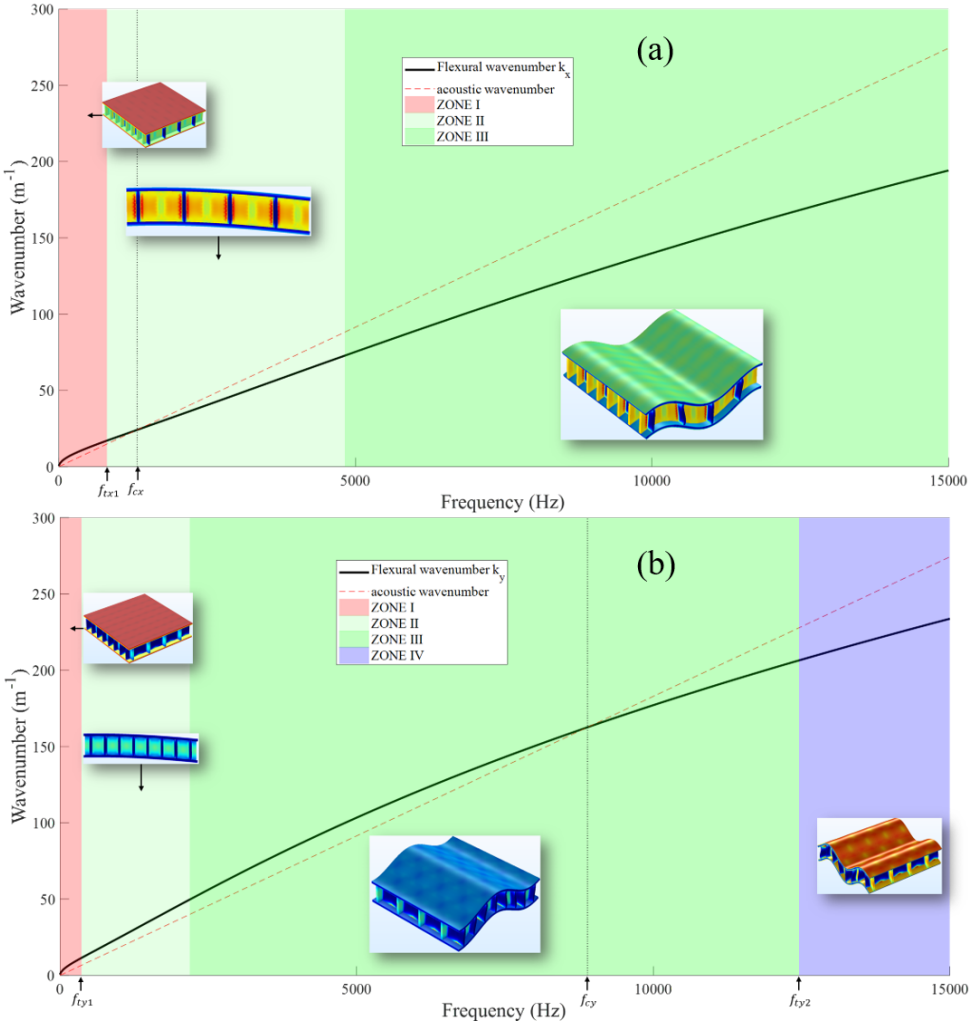

Figure 1.6: Flexural waves of a standard sandwich panel made of a rectangular core (a) k_x and (b) k_y.

- ZONE I : in this frequency range the flexural wave corresponds to a global bending behavior of the sandwich panel.

- ZONE II : it is triggered by the first transition frequency and the shear motion of the core governs the global shape of the sandwich panel. The strain energy is then concentrated in the core. In this zone, the wavenumber is a linear function of *omega* (Section1.6.1).

- ZONE III : the flexural behavior is governed by the bending of the sandwich panel and the strain energy of the core starts to be converted into strain energy storage in the skins.

- ZONE IV : it is triggered by the second transition frequency and the bending behavior is still dominant but concentrated in the skins.

Transition frequencies do not correspond only to the study at specific frequencies but also to transition ranges in which the structure can be characterized by a specific dynamic behavior. It can be defined in terms of wavemotion [70] but also in terms of strain energy [71] storage either in the core or the skins of the sandwich panel.
Currently, the first transition frequency remains the most critical indicator since it occurs at low frequencies. The second transition frequency is triggered earlier along y compared to the direction x since the unit cell seems to be more flexible in this direction. In orthotropic sandwich panels, transition frequencies are defined as the minimum value between the pairs (f_{tx}, f_{ty}). There is a need to understand how these dynamic behaviors are triggered and more generally how to adjust the size of these different regions to modify the dynamic behavior of sandwich panels and thus, their vibroacoustic properties.

1.3.2 Acoustic indicators

Plenty of indicators are used to quantify the acoustic efficiency of sandwich panels. In this thesis, the transmission problem is considered and the STL and the SAC are used as targeted indicators since they give the acoustic efficiency of structures and they are widespread indicators in the industry. Moreover, they can be measured using an impedance tube for normal incidence waves or using anechoic rooms or specific cabins for diffuse acoustic field. The transmission problem is depicted in Fig. 1.7.
The sandwich panel separates two semi-infinite fluid domains considered as air with a density $\rho = 1{,}21$ kg/m^3 and the speed of sound $c_0 = 341$ m/s. The incident acoustic wave impinges on the structure with an angle of incidence θ_i and is oriented by the azimuth angle φ with respect to x and y direction. This produces three acoustic waves which can be represented with their acoustic wave power: W_r, W_a and W_t representing the reflected, absorbed and transmitted wave power. The incident and reflected angle, θ_i and θ_r, are assumed to be equal. It is valid when the top surface is considered as a perfect plane. If the structure is homogeneous, then $\theta_i = \theta_r = \theta_t$ whatever it is included inside. The

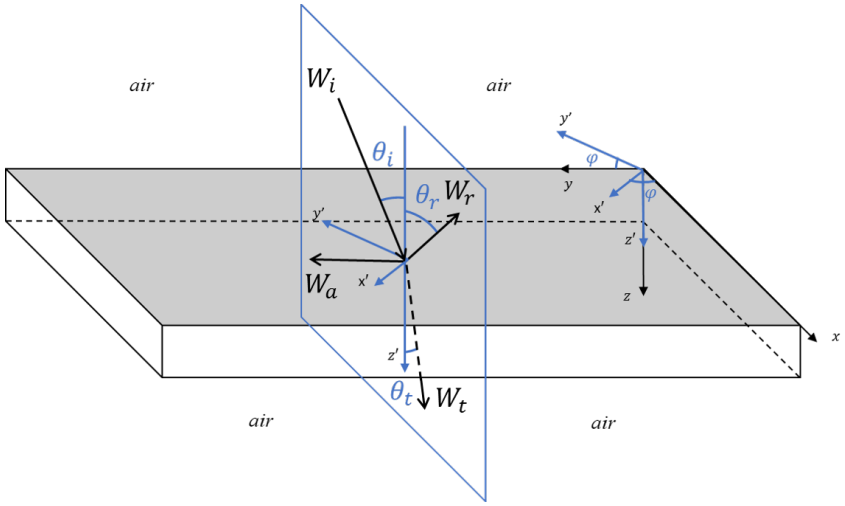

Figure 1.7: Incident, reflected, transmitted and absorbed plane waves at the interface of an infinite sandwich panel.

acoustic wave travelling through the structure leads to a transmitted wave on the other side with an angle θ_t and an absorbed wave which travels inside the structure. The STL of the structure is defined as the ratio of the transmitted wave power (W_t) and the incident wave power (W_i) for each specific angle of incidence θ_i as follows:

$$STL(\theta_i, \varphi, \omega) = -10 \log_{10}(\tau), \tag{1.12}$$

with the acoustic transparency $\tau(\theta, \varphi, \omega) = W_t \ / \ W_i$, while the SAC is defined as follows:

$$SAC(\theta_i, \varphi, \omega) = 1 - \frac{W_r}{W_i} - \frac{W_t}{W_i} \tag{1.13}$$

It is possible to define the STL and the SAC for the diffuse acoustic field by integrating over all incidence angles $\theta_i \in [0°, \theta_{max}\,]$ with $\theta_{max} = 78°$ and $\varphi \in [0°, 360°]$. The limitation of the angle θ_i is due to measurement constraints and the difficulty to capture grazing angles corresponding to angles close to $\theta_i = 90°$ [72]. Consequently, the diffuse acoustic field transmission loss and the diffuse acoustic field absorption are given by:

$$\tau_d\ (\omega) = \frac{\int_0^{2\pi} \int_0^{\theta_{max}} \tau(\omega, \theta, \varphi) \sin(\theta) \cos(\theta)\, d\theta\, d\varphi}{\int_0^{2\pi} \int_0^{\theta_{max}} \sin(\theta) \cos(\theta)\, d\theta\, d\varphi} \tag{1.14}$$

$$SAC_d(\omega) = \frac{\int_0^{2\pi} \int_0^{\theta_{max}} SAC(\omega, \theta, \varphi) \sin(\theta) \cos(\theta)\, d\theta\, d\varphi}{\int_0^{2\pi} \int_0^{\theta_{max}} \sin(\theta) \cos(\theta)\, d\theta\, d\varphi} \tag{1.15}$$

and finally, $STL_d(\theta_i, \varphi, \omega) = -10 \log_{10}(\tau_d)$. The higher is the STL and the SAC, the better the structure is acoustically efficient. The double integration leads to a very high computational cost. In the literature, the calculation of the diffuse acoustic field is rare and the integration is not always fully performed [73, 74]. It is mainly used to compare

models with experimental measurements or to compare different models. Moreover, the integration step for θ and φ needs to be very low to obtain converging results. A typical STL of an sandwich panel calculated for a diffuse acoustic field assuming infinite size structures is given by Fig. 1.8.

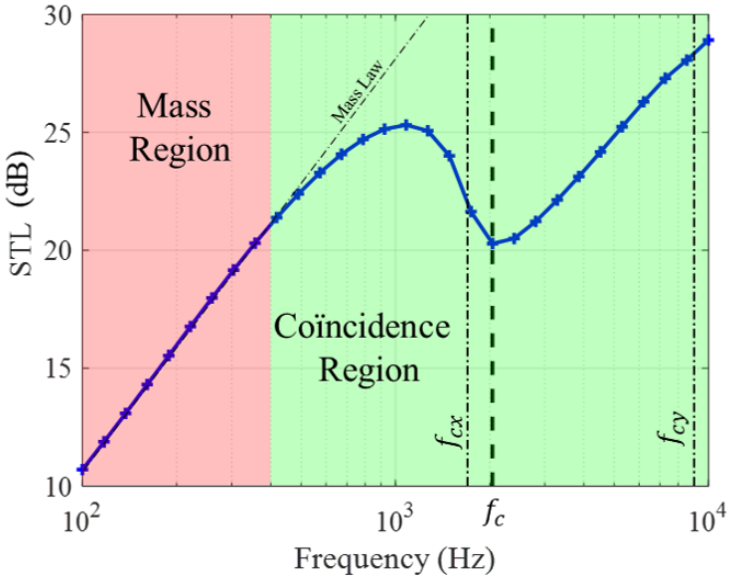

Figure 1.8: STL of the standard sandwich panel made of a rectangular core calculated for a diffuse acoustic field.

The critical frequency of the structure is depicted by f_c and occurs between f_{cx} and f_{cy}. As it can be noticed, the STL drops in this frequency range. At low frequencies and up to the coincidence region the STL is controlled by the mass law. In this frequency range, the STL is governed by the surface density. Besides, the coincidence region is mainly influenced by the damping [75] and the flexural behavior of the structure. For each angle of incidence, there is a coincidence frequency corresponding to the frequency in which the acoustic wavenumber and the flexural wavenumber of the structure are equal. In the diffuse acoustic field, it leads to a smooth region called the coincidence region in which occurs the critical frequency f_c involving all coincidence frequencies of the structure. This later occurs between f_{cx} and f_{cy}. Therefore, the main objective is to shift f_{cx} and f_{cy} to higher frequencies leading to the shift of the critical frequency f_c as well, and thus better acoustic performances in a broadband frequency.

1.4 Sound Transmission Modelling

1.4.1 Overview

Classical sandwich panels was analytically modelled by Kurtze et al. [76] to calculate the STL. The core is considered isotropic and the skins are described as thin plates and

they take the shear effect into account. Even though they obtained a good agreement with measurements, this method doesn't take the size effect into account and the isotropy of the material is not always verified. The finite size effect was predicted by Villot et al. [77] to calculate the sound radiation and the STL by applying a spatial windowing of plane waves. Renji [78] have shown the influence of shear waves in the STL and the increasing in higher frequencies due to the damping loss factor for diffuse acoustic field. Some works focused their study on specific designs as Shen et al. [79] proposing a theoretical model for corrugated cores and predicting the STL of hexagonal cores using a wave propagation approach [80]. Finally, Guillaumie [4] developed an analytical formulation for the STL and some vibroacoustic indicators based on the homogenization of the core and considering very stiff skins compared to the core. In 1992, Lauriks et al. [81] proposed a formulation based on multilayered systems called TMM applied to sandwich panels with porous media cores. Each layer is then characterized by a matrix including all the necessary properties to obtain the acoustic indicators. All matrices are multiplied to consider a multilayered system. A more general method was described by Brouard et al. [21] to be applied to solid, fluid and porous layers. These previous methods were valid for infinite size structures. The finite size effect was introduced in the TMM concept with Ghinet et al. [82] using the expression described by Villot et al. [77]. It was then extended to structures under mechanical excitation [83]. Three extensions of this method were discussed by Atalla et al. [84] to cop with several type of excitations and to deal with coupled panels using the Statistical Energetic Analysis (SEA). Vaicaitis [85] has proposed to model periodic structures when they are under Turbulent Boundary Layer (TBL). Hybrid method is also investigated by Dijkmans et al. [86] for buildings acoustic applications. Numerical modelling has been also developed to predict acoustic indicators in multilayered porous media [87]. WFEM and the PST were firstly combined by Mead et al. [57] and then used by Orrenius et al. [88] to retrieve the STL of a complex aircraft structure and then validated with experimental measurements. Besides, Ben Souf [89] studied the variability of mechanical parameters on the acoustic response. Software as VA-One or the SEA can be used to evaluate the STL of complex connected panels [90, 91]. Finally, some methods have been adapted to curve sandwich panels for the aircraft industry [92, 93, 94] and validated using real-scale curved panels [95]. Recently, the WFEM has been used in the literature to model the STL of complex unit cells. The Transfer Matrix Method (TMM) [20] can be combined with the WFEM as proposed by Parrinello et al. [74]. Besides, Christen et al. [96] proposed the use of nodal surfaces calculations combined with the WFEM as well as Yang et al. [97] but using shape functions. This two methods lead to a high computational cost compared to Parrinello et al. [74] since the entire unit cell is considered. However, they have the advantage to take all the dynamic behavior of the unit cell into account if local dynamic behaviors occur in the

core which is not possible with the TMM. Finally, Deckers et al. [98] uses a hybrid wave based method to model the semi-infinite surrounding acoustic domain of the unit cell considering their mutual dynamic interaction combined with the FEM to calculate the STL and the SAC. The next sections are devoted to the description of the method developed by Parrinello et al. [74] and then Christen et al. [96] which will be used in this thesis.

1.4.2 WFEM combined with TMM

Recently, Parrinello et al. [74] have developed a model combining the TMM and the WFEM. The main steps of this method can be illustrated as follows:

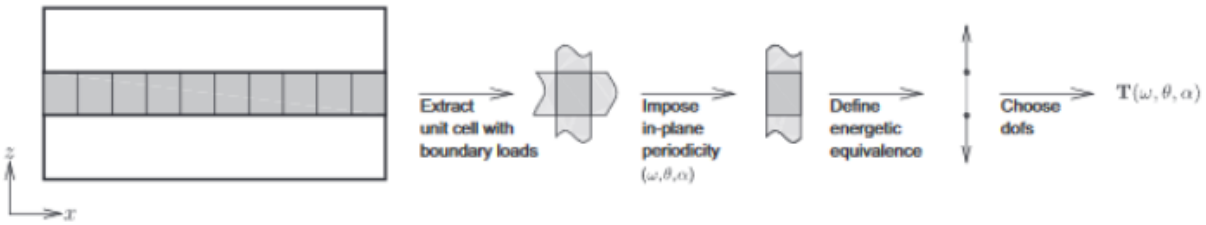

Figure 1.9: Procedure developed by Parrinello et al. [74] to obtain the transfer matrix of a unit cell.

The unit cell is extracted from the sandwich panel and the Bloch Floquet Theorem is applied. Then, an energetic equivalence is proposed calculating the work done by the nodal forces on the top and bottom skin. The transfer matrix $\mathbf{T}'$ of the unit cell is then obtained and leads to :

$$\mathbf{T}' \begin{pmatrix} q_T \\ e_T \end{pmatrix} = \begin{pmatrix} q_B \\ e_B \end{pmatrix} \tag{1.16}$$

where (q_T and q_B) and (e_T and e_B) are the generalized displacement (q) and force (e) on the top (T) and bottom (B) skin of the unit cell. Finally, the interface variables between layers should be modified depending on the model to describe the acoustic field. Three cases corresponding to fluid, solid and mixed interface are listed and given as follows:

$$\mathbf{V}_{fluid} = [p,\ v_z^f] \tag{1.17}$$

$$\mathbf{V}_{solid} = [v_x,\ v_y,\ \sigma_{zz},\ \sigma_{zx'}] \tag{1.18}$$

$$\mathbf{V}_{mixed} = [v_x,\ v_y,\ v_z^f,\ \sigma_{zz},\ \sigma_{zx'},\ p] \tag{1.19}$$

The required variables in the case of fluid interfaces correspond to the pressure and velocity of the fluid while solid interfaces involve the velocity and stress of the solid. Finally, mixed

interfaces include the velocity and stress of the solid as well as the pressure and velocity of the fluid. Therefore, the final calculation of the transfer matrix used in the TMM yields to three different calculations:

- **Fluid interface**

$$\mathbf{T}_{fluid} = \begin{pmatrix} 1 & 0 \\ 0 & 1/(i\omega\rho_0 A) \end{pmatrix} \mathbf{T}' \begin{pmatrix} 1 & 0 \\ 0 & -i\omega\rho_0 A \end{pmatrix}, \tag{1.20}$$

- **Solid interface**

$$\mathbf{T}_{solid} = \begin{pmatrix} i\omega\mathbf{E} & \mathbf{0} \\ \mathbf{0} & -\mathbf{F}/A \end{pmatrix} \mathbf{T}' \begin{pmatrix} \mathbf{E}^T/(i\omega) & \mathbf{0} \\ \mathbf{0} & A\mathbf{F}^T \end{pmatrix}, \tag{1.21}$$

where

$$\mathbf{E} = \begin{pmatrix} C & S & 0 \\ 0 & 0 & 1 \end{pmatrix}, \mathbf{F} = \begin{pmatrix} 0 & 0 & 1 \\ C & S & 0 \end{pmatrix} \tag{1.22}$$

- **Mixed interface**

$$\mathbf{T}_{mixed} = \begin{pmatrix} i\omega\mathbf{E} & \mathbf{G}/(i\omega\rho_f A) \\ \mathbf{G} & -\mathbf{F}/A \end{pmatrix} \mathbf{T}' \begin{pmatrix} \mathbf{E}^T/(i\omega) & \mathbf{G}^T \\ -i\omega\rho_f A\mathbf{G}^T & A\mathbf{F}^T \end{pmatrix}, \tag{1.23}$$

with,

$$\mathbf{E} = \begin{pmatrix} C & S & 0 & 0 \\ 0 & 0 & 1 & 0 \\ 0 & 0 & 1 & 0 \end{pmatrix}, \mathbf{F} = \begin{pmatrix} 0 & 0 & 1 & 0 \\ C & S & 0 & 0 \\ 0 & 0 & 0 & 0 \end{pmatrix}, \mathbf{G} = \begin{pmatrix} 0 & 0 & 0 & 0 \\ 0 & 0 & 0 & 0 \\ 0 & 0 & 0 & 1 \end{pmatrix} \tag{1.24}$$

in which $C = \cos\varphi$, $S = \sin\varphi$ and A is the total area of the unit cell $A = L_x\, L_y$. Therefore, each layer can be characterized by its own transfer matrix and then assembled by imposing interfaces continuity between layers leading to the matrix $\mathbf{H}$ as described by Allard [20]. Since the skins of sandwich panels are mainly made of laminate or simple panels, it is wise to use the usual transfer matrix formulation of solid mediums [20] and thus, settle for applying the described procedure only to the core without the skins leading to a reduced computational cost.

The calculation of the acoustic indicators is then obtained with the expression of the surface impedance of the structure as follows:

$$Z_s = -\frac{\det \mathbf{H}_1}{\det \mathbf{H}_2} \tag{1.25}$$

where $\mathbf{H}_k$ is the matrix in which the k^{th} column of $\mathbf{H}$ is removed. The reflection coefficient is finally given by:

$$R = -\frac{Z_s \cos\theta - Z_0}{Z_s \cos\theta + Z_0} \tag{1.26}$$

and the transmission coefficient by:

$$T = -(1+R)\frac{\det \mathbf{H}_{N-1}}{\det \mathbf{H}_1} \tag{1.27}$$

Finally $\tau = |T(\theta, \varphi, \omega)|^2$ and the calculation of the STL or the SAC is performed using Eq. (1.12) and Eq. (1.13) for specific angles or Eq. (1.14) for diffuse acoustic field.

1.4.3 WFEM combined with nodal surfaces

A finite element method have been developed by Christen et al. [96] using the WFEM combined with the use of nodal surfaces calculations to easily derive the STL from the dynamic behavior of the unit cell. This model has been applied to standard parallelepiped unit cells that can be modeled with 8-nodes brick elements. The unit cell used in this model is shown in Fig. 1.10

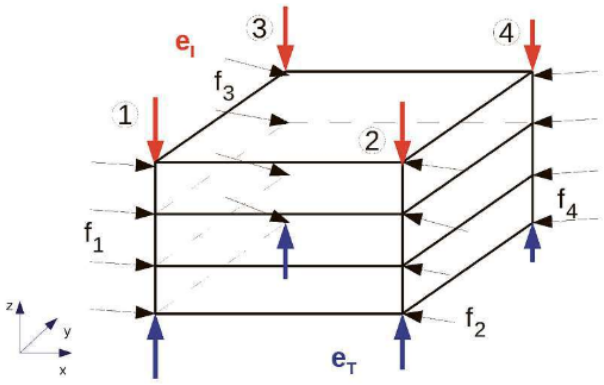

Figure 1.10: FEM of the unit cell given by Christen et al. [96].

where f and e correspond to internal and external forces, respectively. Nodes are located on the four edges of the unit cell. By applying the Bloch Floquet theorem on the unit cell, the following expression is obtained:

$$\tilde{\mathbf{T}}\mathbf{D}\mathbf{T}\mathbf{u}_1 = \tilde{\mathbf{T}}\mathbf{T}\mathbf{e}_1 \tag{1.28}$$

in which u is the displacement on the first edge and where $\tilde{\mathbf{T}}\mathbf{T} = 1/4$ due to the geometry of the unit cell. The external force e_1 is related to the acoustic pressure impinging on the structure and can be expressed as follows:

$$\mathbf{e}_1 = \begin{pmatrix} \mathbf{e}_I \\ \mathbf{e}_O \\ \mathbf{e}_T \end{pmatrix} = \begin{pmatrix} S(p_I + p_R) \\ 0 \\ Sp_T \end{pmatrix} \tag{1.29}$$

with $\mathbf{e}_I$, the external forces on the incident side and $\mathbf{e}_T$ on the transmitted side. All other external forces are included in $\mathbf{e}_0$ and S is the free surface of the element. The dynamic equation can be obtained after applying the dynamic condensation and yields to:

$$\begin{pmatrix} b_{II} & b_{IT} \\ b_{TI} & b_{TT} \end{pmatrix} \begin{pmatrix} u_I \\ u_T \end{pmatrix} = \begin{pmatrix} S(p_I + p_R) \\ Sp_T \end{pmatrix} \tag{1.30}$$

Finally, the Euler equation is used to rewrite u_I and u_T while the acoustic admittance is introduced by $Y_0 = \cos\theta/(i\omega\rho_0 c_0)$ and the final expression is given by:

$$\begin{pmatrix} \mathbf{b}_{II} + \frac{\mathbf{S}}{Y_O} & -\mathbf{b}_{IT} \\ \mathbf{b}_{TI} & -\mathbf{b}_{TT} - \frac{\mathbf{S}}{Y_O} \end{pmatrix} \begin{pmatrix} p_R \\ p_T \end{pmatrix} = \begin{pmatrix} \mathbf{b}_{II} - \frac{\mathbf{S}}{Y_O} \\ \mathbf{b}_{TI} \end{pmatrix} p_I. \tag{1.31}$$

In this case, the incident acoustic pressure $p_I = 1$ and Eq. (1.31) can be solved to retrieve p_R and p_T. They are then used to calculate the STL and SAC as explained in Section 1.3.2.

Both methods developed by Parrinello et al. [74] and Christen et al. [96] assumed an infinite size structure; real wavenumbers and plane waves with the angle of incidence and reflection equal.

Finally, contrary to Parrinelo et al. [74], this method needs the dynamic stiffness of the whole unit cell including skins. Thereby, the number of dofs is higher and strongly affect the computational cost. However,it has the advantage to take all the dynamic of the unit cell into account if local dynamic behaviors within the core.

1.5 Sound Absorption Modelling

On the other hand, the SAC is an acoustic indicator mainly related to porous media due to their high capacity for energy dissipation (see Section 1.1.2). Many models were developed including different physics as viscous and thermal effects as well as the influence of the motion of the solid on the SAC [17, 18]. Most of the models and theories are described by Allard [20].

1.5.1 Poroelastic parameters

Poroelastic materials correspond to structures involving a solid matrix called skeleton filled with a fluid. Such structures can be characterized by specific parameters including the energy dissipation in the pores as well as the dynamic behavior of the solid part. There were all described and given by Biot and Allard [20]. However, in this thesis, only the rigid frame theory is considered and the solid is thus motionless. The wave propagation is then obtained using the six Johnson-Champoux-Allard (JCA) parameters given by:

- The porosity (φ_0) which is the ratio of the volume of the fluid over the total volume of the poroelastic structure including the solid.

- The tortuosity (α_∞) which can be related to the structure form factor, is the average ratio of the square microscopic velocity over a REV around a point M_0 and the square macroscopic velocity at this same point M_0. The minimum value of the tortuosity is 1.

- The viscous characteristic length (Λ_{visc}) describes the viscous energy transfer between the solid and the fluid part. It corresponds to the ratio of the integral of the fluid velocity on the solid-fluid interfaces and the integral over the volume of the fluid velocity.

- The thermal characteristic length (Λ_{therm}) is a geometrical parameter involving only the geometry of the poroelastic structure. It is defined as the ratio of the surface corresponding to the solid-fluid interface and the total volume of the poroelastic.

- The viscous permeability (q_0) is mainly related to the flow resistivity (σ) which is the ratio of the pressure difference with the mean flow of the fluid per unit area. Therefore, the viscous permeability is the ratio of the dynamic viscosity of the fluid and the resistivity.

- The thermal permeability ($q_0^{'}$) is obtained using the thermal equation inside the poroelastic medium and corresponds to the average of the temperature over of the fluid domain.

In all cases, the thermal length and permeability are greater than the viscous length and permeability, respectively. Most of those parameters can be retrieved using experimental measurements [28]. Since the solid phase of the poroelastic medium is considered as rigid, an equivalent fluid model can be applied to obtain its effective bulk modulus K_{eq} and density ρ_{eq} as follows:

$$\rho_{eq}(\omega) = \frac{\rho_0}{\varphi_0}\alpha(\omega) \tag{1.32}$$

$$K_{eq}(\omega) = \frac{\gamma P_0}{\varphi_0}\left(\gamma - \frac{\gamma - 1}{\alpha^{'}(\omega)}\right)^{-1} \tag{1.33}$$

with γ, the specific heat ratio. In addition, $\alpha(\omega)$ and $\alpha^{'}(\omega)$ are the dynamic tortuosity and the thermal tortuosity, respectively, with:

$$\alpha(\omega) = \alpha_\infty - \frac{i\nu\varphi_0}{\omega q_0}\sqrt{1 + \frac{i\omega}{\nu}\left(\frac{2\alpha_\infty q_0}{\varphi_0 \Lambda_{visc}}\right)^2} \tag{1.34}$$

$$\alpha^{'}(\omega) = 1 - \frac{i\nu^{'}\varphi_0}{\omega q_0^{'}}\sqrt{1 + \frac{i\omega}{\nu^{'}}\left(\frac{2q_0^{'}}{\varphi_0 \Lambda_{therm}}\right)^2} \tag{1.35}$$

where ν is the kinematic viscosity and $\nu^{'} = \nu/Pr$ with Pr the Prandlt number. Finally, the equivalent fluid wavenumber k_{eq} and the characteristic impedance Z_{eq} are given by:

$$k_{eq}(\omega) = \omega\sqrt{\frac{\rho_{eq}}{K_{eq}}} \tag{1.36}$$

$$Z_{eq}(\omega) = \sqrt{\rho_{eq} K_{eq}} \tag{1.37}$$

The surface impedance defined by $-iZ_{eq}\cot(k_{eq}H)$ with H the thickness of the poroelastic medium is then used to calculate the SAC of the poroelastic medium as follows:

$$SAC = 1 - |\frac{Z_s - Z_0}{Z_s + Z_0}|^2 \tag{1.38}$$

1.5.2 Micro-perforated panels (MPPs)

Besides, MPPs is usually combined to porous media Fig. 1.11 to increase the acoustic efficiency by targeting the improvement of the SAC at specific frequencies.
MPPs were firstly described by Maa [99, 100] showing the sound absorption efficiency of such concepts. Then, Atalla et al. [101] proposed to model MPPs using the TMM and considering rigid frames. Macro-perforation was also described and combined with porous media by Atalla et al. [102]. In addition, experimental methods to describe MPPs have been also performed as proposed by Lee et al. [103]. When a MPP is backed by a porous media, the surface impedance of the multi-layered systems is given by:

$$Z_A = (\frac{2d}{r} + 4)\frac{R_s}{\varphi} + \frac{1}{\varphi}(\epsilon_e(1 + Re(\alpha_p)) + d)i\omega\rho_0 + \frac{Z_c}{\varphi_0} \tag{1.39}$$

where d is the thickness of the MPP, r is the radius of the perforation, φ is the perforated ratio of the MPP and R_s is called the surface resistance with $R_s = \frac{1}{2}\sqrt{2\nu\omega\rho_0}$. The

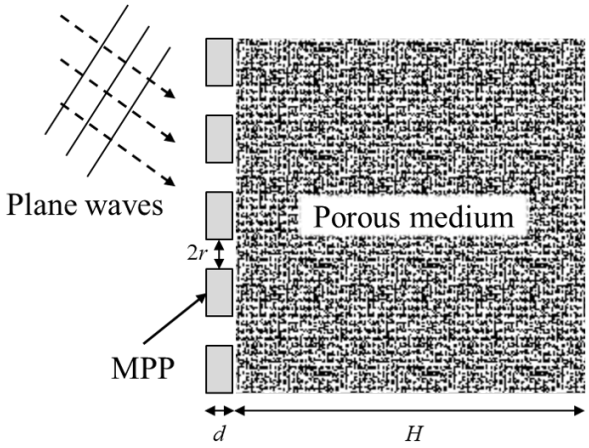

Figure 1.11: MPP backed by a porous media.

coefficient ϵ_e denotes the correction length with $\epsilon_e = 0.48\sqrt{\pi r^2}(1 - 1.14\sqrt{\varphi})$ whereas the dynamic tortuosity of the porous media is α_p. Finally the SAC is calculated using Eq. (1.38). This method was validated using a modal approach as well as an experimental measurement using an impedance tube. A good agreement is obtained as shown in Fig. 1.12

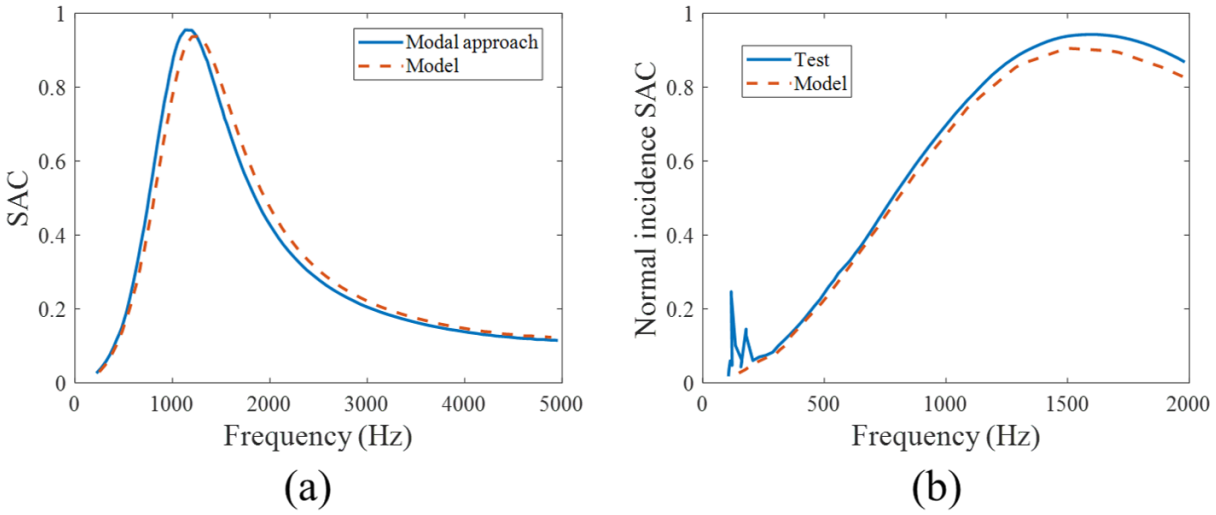

Figure 1.12: SAC of a perforated panel backed by a foam, comparison of the proposed model [101] with (a) Modal approach (b) Measurement using an impedance tube.

1.5.3 FEM model of a porous media

In the case of porous media involving a REV and considering the structure as periodic, it is possible to apply the PST and to be focused on the study of the unit cell. Therefore, the JCA parameters can be retrieved using the FEM of the unit cell. This methods has been applied by Zieliński et al. [104] and Perrot et al. [105]. The principle is to evaluate

the six JCA parameters by implementing 3 main equations in a FEM software as Comsol Multiphysics. Those equations are listed as following:

- **The thermal equation**

$$\nabla^2 T = -1 \tag{1.40}$$
$$T = 0 \text{ on } \Gamma_{sf} \tag{1.41}$$
$$T\ \Omega - \text{periodic} \tag{1.42}$$

- **The Stokes equation**

$$\nabla \cdot [-p\mathbf{I} + \mu(\nabla \mathbf{u} + (\nabla \mathbf{u})^{\mathrm{T}})] + F = 0 \tag{1.43}$$
$$\rho \nabla \cdot \mathbf{u} = 0 \tag{1.44}$$
$$p \text{ and } \mathbf{u}\ \Omega - \text{periodic} \tag{1.45}$$

- **The viscous-inertial problem**

$$\nabla^2 q = 0 \tag{1.46}$$
$$\nabla q \cdot \vec{\mathbf{n}} = \vec{\mathbf{e}} \cdot \vec{\mathbf{n}} \text{ on } \Gamma_{sf} \tag{1.47}$$
$$q\ \Omega - \text{periodic} \tag{1.48}$$
$$\vec{\mathbf{E}} = \vec{\mathbf{e}} - \nabla q \tag{1.49}$$

in which $\vec{\mathbf{e}}$ is the dimensionless unit vector and $\vec{\mathbf{n}}$ is the normal vector of the surface.
The JCA parameters are then expressed as follows:

$$\varphi_0 = \frac{\int_{\Omega_f} d\Omega_f}{\int_{\Omega} d\Omega} \qquad \alpha_\infty^{-1} = < \vec{\mathbf{E}} \cdot \vec{\mathbf{e}} >_\Omega$$

$$\Lambda_{visc} = 2\frac{\int_{\Omega_f} \vec{\mathbf{E}} \cdot \vec{\mathbf{E}} d\Omega_f}{\int_{\Gamma_{sf}} \vec{\mathbf{E}} \cdot \vec{\mathbf{E}} d\Gamma_{sf}} \qquad \Lambda_{therm} = 2\frac{\int_{\Omega_f} d\Omega_f}{\int_{\Gamma_{sf}} d\Gamma_{sf}} \tag{1.50}$$

$$q_{visc} = \nu\varphi_0 < \mathbf{u} \cdot \vec{\mathbf{e}} >_\Omega \qquad q_{therm} = \varphi_0 \frac{\int_{\Omega_f} T d\Omega_f}{\int_{\Omega_f} d\Omega_f}$$

The expressions given in Section 1.5.1 are then used to calculate the SAC.
This method has the advantage to model very complex shapes and to obtain their SAC. However, porous media are assumed to have a rigid frame to be considered as an equivalent fluid. Boulvert et al. [106] compared this process to experimental measurements using an impedance tube. 3D printing samples of micro-lattices were manufactured. A Good agreement has been obtained especially at low frequencies (Fig. 1.13).

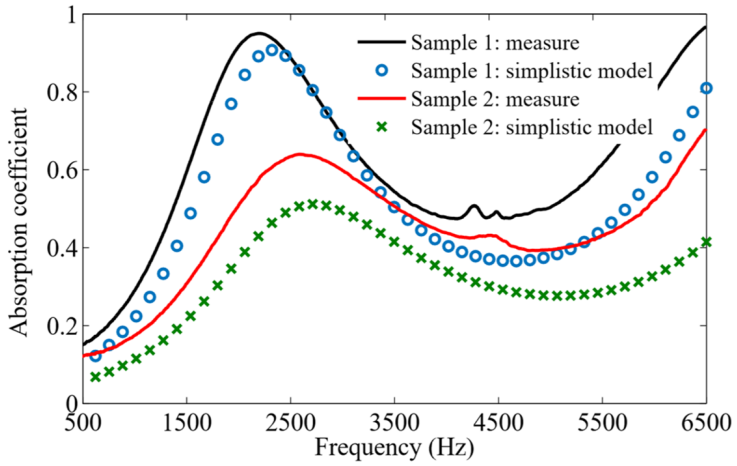

Figure 1.13: Comparison of the SAC between simulations and experimental measurements using an impedance tube [106].

1.5.4 FEM using Comsol Multiphysics

In some specific cases involving very complex shapes and combining different concepts (MPPs, honeycomb cores, MLCTS, periodic structures), it is necessary to use finite element softwares to consider all the physics involved in the structure [107]. Most of the FEM of porous media in the literature were performed using Comsol Multiphysics.

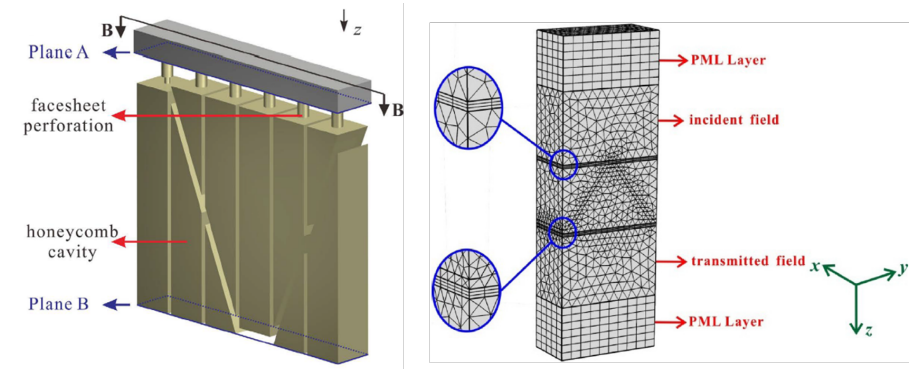

Figure 1.14: (a) FEM used in Tang et al. [108] (b) FEM used in Meng et al. [107].

The Pressure Acoustic module is used to model the incident and transmitted field governed by the Helmholtz equation. The Perfectly matched layer (PML) can be applied on both sides of the unit cell to simulate the anechoic termination. In addition, the solid part can be taken into account with the Solid Mechanics module. Finally, the energy dissipation occurring in the structure can be modelled with the Thermal-Acoustics module simulating the viscous-thermal effect inside the pores. However, there is an increase of the number of variables which leads to a high computational cost. Alternatively, the Narrow Band Acoustics can be used to reduce the number of degrees of freedom. The

interfaces between each physics are automatically considered in the software. Since the structure is periodic, the periodic boundary conditions are applied and the simulation is made considering an infinite size.

In the case of the FEM model (Fig. 1.14a), only the SAC can be calculated using the surface impedance whereas the FEM model used by Meng et al. (Fig. 1.14b) allows to obtain the STL and the SAC using the obtained reflected, transmitted and incident acoustic wave travelling in the domain. It might be noticed that such FEMs are limited to incident acoustic wave under 55° due to the limit of the PML layer [109]. Therefore, they are mainly modelled under normal incidence acoustic waves and verified experimentally using an impedance tube. This FEM has been validated experimentally using an impedance tube with four different samples of sandwich panels including a corrugated core and perforated skins (Fig. 1.15).

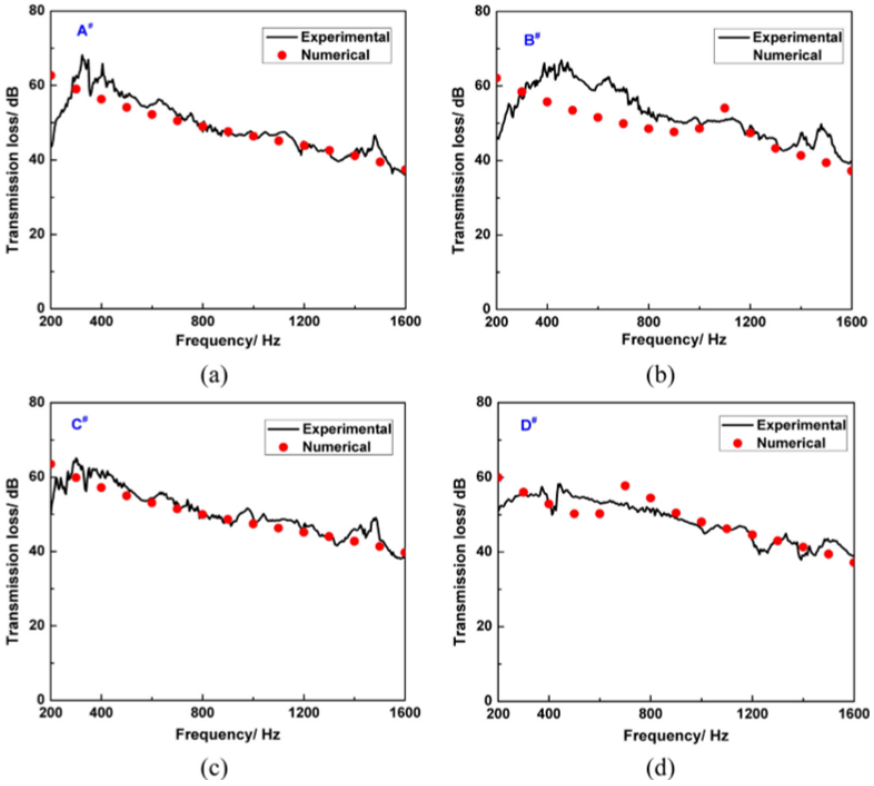

Figure 1.15: Comparison of the STL between the FEM and experimental measurements [107].

1.6 Frequency transition modelling

Transition frequencies were mainly described analytically in the literature for sandwich panels involving an homogenization of the core. Depending on the order of the equation of motion, it is possible to capture either the first, the second or both transition frequencies.

The 4^{th} order allows to obtain the first transition [4] while the 6^{th} is used for the 2^{nd} transition [69]. It can be determined using dispersion curves (obtained analytically or using the WFEM). They separate different dynamic behaviors of the sandwich panel [70]. Several analytic formulations were developed [110, 111]. However, they are limited for more complex structures and it is necessary to develop models based on FEM to consider all the structure's dynamic behavior.

1.6.1 Numerical identification of the first transition frequency

The analytical expression of the flexural wavenumber of a sandwich panel based on the 4^{th} order of the equation of motion is given as follows [4]:

$$\left|k(\omega)\right| = \left(\left(\frac{1}{2S}\right) \left(\rho_s \omega^2 + \omega \left(\rho_s^2 \omega^2 + \left(\frac{4\rho_s S^2}{D} \right)^{1/2} \right) \right) \right)^{1/2}, \tag{1.51}$$

where S is the dynamic shear modulus, D is the dynamic bending stiffness and ρ_s is the surface density of the structure. The first transition frequency occurs when the flexural wave motion of the sandwich panel shifts from a bending behavior to the core shear. Guillaumie [4] proposed an analytical solution for the first transition frequency based on the dynamic bending and shear modulus. The expression is given based on the analytical formulation of the flexural wavenumber Eq. (1.51):

$$f_t = \frac{S}{4\pi} \left(\frac{1}{\rho_s D} \right)^{1/2}. \tag{1.52}$$

Therefore, the analytic formulation of the flexural waves can be used to perform a numerical identification using the WFEM to obtain the values of the dynamic bending and shear modulus and thus, the value of the first transition frequency of the sandwich panel. The dynamic shear modulus can be firstly approximated using a static numerical measurement in both direction x and y of the sandwich panel to obtain the global shear modulus S. Besides, the bending stiffness modulus D is calculated as follows, with E the elastic modulus, ν the Poisson ratio of the material and H the thickness of the core.

$$D = \left(\frac{H^2}{2} t_s + H \cdot t_s + \frac{2}{3} t_s^3 \right) \left(\frac{E}{1-\nu^2} \right). \tag{1.53}$$

The method consists on using the wavenumber expression Eq. (1.51) with initial values of the pair (S, D). The second step is to obtain the dispersion curve of the sandwich panel using the WFEM in both directions and to match the analytic expression Eq. (1.51) by adjusting the value of S and D. Finally, when the fitting process is completed, the new values of S and D are used to calculate the transition frequency Eq. (1.52). This process

is performed for both direction x and y and D is considered identical in both directions. Indeed, in case of isotropic skins, the bending stiffness of the sandwich panel is mainly due to the skins since the honeycomb properties is usually negligible compared to the skins properties. This process can be performed using a non-linear regression.
Similarly, this method can be used to apply the bisection method based on the asymptotic expression of the flexural wavenumber. At low frequencies, the dynamic behavior is dominated by the dynamic bending modulus and the flexural wavenumber can be approximated as follows:

$$k(f \longrightarrow 0) = (\rho_s/D)^{1/4}\sqrt{\omega}, \tag{1.54}$$

whereas it is mainly influenced by the dynamic shear modulus at medium-high frequencies with:

$$k(f) = \omega(\rho_s/S)^{1/2} \tag{1.55}$$

This numerical identification strategy can be applied on the flexural wave group velocity [71, 69]. Other methods based on the analytic formulation of the flexural wave are given by Baho et al. [71]. In this paper, it is shown that such methods can also be applied on the modal density to retrieve the first transition frequency. However, they are only valid for the first and second zone as depicted in Fig. 1.23. To achieve the flexural wave in all the frequency range, it is necessary to develop the 6^{th} order to capture the bending waves located in the skins and occurring at higher frequencies as explained by Droz et al. [69]. The dispersion relation expression in this case yields to:

$$2D_1D_2k^6 - 2D_2I_\rho k^4\omega^2 - (\mu + 2D_2\mu + I_\rho G_c h_c)k^2\omega^2 + G_c h_c D_1(k^2 - \mu\omega^2) + I_\rho\mu\omega^4 = 0 \tag{1.56}$$

in which D_1 and D_2 are the flexural stiffness, G_c is the core's shear modulus, h_c and h_s are the core's thickness and skins' thickness, I_ρ is the mass moment of inertia and μ the surface density. Therefore, more parameters are involved in the dynamic behavior. Moreover, the equation's order does not allow to retrieve an exact solution of the flexural wavenumber k and a non-linear regression is muc more complicated to apply. The asymptotic behavior of the group velocity is changed due to the involvement of the second transition frequency and shear waves are no longer measurable [69]. By assuming a rotation inertia and the honeycomb properties negligible compared to the shear effect and the skins properties, respectively, the 4^{th} order of the dispersion relation can be retrieved leading to the expression of k given in Eq. (1.51).

1.6.2 Wavemode energy method using FEM

Besides, an energetic method based on the calculation of the wavemode energy and the energy storage inside the core and the skins turned out the conversion of bending waves into shear waves located in the core. This latter method is based on the FEM of the unit cell and thus, depends on the accuracy of the mesh. It was described and applied on a sandwich panel made of a honeycomb core by Baho et al.[71]. It is based on the calculation of the wavemode strain energy of the core E_c and the skins E_s along both directions x and y. E_c and E_s are calculated as follows:

$$E_c = \frac{\Phi^T \mathbf{K}_c \Phi}{E_T} \quad \text{and} \quad E_s = \frac{\Phi^T \mathbf{K}_s \Phi}{E_T}, \tag{1.57}$$

where $\mathbf{K}_c$ and $\mathbf{K}_s$ are the full stiffness matrices of the core and the skins while the vector Φ corresponds to the vector of dofs of the displacement related to the wavemode of the core and the skins respectively. They are obtained using the 2D WFEM. Both expressions of wavemode energy are normalized with respect to E_T which is the total strain energy of the unit cell using the full stiffness matrix and the full vector of dofs of the displacement. The first transition frequency is then identified when E_c becomes higher to E_s and the second transition frequency is retrieved when E_s becomes higher again. This method has the advantage to consider the full dynamic behavior of the unit cell since it uses its FEM. Finally, by applying this method to the same case as presented in Section 1.3.1, the zones are verified (Fig. 1.16). Therefore, it is easier to understand the wavemode propagating in the sandwich panel and to obtain the 1^{st} and 2^{nd} transition frequency.
Such a method involves a higher computational cost compared to analytical formulations but can be applied to all complex structures involving sandwich panels. Consequently, the prediction of transition frequencies is possible as long as the accuracy of the mesh is verified.

1.7 Enhancement of vibroacoustic properties

Improving the acoustic efficiency of sandwich panels becomes a great interest in the research field as well as the industry. Currently, many studies are carried out about periodic structures and how to optimize the unit cell to obtain better properties.

1.7.1 Optimization and parametric studies of sandwich panels

In this context, some parametric analysis were performed by modifying geometrical parameters of the honeycomb core [66, 112] to investigate their influence on vibroacoustic indicators (transition frequency and modal density). It occurs that the geometrical shape of the honeycomb core has a negligible effect while the thickness of the core for instance,

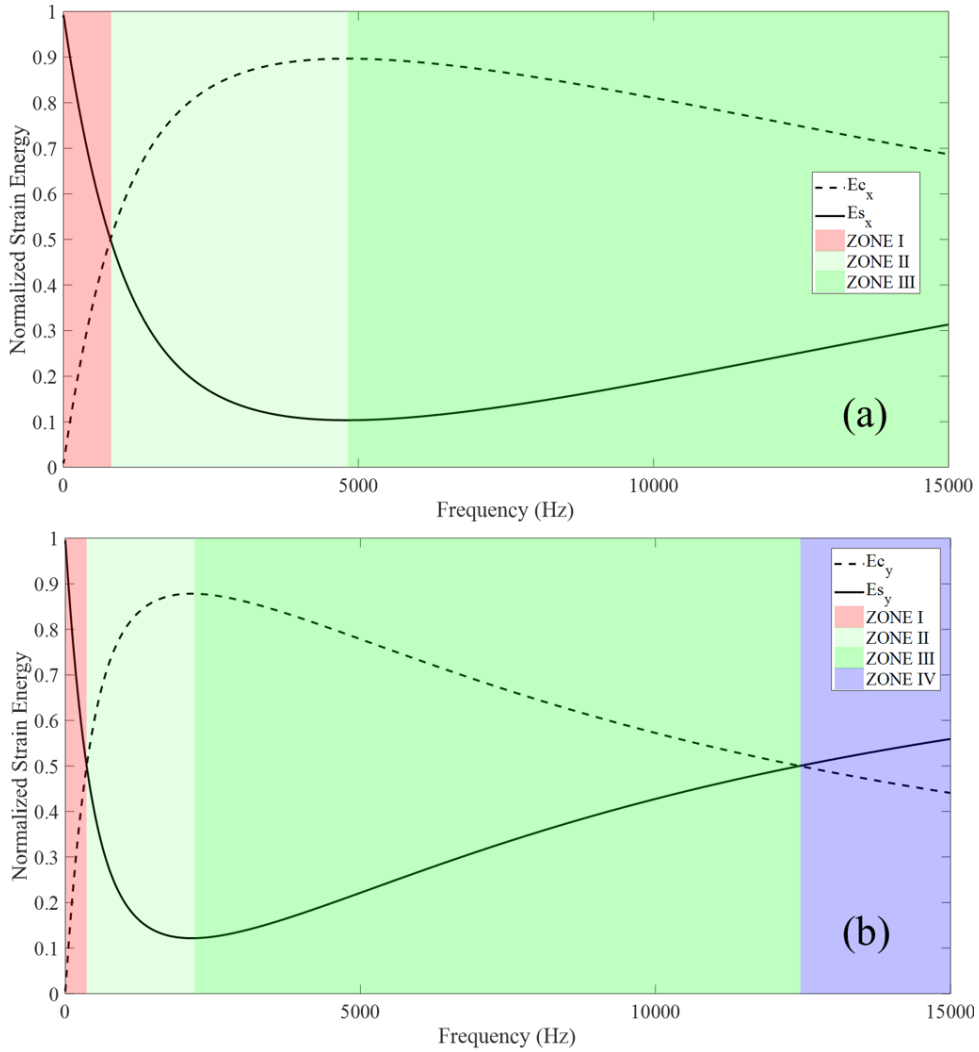

Figure 1.16: Strain energy of the standard sandwich panel made of a rectangular core (a) along x-direction and (b) along y-direction (Fig. 1.6).

is considered as a critical parameter. Different designs of honeycomb cores have been proposed by Droz et al. [113]. The transition frequency, the modal density as well as the group velocity are used to find out the optimal configurations leading to a more complex geometry. Besides, a more complete parametric survey applied to honeycomb core sandwich panels has been performed [114, 115]. The core geometry was gradually changed from an auxetic to a hexagonal shape to target the STL and the acoustic radiation of the panel, respectively. Most of the studies are performed with a constant mass and a constant stiffness. This latter is considered as the more difficult to compute in optimization processes for complex structures, since the calculation needs to be performed by a finite element model included in a loop process when the analytic formulation is not obtained. This step usually leads to a high computational cost. Moreover, Mazloomi et al. [116] obtained a great reduction of the sound insulation constructing the sandwich panel by combining a mixture of different in-plane cores, made of different geometries ranging

gradually from hexagonal to auxetic shape while Franco et al. [117] explored different core configurations and materials to reduce the radiated sound power. Same type of designs is studied [118] for the compression properties enhancement. It helps to understand the location of the deformation before the structure collapses. Furthermore, the gradually cellular deformation reveals a strengthening of the structure during the loading. Kirigami concepts [119, 120] or the 3D printing [121] have been applied to make these sandwich panels with more complexity and open new perspectives for sandwich structure designs. In addition to honeycomb cores, several studies are carried out on web cores focusing their research on the acoustic properties [79, 122] or the bending and vibration behavior [123, 124] more specifically for building applications. Random unit cell designs were found out [125, 126, 127, 128, 129] thanks to multi-objective topology optimizations but requiring heavy processes to be implemented. However, such studies still remain limited in terms of exploration of geometrical parameters and design proposals since only a single core is considered.

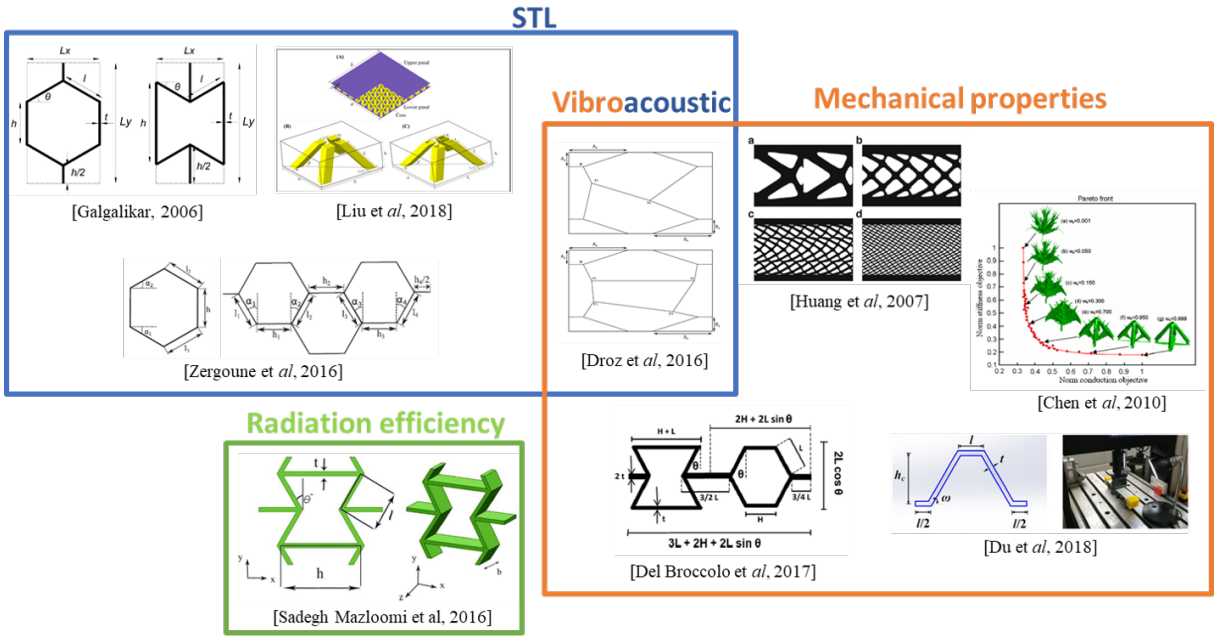

Figure 1.17: Example of parametric analysis and optimizations of sandwich panels made of one single core.

1.7.2 Add-ons structures

Enhancement of the dynamic behavior of sandwich panels can also be obtained by putting add-ons. Often, resonators are included inside the core or externally located to reduce the waves travelling in the structure by creating band-gaps [130, 131, 132, 133, 134, 135].

Recently, Droz et al. [136] have tested such a solution to an aircraft curved panel to improve the STL and Tufano et al. [137] performed an Inhomogeneous Wave Correlation (IWC) to investigate the impact of resonators on the structural damping. Similar analysis have been proposed by Van Belle et al. [138, 139]. However, only some specific frequency zones are targeted and no improvement is obtained in a broadband frequency. Groby et al. [140, 141] proposed an added acrylic and aluminum cylinder inside porous medium to create band-gaps.
Besides, filled foam cores are proposed to couple the rigidity of honeycomb cores with the acoustic absorption performances of foam cores, and have been studied targeting mechanical properties [142, 143, 144, 145, 146] and to lesser extent for acoustic properties [147, 148]. The foam will have an important effect at low frequencies and the more the height of the core is high, the more the foam will positively influence the sound properties. In addition, they demonstrate a great efficiency for reducing the sound radiation by removing the modal effect. Nevertheless, the limitation of such solutions is quickly reached due to the added mass on the structure as well as their integration in operational industrial applications due to the lack of space.

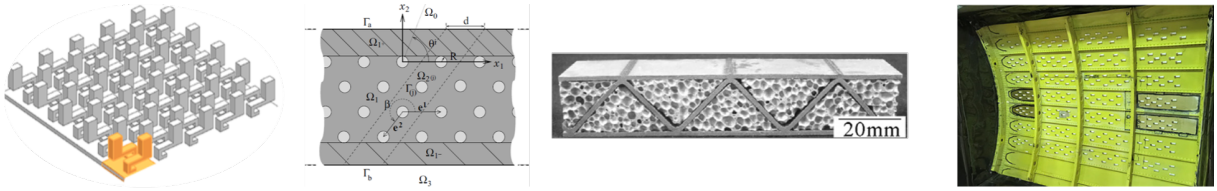

[Melo Filho et *al*, 2019] [Groby et *al*, 2008] [Yan et *al*, 2013] [Droz et *al*, 2019]

Figure 1.18: Examples of add-on structures on sandwich panels.

1.8 Enhancement of the SAC of sandwich panels

Concerning the improvement of the SAC, porous medias are still the most used structures for such applications. Many type of materials (natural fiber, foam, metallic foams [149]...) can be used to modify the physical properties of porous media to enhance the SAC with the alteration of the flow resistivity using different materials [150] or with re-cycled rubber granulate of different sizes [151]. Fouladi et al. [152] used natural fibers as coir fiber from coconut to show their efficiency at low frequencies when it is combined with perforated panels. This later is the second way to produce the energy dissipation to improve the SAC.
Micro-perforated panels (MPPs) are usually made with thin plate (millimeters) followed by an air gap and a rigid wall. They are effective at specific frequencies defined by the size of the perforation and the thickness of the air gap. They allow to increase the acoustic performance of the structure with a reduced mass due to the perforation.

Bucciarelli et al. [153] proposed a multi-layer MPP to overcome the limitation due to the perforation and to obtain a broadband absorption at low frequencies with the combination of different sizes of perforations. Before, Wang et al. [154] studied parallel arrangements of MPPs changing the size of backed cavities achieving similar results. Furthermore, Sgard et al. [155] investigated the concept of double porosity combining porous media with meso-perforations with different profiles, to enhance the acoustic efficiency and energy dissipation inside the pores. Recently, perforations were added to honeycomb sandwich panels as performed by Tang et al. [108] to associate the STL performance with an enhancement of the SAC. Finally, only few works were performed to fully improve both properties, the STL and the SAC. Doutres et al. [156] estimated the STL and the SAC of double panel structures under normal incidence acoustic waves. Meng et al. in 2017 [107] and in 2019 [157] proposed a FEM of MPPs backed by honeycomb cores instead of using skins to show the acoustic efficiency of such structures with a parametric study applied to the perforation. It occurs an improvement of both the STL and the SAC verified then by experimental measurements using an impedance tube. This later solution remains an interesting way to connect two concepts widely used in the industry, honeycomb sandwich panels and MPPs.

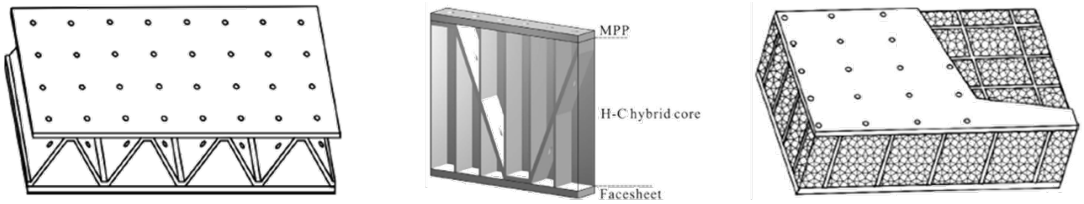

Figure 1.19: Solutions for better SAC of sandwich panels.

1.9 Multi-layered sandwich panels

Multi-layer core topology systems (MLCTS) are recently also being developed starting from the principle of multi-layer porous media and laminates, stacking layers of composite panels, which are wide spread in many applications. An analytic formulation of the deflection and the equivalent stress as well as the critical load and natural frequencies and the shear modulus of a seven-layers rectangular plate with trapezoidal corrugated cores separated by inner skins have been developed based on the Hamilton´ s principle [158, 159, 160]. They are illustrated in Fig. 1.20 in which different designs of corrugated cores are represented.

A FEM and experimental measurements was performed on a three point-bending of a beam in which corrugated cores were directly connected without using skins in between

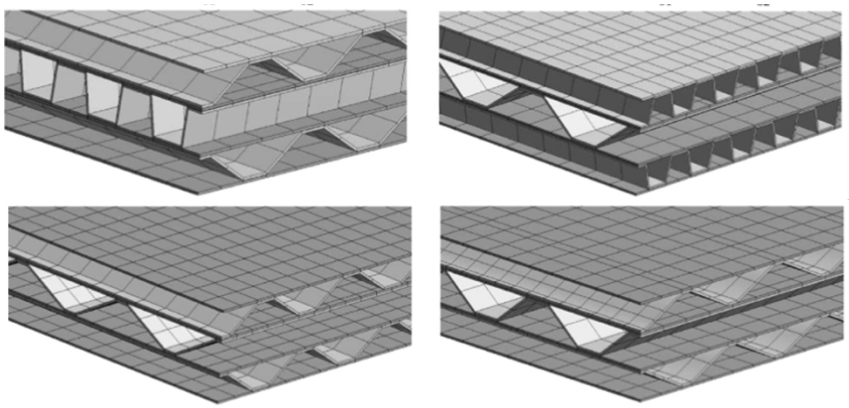

Figure 1.20: Designs of multi-layered corrugated cores sandwich panels [159].

layers [161] Fig. 1.21. Such structures are mainly used for building applications due to their ability for gradual deformations during the compression loading.

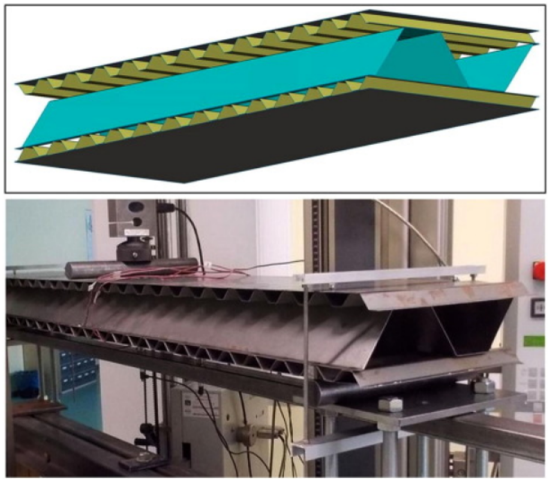

Figure 1.21: A five-layered beam with three corrugated layer core [161].

Moreover, the analytic formulation of the cylindrical bending of a two-layered corrugated and web core Fig. 1.22 is derived and was applied to hybrid combinations of cores showing a great energy absorption under flexural [162] and blast [163] loading.
The weight-saving advantage of multi-layer systems is stressed combining different properties induced by each layer. The influence of the number of layers and the orientation of the core investigating the quasi-static compression behavior of multi-layered corrugated sandwich panels was proposed numerically and validated experimentally by Hou et al. [164]. Based on the previous analysis, Shu et al. [165] studied two sandwich panels made of two layers of corrugated cores with two different orientation of cores under a compression loading using a parametric analysis showing the influence of the core geometry on the impact resistance.
Most of the studies related to multi-layer honeycomb core panels are performed to investigate mechanical properties while sound insulating properties did not receive a lot of

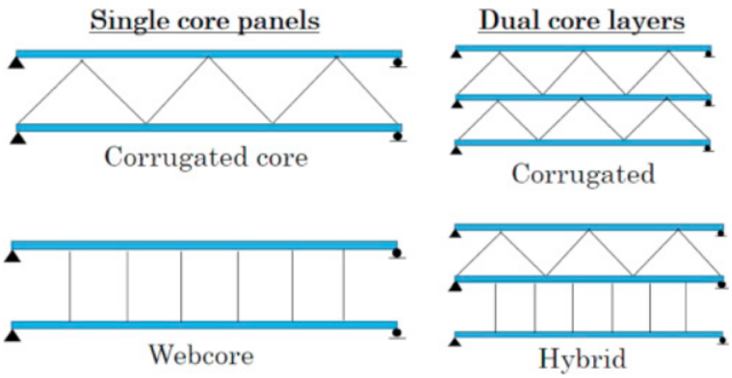

Figure 1.22: Dual core layers designs [162].

attention yet. A double layer honeycomb core separated by a damped layer has been proposed by Wen et al. [166] and a better sound insulation was obtained at low frequencies compared to a honeycomb sandwich panel made of a single core as shown in Fig. 1.23.

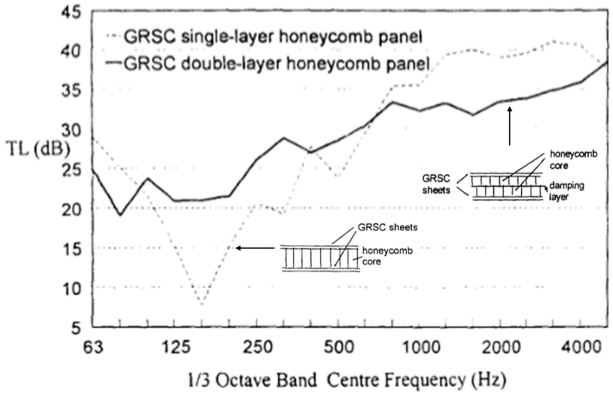

Figure 1.23: Comparison of the STL between a double-layer honeycomb sandwich panel and a standard sandwich panel [166].

Besides, Sui et al. [167] designed a double honeycomb core separated with a damping layer and tested the sample in an impedance tube. A great improvement of the STL is obtained at low frequencies and depicted in Fig. 1.24 opening perspectives of such structures for better acoustical performances. Multi-layer core systems have been also studied in terms of STL in [168].

1.10 Conclusions

During these last decades, the constant research of better mechanical and acoustical properties has led to more complex structure's designs and thus, has involved more complicated dynamic behaviors. In parallel, models have been improved. Therefore, many designs are proposed to investigate their effects on dynamic properties. Finally, a summary of this

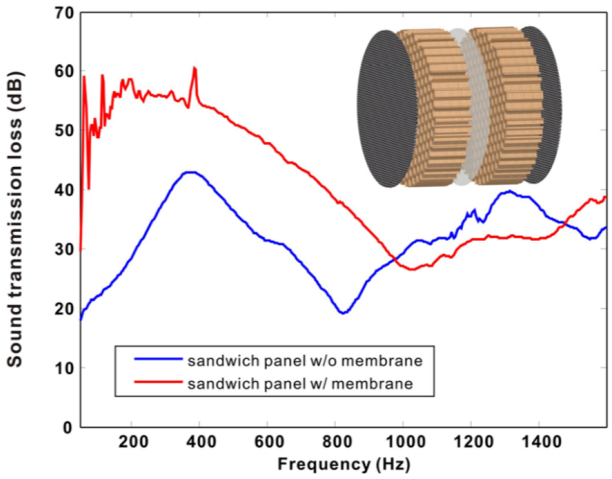

Figure 1.24: Comparison of the STL under normal incidence acoustic waves between a double-layer honeycomb sandwich panel separated by a damped layer and a standard sandwich panel [167].

literature review is proposed in Fig. 1.25. Consequently, there is a need for more detailed information concerning the vibroacoustic behavior of MLCTS.

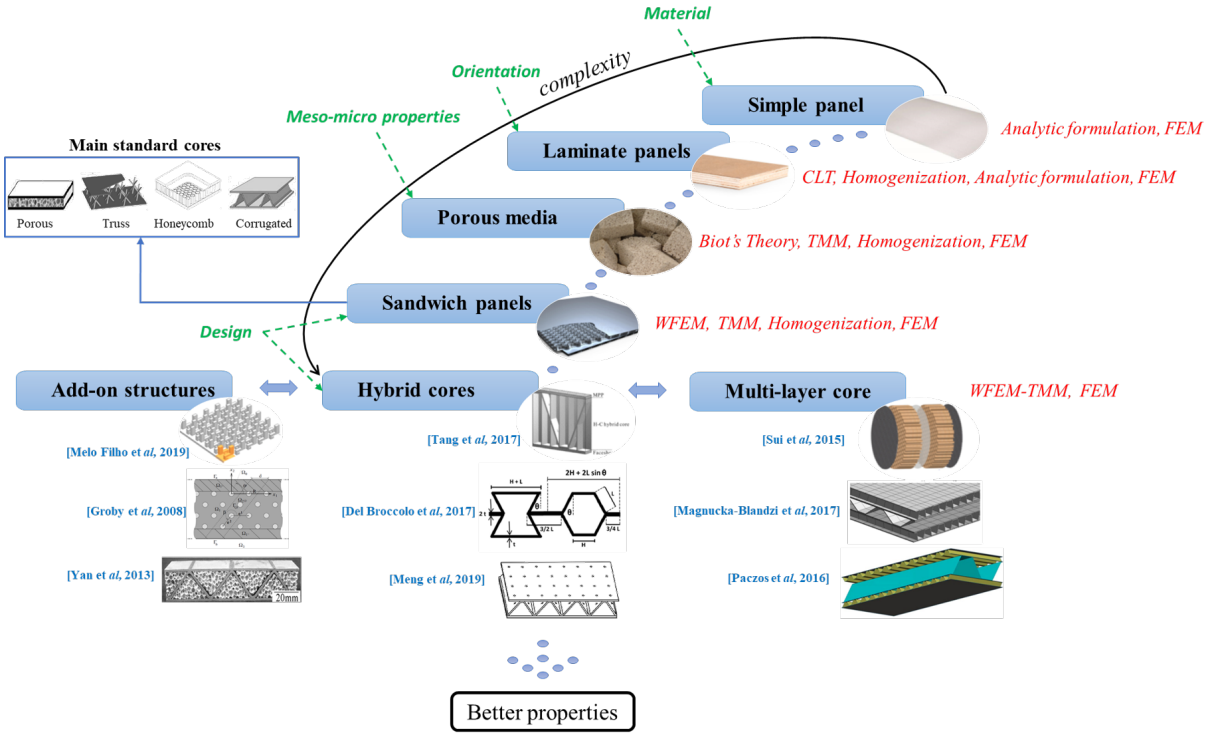

Figure 1.25: Summary of the evolution of design space studied in the literature.

The next chapter is dedicated to the presentation of the proposed designs, the numerical approach used to obtain the STL and the transition frequency and a parametric survey applied on MLCTS.

Chapter 2

Vibroacoustic analysis of multi-layer rectangular core systems (Part I)

This Chapter is related to results included in a submitted paper which is still under review on Mechanical Systems and Signal Processing. The authors are Nassardin Guenfoud (ECL and KUL), Christophe Droz (ECL), Mohamed Ichchou (ECL), Olivier Bareille (ECL), Elke Deckers (KUL) and Wim Desmet (KUL). Some parts are based on a conference paper presented in the 2nd Euro-Mediterranean Conference on Structural Dynamics and Vibroacoustics (MEDYNA 2017) [169].

Abstract

The present Chapter deals with multi-layer rectangular core topology systems (MLRCS) built up by stacking layers made of different rectangular core geometries. Multi-layer systems have been intensively studied in terms of mechanical performances whereas their vibroacoustic behavior, acoustic efficiency and design are however still an open issue. Several design parameters should be considered to fully understand the dynamic and acoustic behaviour of such structures. Therefore, this Chapter focuses on controlling the transition frequency and the STL by modifying geometrical parameters of the unit cell, while keeping the mass constant. Infinite panels and real wavenumbers will be considered in the study. The WFEM is used to obtain the targeted indicators. The proposed designs give the opportunity to shift the transition frequency and to change the flexural behavior propagating in the structure. Besides, the STL is highly improved in the full frequency range of interest compared to a standard sandwich panel made of a single core.

Contents

2.1 Introduction

In these last decades, honeycomb sandwich panels have been increasingly used in many industrial applications within building, transportation and aerospace industry. Indeed, they possess a high stiffness to weight ratio thanks to the combination of a thick and lightweight honeycomb core located in between two thin face-sheets. Changing the geometric shape of the core and its material properties provides the opportunity to improve the honeycomb´ s panel mechanical and acoustic efficiency. Despite being high mechanical performances panels, acoustic properties of such structures are often not considered in the first stage of the design and lead to poor STL and vibroacoustic indicators in general. Therefore, it is necessary to propose new designs of honeycomb cores in order to enhance the acoustic performance while retaining its mass and static stiffness.

Many designs of sandwich panels have been proposed in the literature to enhance their vibroacoustic properties. Most of them are related to sandwich panels made of a single honeycomb core [66, 113] while less are related to multi-layer core systems. Indeed, they are mainly used for building applications [158, 159, 160] even though their acoustic efficiency have been already demonstrated [167, 166]. However, few investigations have been performed to better explain their dynamic behavior. In addition, damped layer or skins are usually located between layers.

Therefore, following the recent developments on MLCTS and design space study of honeycomb sandwich panels, this thesis investigates a new kind of unit cells design based on the stacking of honeycomb cores' layers without inner skins or damped layers located in between. New geometrical parameters are considered, aiming for an alteration of the vibroacoustic properties of the sandwich panel, ultimately allowing the control of critical vibroacoustic indicators. This innovative design approach leads to better acoustic performances and a better control of vibroacoustic properties. In this Chapter, the focus concerning the targeted vibroacoustic indicators is made on the STL and the transition frequency due to their widespread use in the aerospace industry. The STL is associated with the acoustic efficiency of the structure in transmission problems, while the transition frequency is associated with the dynamic behavior of the structure which underlies the overall vibroacoustic properties. They are obtained using the WFEM based on the PST. Three applications are provided to show how the indicators will be altered by the geometry of the unit cell. It will be shown that a high improvement of the STL is obtained with MLCTS while a shifting process of a middle core in the in-plane directions x and y allows to modify the dynamic behavior of a specific direction of the sandwich panel. This Chapter is organized as follows. Section 2.2 describes the proposed design of MLCTS, while Section 2.3 focuses on models allowing to compute the targeted indicators. Then, Section 2.4 illustrates three different realizations of MLCTS made of rectangular cores to investigate how targeted indicators evolve depending on unit cell configurations and

which physical phenomena occurs within such structures. The first realization considers the change of the size of the middle core, the second one shifts the middle core along the x-direction of the unit cell and finally the third one shifts the unit cell along y-direction. The work is concluded in Section 2.5.

2.2 Multi-layer core topology systems (MLCTS)

In this section, MLCTS are described and the main design parameters to take into account are listed. A parametric model is proposed to make different type of periodic cores geometry. Several examples obtained from the parametric model are illustrated and the surface density of each layer is well-controlled.

2.2.1 Description of MLCTS

MLCTS, illustrated in Fig. 2.1, provide periodic structures designs by stacking layers made of different geometries of honeycomb cores (auxetic, hexagonal, rectangular, ...). Therefore, there is the possibility to play with each layer independently to obtain better mechanical and acoustical properties compared to standard sandwich panel made of a single core. The same concept is used in automotive industry with sound packages combining layers of different types to enhance the acoustic efficiency.

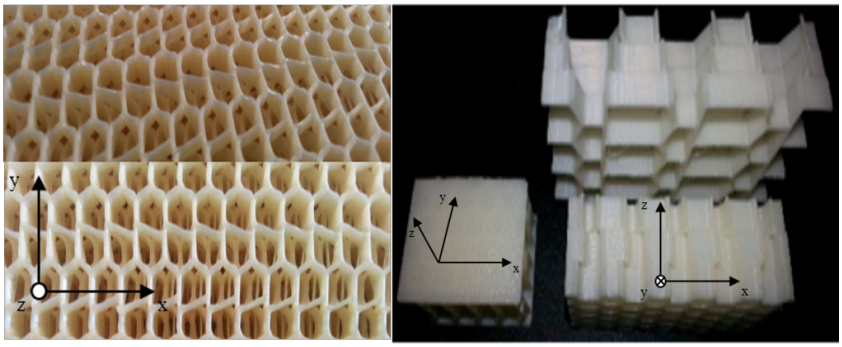

Figure 2.1: MLCTS samples manufactured by an industrial 3D printer.

Such structures involve new design parameters which should be studied to fully understand the dynamic and acoustic behavior. These parameters are listed as follows:

- the shift between layers along x and y direction (Fig. 2.2); it leads to a less rigid connection between two consecutive layers. This might create new phenomena and impedance discontinuities which could alter the vibroacoustic properties. Obviously, some mechanical properties as the compression modulus along z-direction are expected to be decreased depending on the layout of interfaces and due to less rigid contacts between layers;

- the rotation between layers Fig. 2.3; it leads to some difficulties on the modelling part since periodicity properties might be lost. Indeed, it is then not possible to extract a unit cell from the structure and consequently, the WFEM is made difficult to apply. However, with a square unit cell it is possible to consider some specific rotation of layers allowing to extract the unit cell trough the thickness of the core: 90°, 180° and 270°. Otherwise, the whole sandwich panel needs to be modeled, drastically increasing the number of degrees of freedom (dofs) and thus, the computational cost;

- the interaction between geometrical parameters (depth, thickness, angles, ...) of each layer (Fig. 2.4) related to the possibility to change the shape of the unit cell of each layer and the layout of the interfaces, and stacking different type of cores (auxetic, honeycomb, rectangular, ...); it is possible to have different shape for each layer, allowing to combine their characteristic such as the auxeticity of an auxetic core with the mechanical efficiency of a hexagonal core for instance. Each layer can be located in different position between the skins to differently influence the mechanical and acoustical properties of the sandwich panel;

- the size of the unit cell can be different for each layer. This could lead to non periodic structures if some conditions in terms of periodicity between layers are not respected (Fig. 2.5);

- the periodicity of each layer; if the unit cell size of each layer are multiple to each other, this gives the possibility to have different periodicity properties between layers. Both unit cell sizes and periodicity are shown in Fig. 2.5.

Due to some parameters, it is not always possible to extract the unit cell through the whole depth of the structure. The first two parameters (shift and rotation) allow to keep the same mass without modifying the geometry but altering the mechanical properties due to the interface between layers.
To be able to extract the unit cell and to apply the WFEM, it is necessary to have unit cells sizes multiple to each other which characterize the degree of periodicity of each layer. The issue related to the unit cell extraction using MLCTS combining all mentioned parameters is illustrated in Fig. 2.6 using three layers made of three different core topologies (auxetic, square and hexagonal), revealing great challenges in terms of modelling. Since the WFEM will be applied to calculate the STL and the transition frequency, it is necessary to constrain some of these parameters. Therefore, the size of the unit cell is the same for each layer and only rotations of 90°, 180° and 270° can be considered when square unit cells are designed.
Besides, MLCTS reveals interesting characteristic as the creation of an open porosity inside the core. In this way, it will be possible to change certain parameters and to obtain

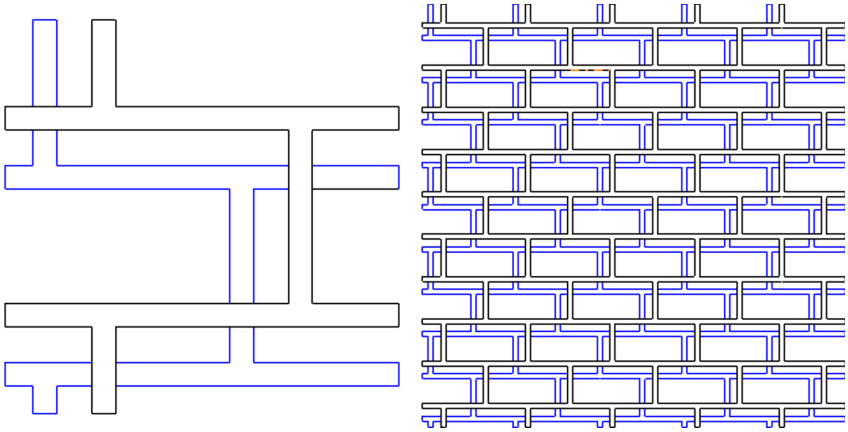

Figure 2.2: Phase shift between layers.

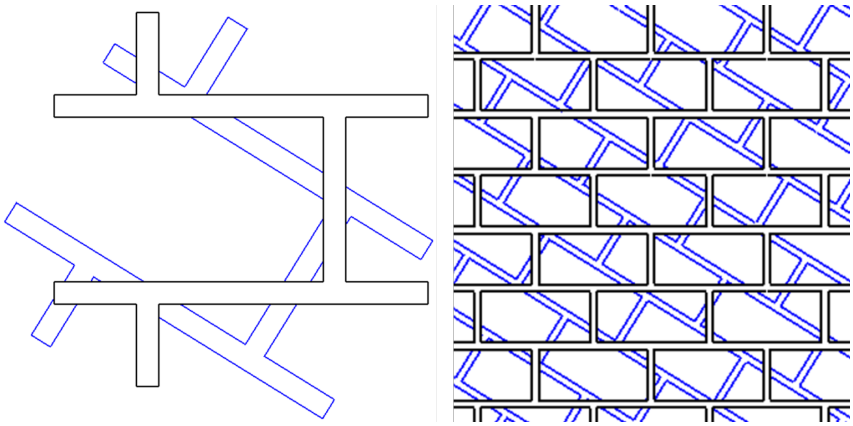

Figure 2.3: Rotation between layers.

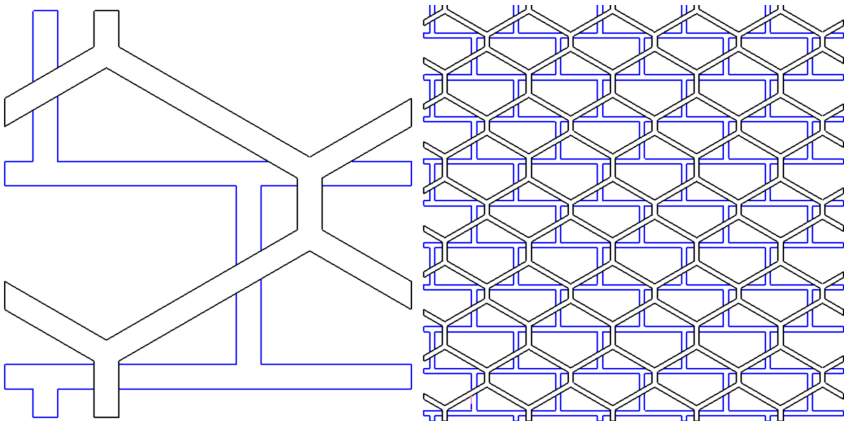

Figure 2.4: Multi-layer core systems with two layers made of two different topologies.

the same effect of a porous media combined with the rigidity of honeycomb cores. This will lead to better performances in terms of SAC (Chapter 5).

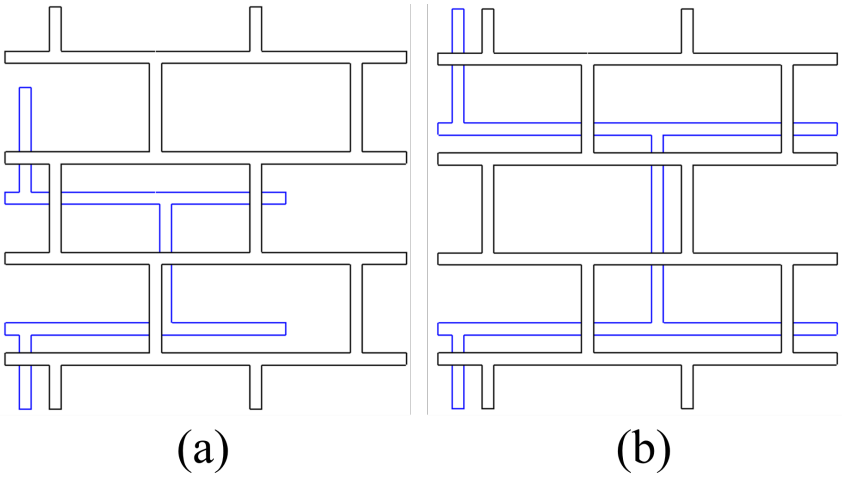

Figure 2.5: (a) two layers with two different unit cells sizes (b) unit cells size multiple to each other.

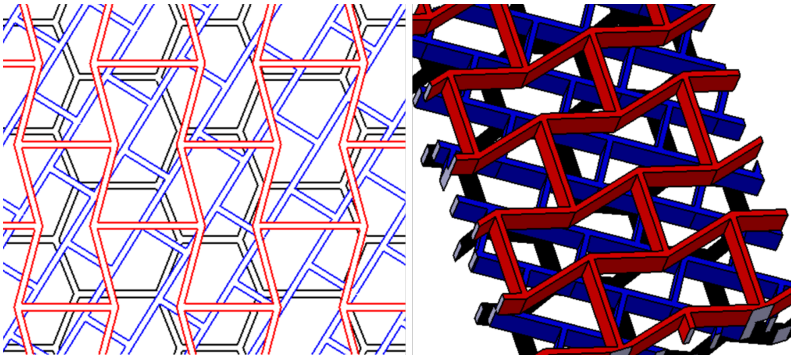

Figure 2.6: Sandwich panel made with three different cores involving rotation and shifted cores, red: auxetic core; blue: rectangular core; black: hexagonal core.

2.2.2 Parametric model

MLCTS proposed in this thesis will be made using the parametric model illustrated in Fig. 2.7. The wall thickness of the core (t_c) and the thickness of the skins (t_s) as well as the thickness of each layer (H_l) are also a part of parameters which can be modified. In addition, the size of the unit cell of each layer is identical while there is no different periodicity between layers. Moreover, the rotation about the z-axis is possible only for 3 values : 90°, 180° and 270° and with a square unit cell. Therefore, the WFEM can be applied.

From this parametric model, it is possible to calculate accurately the mass of the unit cell and then fix the surface density either of each layer or of the complete unit cell. Indeed, the STL is controlled by physical parameters which are the surface density, the dynamic bending stiffness and the damping of the structure. The surface density calculation of each layer, validated with CATIA, is obtained using the following expression:

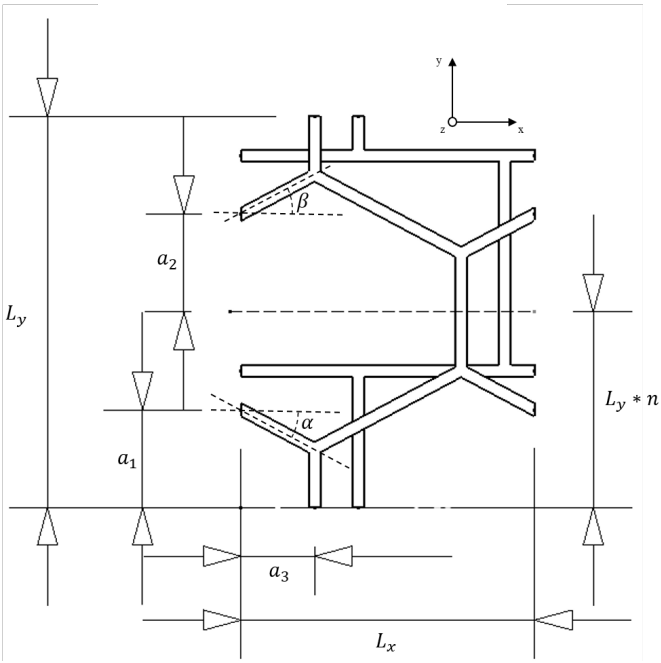

Figure 2.7: Parametric model used to make MLCTS.

$$\rho_s = \frac{\rho \cdot H_{ln} \cdot t_c \cdot \left(L_x \cdot p_1 + L_y - t_c \cdot p_2 \right)}{L_x \cdot L_y}, \tag{2.1}$$

where

$$\begin{aligned} p_1 &= \frac{1}{\cos(\alpha)} + \frac{1}{\cos(\beta)} + \frac{\tan(\alpha)}{2} - \frac{\tan(\beta)}{2} \\ p_2 &= \frac{1}{\cos(\alpha)} + \frac{1}{\cos(\beta)} - \frac{\tan(\alpha)}{2} - \frac{\tan(\beta)}{2} \end{aligned} \tag{2.2}$$

with H_{ln} corresponding to the thickness of the nth layer and where ρ is the density of the material of the core. It is then possible to compare configurations with the same surface density. It has been mentioned by Zergoune et al. [66] that the thickness of a honeycomb core strongly influences vibroacoustic indicators and alter noticeably the dynamic bending stiffness. Therefore, it is relevant to maintain the same thickness of each layer of the proposed MLCTS. In addition, the thickness of the skins and the wall thickness of the core are also identical for each layer. Consequently, only the 5 geometrical parameters mentioned in Fig. 2.7, a_1, a_2, a_3, α and β are changed to investigate their influence on the targeted indicators. All parameters are constrained by a specific range to obtain all possibilities in terms of topology for each layer. A MATLAB script was developed to obtain all possible topologies from the parametric model while guarantying the same surface density. Fig. 2.8 shows examples of MLCTS obtained with the parametric model. Only the bottom skin is represented for a sake of clarity. Finally, it is important to have a fine mesh to accurately capture the dynamic behavior related to the interfaces between

layers. Therefore, in the case of MLCTS, the mesh involves much more dofs than a single core.

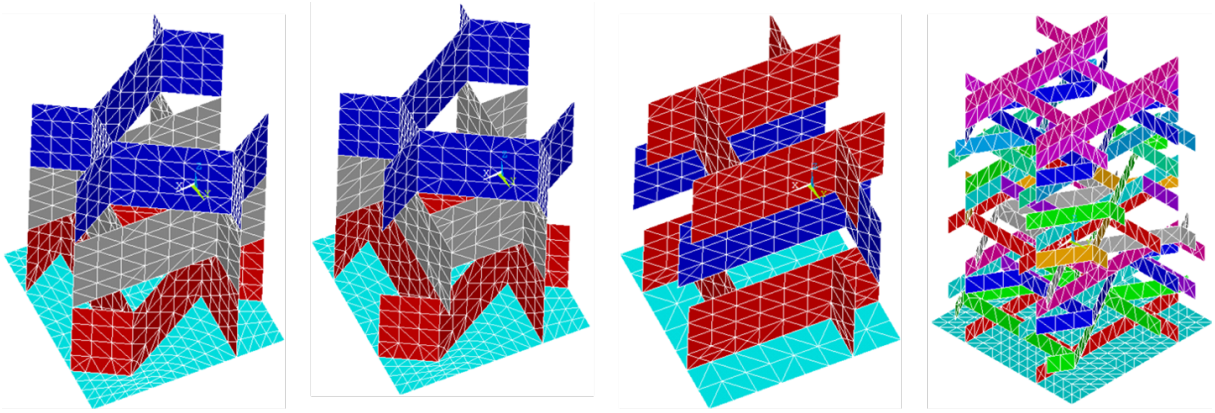

Figure 2.8: Multiple possibility of making MLCTS using the parametric model (a) Hexagonal-Rectangular-Auxetic core (b) Hexagonal-Rectangular (rotated 90°) -Auxetic core. (c) 3 rectangular core layers with a shifted middle core along x and y direction (d) MLCTS made of 15 random cores layers.

2.3 Vibroacoustic modelling of MLCTS inside a WFEM framework

MLCTS could be modeled using analytic formulation or homogenization methods, nevertheless, this is complicated to apply due to the nature of interfaces between layers, leading to heterogeneous properties along the z-axis. With MLCTS, many configurations of interfaces are possible and they all have different effects on the dynamic behavior of the structure. Consequently, it is more relevant to be focused on methods using numerical ways of thinking being able to consider the physics of the whole unit cell with the dynamic stiffness matrix. Considering the FEM of the unit cell of a MLCTS from the parametric model and using the WFEM, it is possible to calculate the STL of MLCTS. The WFEM can be combined with the use of nodal surfaces on the top and bottom skin of the unit cell [96] or with the TMM [74]. In addition, MOR can be applied to drastically reduce the computational cost. In the sound transmission problem, the acoustic wavenumber is defined by the frequency of plane waves exciting the structure and the sound velocity of the fluid (c_0) with $k_0 = \omega/c_0$. Therefore, waves travelling through the structure are fully characterized by oblique incident plane waves with $k_x = k_0 \sin(\theta)\cos(\alpha)$, $k_y = k_0 \sin(\theta)\sin(\alpha)$ and $k_z = k_0 \cos(\theta)$. Since external forces (induced by planes waves) are applied on the unit cell, same periodic relations Eq. (1.8) can be derived for generalized forces at bound-

aries. Only plane waves with real wavenumbers are considered and the STL is calculated for infinite size structures.

2.3.1 CMS applied for transmission problems

In the sound transmission problem, the CMS [61] is not applied to the same internal dofs as the WFEM. The internal dofs (u_I) should be separated in two parts : u_{IB} corresponding to the internal dofs belonging to the top and bottom skins and (u_{inner}) corresponding to the inner nodes Fig. 2.9. The dofs which are not excited by external forces (u_{inner}) will be replaced by modal internal dofs C_m. Indeed, other dofs need to be used to apply the Bloch-Floquet theory and should not be reduced at this step.

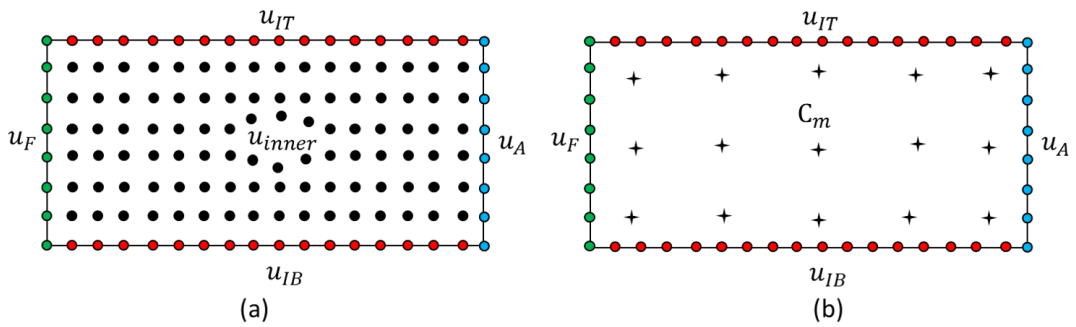

Figure 2.9: Internal dofs in the cross-section (B-B) illustrated in Fig. 1.5.

The vector (u_I) is then partitioned:

$$u_I = [u_{IB} \quad u_{inner}], \tag{2.3}$$

and after applying the CMS, u_I reads:

$$u_I = [u_{IB} \quad C_m]. \tag{2.4}$$

The dynamic condensation is then applied and leads to a reduced dynamic stiffness $\mathbf{D}'$ with less dofs $\mathbf{U}'$:

$$\mathbf{U}' = [u_1 \quad u_2 \quad u_3 \quad u_4 \quad u_L \quad u_R \quad u_A \quad u_F \quad u_{IB}]. \tag{2.5}$$

The matrix Λ (Eq. (1.11)) becomes modified since internal dofs belonging to the top and bottom skin remain to apply the periodic conditions leading to Λ_T with:

$$\Lambda_T = \begin{pmatrix} \Lambda & \mathbf{0} \\ \mathbf{0} & \mathrm{I} \end{pmatrix}. \tag{2.6}$$

This reduction can be applied to both methods explained hereafter.

2.3.2 WFEM combined with the TMM applied to MLCTS

The method developed by Parrinelo et al. [74] can be applied to MLCTS. Although they use the principle of TMM, it is not possible to use it in an optimal way by taking separately each layer. Indeed, the interface between two consecutive layers needs to be taken into account to fully capture the dynamic of the structure. For instance, if a rectangular core is combined with a honeycomb core, both cores cannot be treated separately and the total transfer matrix is not the multiplication of the transfer matrix of each layer. The interface between them should therefore be considered. One possibility is to model the unit cell part by part separating the interface and layers as shown in Fig. 2.10a whereas the other option is to treat the unit cell as one layer (Fig. 2.10b). All transfer matrices are calculated using the solid configuration since the fluid inside the core is not considered. Only one layer of each core and the interfaces are modeled with the finite element software. Each layer is characterized by its transfer matrix using the dynamic stiffness matrix as follow:

$$\mathbf{T} = \begin{pmatrix} 1 & 0 \\ 0 & 1/(i\omega\rho_0 A) \end{pmatrix} \mathbf{T}' \begin{pmatrix} 1 & 0 \\ 0 & -i\omega\rho_0 A \end{pmatrix}, \tag{2.7}$$

where A is the total area of the unit cell ($A = L_x L_y$), $\rho_0 = 1,21$ kg/m^2 is the density of air and $\mathbf{T}'$ is obtained after several operations on the dynamic stiffness matrix as described in Parrinello et al. [74]. Eq. ((2.7)) allows to change the usual displacement-force formulation of the dynamic stiffness toward TMM variables formulation for solid structures. The TMM is then applied [20]. In the illustrated case Fig. 2.10a, the total transfer matrix is evaluated as $\mathbf{T}_{skin} \cdot \mathbf{T}^5_{Hex/5} \cdot \mathbf{T}_{Hex-Rect} \cdot \mathbf{T}^4_{Rect/4} \cdot \mathbf{T}_{Rect-Aux} \cdot \mathbf{T}^5_{Aux/5} \cdot \mathbf{T}_{skin}$ where $\mathbf{T}_{skin}$ is the transfer matrix of the skin using the analytic formulation for a solid layer [20]. $\mathbf{T}_{Hex/5}$, $\mathbf{T}_{Rect/4}$ and $\mathbf{T}_{Aux/5}$ are the transfer matrix of a restricted zone of the hexagonal, rectangular and auxetic core respectively, limited to blue elements. $\mathbf{T}_{Hex-Rect}$ and $\mathbf{T}_{Hex-Rect}$ are the transfer matrix of the interface between the hexagonal and rectangular core and the rectangular and auxetic core respectively. There are highlighted by red elements in Fig. 2.10a.

The other possibility is to consider the core at once and to calculate its transfer matrix to obtain the total transfer matrix as $\mathbf{T}_{skin} \cdot \mathbf{T}_{core} \cdot \mathbf{T}_{skin}$ (Fig. 2.10b). Therefore, the number of dofs is drastically reduced and the physic related to the interfaces is kept.

2.3.3 WFEM combined with nodal surfaces applied to MLCTS

The method developed by Christen et al. [96], considers simple panels and laminates using solid elements. Consequently, it is necessary to adapt the formulation for more complex structures. The matrix $\mathbf{A}$ as described in Christen et al. [96] is given as follows:

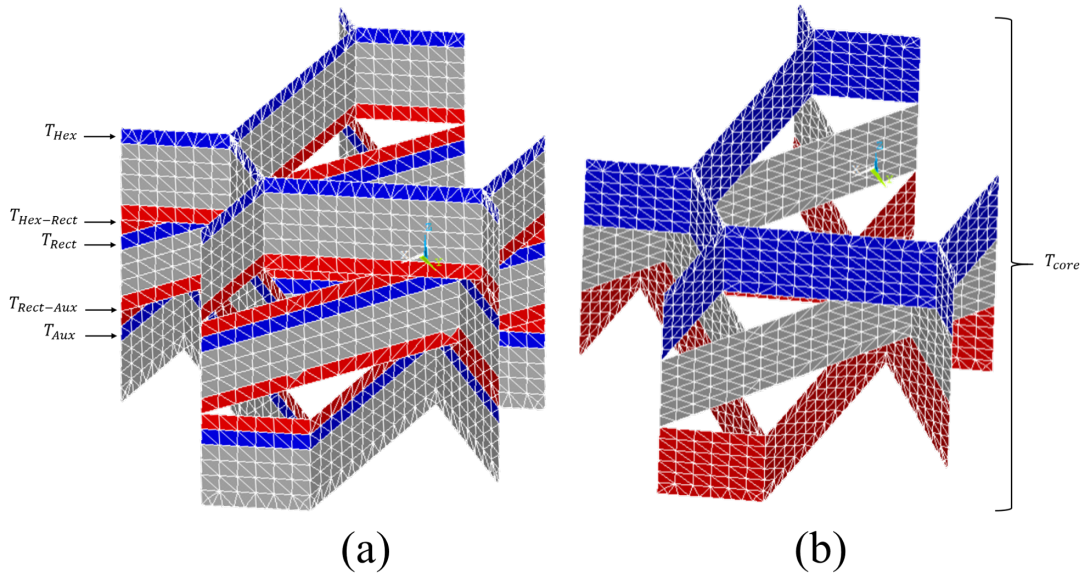

Figure 2.10: Modeling MLCTS with Parrinelo et al. [74] : (a) by slicing the core in several parts (b) or by considering the whole core.

$$\mathbf{A} = \Lambda_T^{-1} \mathbf{D}' \Lambda_T \tag{2.8}$$

with:

$$\mathbf{A}\tilde{\mathbf{U}} = \mathbf{F}. \tag{2.9}$$

where $\mathbf{F}$ is the reduced vector of external forces applied to the reduced vector of dofs $\tilde{\mathbf{U}}$:

$$\tilde{\mathbf{U}} = [u_1 \quad u_L \quad u_A \quad u_{IB}]. \tag{2.10}$$

The external forces are only applied on the top and bottom skin due to acoustic waves. A second dynamic condensation must be performed to condense the dofs which do not belong to the top and bottom skin. Then, the vector of external forces can be expressed as follows after reordering Eq.(2.9) and the second dynamic condensation [96]:

$$\begin{pmatrix} \tilde{\mathbf{F}}_I \\ \tilde{\mathbf{F}}_T \end{pmatrix} = \begin{pmatrix} \mathbf{S_I} & 0 \\ 0 & \mathbf{S_T} \end{pmatrix} \begin{pmatrix} p_I + p_R \\ p_T \end{pmatrix}. \tag{2.11}$$

where $\tilde{\mathbf{F}}_I$ and $\tilde{\mathbf{F}}_T$ are the external forces applied on the skin of the incident and transmitted field, respectively. The matrix $\mathbf{S}$ gathers the nodal surfaces of the skins of the incident and transmitted side respectively, and needs to be partitioned in two diagonal matrices called $\mathbf{S}_I$ and $\mathbf{S}_T$. Finally, the incident pressure p_I becomes a vector evaluated on nodes belonging to the skin on the incident part with the expression $p_I = \exp(i(\omega t - k_x x - k_y y))$. The final equation remains the same with few modifications related to the matrix $\mathbf{S}$:

$$\begin{pmatrix} \mathbf{b}_{II} + \frac{\mathbf{S_I}}{Y_O} & -\mathbf{b}_{IT} \\ \mathbf{b}_{TI} & -\mathbf{b}_{TT} - \frac{\mathbf{S_T}}{Y_O} \end{pmatrix} \begin{pmatrix} p_R \\ p_T \end{pmatrix} = \begin{pmatrix} \mathbf{b}_{II} - \frac{\mathbf{S_I}}{Y_O} \\ \mathbf{b}_{TI} \end{pmatrix} p_I. \tag{2.12}$$

where $Y_0 = \cos(\theta)/(i\omega\rho_0 c_0)$ and where $\mathbf{b}$ is the reduced matrix partitioned as follows, after applying the second dynamic condensation to the matrix $\mathbf{A}$ [96] and the reordering process of the matrix:

$$\mathbf{b} = \begin{pmatrix} \mathbf{b}_{II} & \mathbf{b}_{IT} \\ \mathbf{b}_{TI} & \mathbf{b}_{TT} \end{pmatrix} \tag{2.13}$$

By solving Eq. ((2.12)), the calculation of the acoustic transparency τ yields to Eq. ((2.14)) which is the ratio between the acoustic power of the incident and transmitted side.

$$\tau(\theta, \phi, \omega) = \frac{\mathbf{S}_T \cdot |p_T|^2}{\mathbf{S}_I \cdot |p_I|^2} \tag{2.14}$$

This model has been validated with two sandwich panels made of a single core [170]. They have been made using an industrial 3D printer. The measurements were performed using a Beta Cabine and results are given in third octave bands Fig. 2.11. A global good agreement is obtained between the model and measurements. The global trend is kept, and the comparison between standard and optimized panels are similar. The discrepancies are mainly due to manufacturing defects.

2.4 Vibroacoustic design of MLCTS

By using MLCTS, interfaces between layers lead to impedance discontinuities and often softer cores are applied, resulting in the modification of transition frequencies and more energy dissipation in the core. Therefore, altering configurations of each layer of a MLCTS will allow to modify the transition frequency with respect to the target industrial application. This section is devoted to the vibroacoustic design of MLCTS and the influence of the layout of MLCTS on the STL and the transition frequency. A number of applications have been implemented to determine the transition frequencies according to the calculation of the strain energy (Section 1.6.2 and to compute the STL using the described model Section 2.3.3. In addition, the orthotropy of skins are generally taken into account while they are considered isotropic in this thesis. Therefore, the mains directions of the sandwich panel are x and y due to the core design. Consequently, the focus has been made on directional STL as defined in Eq. (1.12). It is obtained by calculating the STL with an acoustic wave impinging the structure in both main directions x and y of the sandwich panel corresponding to an azimuth angle $\varphi = 0°$ and $\varphi = 90°$, respectively. Moreover, the angle of incidence $\theta_i = 78°$ corresponds to the lowest measurable angle and also to the

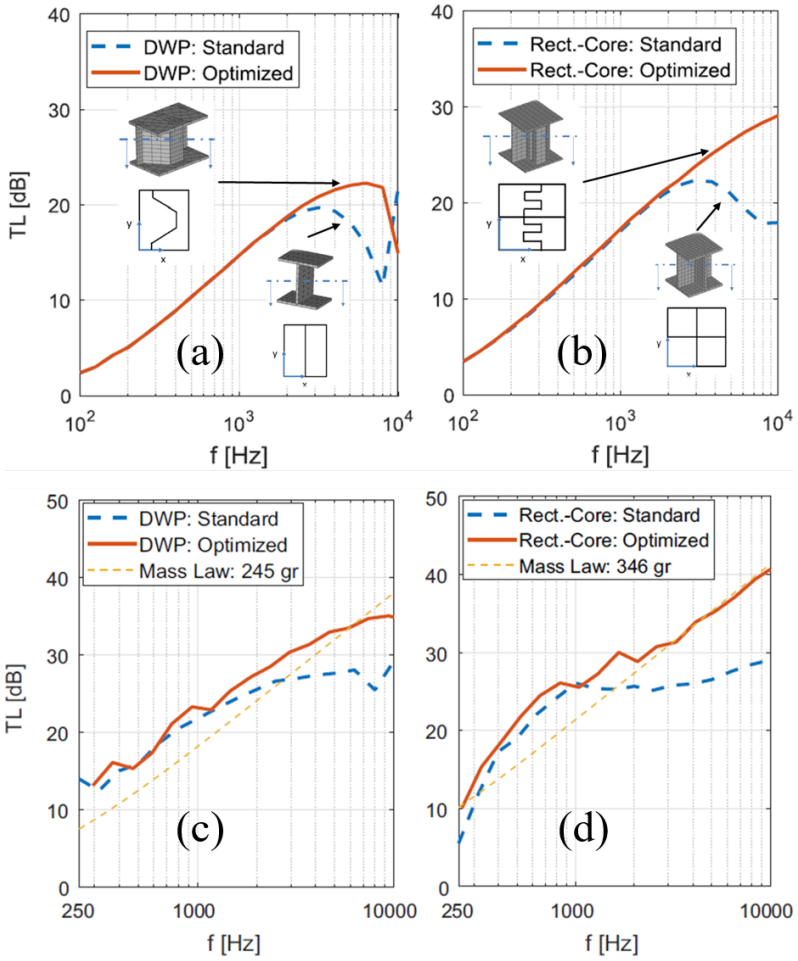

Figure 2.11: Validation of the model using sandwich panels made by 3D printing [170] (a) Double Wall panels (b) Rectangular core sandwich panels (c) measurement for double wall panels (d) measurement for rectangular core sandwich panels.

lowest coincidence frequency for the sandwich panel. Consequently, the directional STL is used as the acoustic indicator calculated for ($\varphi = 0°$, $\theta_i = 78°$) and ($\varphi = 90°$, $\theta_i = 78°$). Since the main directions of the sandwich panel are excited with the directional STL, it is expected to keep the same range of performances and to have a relevant qualitative acoustic indicator showing how the structure behaves depending on the direction. Many configurations have been tested which would have led to a very high computational cost in case of a diffuse acoustic field calculation. However, an integration over the azimuth angle φ will be proposed to better quantify the acoustic efficiency and to give a better estimation of the STL of MLCTS. The main conclusions and interpretations given in this thesis about the STL can be thus applied to a diffuse acoustic field calculation.
All applications are performed with skins made of Aluminium and the core made of ABS with the same characteristic used in Section 1.3. Geometrical parameters of the unit cell are : $L_x = 12$ mm, $L_y = 12$ mm, $t_s = 1$ mm, $t_c = 1$ mm and $H = 9$ mm.
The standard unit cell is obtained with $a_1 = L_y/4$, $a_2 = L_y/4$ and $a_3 = L_x/4$. All next

compared configurations have the same surface density. Finally, unit cells have been modelled using shell elements in ANSYS software and the mesh convergence has been verified for the frequency range [100 Hz, 10000 Hz]. The number of dofs for all configurations are almost similar and around 4200 dofs.

2.4.1 Shifted core size effect

This first application gives the opportunity to know which size the middle core should have to obtain the best vibroacoustic properties. The rectangular core is discretized such as 9 layers of 1 mm can be shifted independently. The first design is intended to investigate the influence of increasing the size of the shifted middle core of a sandwich panel made of a multi-layer rectangular core. The geometry of the shifted core corresponds to $a_1 = 3L_y/8$, $a_2 = 3L_y/8$ and $a_3 = 3L_x/8$. The thickness of the middle core takes the values given in Table 2.1. Therefore, 4 configurations are implemented and are compared to the standard unit cell as shown in Fig. 2.12.

Table 2.1: Thickness of the middle core for each configuration.

	Standard	Config 2	Config 3	Config 4	Config 5
Thickness (mm)	0	1	3	5	7

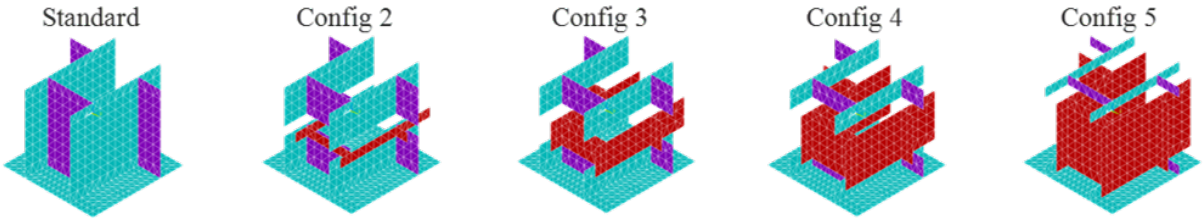

Figure 2.12: Configurations for shifted core size effect.

The STL is calculated for both directions x and y and considerably improved as shown in Fig. 2.13. Indeed, the interfaces between layers creates more flexible structures leading to a reduction of the dynamic bending and shear modulus (Eq. (1.54) and Eq. (1.55)) and thus, higher flexural wavenumbers (Fig. 2.14). Therefore, the coincidence frequency for both calculated angles are shifted to higher frequencies. Since the shifting is performed in both direction x and y, the loss of mechanical rigidity occurs in both directions and is relatively comparable.

All shifted configurations have the same global acoustic efficiency as compared to the standard structure since the middle core is shifted in the same way and only the size is modified. However, the 3^{rd} configuration seems to exhibit a better STL in both directions.

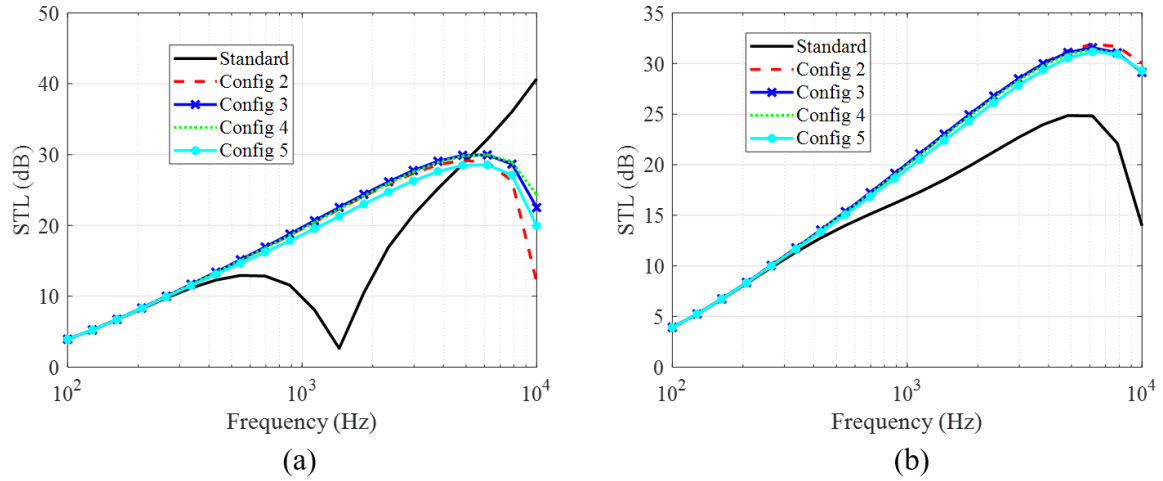

Figure 2.13: Influence of the shifted layer size on the STL (a) x direction (b) y direction.

Results are strongly dependent on the considered direction due to the orthotropy and because the structure is stiffer along the x-direction.

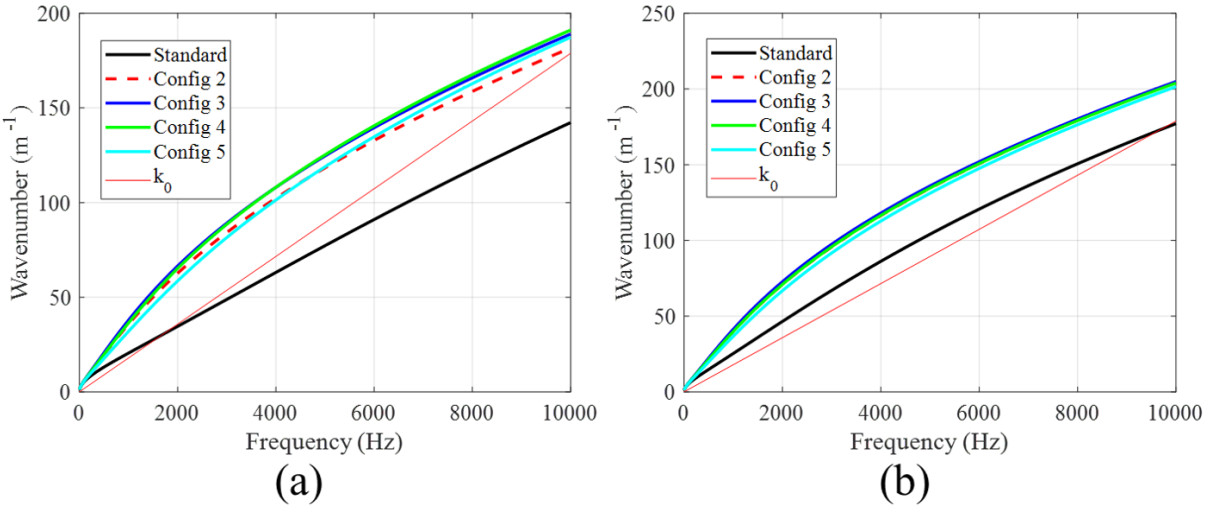

Figure 2.14: Flexural waves (a) k_x (b) k_y.

Finally, by integrating over the azimuth angle φ, it is possible to better quantify the acoustic efficiency and get closer to a diffuse acoustic field. Therefore, the shifting in both directions as well as the MLCTS design gives a high improvement in a broadband frequency Fig. 2.15. The mass law can still be applied up to 2000 Hz compared to the standard design and thus, a better STL at low frequencies. It is then expected to obtain a comparable result for diffuse field measurement.

Besides, as shown in Fig. 2.16, even a small shift between layers produces a drop of transition frequencies. This result is particularly stressed along the y-direction (Fig. 2.16b). The second transition frequency f_{ty2} occurs before 10000 Hz, except in the standard sand-

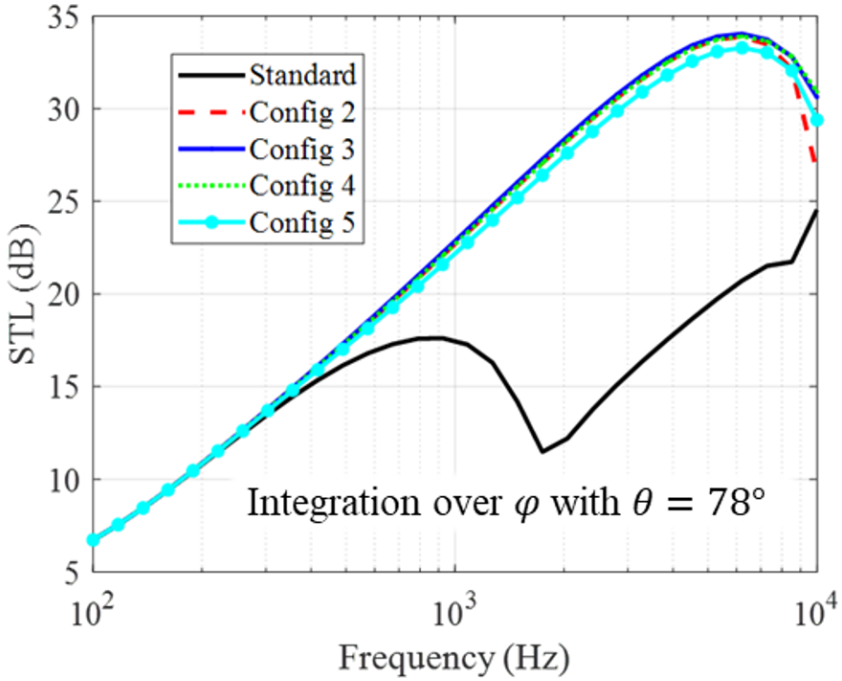

Figure 2.15: Influence of the shifted layer size on the STL integrated over the azimuth angle φ with $\theta = 78°$.

wich panel. In the x-direction, the first transition frequency f_{tx1} is altered depending on the configuration whereas the differences for the second transition frequency are not always observable. The first transition frequency reaches the lowest values when the size of the shifted core is 3 mm (Config 3) and thus corresponds to 1/3 of the total thickness of the core. However, configuration 3 leads to a higher second transition frequency than configurations 4 and 5 along x-direction (Fig. 2.16a) but turned out to be the lowest in the y-direction. To summarize, in MLCTS, transition frequencies are generally lower than standard structures since both, the dynamic bending and shear modulus are lower. This is due to the low rigidity introduced by interfaces between layers. Moreover, it can be concluded that the 3^{rd} configuration has the higher STL and thus the best acoustic efficiency in all the frequency range.

The enhancement of the STL as well as the diminution of transition frequencies in MLCTS configurations is mainly related to the reduction of the bending and shear modulus. However, the shifting process can be used to modify the dynamic behavior in both directions x and y and thus, to better manipulate the dynamic properties of the sandwich panel. In the next Sections, the size of the shifted middle core is 3 mm.

2.4.2 Shifted middle core along x-direction

The second application corresponds to a shifted middle core in which the thickness of the layer is 3 mm. The shift is achieved along the x-direction and results in 6 different core

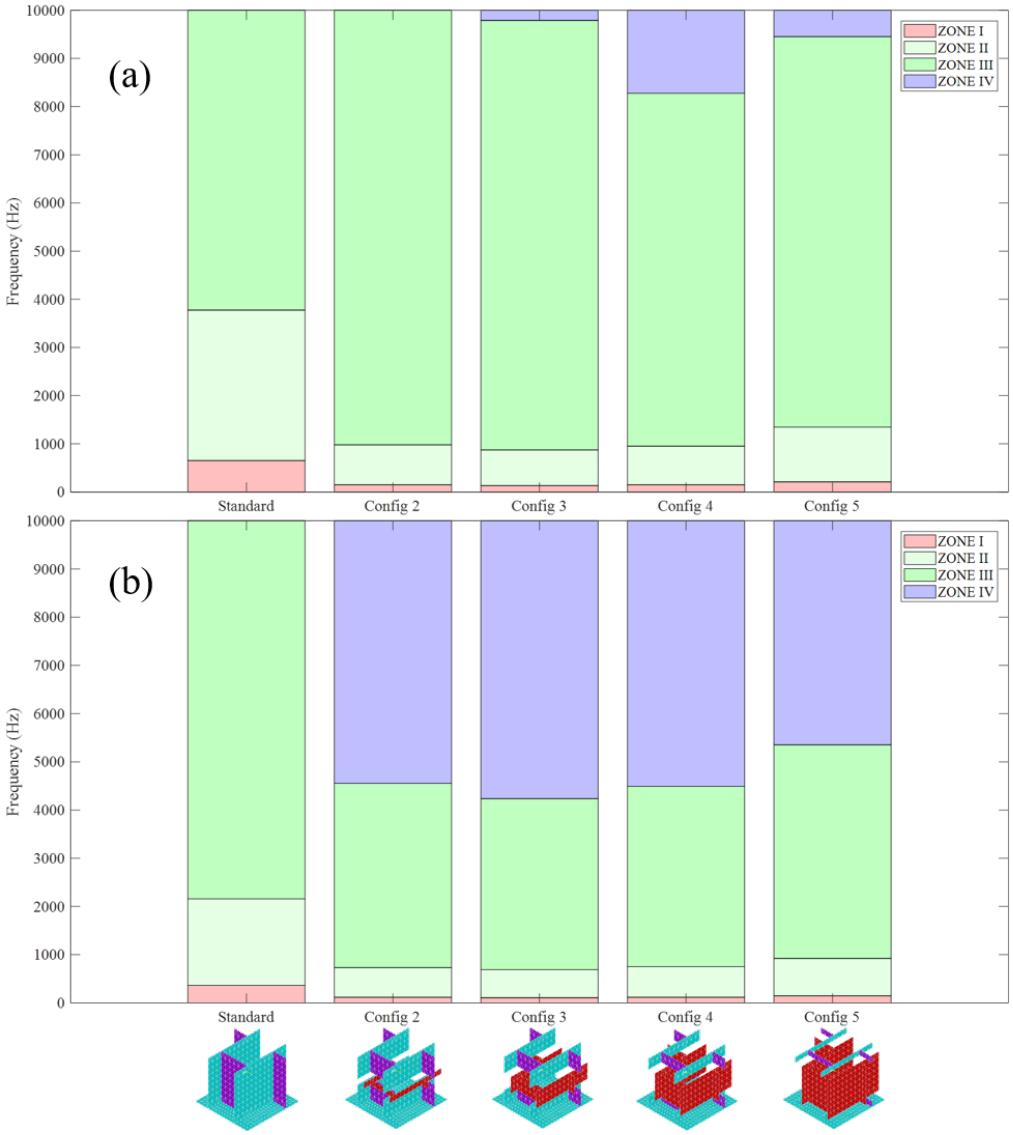

Figure 2.16: Influence of the shifted layer size on transition frequencies (a) x direction (b) y direction.

configurations given in Table 2.2. These configurations are shown with the shifted parts in a red colour at the bottom of Fig. 2.21 and in the following figure:

Table 2.2: Values of a_3 for the shifting process in x-direction.

	Config 1	Standard	Config 3	Config 4	Config 5	Config 6
a_3	$L_x/8$	$L_x/4$	$3L_x/8$	$5L_x/8$	$6L_x/8$	$7L_x/8$

Concerning the STL, shifting the middle layer along x-direction does not change the STL (Fig. 2.18a) when the acoustic wave is propagating along x while a strong improvement is noticed when the propagation is along y (Fig. 2.18b). Indeed, the flexural wave

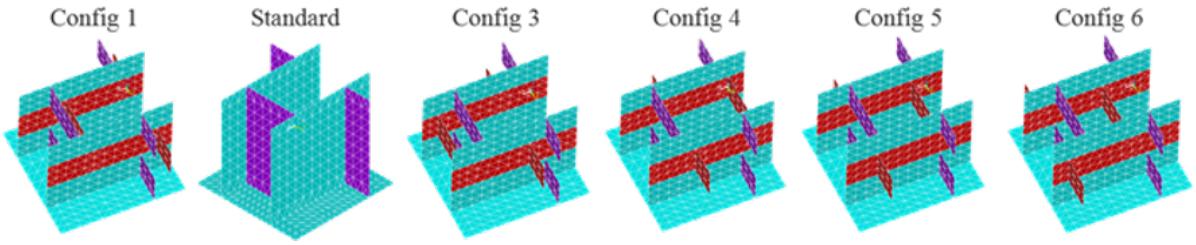

Figure 2.17: Configurations for shifted middle core along x-direction.

of the structure remains the same in the x-direction (Fig. 2.19a). Therefore, the dynamic behavior in x-direction is not altered and the dynamic properties such as the bending and shear modulus are similar to the standard panel. It can be seen at higher frequencies a slight enhancement of the dynamic rigidity corresponding to lower flexural wavenumbers (Fig. 2.19a). Oppositely, the structure is more flexible in the direction y, which results on a shift of the coincidence to a higher frequency. Thus, the STL of MLCTS can be hugely improved when the acoustic wave is travelling along the direction y.

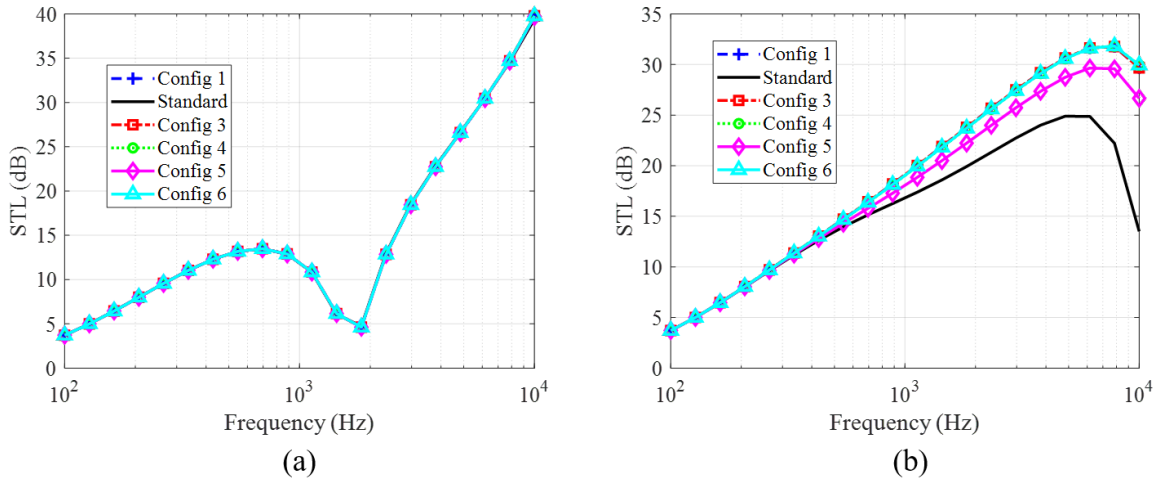

Figure 2.18: Influence of the shifted middle layer along the direction x on the STL (a) x direction (b) y direction.

Finally, after the integration over φ, the STL is slightly improved in the case of shifted structures (Fig. 2.20). The dynamic behavior is mainly related to wave properties in the direction x since the STL results are similar. It is thus expected to have non negligible improvement for diffuse acoustic field. However, the critical frequency will probably not be strongly shifted compared to the standard structure.
Meanwhile, the flexural behavior along the x-direction (Fig. 2.21a) is globally not altered but Zone II in configuration 6 is enlarged and the shear motion of the core is expected to have a stronger influence on the global behavior of the structure. Moreover, this demonstrates that it is possible to shift the first transition frequency to higher values.

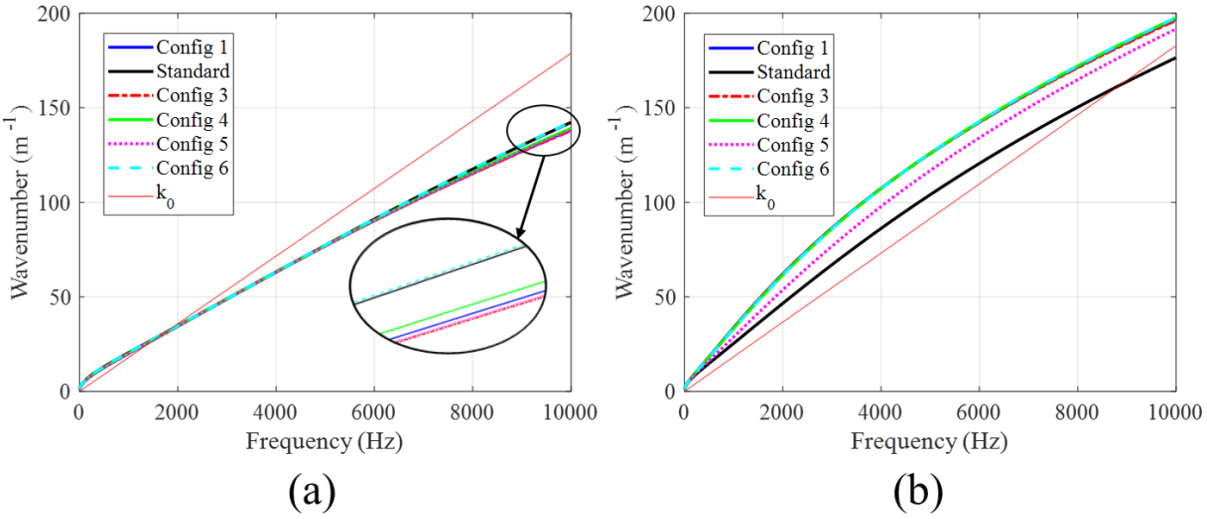

Figure 2.19: Flexural waves of shifted middle layers along x direction (a) k_x (b) k_y.

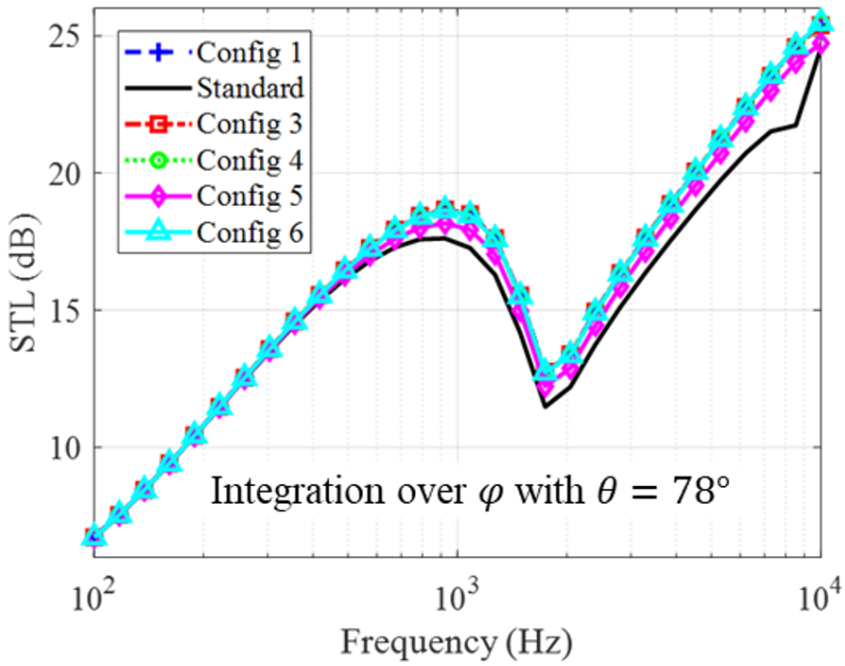

Figure 2.20: Influence of the shifted middle layer along the direction x on the STL integrated over the azimuthal angle φ with $\theta = 78°$.

Besides, along y-direction (Fig. 2.21b), the influence of the shifted core becomes more important. In this case, all MLCTS exhibit lower transition frequencies. These values are approximately the same for all configurations, except for the 5^{th} configuration, in which the first and second transition frequency occur in the upper frequency bandwidth. In this latter configuration, the shifted core walls are aligned with the top and bottom layer and increase the global rigidity of the structure.

Although the STL has been slightly improved, both transition frequencies along the direction y occurs below 10000 Hz. The dynamic properties are strongly altered and shifting

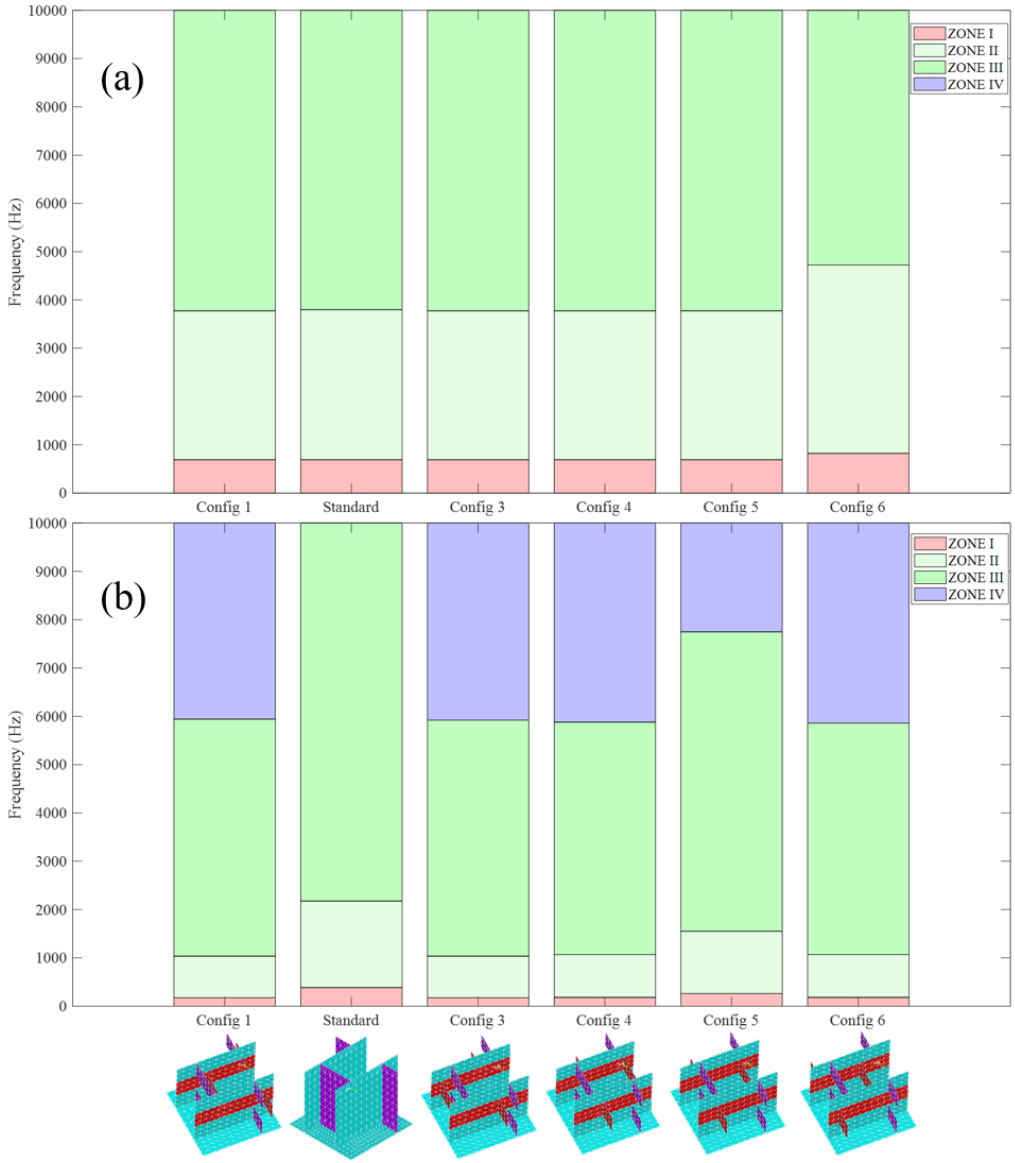

Figure 2.21: Influence of the shifted middle layer along the direction x on transition frequencies (a) x direction (b) y direction.

the core along the direction x does not seem to be a relevant solution. Therefore, the next step is to shift the core only along the direction y.

2.4.3 Shifted middle layer along y-direction

The last application is a shifted middle core with a layer thickness of 3 mm and $a_3 = L_x/4$. Now, the layer is shifted only in the y-direction, resulting in 9 configurations corresponding to the pairs listed in Tab 2.3. The configurations are illustrated in Fig. 2.22.

Contrary to the shifted middle core along x-direction, it is now the x-direction which is strongly influenced by the shifting process (Fig. 2.23) and (Fig. 2.26a). The symmetry of

Table 2.3: Values of the pairs (a_1, a_2) for the shifting process in y-direction.

	a_1	a_2
Config 1	$L_y/8$	$L_y/8$
Config 2	$L_y/8$	$L_y/4$
Config 3	$L_y/8$	$3L_y/8$
Config 4	$L_y/4$	$L_y/8$
Standard	$L_y/4$	$L_y/4$
Config 6	$L_y/4$	$3L_y/8$
Config 7	$3L_y/8$	$L_y/8$
Config 8	$3L_y/8$	$L_y/4$
Config 9	$3L_y/8$	$3L_y/8$

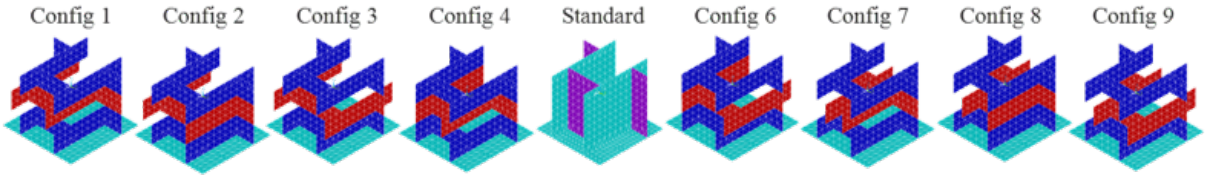

Figure 2.22: Configurations for shifted middle core along y-direction.

the shifting process is clearly demonstrated.

The STL of all configurations are shown in Fig. 2.23. Results are intentionally split for the sake of clarity. All configurations of MLCTS have the advantage of improving the STL in both directions but more significantly along the x-direction (Fig. 2.23a,b,c) while the enhancement is negligible along the y-direction (Fig. 2.23d,e,f).

The dynamic properties of shifted structures are still reduced and the flexural wavenumber becomes higher. Therefore, the coincidence frequency is shifted to a higher frequency. Along the direction y (Fig. 2.24b), the flexural wave remains similar compared to the standard panel and the bending and shear modulus in that direction are not altered.

Finally, the integration of the STL over the angle φ shows a strong improvement of the STL comparable to the results obtained in Section 2.4.1. The coincidence frequency occurs at a higher frequency and it is thus expected to have similar results in the case of diffuse acoustic field (Fig. 2.25).

Besides, it is possible to keep a large second zone (Zone II) where the bending of the structure will be consequent when $a_1 = L_y/4$ independently to the value of a_2, and to avoid a fourth zone (Zone IV) with the bending of the skins triggered before the frequency range of interest. The same observation can be made along y-direction (Fig. 2.26b) but with lower differences. The global behavior of the structure in this direction remains comparable to the standard sandwich panel. In the case of Configurations 2, 4, 6 and 8, transition

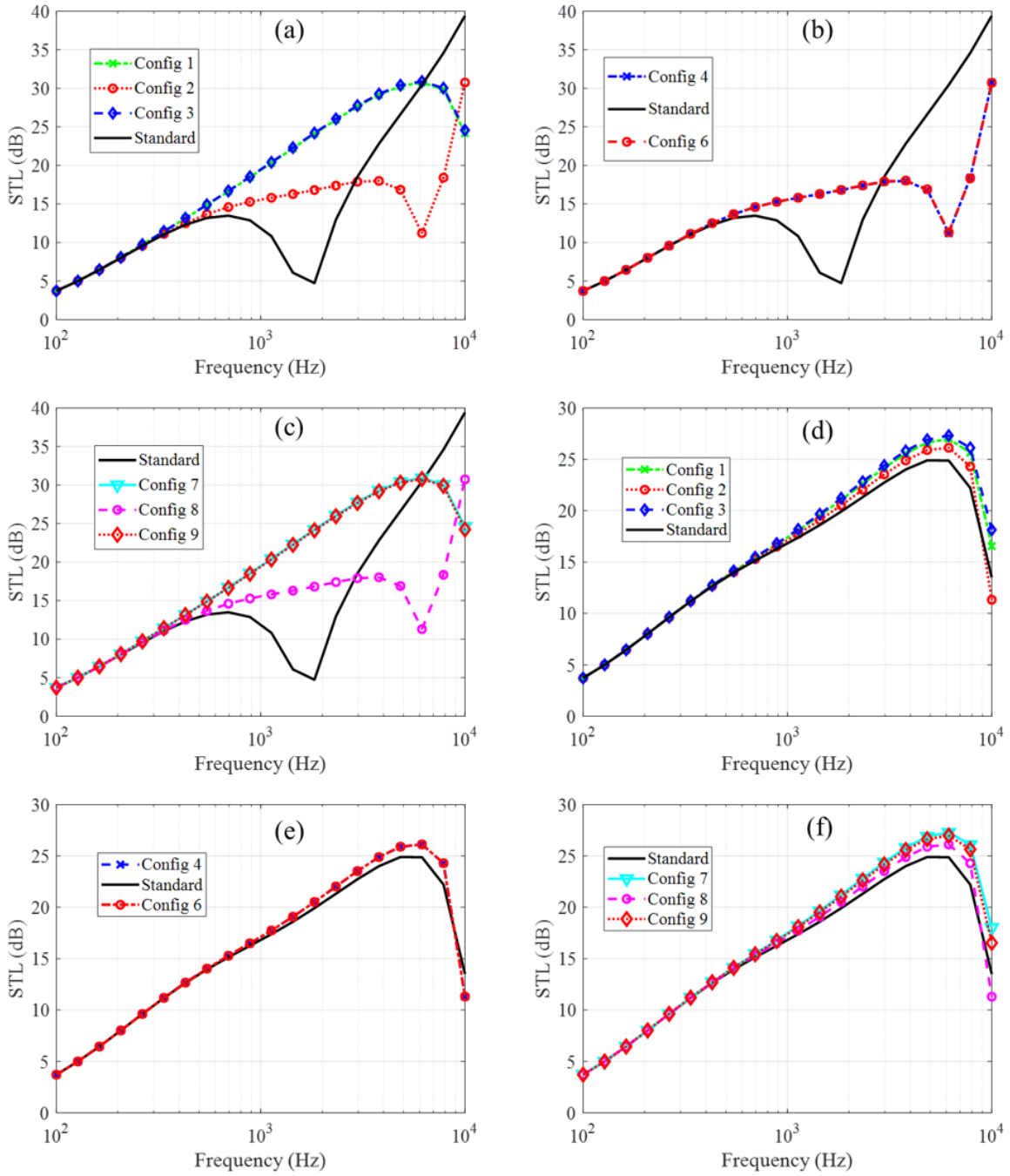

Figure 2.23: Influence of the shifted middle layer along the direction y on the STL (a) 1^{st}, 2^{nd} and 3^{rd} configuration (b) 4^{th} and 6^{th} configuration (c) 7^{th}, 8^{th} and 9^{th} configuration; and along the direction y (d) 1^{st}, 2^{nd} and 3^{rd} configuration (e) 4^{th} and 6^{th} configuration (f) 7^{th}, 8^{th} and 9^{th} configuration compared to the standard unit cell 5^{th} configuration.

frequencies in both directions are not strongly modified compared to the standard structure. In addition, they exhibit a high improvement of the STL in a broadband frequency. The STL can still be improved by a parametric analysis of the combination of the shifting in x and y direction as done in the study of the layer size Section 2.4.1. Nevertheless, the

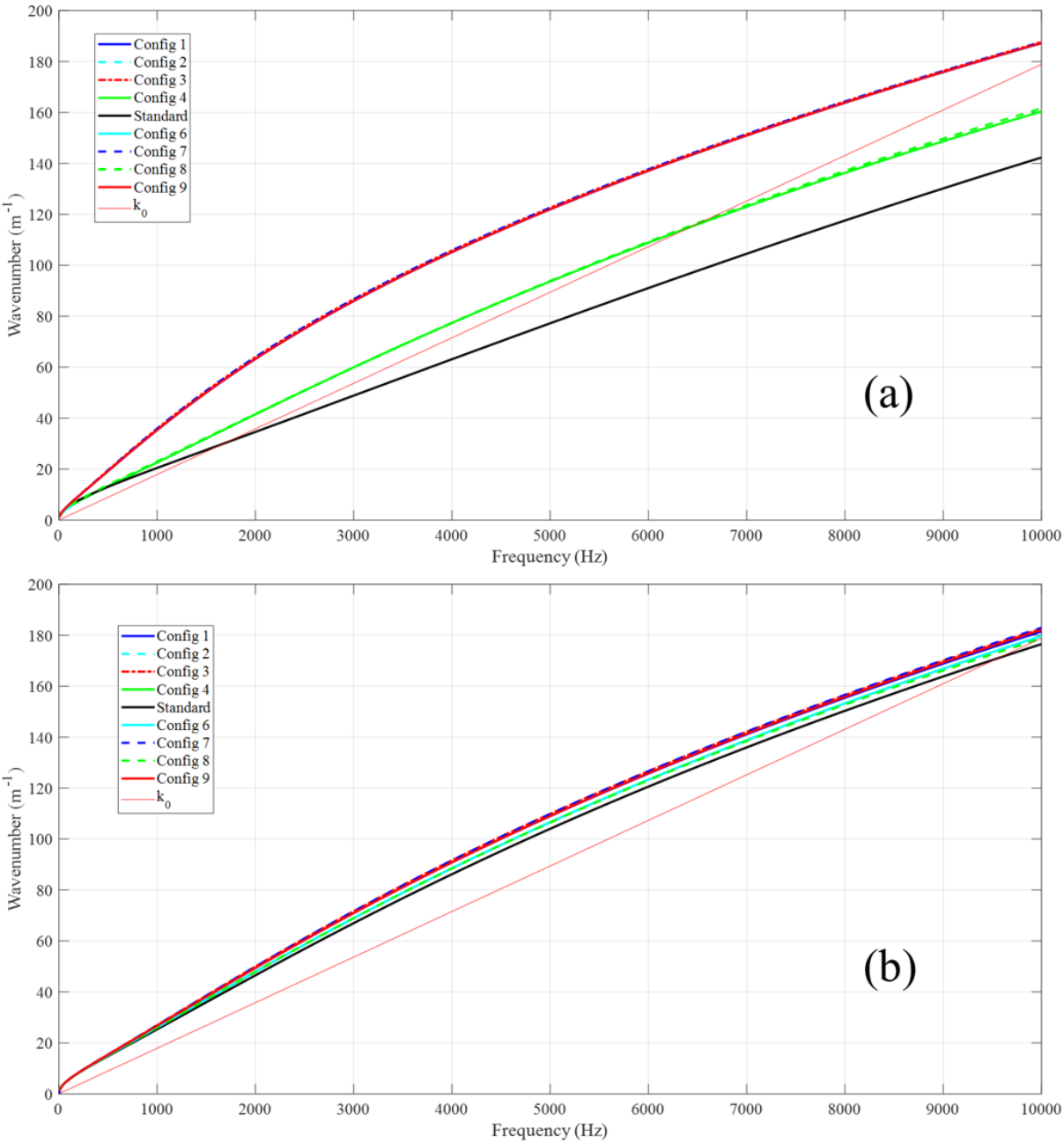

Figure 2.24: Flexural waves of shifted middle layers along y direction (a) k_x (b) k_y

drop of the dynamic properties will occur in both directions of the structure which is not desirable on some applications unless the only target is the acoustic efficiency.

Most of time, transition frequencies and more specifically the first transition frequency are expected to be shifted at higher frequencies, especially in aerospace industry. However, the increase of the transition frequency does not lead to a higher STL in all applications. Therefore, it is interesting to study specific designs allowing to play with the dynamic behavior of the structure to find out the correct balance between vibroacoustic properties. Consequently, it has been shown that the shifted middle core should have a size corresponding to 1/3 of total height of the core to obtain the highest STL efficiency.

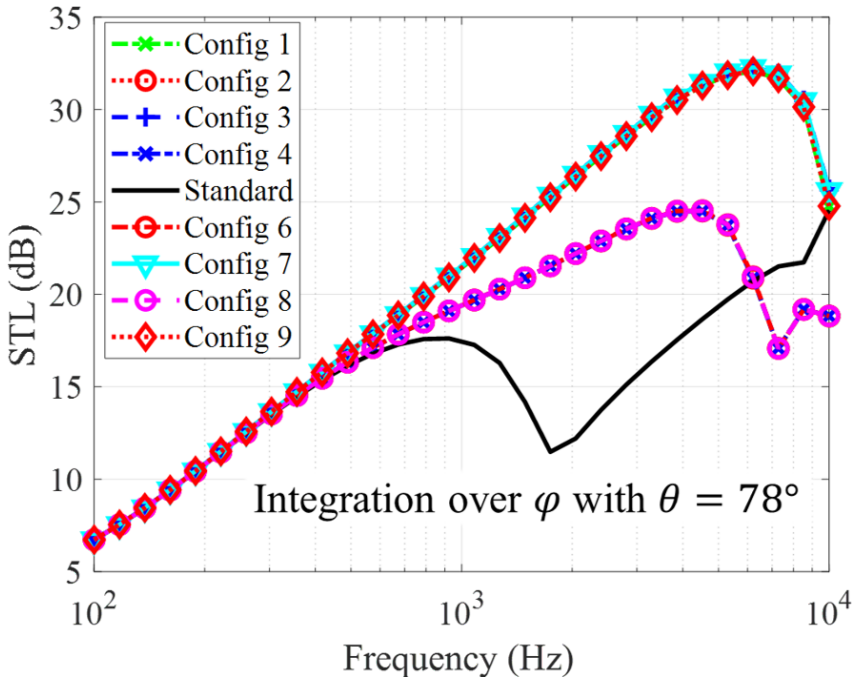

Figure 2.25: Influence of the shifted middle layer along the direction y on the STL integrated over the azimuthal angle φ with $\theta = 78°$.

Moreover, the core should be shifted in the direction y similarly to the configuration 2, 4, 6 and 8. Indeed, they give the possibility to not highly alter the dynamic properties of the structure in both directions x and y compared to the standard panel and the STL is considerably improved in all the frequency range of interest.

2.5 Conclusions

In this Chapter, MLCTS has been introduced to present the main issues related to their geometries, leading in some cases, to non-periodic structures. However, by using a constrain parametric model, MLCTS can be considered as periodic structures and the unit cell can be extracted. In addition, it has been shown that such designs offer the possibility to keep the mass constant if layers are simply shifted. New parameters should be taken into account and many configurations can be created opening new perspectives in terms of design space study.

Besides, two models has been proposed. The first [74] is already explained in the literature while the second has been extended and improved to be applied to more complex structures such as MLCTS, compared to the previous formulation [96]. This later was validated experimentally in diffuse acoustic field using sandwich panels manufactured by a 3D printer.

An introduction to MLCTS vibroacoustic designs is performed with the analysis of transition frequencies and the STL. Different models have been applied to a sandwich panel

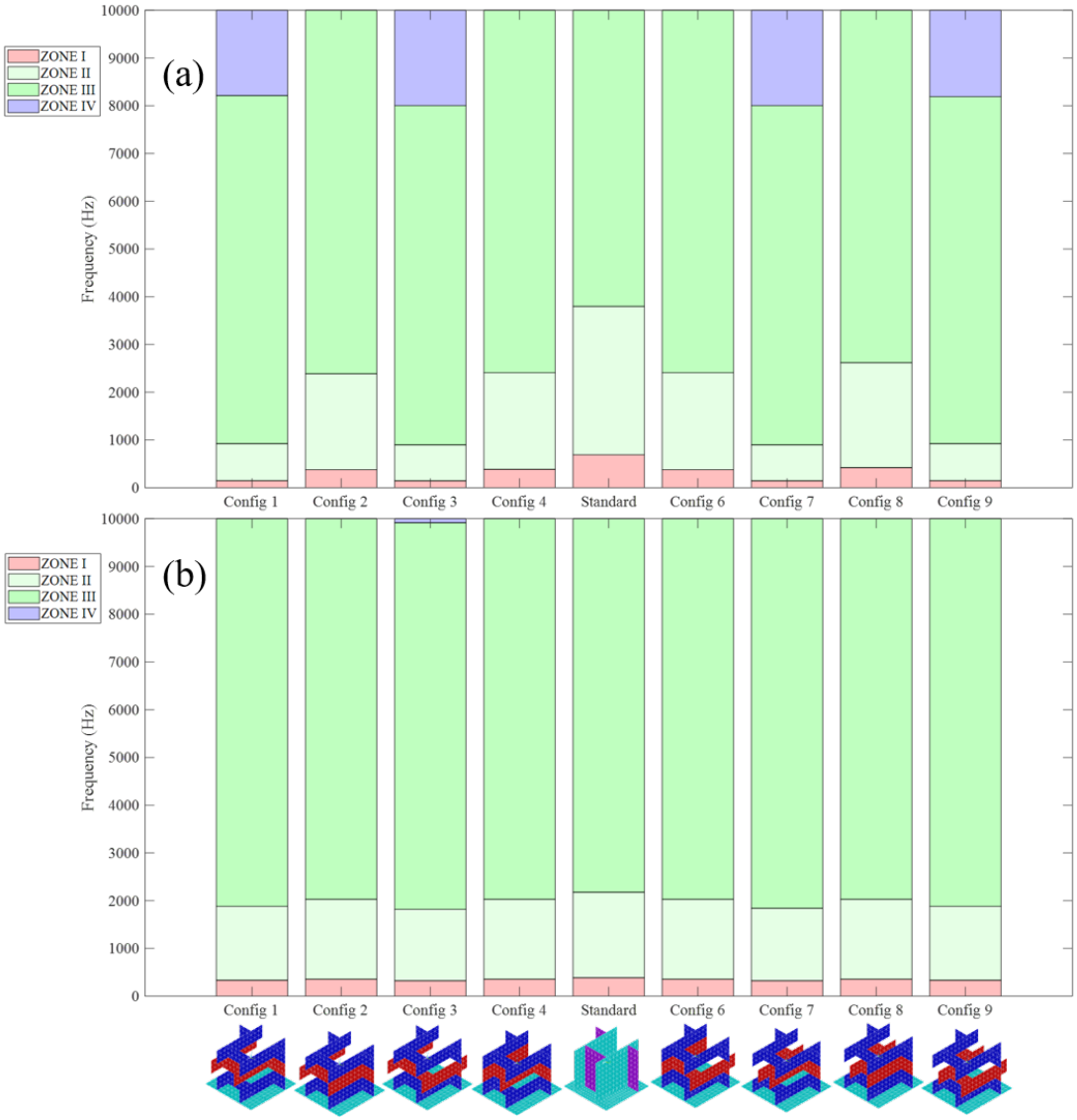

Figure 2.26: Influence of the shifted middle layer along the direction y on transition frequencies (a) x direction (b) y direction.

made of a rectangular core unit cell and then modified to make a multi-layer rectangular core system, maintaining the mass constant and using a shifting process on one layer. Often, transition frequencies are studied as a consequence of the dynamic behavior of the structure while, in this thesis, it was proposed to control them with MLCTS designs.
The first application corresponds to the modification of the size of a middle core and allows to exhibit that the improvement of the STL is maximum when the thickness of the middle layer core is 1/3 of the total thickness of the core. Besides, transition ranges are altered in both directions leading to a different dynamic behavior in the frequency range of interest. The same size for the middle core is used in the second and third application and have shown the possibility to alter the transition ranges in specific directions without altering dynamic properties of the other directions. Generally, both transition frequencies

are shifted to lower frequencies with MLCTS. It is possible to modify and adjust the frequency range of each zone. This could be a great interest for some industrial applications to control the dynamic behavior of the structure. It is also an easy way to quickly change the first and second frequency transition and thus, trigger a specific flexural behavior of the sandwich panel. This indicator is particularly used in aerospace industry where the shear core effect of sandwich panels is under investigation. In some cases, the existence of the first and second zone and thus, the shear effect and the global bending of the structure, is drastically reduced. The study was performed for both direction x and y, related to the main directions of the structure, and the influence of the shifting process turned out to be different for both directions. Moreover, it is shown that MLCTS strongly enhance the STL in a broadband frequency while the mass is kept constant although transition frequencies becomes lower. Nevertheless, a good balance between the STL and the trigger of the first and second transition frequency can be found to propose an optimal design of unit cells according to the industrial application. Finally, it was shown that MLCTS easily overcome the design limitation related to the mass constraint in the research of the improvement of the acoustic efficiency, and open large perspectives of design space. Nevertheless, the static stiffness of MLCTS still needs to be improved because of the weaknesses introduced by the interfaces.
The mechanism allowing to trigger the transition frequencies still need to be investigated. Ultimately, a complete parametric survey as well as an optimization process can be performed to investigate how vibroacoustic indicators will evolve with more geometrical parameters defined in the parametric model. Such study could be performed for a diffuse acoustic field if the number of dofs is lower or by integrating only the azimuth angle φ as performed in this paper. The interface between layers involves meshing accurately the MLCTS to capture correctly the local dynamic behavior induced by the connecting points. The robustness of this study relies on this accuracy. Therefore, the results of the shifting process remain stable. However, this leads to an increase of the dofs compared to standard sandwich panel. It could be reduced using simpler core designs. Finally, measurements of the STL in diffuse acoustic field can be performed to verify the acoustic efficiency of the proposed designs of MLCTS.

The next Chapter is focused on local dynamic behaviors of MLCTS and their influence on the STL.

Chapter 3

Vibroacoustic analysis of multi-layer rectangular core systems (Part II)

Abstract

The purpose of this chapter is to analyze resonant behaviors and the veering effect occurring in the wave propagation of multi-layer rectangular core systems (MLRCS) consisting on stacking layers of rectangular cores, and to carry out a study of their influence on the STL. The veering effect is related to the coupling of the flexural and shear wave due to the interfaces between layers while the resonant behaviors occurs at specific coincidence frequencies. MLRCS are modeled with two methods ([74, 96]) considering either the whole unit cell or the skins and the core separately applying the TMM. Both are combined with the WFEM. A high improvement of the STL is obtained in the critical frequency region where the veering effect occurs. Results can be compared to internal resonators since the core influences the flexural wave propagation by converting the bending strain energy into shear strain energy. This chapter proposes to take advantage of the veering effect to highly improve the STL with no added mass. Finally, it is shown that the veering effect can be controlled by modifying the geometrical parameters of the MLRCS.

Contents

3.1 Introduction

Dispersion curves and more specifically flexural waves can be used to predict coincidence frequencies and critical frequencies of sandwich panels. However, in certain cases, different waves can be coupled in the structure combining different dynamic behaviors and leading to veering effects occurring at specific frequencies as explained by Mace and Manconi [171, 172]. The veering effect can be defined by two parameters which are the frequency in which the veering is triggered (mainly governed by the local dynamic behavior introduced by the structure) and the size of the veering, governed by the structural damping. This veering behavior has been mostly studied with theoretical aspects considering wave-guides in which string coupling systems allow to easily modify the rigidity, mass and damping of the structure [171, 172] to investigate their effect on the wave propagation. In addition, the local dynamic behavior of certain structures induces resonant behaviors and different types of coincidence frequencies, while in the literature, the bending behavior of honeycomb sandwich panels mainly governed by the flexural behavior of the skins, is sufficient to predict the STL.
In this chapter, veering effects and resonant behaviors are observed in MLRCS depending on the core geometry and particularly the shift between layers. The main purpose is to investigate their effect on the STL and the dispersion curves. Firstly, in Section 3.2 a MLRCS is compared to a standard structure to show how the veering effect occurs. Then, Section 3.3 is focused on the study of the resonant behavior of the MLRCS by calculating the STL for specific acoustic incidence angles followed by the analysis when acoustic waves are coupled with the veering effect in Section 3.4. Finally, in Section 3.5, the influence of several geometrical parameters is explored to evaluate their impact on the wave propagation and thus, on the acoustic efficiency of the structure. The chapter is concluded in Section 3.6.

3.2 Dispersion curve analysis

In this section, the geometrical parameters of the unit cell are : $L_x = 10$ mm, $L_y = 10$ mm, $t_s = 1$ mm, $t_c = 1$ mm and $H = 20$ mm. All next compared configurations have the same surface density.

3.2.1 MLRCS and standard sandwich panel geometry

The main purpose is to investigate the influence of the dynamic behavior of the structure on the STL performance. The critical frequency of the structure is related to all coincidence frequencies. Therefore, it is necessary to understand the mechanism triggering them to attenuate their impact on the diffuse acoustic field and thus, reduce the STL

drops.

In this section, a MLRCS made of rectangular cores (Fig. 3.1) is compared to a standard sandwich panel made of a single rectangular core. Only the bottom skin is illustrated for sake of clarity. Both structures are made having the same surface density since only a shifting process in x and y direction is performed between layers. The MLRCS is made of stacking 4 layers of rectangular cores in which the second and third layer are configured as follows: ($a_1 = 3L_y/8$, $a_2 = 3L_y/8$, $a_3 = 3L_x/8$) and ($a_1 = L_y/8$, $a_2 = L_y/8$, $a_3 = L_x/8$), respectively. In the case of the MLRCS, the size of each layer is 5 mm and the total depth for both structure without the skins is 20 mm. The model is made of solid elements "solid185" using Ansys apdl. The average size of the element is 1 mm leading to 6978 dofs for the MLRCS and 6258 dofs for the standard structure. The number of dofs of the MLRCS is higher since a more accurate mesh is needed in the interfaces between layers to better capture the local dynamic behavior.

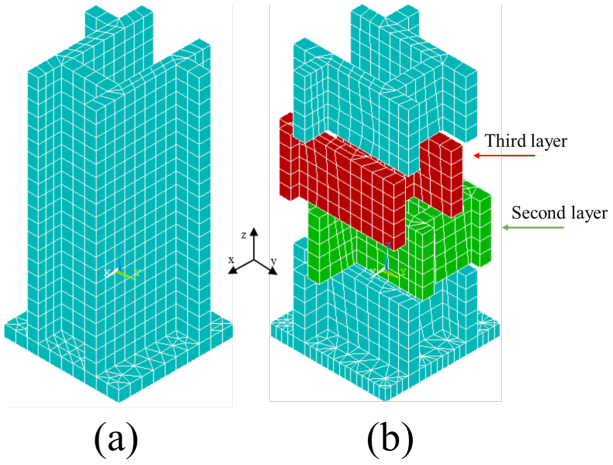

Figure 3.1: (a) standard structure (b) MLRCS.

Dispersion curves are obtained using the WFEM and described in the next subsection. Due to the orthotropy of both structures, both directions x and y are studied. Two different cases are considered for the sandwich panel: aluminium skins and a core made of ABS, and all the structure made of ABS.

3.2.2 Aluminium/ABS VS all ABS

Many sandwich panels designs have been studied in the literature. Most of time, they are made of stiff skins and a soft core. Therefore, two materials with a high gap of properties are commonly used such as the combination of Aluminium skins and a Nomex core. This leads to a global dynamic behavior of the sandwich panel governed mainly by the bending of the skins. Many homogenization theory are based on this assumption and only the expression of the flexural wavenumber is needed to calculate the sandwich

panel properties [4, 66]. This results in flexural wavenumbers much higher compared to other waves propagating in the structure (Fig. 3.2). Therefore, none of them are no longer interacting with the flexural wave.
On the opposite side, sandwich panels made of one material such as the ABS, shows a different dynamic behavior. Indeed, flexural wavenumbers are now at the same order of magnitude compared to shear wavenumbers (Fig. 3.2) while they can be the highest in the direction x (Fig. 3.2a and Fig. 3.2b) at high frequencies. Moreover, veering effects are observed in both directions in the case of MLRCS (Fig. 3.2b and Fig. 3.2d). As explained by Manconi and Mace [172], the veering effect is introduced by coupling waves in the structure. The interfaces between layers involve impedance discontinuities and a drop of mechanical properties leading to coupled flexural and shear waves in the direction x (Fig. 3.2b). Therefore, a part of the strain energy related to the flexural wave is thus converted into shear waves. In the direction y (Fig. 3.2d), two veering effects are displayed corresponding to couplings involving compression, shear and torsion waves.
Finally, as expected, the global trend of the flexural wave reveals a less rigid structure in case of sandwich panels made of all ABS since flexural wavenumbers are higher in all the frequency range of interest. Besides, the vibroacoustic analysis of the transition frequency as performed in the previous Chapter is much more complicated to apply. Indeed, the veering effect introduces a local dynamic behavior which modifies the asymptotic behavior of the flexural wave near the veering frequency region. Consequently, the analysis of the transition frequency should be limited to low frequencies before the veering effect is triggered. The flexural wavenumber expressions developed in the literature for sandwich panels are no longer applicable to describe correctly the dynamic behavior of MLRCS.

3.2.3 Single core VS MLRCS

The following study is performed for sandwich panels made of ABS. The intersection between the acoustic wave and the dispersion curves leads to the determination of coincidence frequencies where the STL is drastically reduced. However, the acoustic wave has to propagate in the same direction of the studied dispersion curves. Due to incidence angles dependency, six acoustic waves with specific incidence angles are used to verify the STL in the oblique coincidence frequency region. For the direction x, the azimuth angle corresponds to $\varphi = 0°$ and the studied incidence angles θ are 8°, 59° and 75° whereas $\varphi = 90°$ in the case of the direction y, with incidence angles θ corresponding to 15°, 40° and 58°. Therefore, directional STL are calculated and the influence on the diffuse acoustic field will be verified. Those angles are selected to bring out different dynamic behaviors involved in MLRCS and occurring at different frequencies.
Two different zones can be defined. The first zone (Zone 1) involves small angles and the coincidence frequency region is expected to be at high frequencies while the second zone

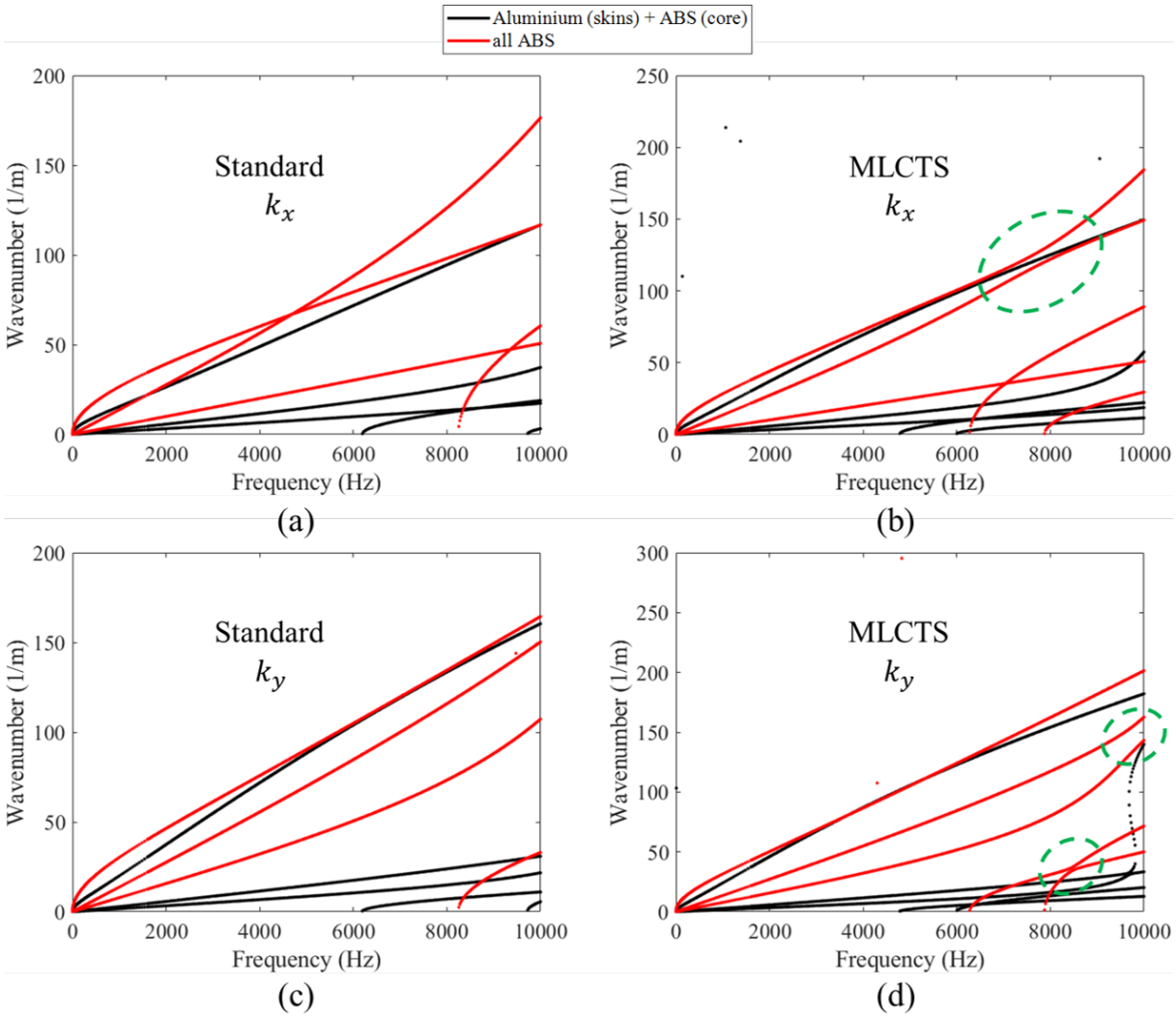

Figure 3.2: Dispersion curves of a standard sandwich panel and the MLRCS made either of Aluminium skins and ABS core or all ABS (a) k_x standard (b) k_x MLRCS (c) k_y Standard (d) k_y MLRCS.

(Zone 2) is related to flexural and shear waves in which coincidence frequencies occurs in a broadband frequency (Fig. 3.3c and Fig. 3.4c). In addition, since the wavenumbers of the MLRCS are higher compared to the standard structure (Fig. 3.3d and Fig. 3.4d), it can be considered as more flexible and can be explained with the involvement of the interfaces between layers which introduce weaknesses and reduce the global dynamic rigidity of the structure especially for out-of plane compression loading. Besides, the standard structure seems having more coincidence frequencies (5) compared to the MLRCS (3) and are listed in the following table for both directions:

For the first zone, in the direction x and y, coincidence frequencies occurs at high frequencies. In this zone, the dynamic behavior of the MLRCS is shifted at lower frequencies compared to the standard structure due the drop of the dynamic rigidity.

Besides, the second zone involves grazing angles (angles near 78°) in which the coincidence

Table 3.1: Coincidence frequency in x and y direction.

	θ (°)	**Standard** (Hz)	**MLRCS** (Hz)
x	8°	8486	[6646, 9306]
	59°	[3650, 7855]	/
	75°	[2535, 9937]	[4575, 9306]
y	15°	/	[8633, 9390]
	40°	/	9033
	58°	/	9453

frequency occurs at low frequencies. However, the MLRCS allows to shift this coincidence at higher frequencies in the direction x, with 4575 Hz for the MLRCS and 2535 Hz for the standard structure (Fig. 3.3a and Fig. 3.3b). This behavior is mainly connected to the increase of the flexural wavenumbers due to a more flexible dynamic behavior related to the interfaces between layers. However, the involvement of the shear wave at high frequencies leads to a coincidence at a lower frequency in the case of the MLRCS when $\theta = 75°$ with 9306 Hz for the MLRCS and 9937 Hz for the standard structure. Finally, a veering effect comes out between 7000 and 8000 Hz (Fig. 3.3d). This leads to an oblique band-gap with no coincidence frequency when the appropriate incidence angle θ is chosen. In the case of the standard structure, the flexural and shear wave cross each other and neither interactions nor couplings are observed (Fig. 3.3a). Therefore, the standard structure is still mainly governed by the bending behavior as expected.

The dispersion curves in the direction y show higher wavenumbers than the direction x which means a more rigid structure along the direction x. Moreover, no coincidence frequencies in the frequency range of interest are noticed with the standard structure. However, four coincidence frequencies occurs for the MLRCS for all selected incidence angles θ. In addition, two veering effects are obtained at high frequencies. However, it is not possible to use it to interact with the acoustic wave as performed in the direction x.

3.3 Resonant dynamic behaviors

This section is devoted to the analysis of the vibroacoustic behavior of the MLRCS in the coincidence frequency region. The calculation of the STL is performed using both methods described in Section 2.3. The obtained result from the method developed by Parrinello et al. [74] using the TMM will be compared with the extended method of Christen et al. [96], to evaluate the coupling occurring in the veering frequency region and to show the local dynamic behavior leading to resonant behaviors involved in the MLRCS.

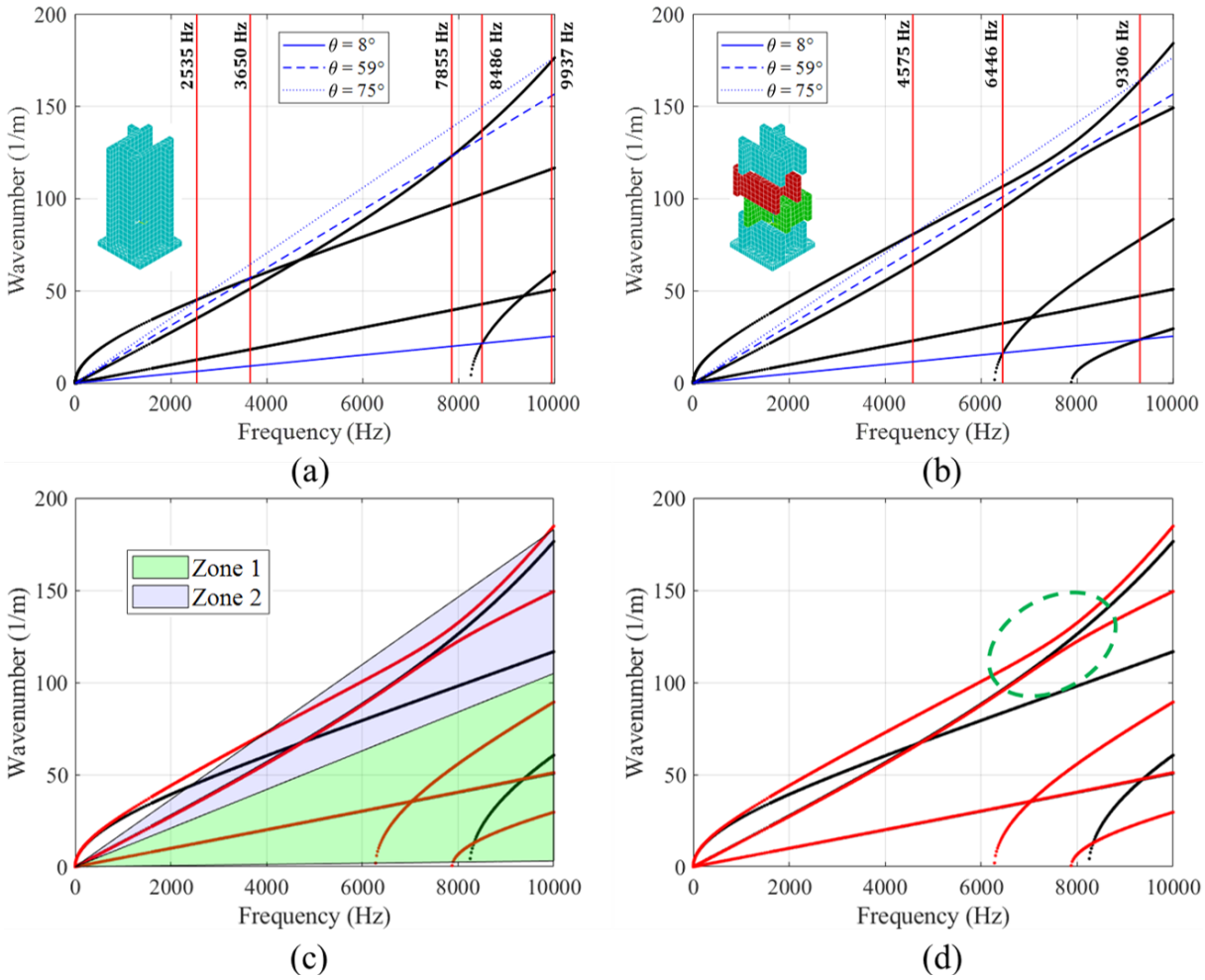

Figure 3.3: Comparison of the dispersion curves in x direction between the standard structure and the MLRCS (a) standard structure with coincidence frequencies (b) MLRCS with coincidence frequencies (c) identification of low and high angles θ (d) comparison between the standard structure and the MLRCS.

3.3.1 Direction y

For the direction y, four coincidences have to be investigated. When θ is equal to 15°, two coincidence frequencies occur at 8633 Hz and 9390 Hz. At those frequencies, the wavemode shapes are depicted in Fig. 3.5. At 8633 Hz, the wave propagation in the MLRCS corresponds to shear waves located in the skins (Fig. 3.5a). The displacement of both layers connected to the skins is much higher than both middle layers. The core displacement is mainly governed by the shear waves resulting from the displacement of the skins. Both skins are decoupled leading to out-of-phase displacement.
Besides, the wavemode shape corresponding to the frequency 9390 Hz is illustrated in Fig. 3.5b. It is governed by flexural waves located in the skins in which the wavelength is at the same order of the unit cell size and both middle layers introduce an out-of-phase displacement between both skins.

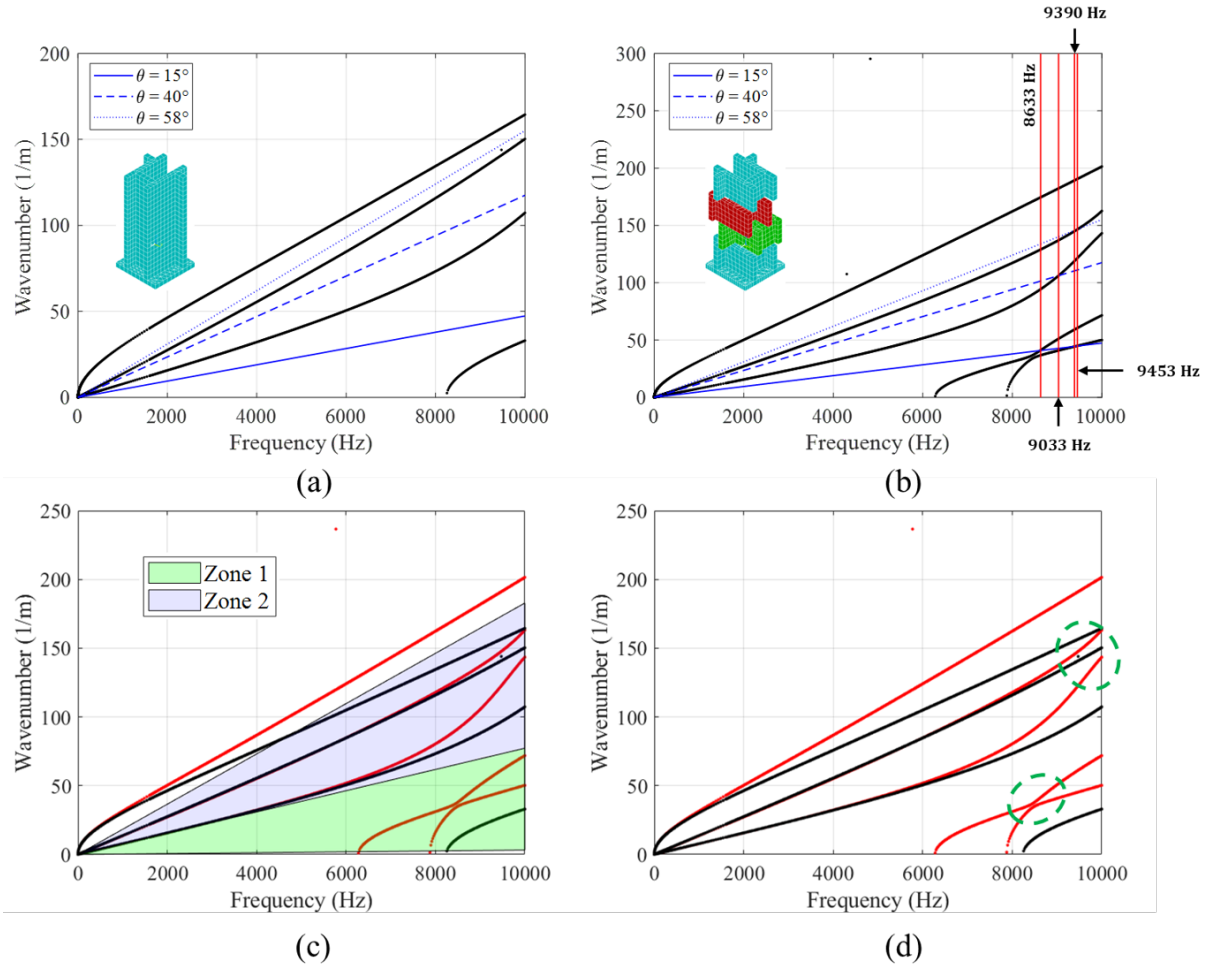

Figure 3.4: Comparison of dispersion curves in y direction between the standard structure and the MLRCS (a) standard structure with coincidence frequencies (b) MLRCS with coincidence frequencies (c) identification of low and high angles θ (d) comparison between the standard structure and the MLRCS.

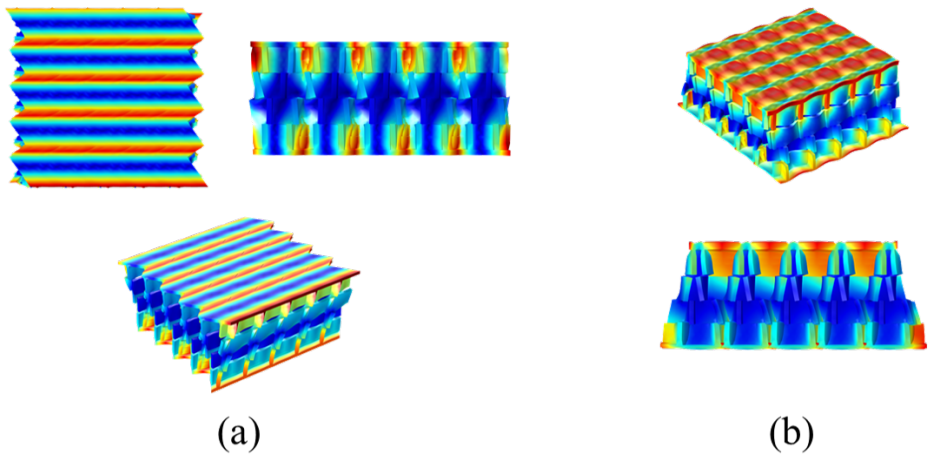

Figure 3.5: Wavemode shape at (a) 8633 Hz and (b) 9360 Hz.

In terms of STL, both coincidence frequencies have an influence on the acoustic efficiency of the MLRCS. The first coincidence related to the wavemode shape at 8633 Hz leads to a low improvement of the STL captured when all the unit cell is modelled [96] (Fig. 3.6b). Besides, the coincidence frequency at 9360 Hz has a stronger impact on the STL with a resonant behavior with an increase of the STL followed by a drop. Globally, the influence of the wavemode shapes are reasonable and occurs at very high frequencies. Compared to the standard sandwich panel, the STL is slightly reduced. When the TMM is applied [74], the coupling dynamic behavior between the core and the skins is not considered and the wavemode shape occurring at 8633 Hz cannot be captured. However, the bending behavior of the skins at 9360 Hz is obtained but shifted at a higher frequency. Indeed, the involvement of the core forces the wavemode shape (Fig. 3.5b) to show up at a lower frequency and can be captured correctly only when all the unit cell is considered.
Concerning the coincidence frequency when $\theta = 40°$, the wavemode shape is mainly related to the core motion (Fig. 3.6d). Consequently, the impact can be captured by both methods but the resonance behavior is still shifted at a higher frequency when the TMM is applied since the skins are decoupled to the core and do not constraint this later. The STL of the standard structure is still better than the MLRCS in a broadband frequency even though a strong improvement is obtained after the STL drop.
Finally, for the angle $\theta = 58°$, the differences between both applied methods is more significant for both configurations (Fig. 3.6e). The coincidence frequency for the MLRCS is still captured and displacements are mainly related to the core motion. The coincidence frequency with the TMM is still shifted at a higher frequency and the STL is now strongly improved for the MLRCS compared to the standard structure.

3.3.2 Direction x

For the direction x and the angle $\theta = 8°$, two coincidence frequencies are obtained for the MLRCS at 6446 Hz and at 9306 Hz but only one coincidence frequency for the standard structure at 8486 Hz. The STL is slightly reduced for the MLRCS (Fig. 3.7). The wavemode shapes for both coincidence frequencies are depicted in Fig. 3.8. The method using the TMM cannot capture the first coincidence while the second is correctly obtained for both methods. The first wavemode (Fig. 3.8a) corresponds to skins shear displacements leading to the torsion of the core while the second wavemode shape (Fig. 3.8b) is the traction of both skins.
Besides, there is no coincidence frequency for the standard structure which does not produce any improvement or reduction of the STL (Fig. 3.7).
The variation of θ around 8° (Fig. 3.9) leads to the shift of the coincidence frequency at higher frequencies with an increase of the amplitude of the resonant behavior due to higher wavenumbers. Similar results are expected for other coincidences when the angle

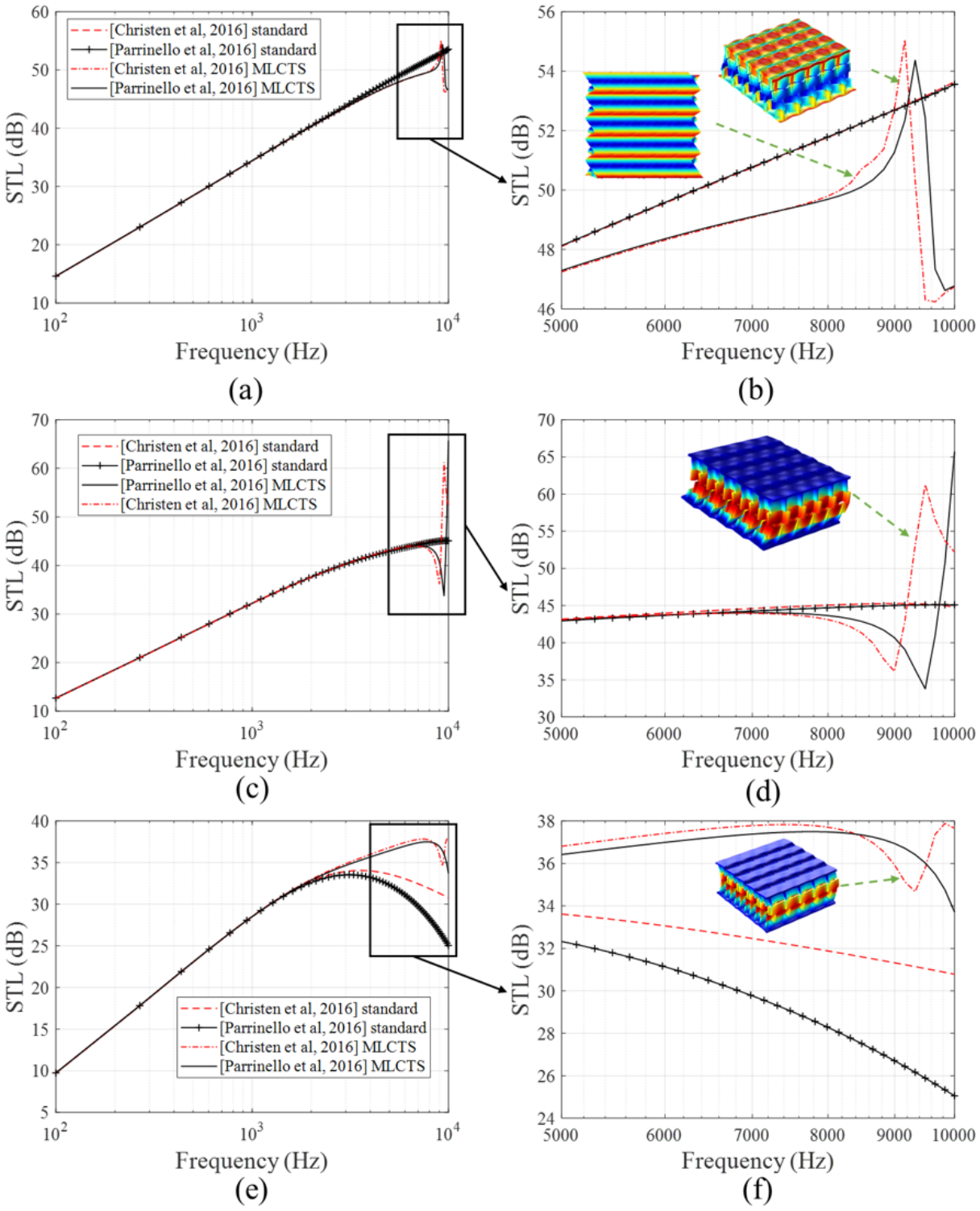

Figure 3.6: STL calculated for $\varphi = 90°$ with (a) $\theta = 15°$ (c) $\theta = 40°$ and (e) $\theta = 58°$.

θ varies.

When the incidence angle θ get closer to grazing angles, the acoustic wave starts to interact with shear waves. In the case of the MLRCS, the veering effect couples the flexural wave with the shear wave (Fig. 3.11b) and a coincidence frequency can be captured at 9306 Hz (Fig. 3.10a). A resonance effect (Fig. 3.10b) is then obtained due to the core motion.

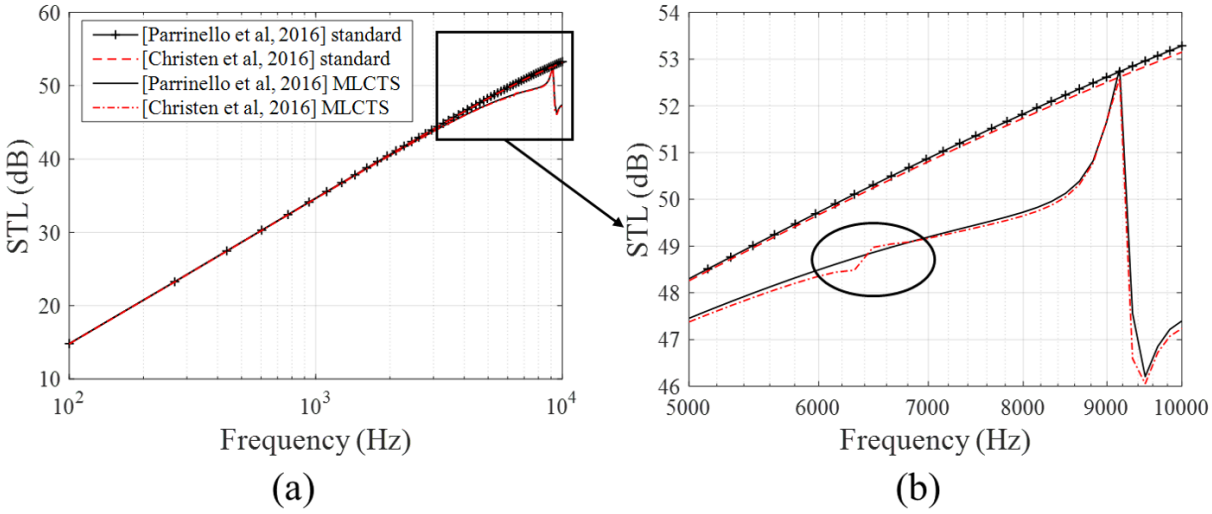

Figure 3.7: STL calculated for $\theta = 8°$ and $\varphi = 0°$.

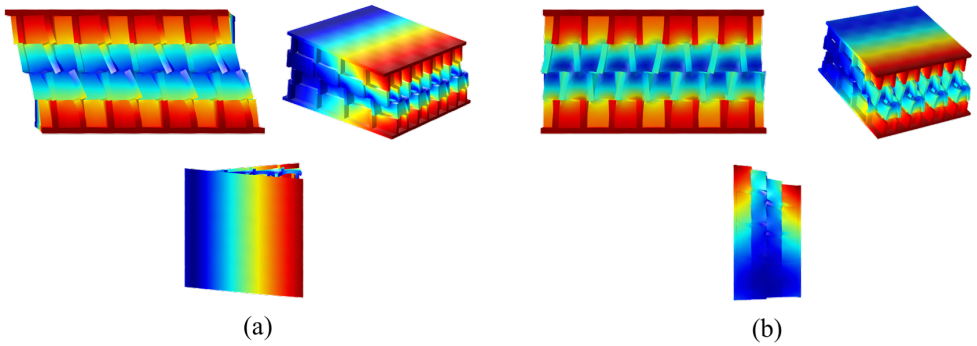

Figure 3.8: Wavemode shapes at (a) 6446 Hz (b) 9306 Hz.

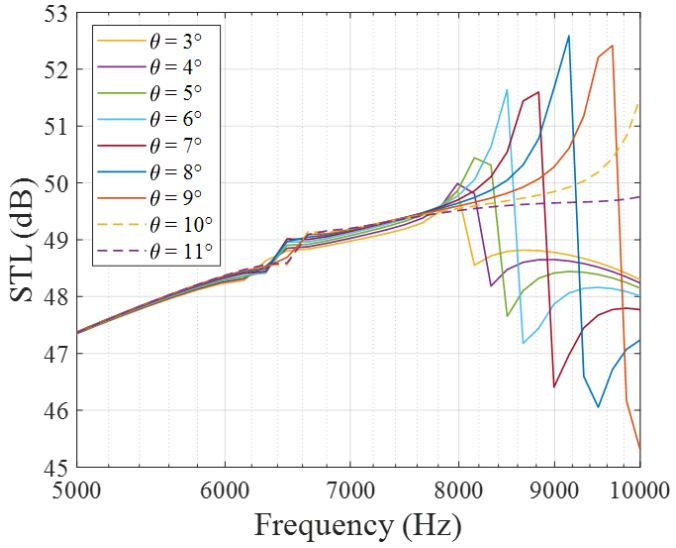

Figure 3.9: Variation of the angle θ around 8° for an acoustic wave propagating in the direction x.

For the standard structure, since no veering occurs, the flexural wavenumber continues being the main dynamic behavior governing the structure in all the frequency range. This coincidence frequency is not obtained with the TMM. Besides, for both structures, the coincidence frequency related to the flexural wave (Fig. 3.11a and Fig. 3.11c) is well-captured and leads to the common dynamic behavior of simple panels with a strong reduction of the STL at 2535 Hz and 4575 Hz. Therefore, the shift of the first coincidence frequency allows to improve the STL in a wider frequency range.

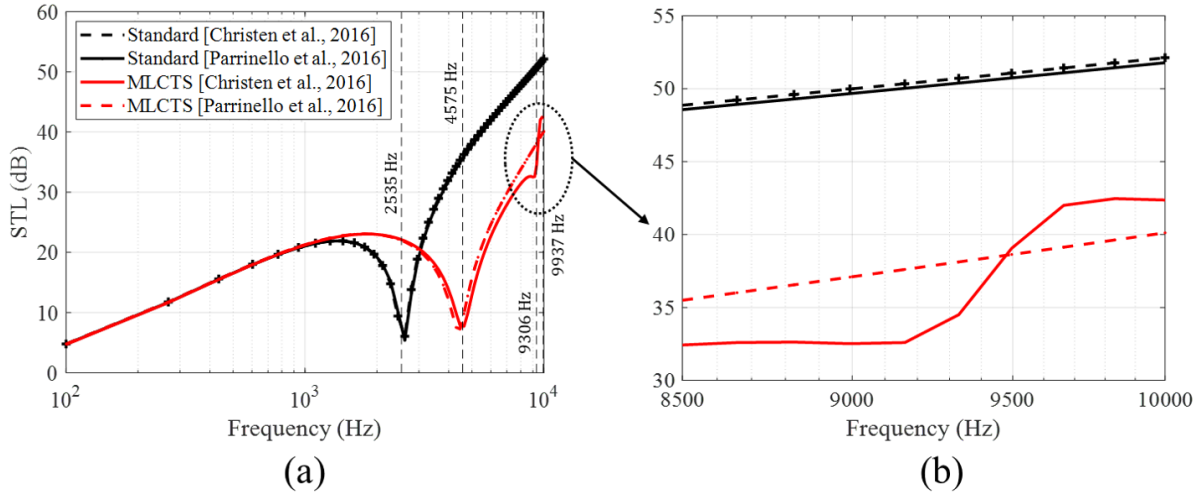

Figure 3.10: STL calculated for $\theta = 75°$ and $\varphi = 0°$.

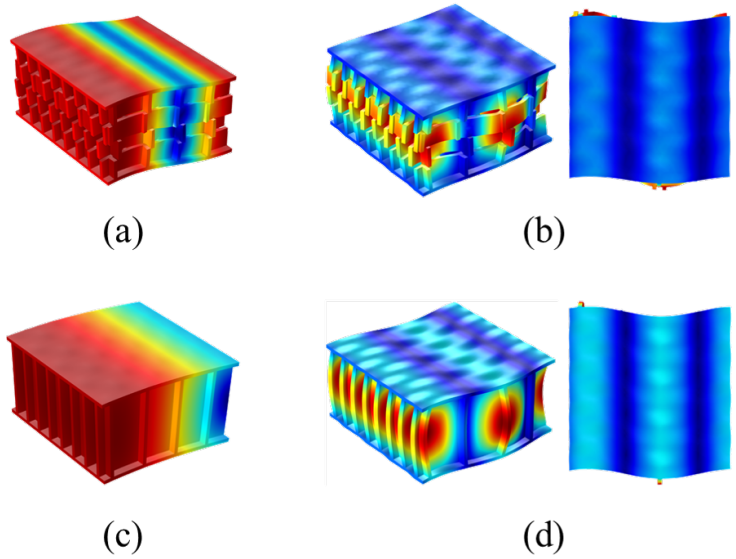

Figure 3.11: Wavemode shapes for MLCTS at (a) 4575 Hz (b) 9306 Hz and for standard structure at (c) 2535 Hz (d) 9937 Hz.

3.3.3 In-phase and out-of-phase behaviors

The vibroacoustic behavior for each case is different depending on the wavemotion of the structure. In the case of $\theta = 15°$ in the direction y and $\theta = 8°$ in the direction x, the STL begins with an anti-resonance followed by a resonance effect (Fig. 3.12a and Fig. 3.12e) while the opposite behavior is obtained for θ equal to 40° and 58° in the direction y (Fig. 3.12b and Fig. 3.12c) and 8° and 75° in the direction x (Fig. 3.12d and Fig. 3.12f). These results are related to the in-phase and out-of-phase motion of both shifted middle layers as shown in Fig. 3.12. The in-phase resonant behavior is defined by cores motions in the same direction while the out-of-phase is related to opposite displacements in the same layer. The core motion in Fig. 3.12b, Fig. 3.12c and Fig. 3.12f corresponds to bending behaviors while the dynamic behavior of the core in Fig. 3.12d consists on shear motion.

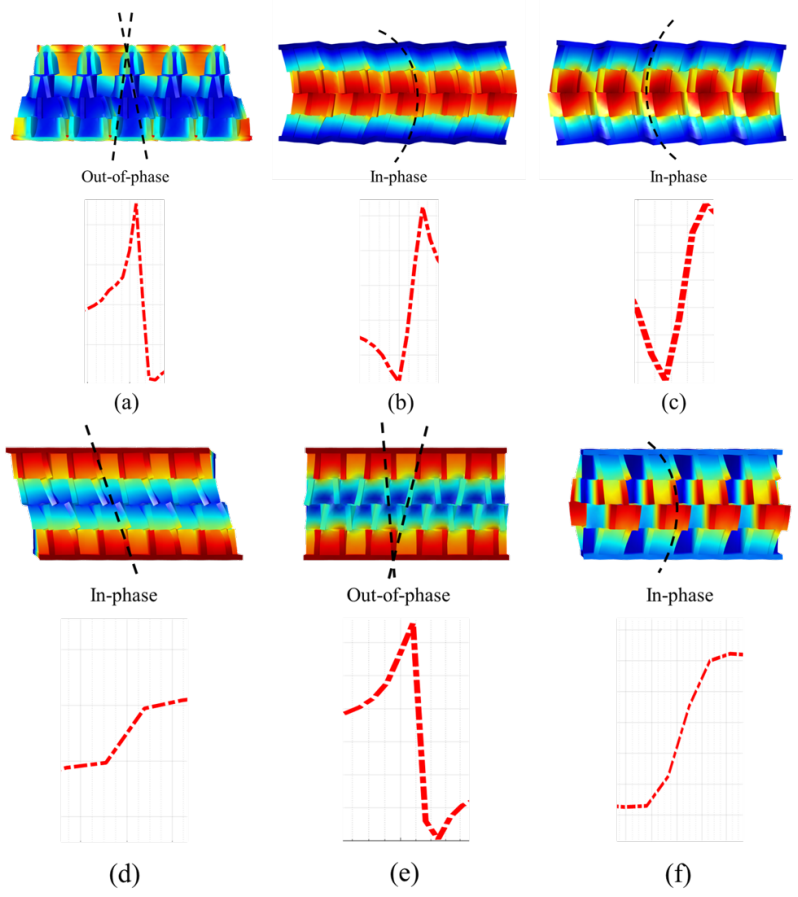

Figure 3.12: Direction y with (a) Out-of-phase resonance $\theta = 9°$ (b) In-phase resonance $\theta = 40°$ (c) In-phase resonance $\theta = 58°$; and direction x with (d) In-phase resonance when $\theta = 8°$ and at 6446 Hz (e) Out-of-phase resonance when $\theta = 8°$ and at 9306 Hz (f) In-phase resonance when $\theta = 75°$ and at 9306 Hz.

3.4 The Veering effect

Besides resonant behaviors studied in the previous section, a strong veering effect occurs in the direction x around 8000 Hz. The next sections are dedicated to the analysis of the veering effect and its influences on the STL.
When the structure is excited by an acoustic wave with an incidence angle $\theta = 59°$, no coincidence frequency is obtained. The effect on the STL is depicted in Fig. 3.13a. A strong improvement is noticed in the same frequency range of the veering without the drawback of a resonance effect including a drop of the STL. When the damping of the material is increased, the STL peak is attenuated as illustrated in Fig. 3.13b. In a broadband frequency, the STL is strongly enhanced compared to the standard structure in which the coincidence frequency related to the bending behavior of the structure reduces drastically the STL efficiency. In addition, the veering effect is not captured when the TMM is applied since the coupling between the core motion and the global bending is not considered. Therefore, the core works as a resonator and turns a part of the global bending strain energy into shear strain energy. The global wavemotion combines two dynamic behaviors: bending and shear displacements. The wavemode shapes given in Fig. 3.14a and Fig. 3.14b shows how both waves interact with each other.

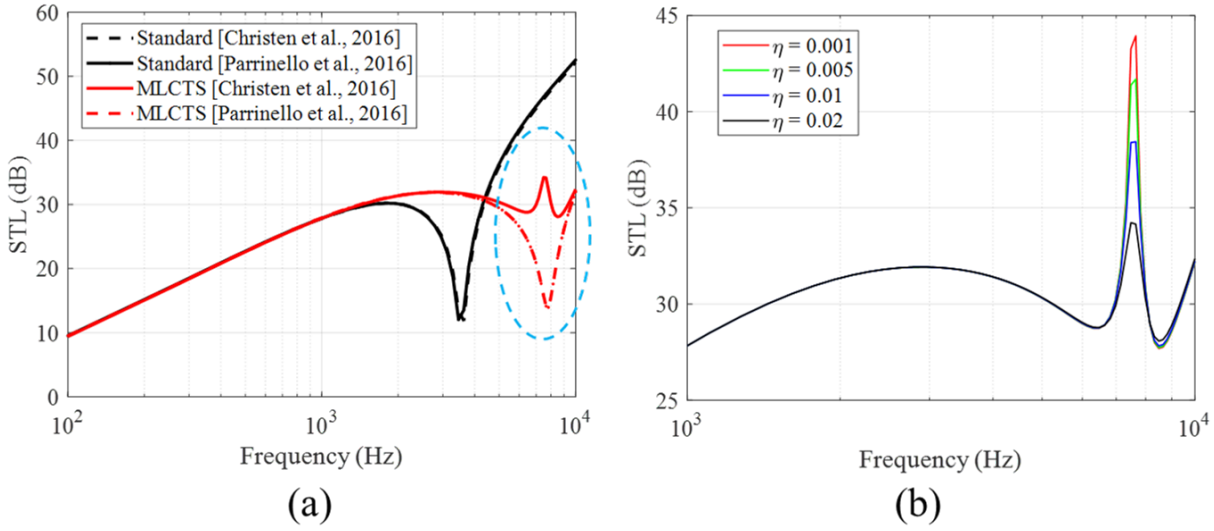

Figure 3.13: STL calculated for (a) $\theta = 59°$ and $\varphi = 0°$ and (b) for different damping values.

The veering effect can be compared to an oblique band-gap (Fig. 3.15) in which coincidence frequencies result in an improvement of the STL (Fig. 3.16). By varying the angle θ inside the veering region, the STL peak is shifted in all the band-gap (Fig. 3.16), with a possibility to cancel the expected coincidence frequency. The drop of the STL is either before or after the STL peak. This drop corresponds to a "virtual" coincidence frequency occurring if wavemodes were not coupled. The STL in the veering region is angle-dependant and

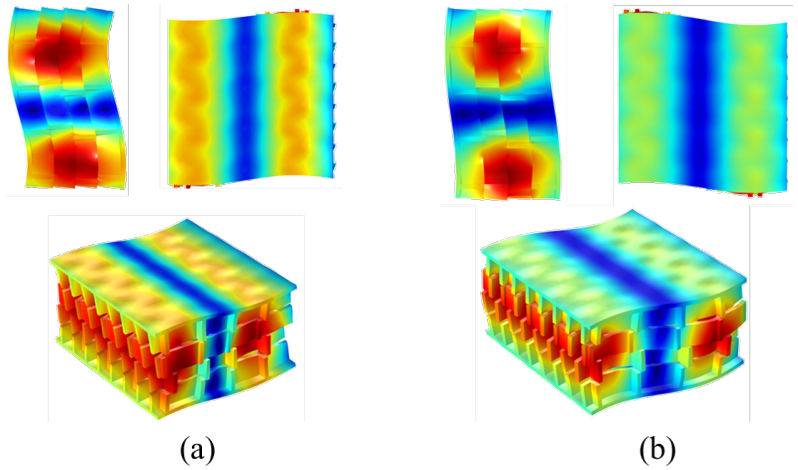

Figure 3.14: Wavemode shape occuring at 7500 Hz.

the size of the band-gap is related to the damping introduced in the structure [172]. The more the MLRCS influences the bending behavior of the skins, the wider is the veering band-gap leading to a stronger impact on the STL with a wider STL peak.

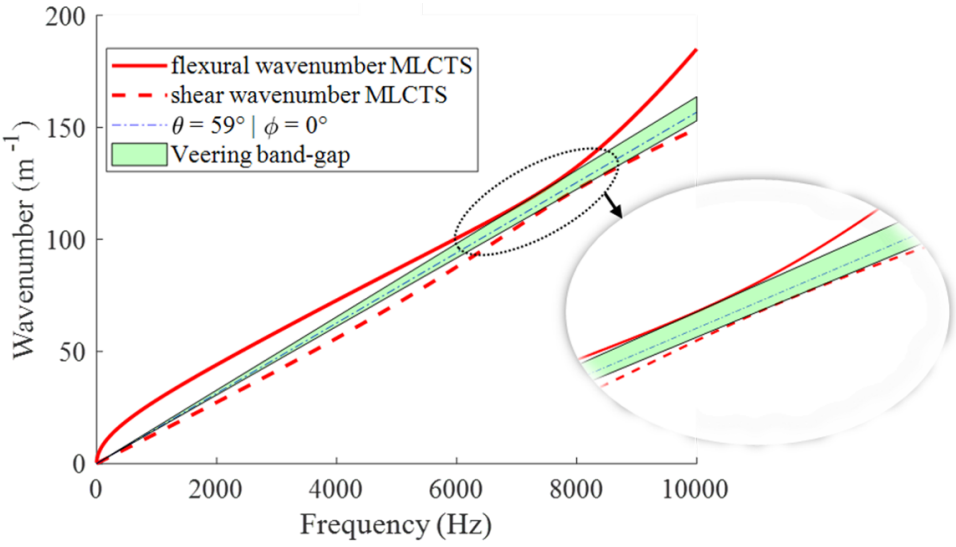

Figure 3.15: Veering band-gap.

Finally, since the impact of the veering on the STL is mainly connected to the incidence angle values, it is necessary to verify the influence of the coupling in a diffuse acoustic field. Indeed, there is a risk that the STL peak due to the veering is covered by the global dynamic behavior of the bending wave. Therefore, the diffuse acoustic field calculation for the MLRCS was performed up to an angle $\theta = 63.5°$ and with an integration step of θ and φ of 0.5° to ensure the convergence, although the computational cost is extremely high taking few days to be completed. The angle $\theta = 63.5°$ corresponds to the limit in which the acoustic wave does not interact with the flexural and shear wave of the MLRCS. Beyond this angle, the veering effect does not influence the STL. The results are expected

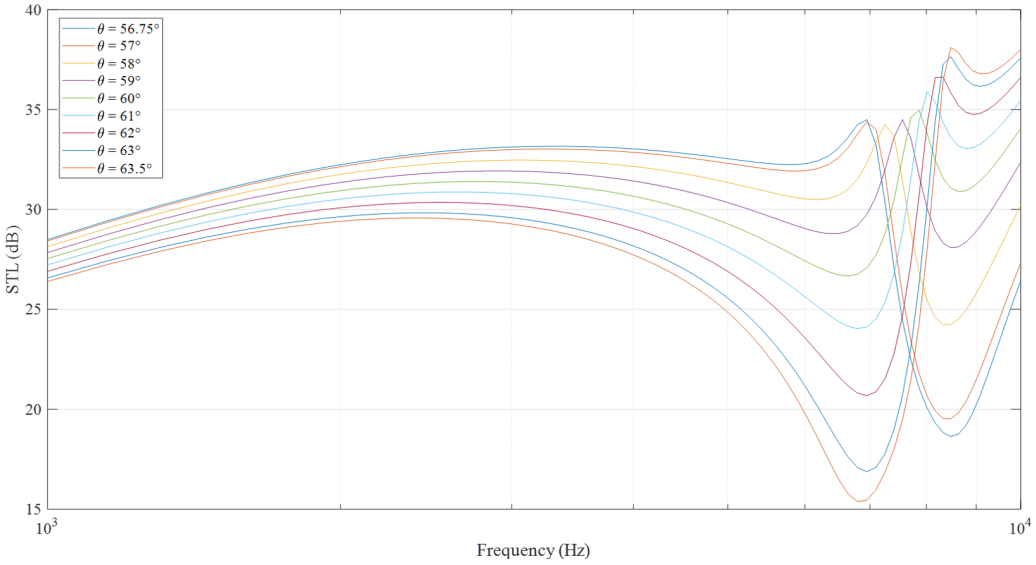

Figure 3.16: Variation of the veering effect on the STL depending on θ.

to be the same if the veering effect would occur for incidence angles around 78°. The STL diffuse acoustic field is depicted in Fig. 3.17.

In the case of the MLRCS, a high improvement of the STL is obtained in the frequency range related to the veering region whereas other resonant behaviors described in the previous sections have no effect on the diffuse acoustic field calculation. The global behavior is mainly governed by the direction x of the MLRCS since the structure is more rigid in that direction. The main advantage of using the veering effect to enhance the STL is that no mass is added and the improvement is not followed by a drop of the STL as it usually occurs when add-ons resonators are used. In addition, a strong improvement in all the frequency range of interest is noticed mainly due to the reduction of the dynamic rigidity introduced by the interfaces between layers leading to higher flexural wavenumbers and shifting the critical frequency at a higher frequency. Consequently, the MLRCS combines a higher STL in broadband frequency with the enhancement of the STL at a targeted frequency using the veering effect compared to the standard structure. The veering effect is specifically efficient in the coincidence frequency region. It is not possible to have a similar effect in the low mass region. However, the main issue related to the transmission problem for panels is the critical frequency region where the STL is highly dropped. The veering effect focuses the improvement on this region.

3.5 Parametric survey

Since the veering effect can strongly improve the STL efficiency of MLRCS, it is interesting to investigate the influence of the core geometry and geometrical parameters to study their influences on the veering in terms of targeted frequency and oblique band-gap size. The

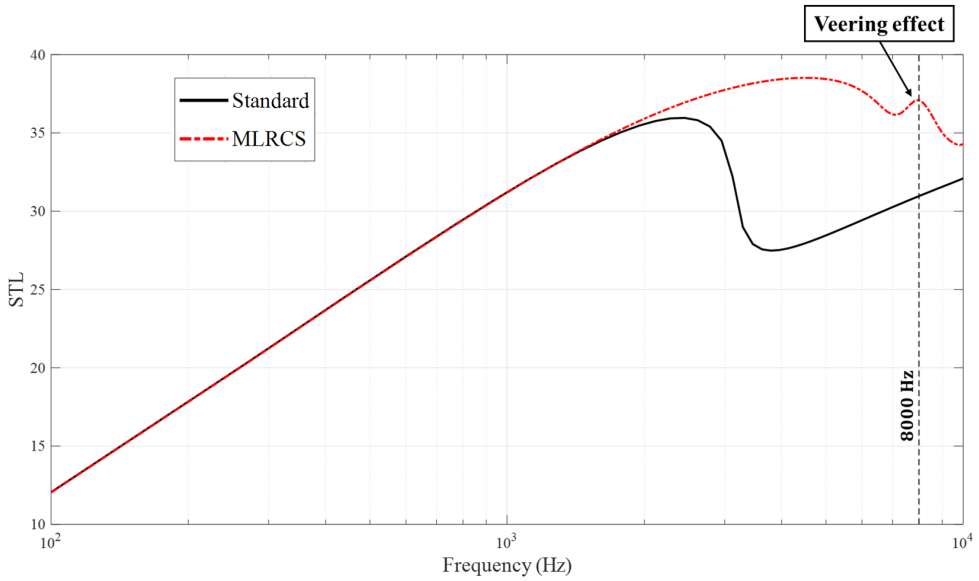

Figure 3.17: Diffuse field calculation.

first study is related to the shifting analysis while the second and last study are mainly focused on the effect of the thickness of the skins and the core, and the unit cell size, respectively. The dynamic behavior of the studied MLRCS is mainly governed by the wave propagation in the direction x, moreover, the veering effect is related to the flexural and shear wave of the structure. Consequently, the study is performed in the direction x and only the flexural and shear wave are investigated. The surface density of all compared configurations is still maintained constant.

3.5.1 Influence of the shift between layers

In this part, the shift between layers is modified to show how it influences the veering effect. It allows to open perspectives for further studies to analyse with more details the core geometry influence.

The veering effect is defined by two characteristics: the frequency in which the veering occurs and the size of the oblique band-gap. The first parameter is related to the rigidity of the structure while the second is governed by the structural damping. In the following study, $a_1 = a_2 = a_3 = \zeta_i$ with $i = 2$ or 3 corresponding to the second ($i = 2$) and third ($i = 3$) layer.

Table 3.2: Values of ζ for the 2^{nd} and 3^{rd} layer depending on the configuration.

Configuration	**1**	**2**	**3**	**4**	**5**	**6**	**7**	**MLRCS**	**8**	**9**
ζ_2 (mm)	4.4	4.3	4.2	4.1	4	3.9	3.8	**3.75**	3.7	3.6
ζ_3 (mm)	0.6	0.7	0.8	0.9	1	1.1	1.2	**1.25**	1.3	1.4
ζ_3/ζ_2	0.14	0.16	0.19	0.22	0.25	0.28	0.32	**0.33**	0.35	0.39

Those values have been selected to avoid overlapping areas between layers and to allow a strong impedance discontinuity due to the interfaces. Three cases are illustrated in the following figure showing a non-valid (Fig. 3.18b and Fig. 3.18c) and a valid shift (Fig. 3.18a). Indeed, when two core sides are overlapping, the rigidity turns out to be drastically increased and the dynamic behavior is modified out of our interest in this study. In addition, a small overlapping forces the unit cell to be meshed more accurately in the overlapping region to guarantee the convergence of the calculations and to correctly capture the dynamic behavior.

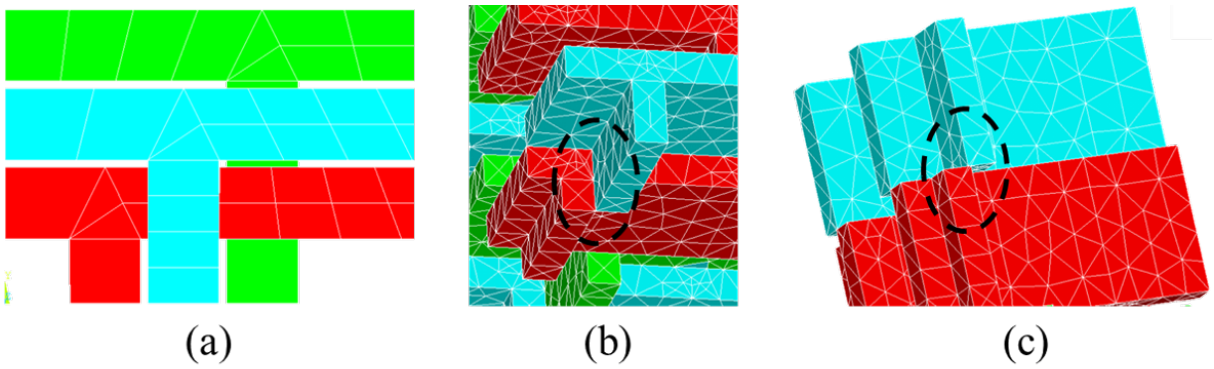

Figure 3.18: (a) Valid shifting (b) non valid shifting (c) non valid shifting.

The influence of the parameter ζ is depicted in Fig. 3.19 and shows that the global dynamic rigidity is not altered at low frequencies. However, after 4000 Hz and near the veering region, the size of the oblique band-gap is modified. The more the ratio increases, the wider the veering bang-gap is. In addition, the frequency in which the veering occurs is the same for all configurations which means that the structural damping is modified. Indeed, the shifting process allows to increase the coupling effect between flexural and shear waves. In the case of a wide veering band-gap, contact surfaces between layers are moved away from each other leading to higher inertial moment at the interfaces and thus a stronger interaction with the skins' bending. This leads to higher shear wavenumbers as well. The more the structural damping is low, the more the band-gap is open [171]. Therefore, the structural damping introduced by the shifting can be reduced leading to wider veering vand-gap. This later result is not related to the ABS damping but mainly to the damping introduced by the local dynamic involved in the MLRCS and allowing to modify the damping of the structure in a specific frequency range in which the acoustic efficiency will be improved.
With any configurations of MLRCS, the veering effect is introduced since the interfaces lead to waves coupling. However, the veering band-gap can be narrow or wider depending on the core geometry.

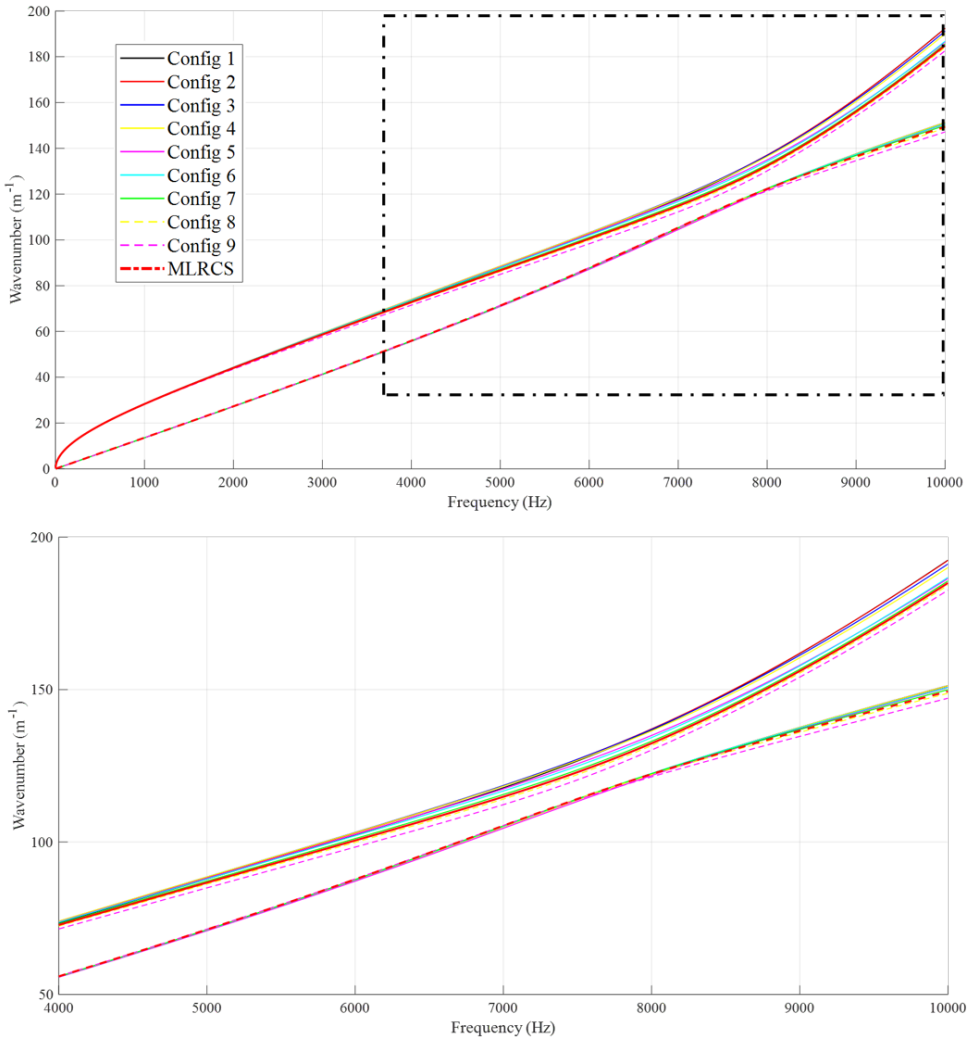

Figure 3.19: Influence of the ratio ζ_3/ζ_2 on the veering.

3.5.2 Influence of the skins thickness to core thickness ratio

The second application is related to the modification of the skins to core thickness ratio. The surface density of all configurations has been kept constant and the thickness of the skins and the core are listed in the following table for each configuration:

Table 3.3: Values of t_c and t_s depending on the configuration.

Config	**1**	**2**	**3**	**4**	**5**	**6**	**7**	**MLRCS**	**8**	**9**	**10**
t_c (mm)	0.3	0.4	0.5	0.6	0.7	0.8	0.9	**1**	1.1	1.2	1.3
t_s (mm)	2.9	2.6	2.4	2.1	1.8	1.5	1.3	**1**	0.74	0.48	0.22
t_c/t_s	0.10	0.15	0.21	0.29	0.39	0.52	0.71	**1**	1.49	2.50	5.79

Results are depicted in Fig. 3.20 and divided for the sake of clarity in Fig. 3.21. In all configurations, a veering effect occurs. Moreover, the veering frequency region as well as the size of the band-gap are different. Changing the ratio mainly influences both the

flexural and shear wave. The dynamic bending behavior is mainly governed by the skins however this later is influenced by the dynamic rigidity of the core and both interact. Therefore, when the ratio is low, the skins will be deformed more easily and the flexibility of the structure increases leading to higher wavenumbers. The dynamic behavior is thus shifted at lower frequencies and the veering effect as well. On the opposite, a higher ratio leads to more rigid structures. In addition, the core have a stronger impact on the skins' bending and the coupling between the flexural and shear wave is stronger leading to a wider veering band-gap.

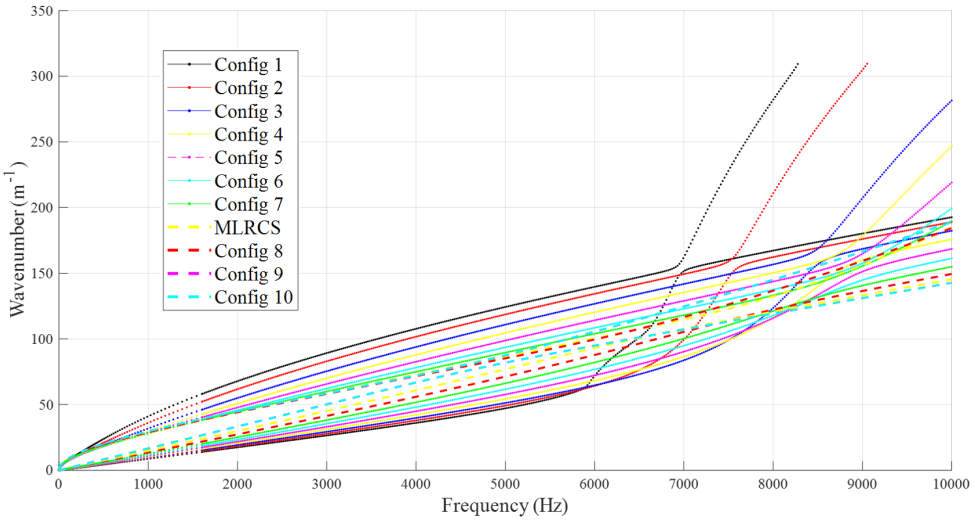

Figure 3.20: Influence of the ratio t_c/t_s on the veering (I).

3.5.3 Influence of the unit cell size

The last application is related to the modification of the unit cell size and results are shown in Fig. 3.22. The surface density of all configurations is still kept constant and the thickness of the skins and the core is maintained at 1 mm. The following table lists the values of L_x and L_y for each configuration:

Table 3.4: Values of L_x and L_y depending on the configuration.

Config	**1**	**2**	**3**	**4**	**5**	**MLRCS**	**6**	**7**	**8**	**9**	**10**
L_y (mm)	9	9.2	9.4	9.6	9.8	**10**	10.2	10.4	10.6	10.8	11
L_x (mm)	13.5	12.5	11.7	11	10.5	**10**	9.6	9.2	8.9	8.6	8.3
L_y/L_x	0.67	0.74	0.80	0.87	0.93	**1**	1.06	1.13	1.19	1.26	1.32

On the whole, the dynamic rigidity of the structure is maintained in all the frequency range of interest. The modification is mainly related to the asymptotic behavior of the shear wave. The main differences are noticed for the veering frequency region which is

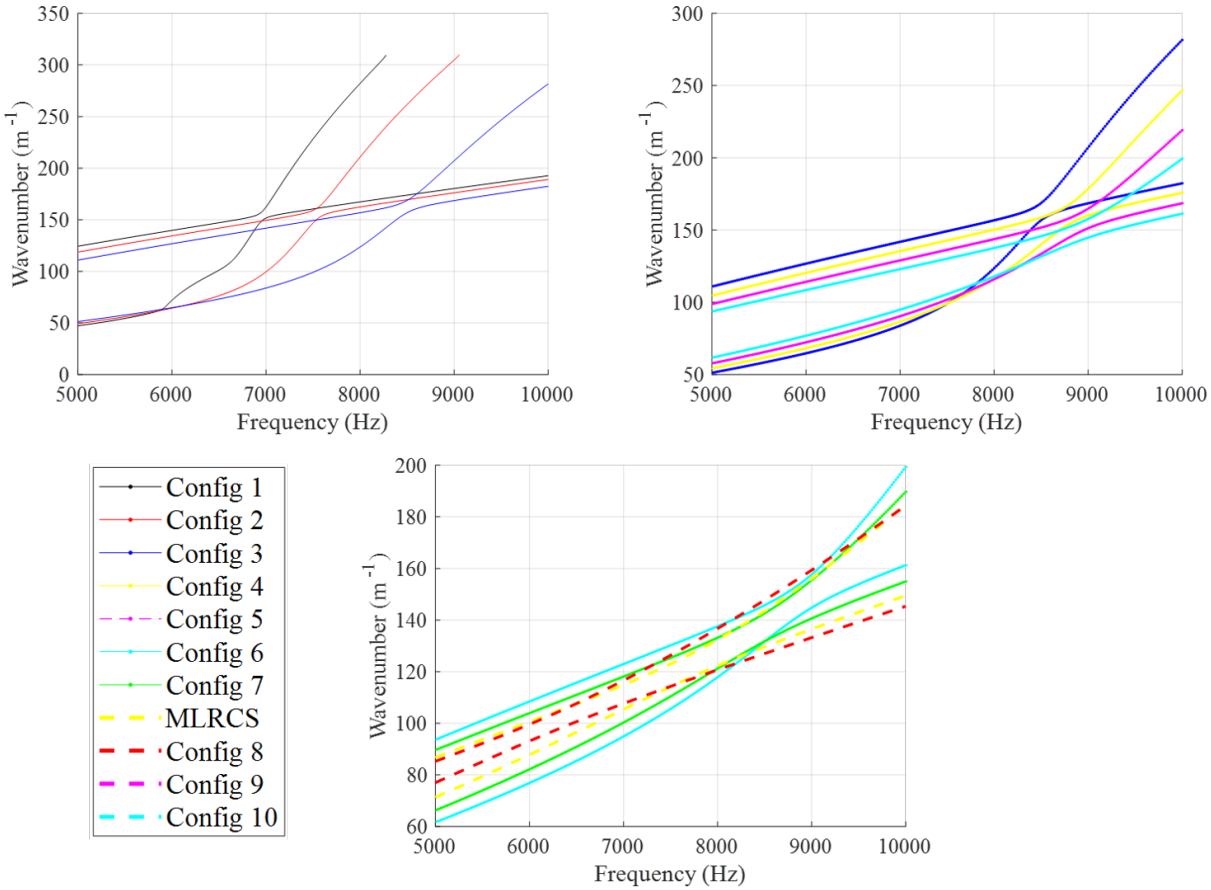

Figure 3.21: Influence of the ratio t_c/t_s on the veering (II).

shifted at higher frequencies when the ratio L_y/L_x is high since the size of L_x is reduced, leading to high frequency local dynamic behavior in this direction. In addition, the band-gap size is wider when the ratio increases. Indeed, the core has a stronger influence on the bending behavior of the skins due to a higher core rigidity in the direction x since L_x is reduced.

3.6 Conclusions

In this chapter, a MLRCS has been studied and compared with a standard sandwich panel made of a single core. Several geometrical parameters were then modified maintaining the mass constant to investigate their influence on the local dynamic behavior of the structure and their impact on the STL.

The global dynamic behavior of the MLRCS shows a lower dynamic rigidity leading to the increase of the wavenumbers and thus, a shift of the critical frequency at a higher frequency. Therefore, the STL is improved at low frequencies compared to the standard structure since the mass low is extended. In addition, the interfaces between layers introduce local dynamic behavior leading to resonance effects for certain coincidence frequen-

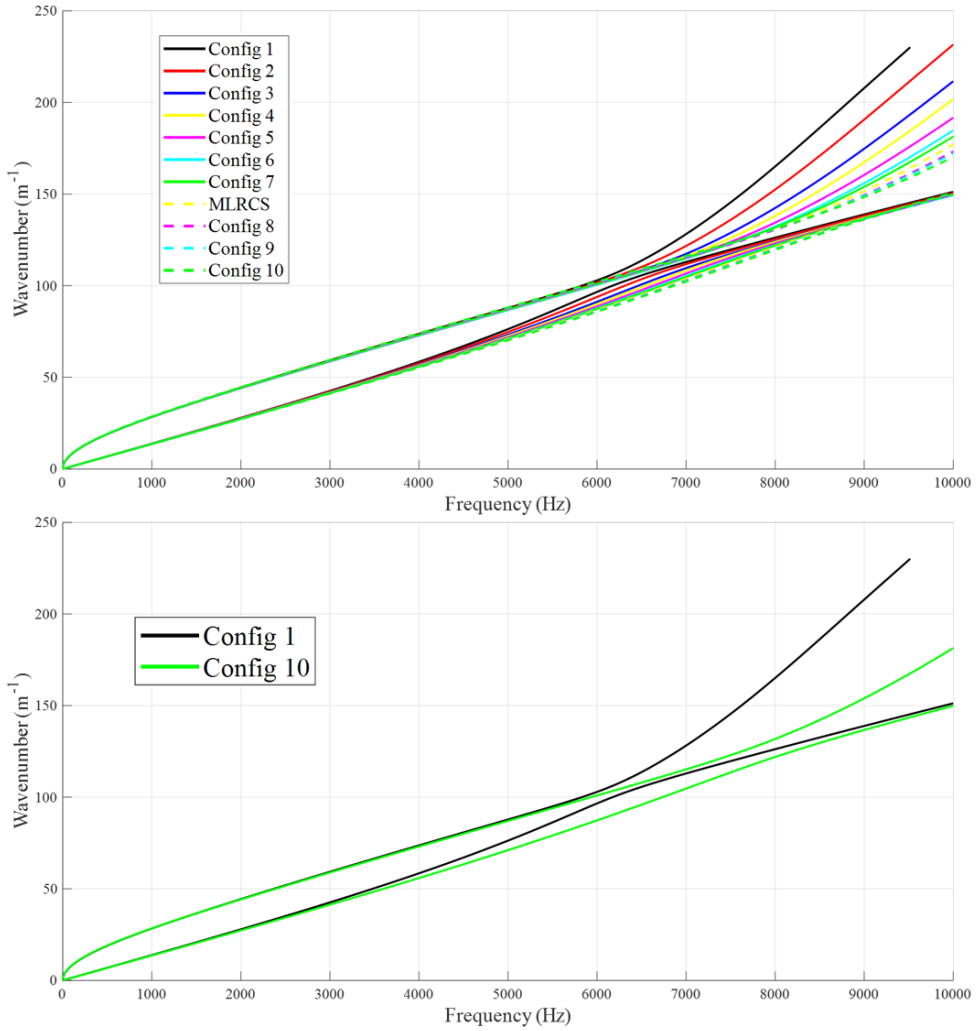

Figure 3.22: Influence of the ratio L_y/L_x on the veering.

cies especially in the direction y. The extended method of Christen et al. [96] proposed in this thesis allows to capture the local dynamic behaviors of the MLRCS contrary to the TMM even though the computational cost is much lower. By comparing the STL between both methods, it has been possible to show if the dynamic behavior involves a coupling between the skins and the core or not. The in-phase and out-of-phase resonant behavior at the coincidence frequency can be predicted with the study of the wavemode shape and more specifically the core motion.

Besides, it has been shown that MLRCS can produce a veering effect at a specific frequency. This veering is due to the interface between layers which lead to the flexural and shear wave coupling. Therefore, the strain energy of the flexural wave is transmitted to the core. This later behaves as an internal resonator and leads to an improvement of the STL in a narrow frequency region defined by the veering frequency. Such an improvement is obtained when the acoustic wavenumber crosses the veering band-gap. Only some specific incidence angles are involved but a wider veering band-gap increases the angles

range. The virtual coincidence frequency (when there is no coupling) is then eliminated and a strong STL peak is obtained. The main advantages is that no mass is added since the veering comes from the structural dynamic behavior itself and it leads to an STL peak which is not followed by a drop as it usually occurs when using add-ons resonators. The effect of the veering on the diffuse acoustic field is verified and shows a strong improvement in the critical frequency region while the resonant behaviors observed in the direction y have been covered.
Shifting the core geometry of the second and third layer leads to a wider veering frequency region without altering the dynamic rigidity of the structure at low frequencies. The ratio t_c/t_s shows a strong modification of the dynamic rigidity in all the frequency range of interest with a shift at higher frequencies of the veering when the ratio is high. The influence is also noticed on the veering band-gap size which becomes wider. Lastly, the ratio L_y/L_x keeps the dynamic rigidity constant while the asymptotic behavior of the shear wave is modified leading to a shift at higher frequencies of the veering and a wider band-gap as well.
Finally, it is possible to modify the core geometry combining different shapes (auxetic, hexagonal, rectangular, ...) to study how the veering effect evolves. In addition, it could be possible to evaluate the structural damping occurring in the veering frequency region to show how it is modified when the veering band-gap becomes wider.

The next Chapter concerns an optimisation and a parametric analysis of the geometrical parameters of MLCTS involved in the proposed parametric model on the STL and static mechanical properties.

Chapter 4

Optimisation and Parametric analysis of the core geometry

This Chapter is based on a conference paper presented in the 9th Eccomas Thematic Conference on Smart Structures and Materials (SMART 2019) [173]. The authors are Nassardin Guenfoud (ECL and KUL), Christophe Droz (ECL), Mohamed Ichchou (ECL), Olivier Bareille (ECL), Elke Deckers (KUL) and Wim Desmet (KUL).

Abstract

In this Chapter, the study is focused on MLCTS consisting on stacking 3 layers of honeycomb cores. The main objective is to analyse the influence of geometrical parameters comparing designs having the same surface density. The targeted indicator is the STL while the compression and shear modulus are also investigated. The structure is considered as an infinite panel impinging by acoustic plane waves. The model is implemented using MATLAB and ANSYS apdl. The ABS is used as the material for the study. Two parametric analysis are performed with the following configuration: Rectangular-Random-Rectangular core (ROR) and Rectangular-Random-Optimized core (ROO). The optimized core is obtained from the first parametric analysis. A high improvement of the STL is obtained in a broadband frequency for both parametric surveys. However, it goes along with a drop of mechanical properties.

Contents

4.1 Introduction

Many unit cell designs have been proposed in the literature to improve sandwich panels vibroacoustic properties. Zergoune et al. [66] studied the geometrical parameters of honeycomb cores by performing a parametric survey while Droz et al. [113] have considered different designs of unit cells investigating the transition frequency, the modal density and the group velocity. Besides, Griese et al. [114] as well as Galgalikar [115] have changed gradually the core from a honeycomb to an auxetic unit cell to improve the acoustic radiation and the STL, respectively. However, sandwich panels made of a single core leads to limited design space study.

Besides, MLCTS involve more geometrical parameters and configurations. They introduce local dynamic behaviors and lead to a great enhancement of the STL in a broadband frequency by shifting the critical frequency at a higher frequency. The recent developments in terms of modelling and model order reduction allows to model complex unit cells with lower computational cost. Therefore, it is possible to use optimisation processes to compute large number of designs to obtain an optimal unit cell with better acoustical and mechanical properties.

This Chapter intends to perform two parametric surveys with the involvement of new geometrical parameters introduced by MLCTS and to compare a huge amount of designs having the same surface density. The targeted indicator is the STL to find out the optimized structure. Besides, the compression and shear modulus are calculated to be investigated. Both parametric surveys are characterized by a study of the geometrical parameters of a MLCTS stacking 3 layers of honeycomb cores. Firstly, in Section 4.2, a description of the analysis is given defining the study constraints and to explain the algorithm used to obtain the design space. Section 4.3 is focused on the following configuration: Rectangular-Random-Rectangular core (ROR) while Section 4.4 uses the optimized unit cell given by the first study to perform a parametric survey on the new following configuration: Rectangular-Random-Optimized core (ROO). Finally, both obtained optimal unit cells designs are compared in terms of acoustic efficiency and mechanical properties in Section 4.5. Conclusions are given in Section 4.6.

4.2 Description of the conducted analysis

In this section, a description of the analysis is given by defining the study's parameters. Moreover, the algorithm allowing to explore the design space is described.

4.2.1 Definition of the study parameters

Both parametric surveys are performed using the parametric model described in Section 2.2.2. To reduce the problem size, the geometrical parameters a_1 and a_2 are considered equal and $n = 1/2$. Therefore, only α, β, a_1 and a_3 are modified. The size of the unit cell is given by $L_x = 5$ mm and $L_y = 10$ mm. The thickness of the core and the skins is 0.6 mm and all the structure is made of ABS. The size of each layer is 5 mm. The unit cell is modelled using Ansys apdl with shell elements and the STL is calculated with the model described in Section 2.3.3 while a second model is made using Solid elements to evaluate the compression (E_{zz}) and shear modulus of the structure (S_{xy}) in both directions (S_{xx} and S_{yy}). The choice of using shell elements for the STL is made to reduce the number of dofs leading to a lower computational cost. Although the use of solid elements could lead to more accurate results, it is expected to keep the same dynamic behavior using shell elements and to obtain the same conclusions. The standard structure consists on a sandwich panel made of a single rectangular core with the surface density $\rho_s = 1.1$ kg/m^2.

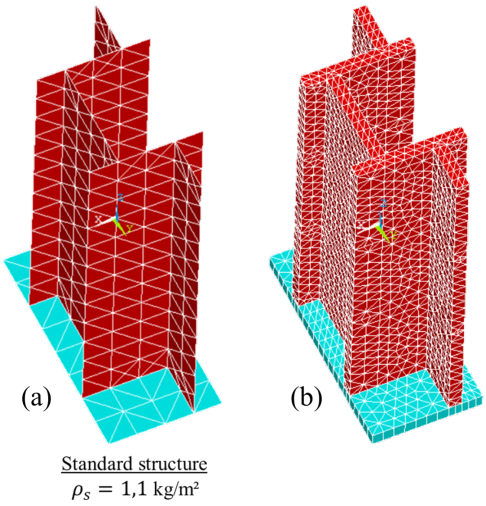

Figure 4.1: Mesh of the standard unit cell with (a) shell elements (b) solid elements.

The targeted indicator is the STL calculated for an incidence angle $\theta = 78°$ and integrated over φ. The calculation is expressed in Eq. (1.14). This later will be then integrated over the frequency (STL_{int}) to evaluate the acoustic efficiency of the structure in a broadband frequency as performed by Galgalikar [115] and allowing to simplify the analysis. The higher is the value, the more the structure is acoustically efficient. The frequency range of the study is [100, 10000] Hz. In addition, the compression and shear modulus are obtained using Ansys apdl by simulating a static test on the unit cell.

4.2.2 Range of parameters

In the first stage, the range of each geometrical parameter needs to be defined. Therefore, the point A and B of the parametric model depicted in Fig. 4.2 are limited to the red and green zone, respectively. Indeed, the thickness of the core constrains the model to be valid when solid elements are used. If the points A and B are located in the grey zone, the unit cell solid model is no more valid since the core sides will be out of the unit cell region. The range of the parameters a_1 and a_3 are then defined by:

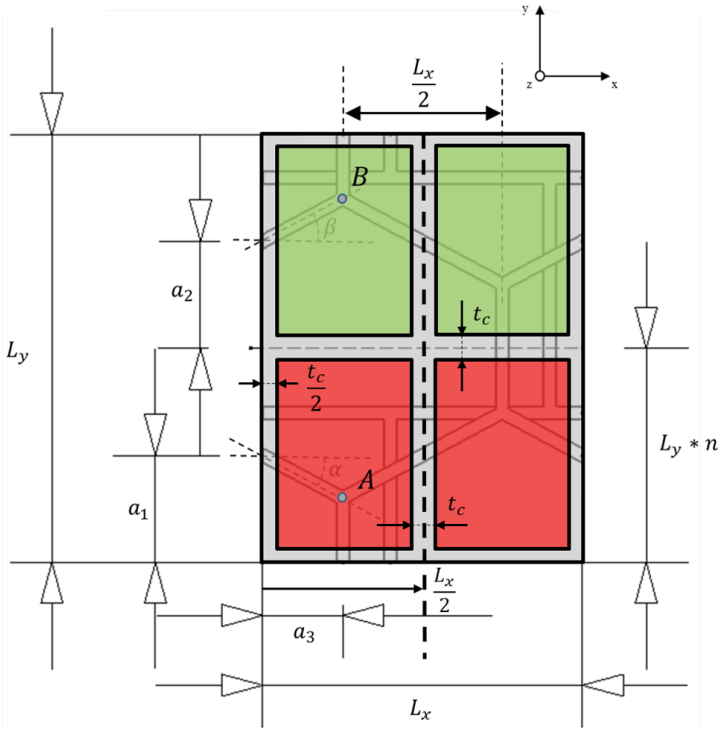

Figure 4.2: Parametric model and constraint of the multi-layer core unit cell.

$$\frac{t_c}{2} < a_1 < nL_y - \frac{t_c}{2} \qquad \begin{matrix} \frac{t_c}{2} < a_3 < \frac{L_x}{2} - \frac{t_c}{2} \\ \frac{L_x}{2} + \frac{t_c}{2} < a_3 < L_x - \frac{t_c}{2} \end{matrix} \tag{4.1}$$

For each value of a_1, it is possible to define the range of the angles α and β. The value of a_3 is fixed at $L_x/4$ in the algorithm and modified in a second phase after obtaining the design space. Therefore, the angles range of α and β are given by:

$$\begin{cases} \text{if } a_1 < \frac{nL_y}{2} \text{ then } -\left|\arctan(\frac{t_c - a_1}{a_3})\right| < \alpha, \beta < \left|\arctan(\frac{t_c - a_1}{a_3})\right| \\ \text{if } a_1 \geq \frac{nL_y}{2} \text{ then } -\left|\arctan(\frac{nL_y - t_c - a_1}{a_3})\right| < \alpha, \beta < \left|\arctan(\frac{nL_y - t_c - a_1}{a_3})\right| \end{cases} \tag{4.2}$$

Finally, 5 values of a_1 and 14 values of a_3 have been taken in this study defined as follows:

$$\begin{cases} a_1 = 0.83,\ 1.67,\ 2.5,\ 3.33,\ 4.17 \text{ mm} \\ \\ a_3 = \frac{iL_x}{16},\ i \in \mathbb{N} \text{ with } 0 < i < 16 \text{ and } i \neq \{0,\ 8,\ 16\} \end{cases} \tag{4.3}$$

Then, 13 values of α and β are taken in each interval defined by the value of a_1. These values have been chosen to have a reasonable number of configurations to compute.

4.2.3 Algorithm description

In order to obtain the studied design space, it has been necessary to develop an algorithm (Fig. 4.3) allowing to determine the geometrical parameters leading to the comparison of different designs with the same surface density. The primary data are the material density (ρ), the thickness of the core (t_c), the core's height (H_l) and the unit cell size (L_x and L_y). In addition, the number of values in the range of all geometrical parameters has to be defined. Then, each value of a_1 leads to the angles range α and β as explained previously. This algorithm description has been simplified to be applied to the study case. However, it is also possible to consider $a_1 \neq a_2$ and to obtain a more complete design space but leading to a drastic increase of the number of configurations and thus, a high computational cost to perform the parametric analysis.

Finally, the surface density is calculated for each configuration using Eq. (2.1) and leads to the distribution illustrated in Fig. 4.4 which is similar to a Gaussian distribution. For each interval of the surface density, a certain number of configurations can be compared. Since the surface density of the standard structure is $\rho_s = 1.1$ kg/m^2, there are 276 configurations that could be used when $a_3 = L_x/4$. However, 14 values of a_3 are used and the total number of configurations for the parametric analysis reaches 3864. The range of the surface density could be modified to change the distribution and thus, the number of configurations. However, a wider range leads to more important mass differences between the compared unit cells and a higher number of configurations, while a lower range reduces the number of configurations leading to a lower design space to study.

The distribution of each geometrical parameter is illustrated in Fig. 4.5. They have been obtained from the surface density distribution when ρ_s belongs to the range [1.1, 1.15] kg/m^2. A Gaussian distribution can be observed for α and β while a_1 has no particular distribution. The parameters α and β have anti-symmetric distribution due to the compensation of both sides of the parametric model to maintain a constant surface density.

Fig. 4.6 shows the pairs (α, β) plotted for each of the 276 configurations. It turns out a dependency between both parameters and the possibility to reduce the size of the

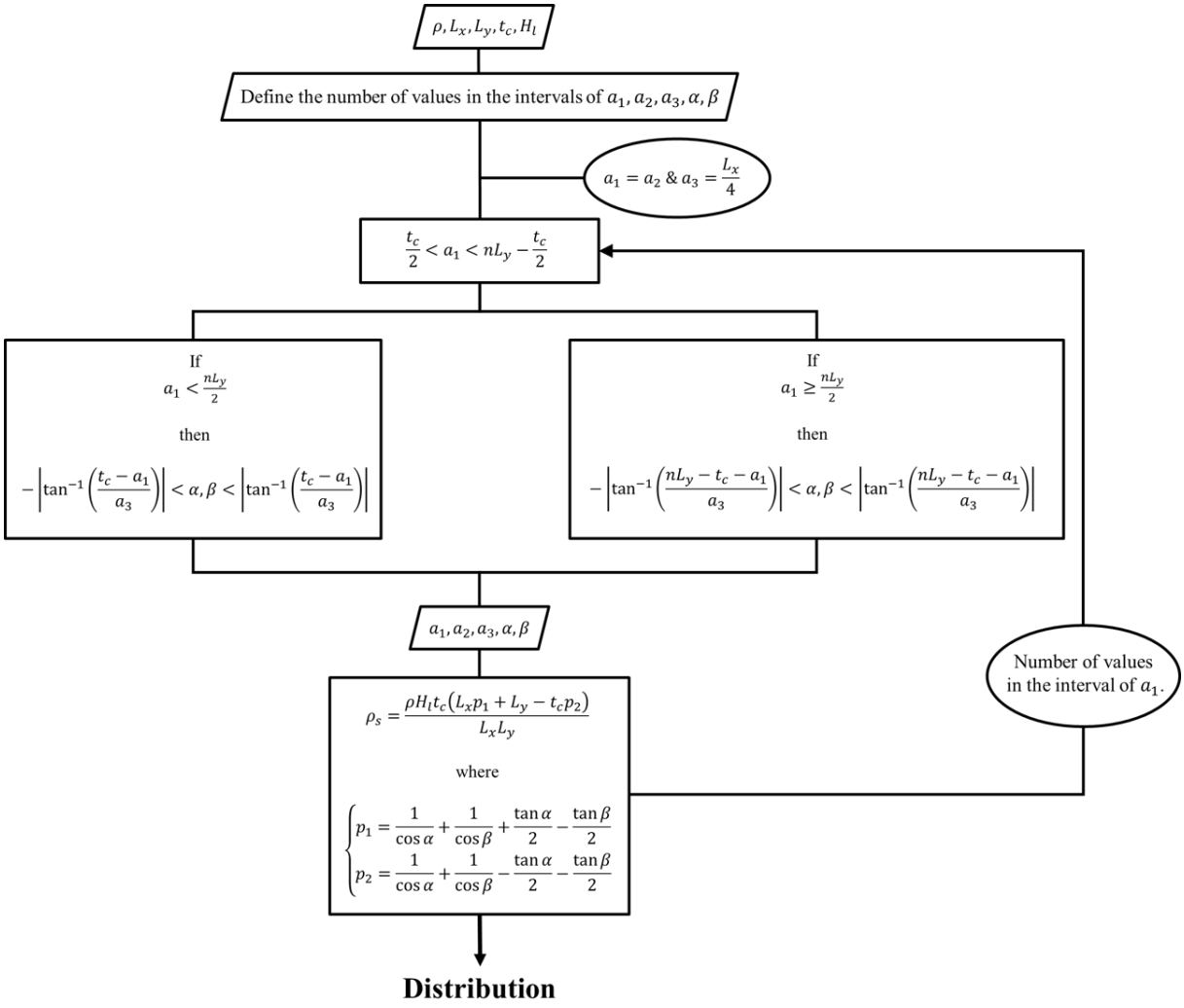

Figure 4.3: Algorithm developed to obtain the design space.

parametric survey. This dependency is not observed for the other parameters which means that only a_1, a_3 and α or β would be needed for the study. However, since the law describing the function between α and β has not been calculated, the four geometrical parameters are included in both next parametric analyses.

4.3 Rectangular-Random-Rectangular configurations

The following parametric survey is performed for a MLCTS considering 3 layers with the first and third layer made of a rectangular core, while the middle layer core is a random core which is designed by the geometrical parameter $a_1 = a_2$, a_3, α and β obtained with the algorithm. In this case, a symmetry can be observed for the parameter a_1 (and thus a_2) allowing to study the values belonging only to the range $[t_c, Ly/4]$. The computed

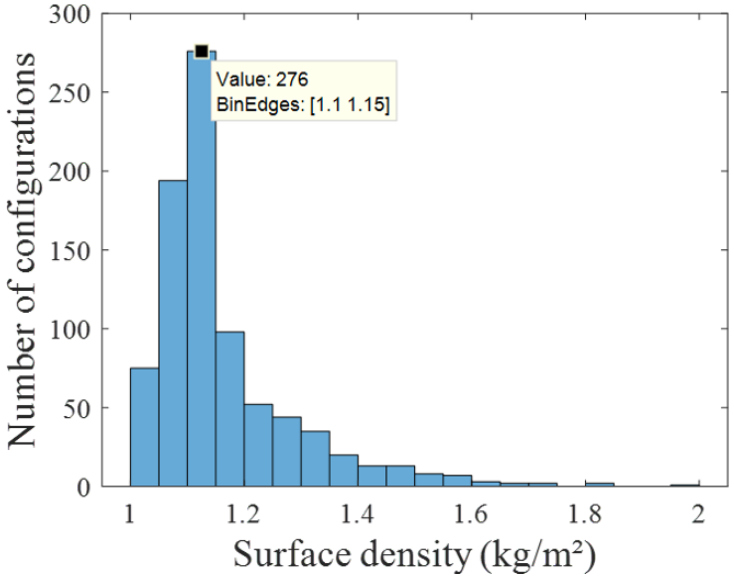

Figure 4.4: Distribution of the surface density with a range width of 0.14 kg/m^2.

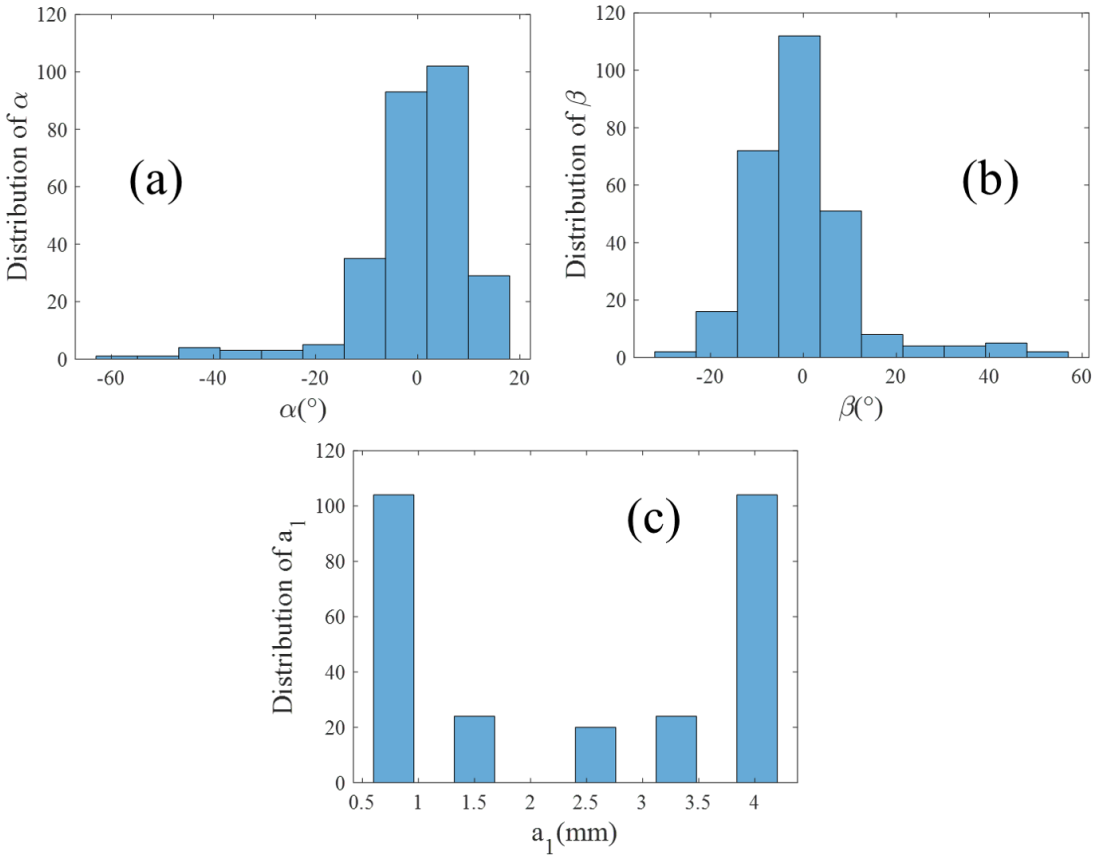

Figure 4.5: Distribution of (a) the angle α, (b) the angle β and (c) the parameter a_1.

configurations total number is then divided by two, leading to 1932 unit cell designs which took 5 days to be calculated. The following figure (Fig. 4.7) illustrates both used finite element meshes.

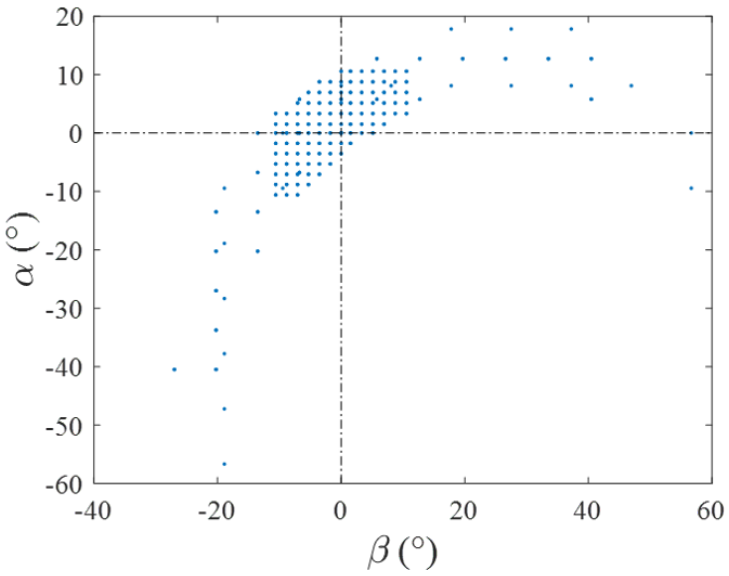

Figure 4.6: Pairs (α, β) given for each configuration when ρ_s belongs to the range [1.1, 1.15] kg/m^2.

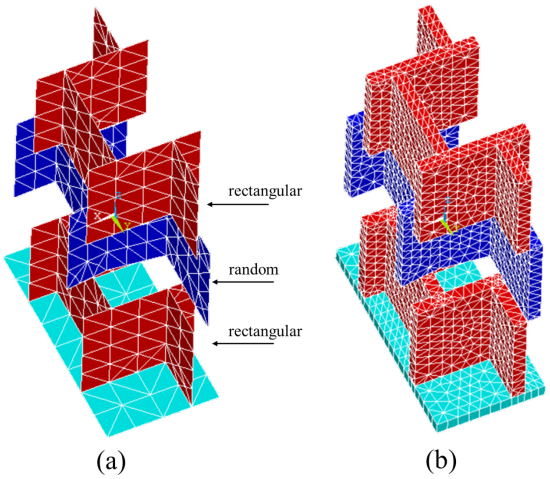

Figure 4.7: Unit cell designs for the first parametric survey with (a) shell elements (b) solid elements.

4.3.1 Global analysis

The obtained results in the design space are illustrated in Fig. 4.8 and Fig. 4.9 calculated for all indicators. For the static mechanical properties, results are shown by normalizing the result with the shear and compression modulus obtained with the standard case. Moreover, for some configurations, the values have not been retrieved since the unit cell has not been correctly meshed by the software. Those designs would involve a very fine mesh which was not possible using Ansys apdl. However, most of the configurations have been modelled correctly.

As expected, the interfaces between layers involve the drop of mechanical properties and

the maximum values are obtained for the standard case. However, in the direction y, it is possible to slightly improve the shear modulus S_{yy} for some configurations (Fig. 4.8c). Consequently, no optimal designs leading to the improvement of both, the STL and mechanical properties can be found out.

Concerning the STL, a periodic result is obtained and a symmetry related to the direction x (a_3) can be noticed. Therefore, the study could be limited to values of a_3 in the range of [t_c, $L_x/2$ - t_c]. This behavior is related to the geometry of the top and bottom layer. The maximum value of the STL_{int} is obtained when the shift a_3 is near to 0 mm, $L_x/2$ and L_x. This means that the middle layer core sides orthogonal to the direction x are located in the middle of the core sides belonging to the top and bottom layer orthogonal to the direction x. In addition, the values of the STL_{int} are maximum when $a_1 = 0.83$ mm and then drastically reduced for $a_1 = 1.67$ mm and $a_1 = 2.5$ mm. When $a_1 = 0.83$ mm, the gap between the core sides orthogonal to the direction y and belonging to the middle layer and the core sides along y direction of the top and bottom layer is the maximum. Besides, the mechanical properties are maximum when $a_3 = L_x/4$ and when a_1 is near to $L_y/4$.

Consequently, the distance between the contact areas between layers have to be high to increase the inertia and the flexibility within the core and to improve the STL. However, such designs lead to a drop of mechanical properties by creating a lower rigidity.

Regarding the obtained results for the STL_{int}, the focus has been made on the values $a_3 = L_x/4$ (minimum values of the STL_{int}) and $a_3 = 15L_x/16$ (maximum values of the STL_{int}). The results are depicted in Fig. 4.10 and are obtained depending of the angles α and β and when all the range of a_1 is studied. When $a_3 = L_x/4$, the STL_{int} drops when a_1 is low. In addition, the influence of the angles α and β on the STL_{int} is maximum when $a_1 = 1.67$ mm while it is the lowest when $a_1 = 0.83$ mm. Therefore, a wider range of results is obtained due to the involvement of the angles α and β. Although the MLCTS involves a higher critical frequency, this does not mean a higher STL in all the frequency range of interest since after the critical frequency a higher drop of the STL can be obtained compared to the standard structure. The next study is focused on unit cell designs involving $a_1 = 0.83$ mm.

4.3.2 Parametric survey

An average value of the STL_{int} as well as the standard deviation for all angles α and β is calculated when $a_1 = 0.83$ mm and for each value of a_3 represented in Fig.4.11. The variation of the STL_{int} is thus mainly related to a_3 compared to the variation of the pairs (α, β) (Fig.4.11a). The same observation can be made for mechanical properties (Fig.4.11b)c)d)e) when a_3 is between [$t_c/2$, $L_x/2 - t_c/2$]. However, when a_3 belongs to range [$L_x/2 + t_c/2$, $L_x + t_c/2$], the variation of the angles induced a higher variation

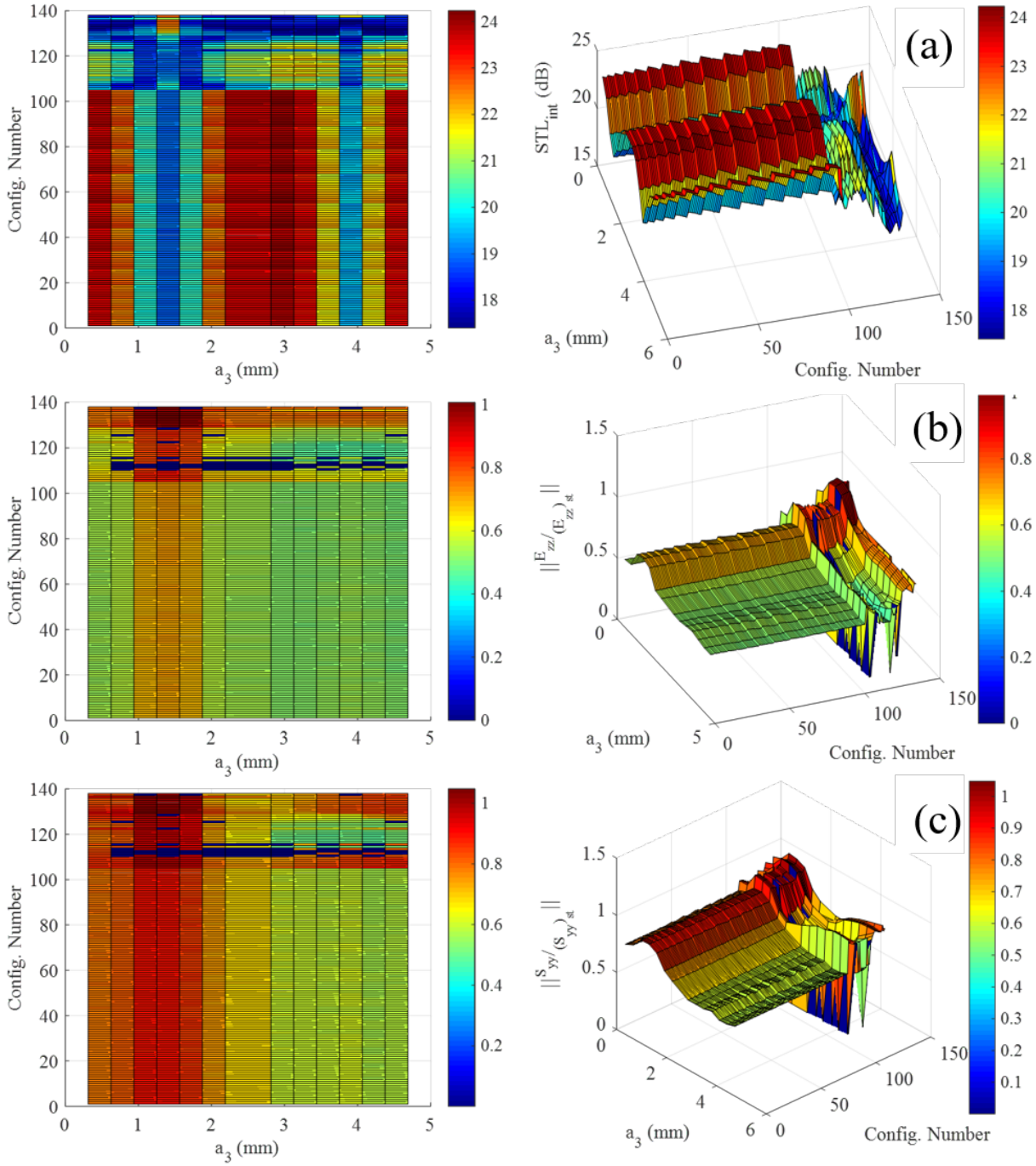

Figure 4.8: Design space of the ROR (a) STL_{int} (b) E_{zz} (c) S_{yy}.

of the STL_{int} and the influence of the angles α and β becomes more significant.

Finally, when $a_3 = 15L_x/16$ and $a_1 = 0.83$ mm, the influence of the pairs (α, β) on the STL_{int} is illustrated in Fig.4.12. The pair (α, β) corresponds to a linear function depending on the value of the STL_{int}, in which the intercept has a critical influence. The highest value of the STL_{int} occurs when the intercept of the linear function is the lowest. Finally, the optimal configuration for this first study is obtained when $a_1 = 0.83$ mm, $a_3 = 15L_x/16$, $\alpha = 3.3°$ and $\beta = -10.6°$.

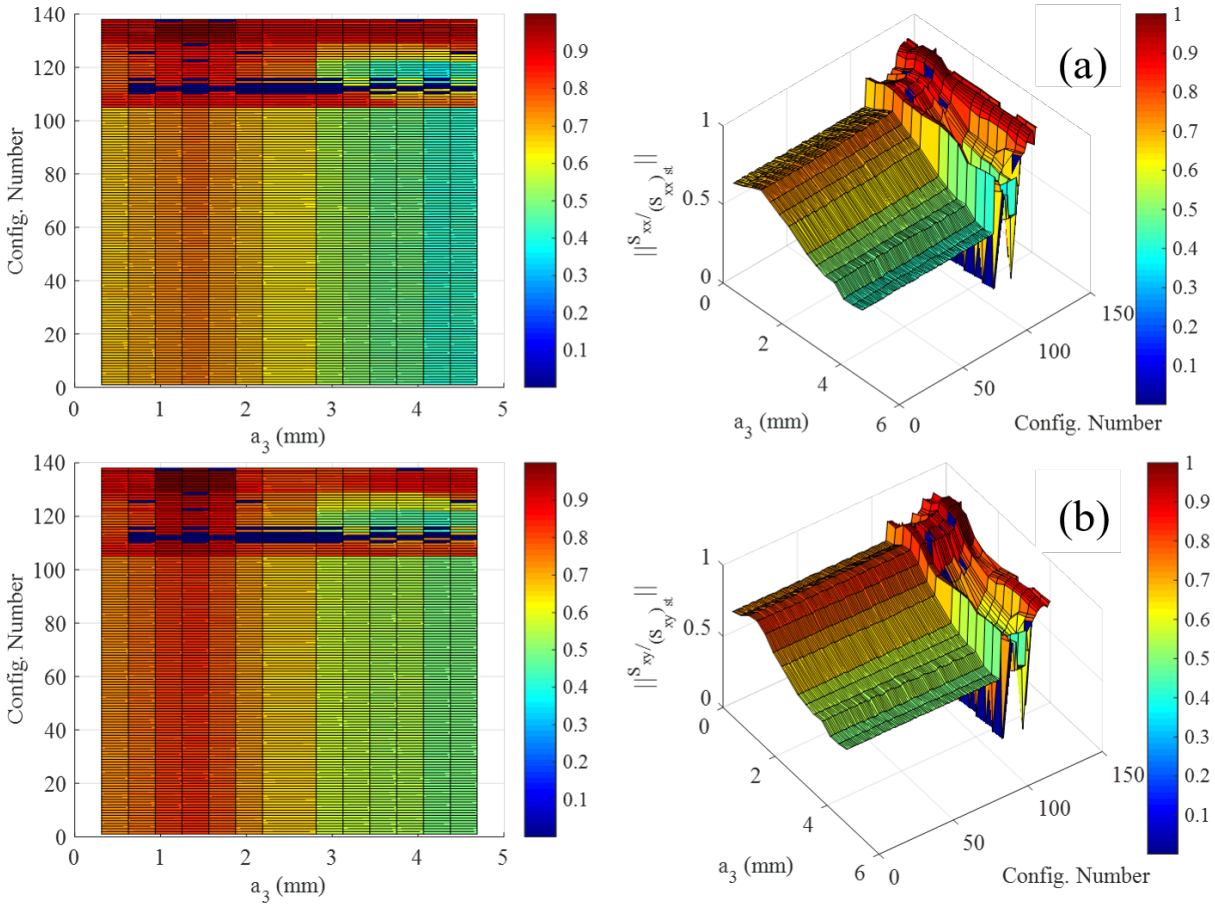

Figure 4.9: Design space of the ROR (a) S_{xx} (b) S_{xy}.

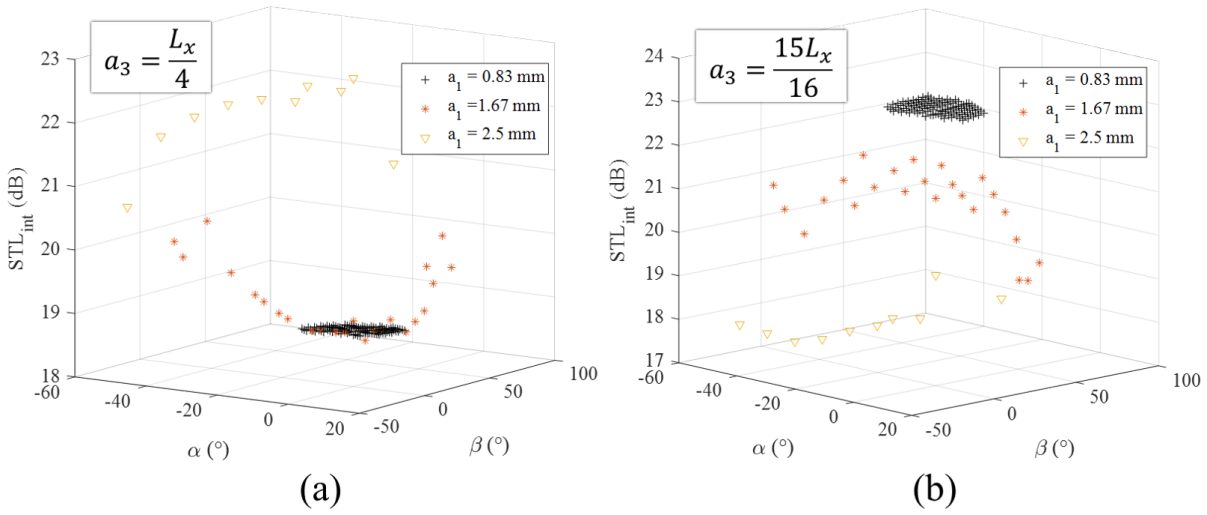

Figure 4.10: Influence of the angles α and β depending on the parameter a_1 when (a) $a_3 = L_x/4$ and (b) $a_3 = 15L_x/16$.

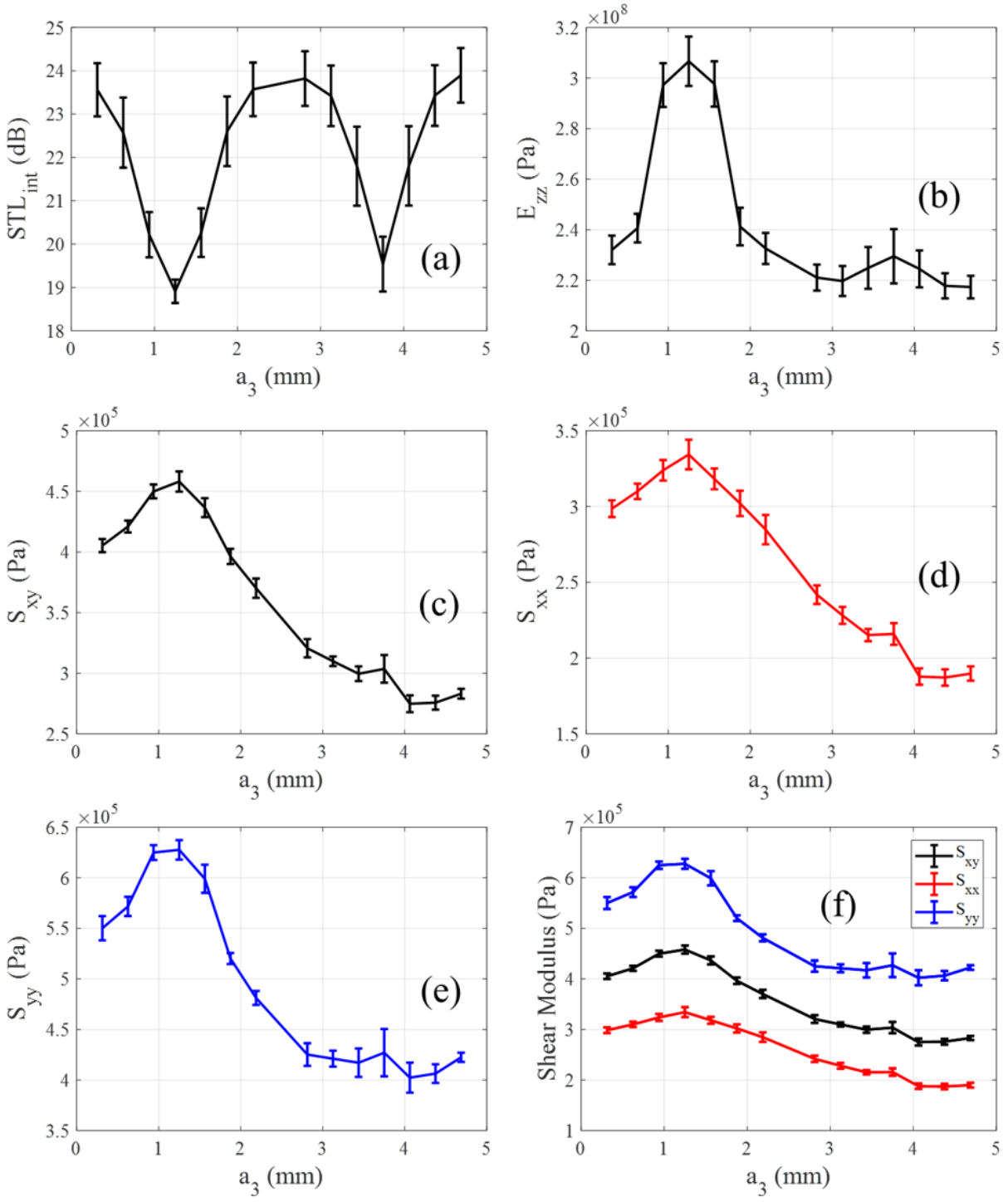

Figure 4.11: Standard deviations and average values of the STL_{int} over all angles α and β for each value of a_3 when $a_1 = 0.83$ mm of (a) the STL_{int} (b) E_{zz} (c) S_{xy} (d) S_{xx} (e) S_{yy} and (f) the comparison of the global and directional shear modulus.

4.4 Rectangular-Random-Optimized configuration

The next parametric survey is performed for a MLCTS considering 3 layers where the first is made of a rectangular core and the third layer is made of the optimal configuration

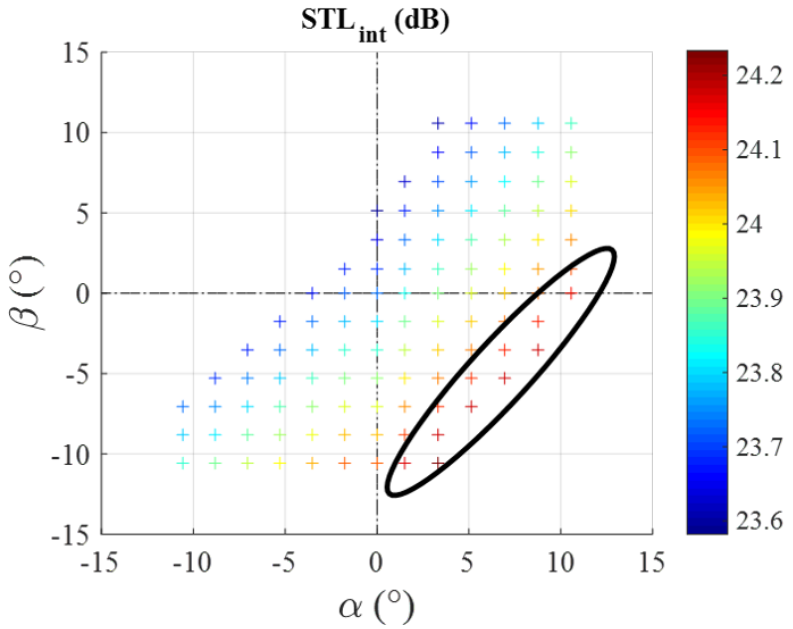

Figure 4.12: Influence of the pair (α, β) on the STL_{int} given when $a_3 = 15L_x/16$ and $a_1 = 0.83$ mm.

obtained previously. The middle layer core is a random core designed with the same design space described previously. The unit cell is called ROO. In this case, the symmetry is no longer valid and the design space becomes wider. The total number of computed configurations is thus multiplied by two leading to 3868 designs and took 10 days to be calculated. The following figure Fig. 4.13 illustrates the used finite element mesh for the calculation of the STL.

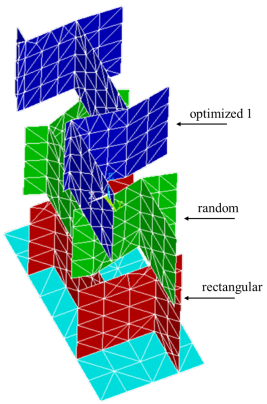

Figure 4.13: Unit cell designs for the second parametric survey modelled using shell elements.

4.4.1 Global analysis

The results obtained in the studied design space are illustrated in Fig. 4.14. Mechanical properties are still shown by normalizing the values with the compression and shear modulus of the standard case made of rectangular cores.
The STL_{int} still leads to periodic geometrical results obtained when the parameter a_3 of the middle layer takes values between $[L_x/16, 4L_x/16]$, $[4L_x/16, 7L_x/16]$, $[7L_x/16, 12L_x/16]$ and $[12L_x/16, 15L_x/16]$. Four maximum values of STL_{int} are noticed when $a_3 = L_x/16$, $a_3 = 6L_x/16$, $a_3 = 10L_x/16$ and $a_3 = 13L_x/16$ corresponding to the core sides along y direction belonging to the middle layer located between the core sides along y direction of the first and third layer. Contrary to the previous analysis, STL_{int} is maximum when $a_1 = 4.17$ mm. In this case, the distance between the core sides in both direction x and y of all layers is high leading to an increase of the inertia and the flexibility inside the core improving the STL.
Besides, the mechanical properties are still reduced, and the maximum values are obtained when $a_3 = L_x/4$ and when $a_1 = 0.83$ mm. In addition, the compression modulus (E_{zz}) and the shear modulus in the direction x (S_{xx}) as well as the global shear modulus (S_{xy}) are mainly influenced by the parameter a_3 while the shear modulus in the direction y (S_{yy}) is impacted by the parameter a_1.
Regarding the obtained results for the STL_{int}, the focus is now made on the values $a_3 = L_x/4$ (minimum values of the STL_{int}) and $a_3 = 10L_x/16$ (maximum values of the STL_{int}). Results are depicted in Fig. 4.15 and obtained depending on the angles α and β for each value of a_1.
Contrary to the previous parametric analysis, when $a_3 = L_x/4$ and $a_3 = 10L_x/4$ no inversion is noticed and the global behavior remains the same. Therefore, the STL_{int} is high when $a_1 = 4.17$ mm whatever is the value of a_3. In addition, the influence of the angles α and β on the STL_{int} increases when a_1 is near to $L_y/4$. However it seems that this influence is the lowest when $a_1 = 4.17$ mm. The next study is focused on unit cell designs with $a_1 = 4.17$ mm.

4.4.2 Parametric survey

The average value of the STL_{int} and the standard deviation for all angles α and β is calculated when $a_1 = 4.17$ mm (Fig.4.16). The variation of the STL_{int} is now related to both parameters a_3 and the pairs (α, β) (Fig.4.16a). However, the influence of the parameter a_3 is more important than the influence of the pairs (α, β) on mechanical properties (Fig.4.16b, Fig.4.16c and Fig.4.16e) except for the shear modulus along the direction x (Fig.4.16d) where the angles induce higher variations.
Finally, when $a_3 = 10L_x/16$ and $a_1 = 4.17$ mm, the effect of the pair (α, β) is

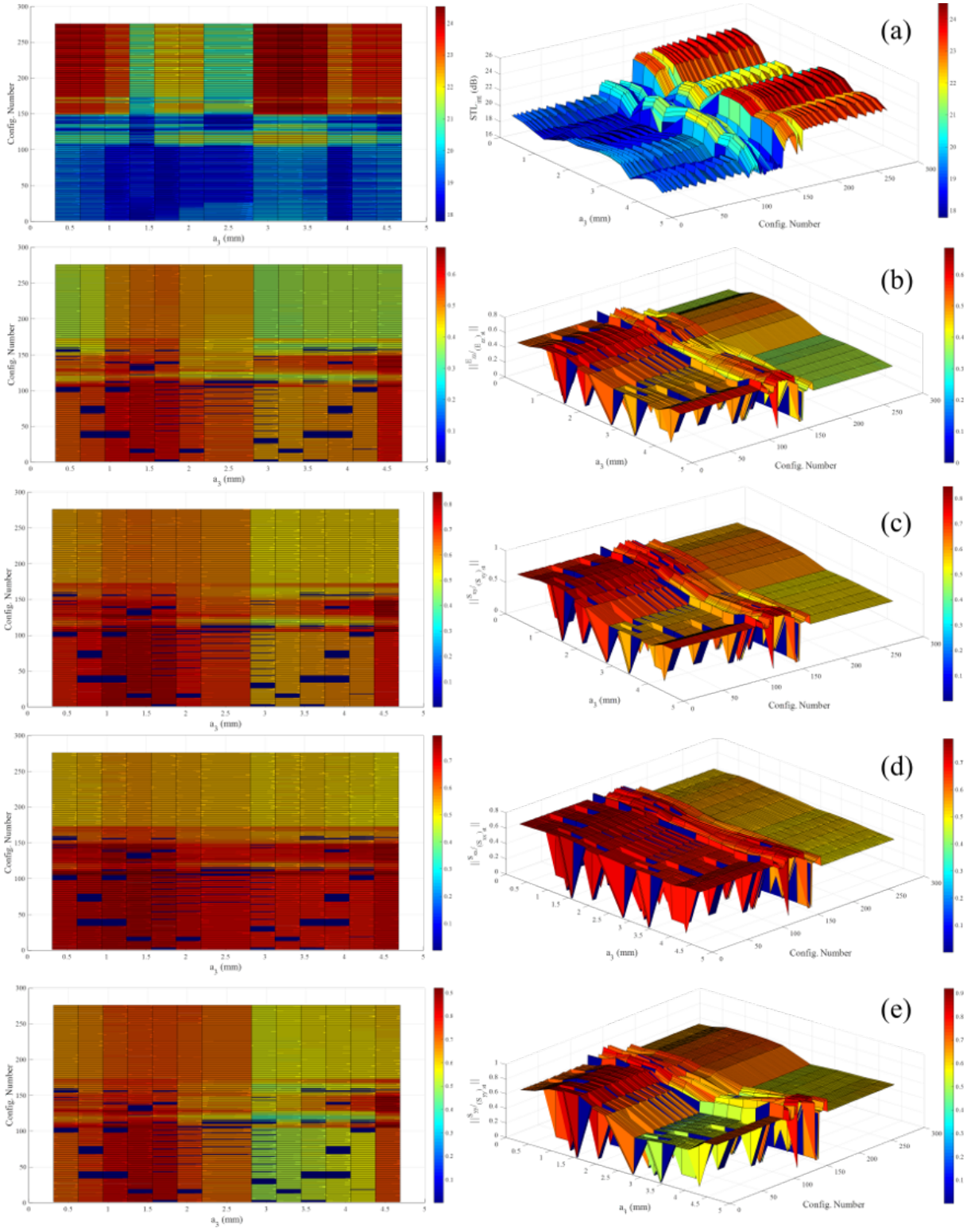

Figure 4.14: Design space of the ROO configuration (a) STL_{int} (b) E_{zz} (c) S_{xy} (a) S_{xx} (b) S_{yy}.

illustrated in Fig.4.17. Again, the pair (α, β) corresponds to a linear function depending on the value of the STL_{int} in which the intercept has a critical influence. The highest value of the STL_{int} occurs when the intercept is the lowest and the optimal configuration

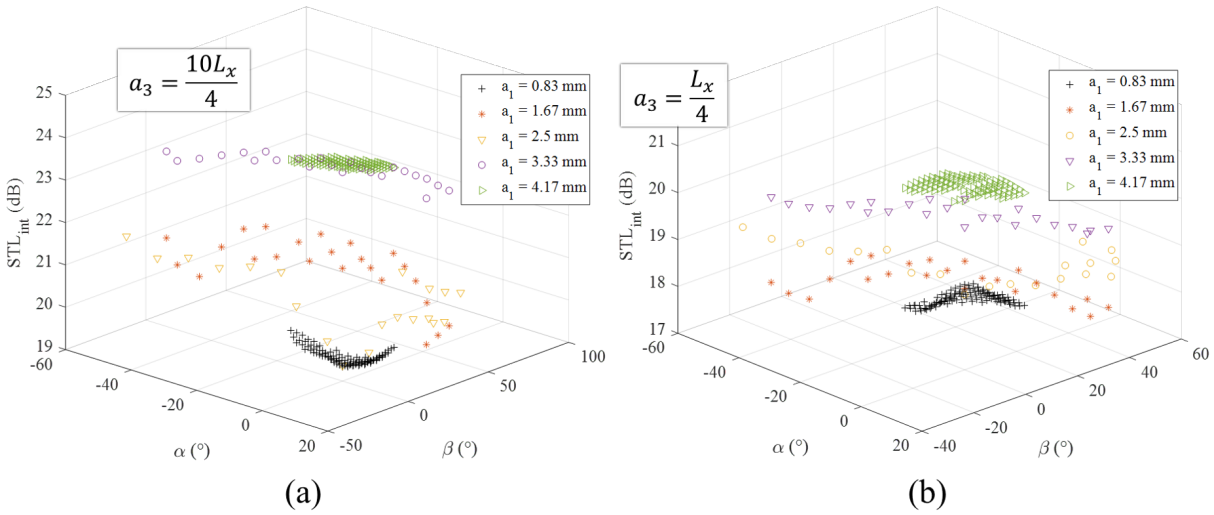

Figure 4.15: Influence of the angles α and β depending on the parameter a_1 when (a) $a_3 = 10L_x/16$ and (b) $a_3 = L_x/4$.

is obtained when $a_1 = 4.17$ mm, $a_3 = 10L_x/16$, $\alpha = 3.3°$ and $\beta = -10.6°$. The obtained optimal configuration is thus the same of the previous analysis with a different shift along x direction (a_3) and y (a_1) direction.

4.5 Optimized unit cells comparison

Both optimal configurations resulting from both previous parametric analysis are illustrated in (Fig. 4.18b and Fig. 4.18c) compared to the standard unit cell (Fig. 4.18a). Both optimized layers correspond to auxetic cores which could lead to a negative structural Poisson ratio [119]. The compression and shear modulus of both optimized unit cells are listed in the following table:

Table 4.1: Comparison between the optimized unit cells and the standard structure.

	Standard	Optimized 1	Optimized 2
E_{zz} (MPa)	433	219	157
S_{xx} (MPa)	0.45	0.19	0.23
S_{yy} (MPa)	0.7	0.42	0.39
S_{xy} (MPa)	0.56	0.28	0.3

The compression modulus is divided by 2 for the first optimized unit cell while it is divided by 3 for the second. The shear modulus is divided by 2, however, the global shear modulus of the second optimized structure is slightly improved due to the increase of the shear modulus in the direction x. Finally, all calculated mechanical properties are reduced for

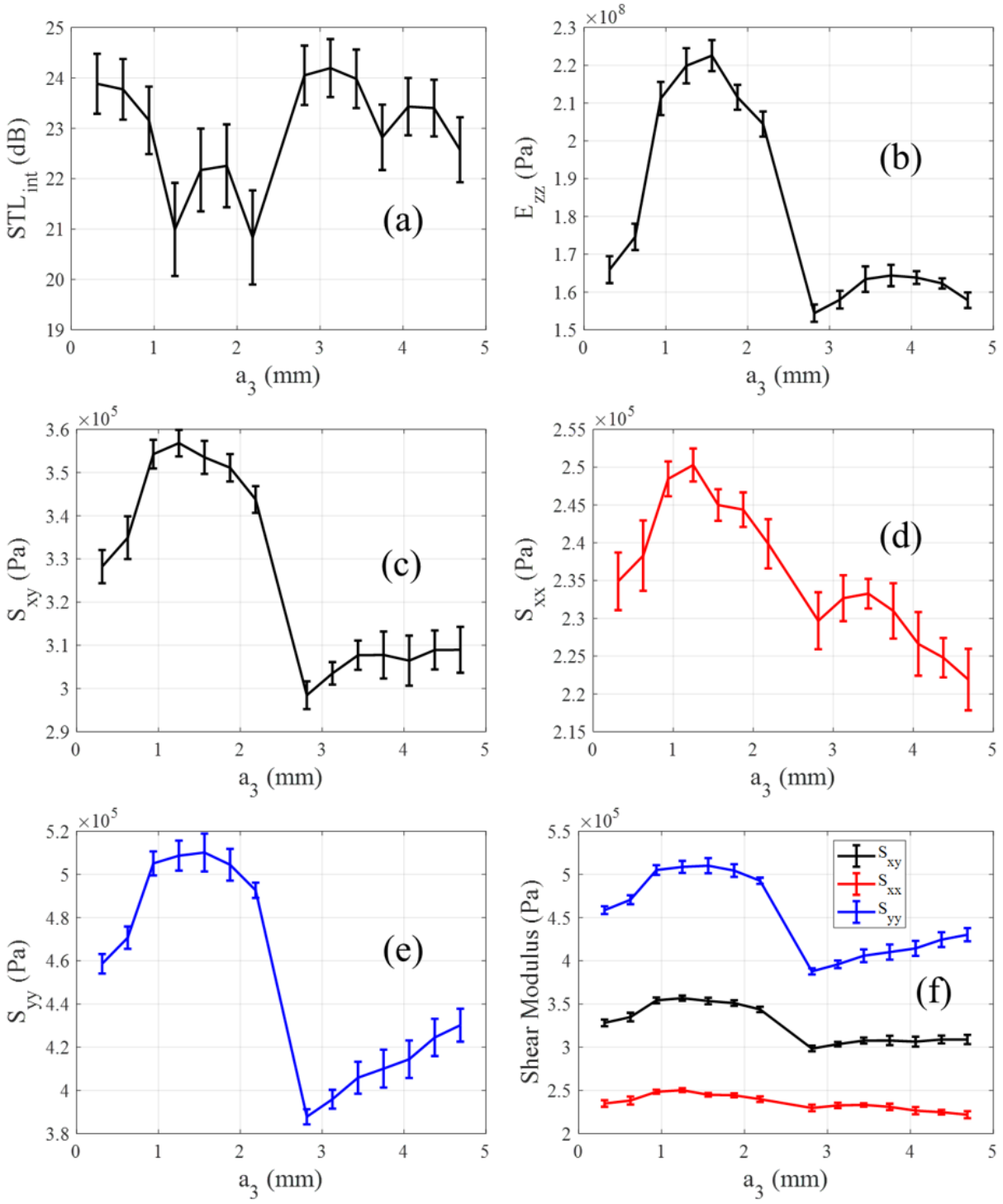

Figure 4.16: Standard deviations and average values of the STL_{int} over all angles α and β for each value of a_3 when $a_1 = 4.17$ mm of (a) the STL_{int} (b) E_{zz} (c) S_{xy} (d) S_{xx} (e) S_{yy} and (f) the comparison of the global and directional shear modulus.

the optimized unit cells compared to the standard unit cell.

The comparison of the STL_{int} between the optimized unit cells and the standard structure is shown in Fig. 4.19. A great improvement is obtained in the whole frequency range of

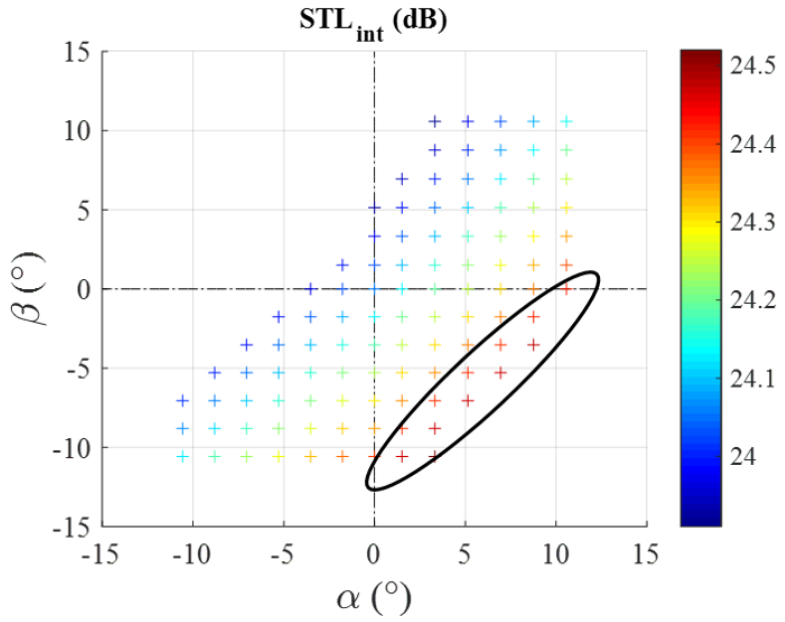

Figure 4.17: Influence of the pair (α, β) on the STL_{int} given when $a_3 = 10L_x/16$ and $a_1 = 4.17$ mm.

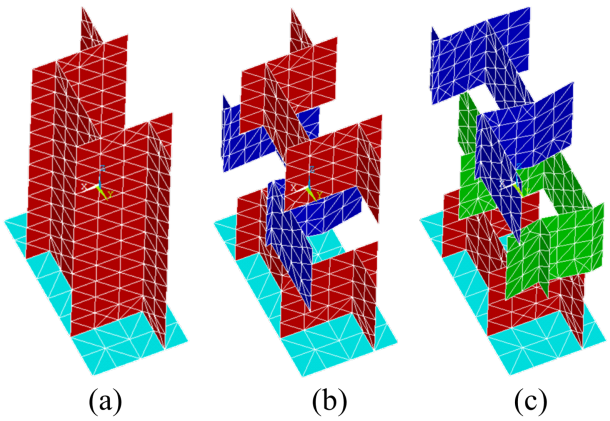

Figure 4.18: (a) Standard unit cell (b) first optimized unit cell (ROR) and (c) second optimized unit cell (ROO).

interest and the critical frequency is shifted at a higher frequency. A slight improvement is noticed between both optimal unit cells. Therefore, it is not necessary to use the ROO configuration since the mechanical properties are better for the ROR unit cell. A better balance between the STL and mechanical properties is obtained for this later. The main reason leading to the improvement of the STL is still due the added flexibility on the unit cell with the use of MLCTS designs induced by the contact areas between layers which lead to higher flexural wavenumbers (Fig. 4.20). The calculation has been made using solid elements to bring the model closer to the reality. Therefore, the structure is more rigid as compared to the shell elements used to compute the STL and the critical

frequency is shifted at a lower frequency. However, this does not change the conclusions on the dynamic and vibroacoustic behavior of the calculated configurations.

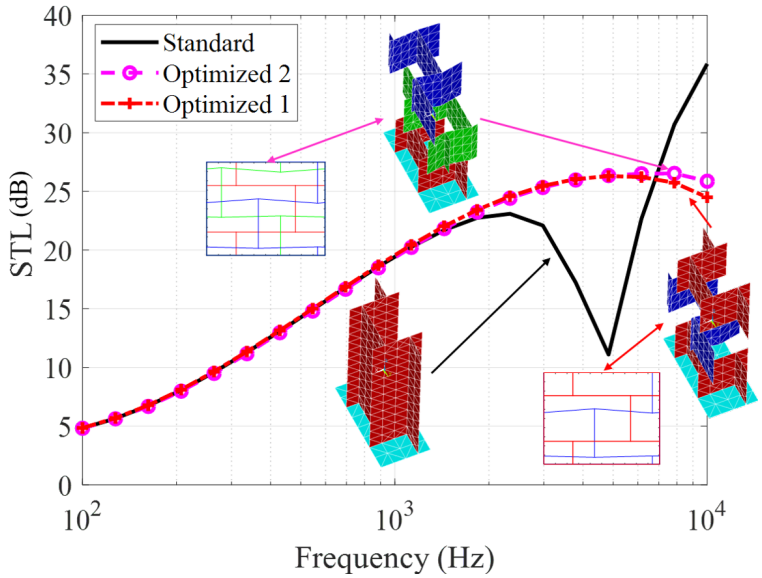

Figure 4.19: Comparison of the STL with $\theta = 78°$ and integrated over φ between the optimized structures and the standard sandwich panel.

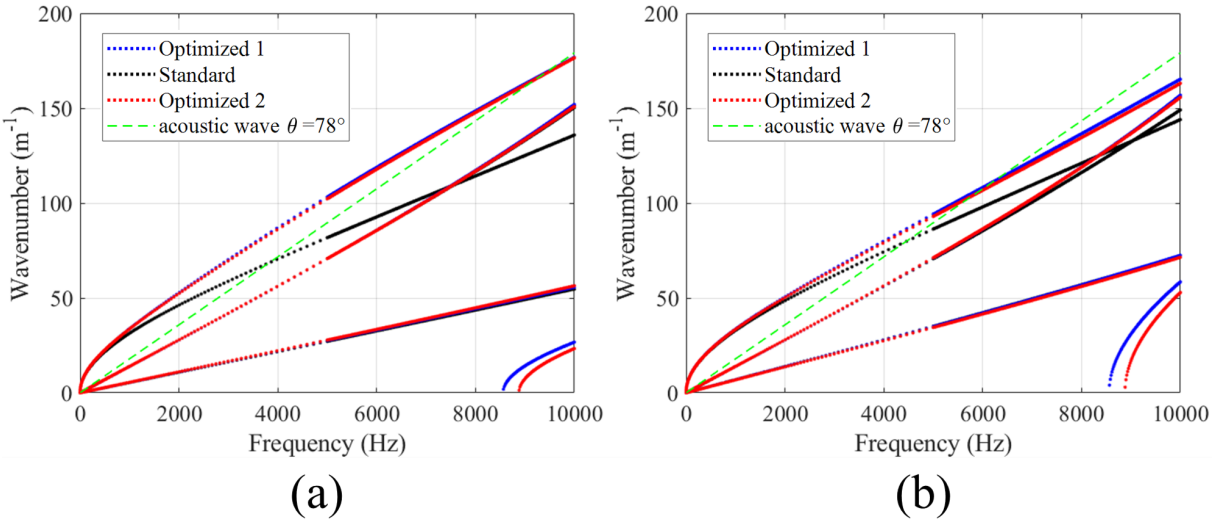

Figure 4.20: Dispersion curves with (a) k_x (b) k_y.

4.6 Conclusions

This chapter has been focused on the study of MLCTS made of 3 layers. The first study was concentrated on a configuration made of a rectangular core in the top and bottom layer with a random middle core. When the optimal design of the first study was obtained, a second parametric study has been performed for a bottom layer made of a rectangular

core, a middle random core and a top layer made of the first obtained optimal unit cell. The main purpose is to study the influence of the geometrical parameters involved in MLCTS, on the STL and the compression and shear modulus. In addition, an optimal unit cell has been obtained for both studies to improve the STL in a broadband frequency while maintaining the mass constant. To simplify the analysis, the targeted indicator consisted on the integration of the STL over the frequency range.

In the first parametric analysis, the symmetry of the unit cell led to the reduction of the design space study. It occurs that a_1 should be equal to 0.83 mm to obtain the highest values of the STL while in the second parametric analysis a_1 is equal to 4.17 mm. In addition, results show that the parameter a_3 involves a high variation of the STL which is always maximum when the core sides along the direction y of the middle layer is located between the core sides of the top and bottom layer. The variations are stronger in the first parametric analysis. Moreover, depending on the value of a_3, it is preferable to increase or decrease the value of a_1 to target a better STL when the top and bottom layer are rectangular, while, in the second analysis, there is a constant decrease of the STL when a_1 is reduced. Finally, after fixing the value of a_3 and a_1 for both parametric analysis, it was shown that the pair (α, β) turned out a linear relationship according to the value of the STL. Thereby, the optimized pair (α, β) corresponds to the equation with the lowest intercept.

Besides, the interfaces between layers lead to a drop of mechanical properties and all configurations for both parametric surveys have a reduced compression and shear modulus except in the direction y, when the top and bottom layer are rectangular. In this configuration, it is possible to design the unit cell to have a slight improvement of the shear modulus along y direction (S_{yy}). In addition, contrary to the first parametric survey in which a_3 involved a high variation of the shear modulus in the direction x (S_{xx}), the second parametric survey shows a higher variation related to the angles α and β.

Finally, two optimized structures with the same surface density of the standard structure was obtained as well as the understanding of the influence of each geometrical parameter involved in the proposed parametric model. The mechanical properties of both optimal configurations are reduced as well as the dynamic rigidity of the structure.

Ultimately, the parametric analysis may introduce more studied parameters when a_1 is different to a_2. In addition, a sensitive analysis could be used to show how the parameters influences all indicators. Moreover, all results could be investigated using data mining since many configurations are implemented. Therefore, the law between the geometrical parameters and the targeted indicators will be known and simplify the parametric analysis.

The next Chapter investigates the influence of the core geometry on the SAC and the STL of MLRCS.

Chapter 5

Multi-layer rectangular core systems inside a sound absorption framework

Abstract

The following work is focused on the improvement of the SAC and the STL under normal incidence acoustic waves using MLRCS. The thermal-viscous effect is taken into account inside the core and perforations are added in the upper skin. Different configurations are investigated using a FEM and an equivalent fluid model involving the Johnson-Champoux-Allard parameters to retrieve the STL and the SAC. Proposed designs show a great improvement of both indicators at low and broadband frequency.

Contents

5.1 Introduction

A lot of research has been carried out to propose solutions including new designs, new materials or using add-ons to enhance the acoustic performances of sandwich structures involving periodic cores. Most of these studies and proposals were focused on the STL and less regarding the SAC which was mainly related to porous media. Moreover, the STL is governed by three parameters: the mass law at low frequencies, the damping in the critical frequency region and finally the global stiffness; while the SAC involves more parameters as described in the Biot's theory [17, 18]. Therefore, it seems necessary to enhance both properties, the STL and the SAC to meet the best requirement in terms of acoustic efficiency of honeycomb cores while the mass is maintained constant.
Another solution proposed by Arunkumar et al. [148] and Fu et al. [147] corresponds to filled foam cores combining the high stiffness of honeycomb or corrugated cores with the acoustic absorption of foams. Such solutions are limited due to the added mass on the structure and since it focuses their efficiency on specific frequencies. Besides, MPPs replace the sandwich panel's skins to obtain an improvement of the SAC at a specific frequency. It is also possible to combine several MPPs with different perforation sizes to have a wider frequency range of acoustic efficiency [153]. The STL and the SAC have been also improved using MPPs on honeycomb sandwich panels [107, 157]. A hybrid honeycomb-corrugated core with MPPs has been proposed by Tang et al.[108] for broadband low frequency enhancement.
Therefore, dealing with complex structures lead to the use of FEM softwares to calculate the STL and the SAC [107, 108] or to retrieve the Johnson-Champoux-Allard parameters [174]. Those later are obtained using the thermal, Stokes and viscous-inertial equation [104]. Besides, the MPPs formulations developed by Maa [99, 100] and Sgard et al. [84] can be used to retrieve the acoustic impedance when the MPPs is backed by a porous media thanks to a dynamic tortuosity correction. Most of the studies are performed for normal incidence acoustic waves to simulate experimental measurements with an impedance tube since the diffuse acoustic field calculation is very difficult to obtain due to the high computational cost.

Based on current researches, this chapter deals with MLRCS. The principle consists on stacking layers of rectangular cores. The STL is mainly related to the dynamic behavior of the sandwich panel but can be improved with the energy dissipation inside the core. This later is associated with the SAC including the thermal and viscous effect. The main focuses is to change the core geometry while the mass is maintained constant with an in-plane shifting process to alter the properties and then to influence both the STL and the SAC. Therefore, it is possible to target specific frequencies and to improve the acoustic efficiency at low frequencies. These results are obtained using Comsol Multiphysics considering the motion of the solid part, the acoustic area on both sides of the sandwich

panel and the thermal-viscous effect inside the core. Moreover, the Johnson-Champoux-Allard parameters are retrieved to investigate how they are modified when MLRCS are considered. The calculations are performed for normal incidence acoustic waves. Three applications are provided: MLRCS with meso-scale unit cells and no viscous-thermal effect in the core, then, MLRCS without the upper skin and finally, sandwich panels with an upper MPP including one or two perforations. In this last two configurations, a micro-scale unit cell is designed. It is demonstrated that the STL and the SAC are improved for broadband or specific frequencies, and it is also possible to modify the SAC and the STL peak depending on the shift introduced in the MLRCS. Section 5.2 is devoted to the description of the parametric model, the FEM and the equivalent fluid model while Section 5.3 is related to MLRCS with meso-scale unit cells. Section 5.4 is focused on the study of micro-scale unit cells with 2 configurations corresponding to MLCRS combined with a MPP of one perforation, and a MLRCS with a removed upper-skin and a MPP of two perforations. It includes thermal-viscous effects within the core. Finally, the paper is concluded in Section 5.5.

5.2 Description of the FEM

In this section, the parametric model as well as the FEM made with Comsol Multiphysics allowing to retrieve the SAC and the STL are described. In this Chapter, normal incidence acoustic waves are considered.

5.2.1 Parametric model

MLRCS is a possible way to change a standard core into a structure similar to porous media. It is then possible to take advantage of porous media characteristics to create an energy dissipation within the core and to enhance the SAC by modifying the geometry of the MLCTS. This can be illustrated in Fig. 2.6 when rotations of several honeycomb core layers are considered to produce such a design. Therefore, combining different designs of honeycomb cores, and by adding rotations, structures similar to porous media can be made and physical parameters such as the porosity, the flow resistivity and so on can be involved in the acoustic properties calculations. Afterwards, these parameters can be adjusted by changing the core geometry of each layer. However, rotations lead to non-periodic structures and the unit cell can not be extracted. The entire structure needs to be modeled. For this reason, rotations are not considered and only shifts on both directions x and y are possible.
The parametric model of the MLRCS unit cell used in this Chapter is depicted in Fig. 5.1 and only 3 layers are illustrated for the sake of clarity (Fig. 5.1a). However, 9 similar stacked layers are considered with the same depth and their geometry can be modified

independently. The size of the unit cell is defined by L_x and L_y. The thickness of the layer corresponds to H_l. The thickness of the core and the skins are given by t_c and t_s respectively. The parameter n can be modified but it is equal to 1/2 in this study. Finally, the perforation diameter is d. Moreover, the core can be designed using the 3 following parameters: a_1, a_2 and a_3 (Fig. 5.1b). Two perforation cases are studied and illustrated in Fig. 5.1c and Fig. 5.1d. The first corresponds to a fluid flow travelling within the core while the fluid crosses all the core in the second case. The standard unit cell is retrieved when $a_1 = L_y/4$, $a_2 = L_y/4$ and $a_3 = L_x/4$ for all layers.

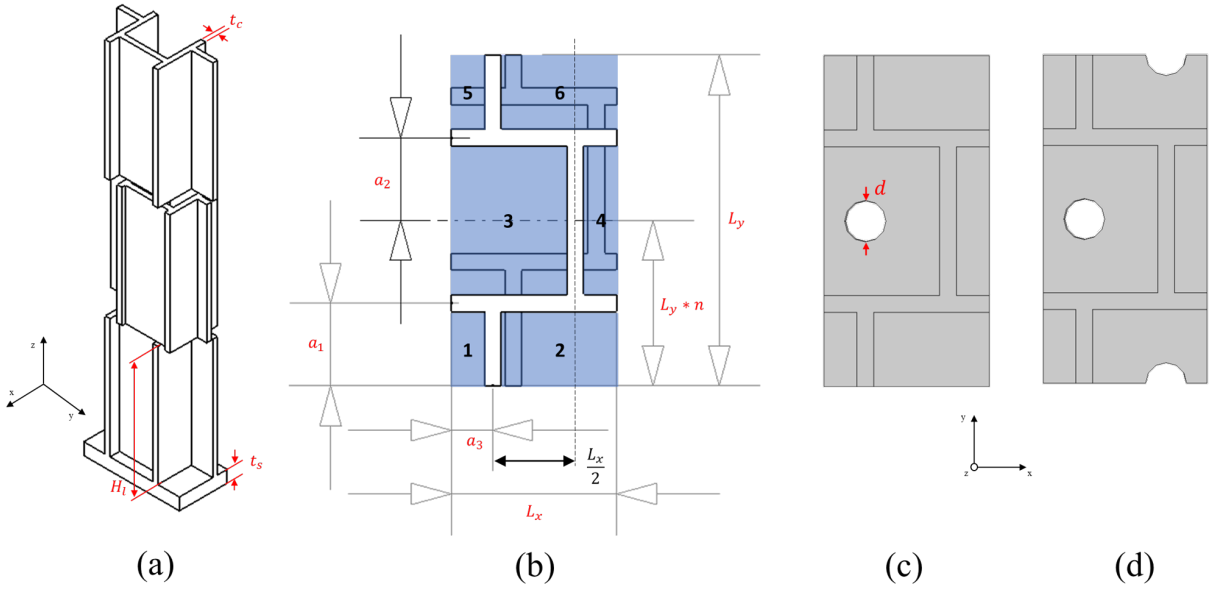

Figure 5.1: Parametric model of MLRCS.

5.2.2 FEM of the MLRCS

The FEM used in this chapter was already described in details by Meng et al.[107] and already mentioned in Fig. 1.14. An incident acoustic wave P_i impinges the sandwich panel and leads to a transmitted P_t, reflected P_r and absorbed wave P_a. The incident plane wave excitation is defined in Comsol Multiphysics by the following expression $P_i = \exp(-ik_z z)$ with $k_z = k_0 = \omega/c_0$ since only normal incidence acoustic waves are considered with c_0, the speed of sound.

The skins and the core are modelled using the Solid Mechanics module. The solid part is modelled to calculate the STL mainly due to the vibroacoustic behavior of the sandwich panel.

The incident and transmitted field are modeled using the Pressure Acoustics module. The Perfectly Matched Layer (PML) leads to a non-reflecting acoustic domain. It can be mentioned that the efficiency of PML layers are limited to acoustic waves with an angle of incidence under 55° [109]. The angle dependence of the SAC has been already

investigated but the measurement under a specific angle is still difficult to be done [175]. In the case of the perforated sandwich panel, the air inside the perforation is modeled using the Thermal-Acoustics module due to the comparable size between the perforation's diameter and the thermal and viscous boundary thickness. The Thermal-Acoustics module adds many dofs in the model due to the number of physical parameters involved in the calculation (the sound pressure, the temperature and the particle velocity in the direction x, y and z) leading to 5 dofs per node and thus a high computational cost.
Finally, the air within the core consisting on 6 narrow regions (Fig. 5.2b) for each layer and located between the skins is modelled using the Pressure Acoustics module or the Thermal-Acoustics module depending on the pores' size.
The periodic boundary conditions are added in the FEM and the structure is considered as infinite. Only tetrahedral elements are used, except for the PML which is meshed using swept mesh. When the Thermal-Acoustics module is used within the core, the solid-fluid interface has to be meshed accurately to capture the viscous-thermal effect on the boundary. The air is characterized by 7 parameters listed in Tab 5.1.

Table 5.1: Physical parameters of the air.

Parameters	Value
Density	$\rho_0 = 1.21$ kg/m^3
Sound speed	$c_0 = 343$ m/s
The equilibrium pressure	$P_0 = 101320$ Pa
Temperature	$T_0 = 293.15$ K
Dynamic viscosity	$\eta = 1.81 \cdot 10^{-5}$ Pa.s
Thermal conductivity	$K_T = 0.026$ W/(m.K)
Heat capacity at constant pressure	$C_p = 1004$ J/(kg.K)

The calculation of the STL and the SAC is described by Meng et al. [107]. The total acoustic wave power E is calculated as follows:

$$E = E_r + E_t + E_a, \tag{5.1}$$

where E_r, E_t and E_a are the acoustic wave power of the reflected, transmitted and absorbed acoustic wave, respectively. The total acoustic wave power is obtained using the following expression:

$$E = \frac{1}{2} Re \int_S P_i \cdot v_i^* \, dS \tag{5.2}$$

in which v_i^* is the complex conjugate of the velocity of the incident wave calculated using the Euler expression and S is the surface area of the incident plane of the FEM. The reflected acoustic wave power yields to:

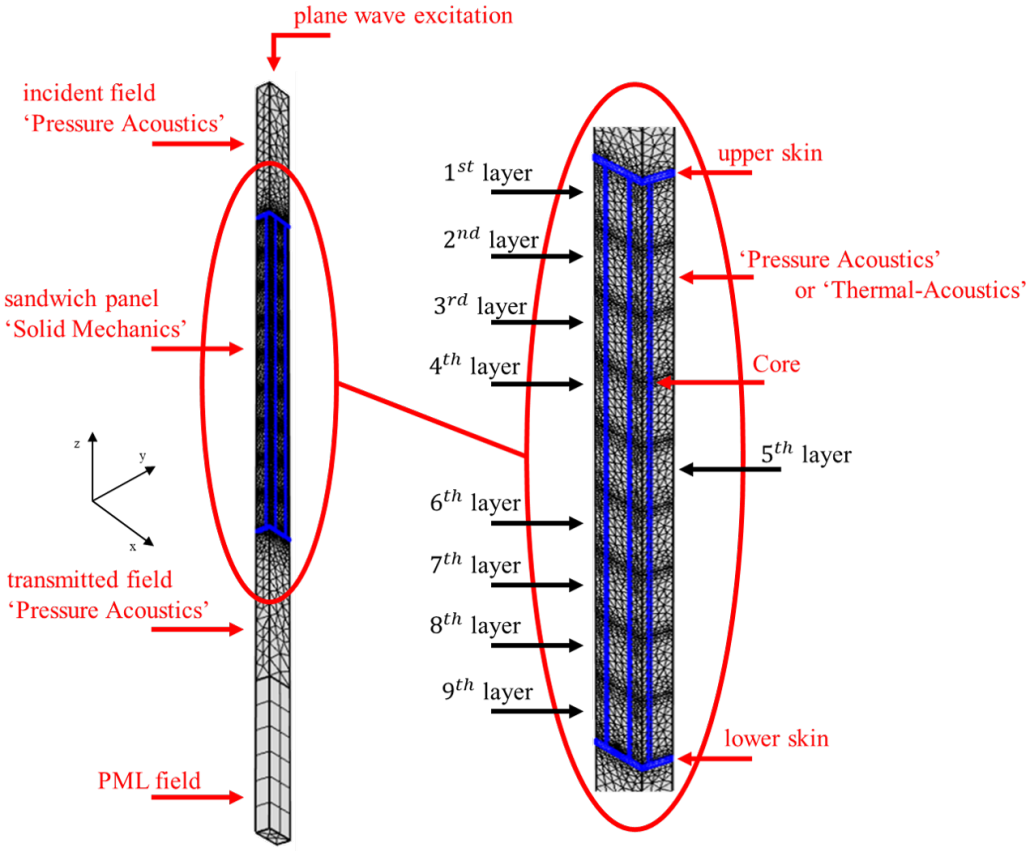

Figure 5.2: FEM made with Comsol Multiphysics.

$$E_r = \frac{1}{2} Re \int_S (P_1 - P_i) \cdot (-v_1 + v_i)^* \, dS \tag{5.3}$$

with P_1 and v_1, the total sound pressure and velocity of the incident plane, respectively. Only the velocity in the direction z is needed in the calculation. Finally, the transmitted acoustic wave power is obtained with:

$$E_t = \frac{1}{2} Re \int_S P_t \cdot v_t^* \, dS \tag{5.4}$$

where P_t and v_t are the sound pressure and velocity of the transmitted plane. Consequently, the STL and the SAC are calculated using the following expressions:

$$STL = 10 \log_{10} \frac{E}{E_t} \tag{5.5}$$

$$SAC = 1 - \frac{E_t}{E} - \frac{E_r}{E}. \tag{5.6}$$

5.2.3 Equivalent fluid model of MLRCS

When the structure is considered as a porous media, it can be described by the Johnson-Champoux-Allard parameters. These parameters include the viscous and thermal length

(Λ_{visc} and Λ_{therm}), the viscous and thermal permeability (q_{visc} and q_{therm}) and the tortuosity (τ_∞). They are calculated using the Eq. (1.50). However, the Thermal, Stokes and viscous-inertial problem need to be solved. Therefore, it is necessary to model the unit cell and specifically the fluid part using the FEM (Fig. 5.3a). Indeed, the solid part is considered as a rigid frame and can be decoupled from the air. However, only the SAC can be calculated since the vibroacoustic behavior of the structure is not taken into account. Moreover, a very fine mesh is needed on the solid-fluid interface to correctly simulate the fluid flow on the boundaries. The principle is to consider the MLRCS as an equivalent fluid. The method is described in details (Section 1.5.3) and all differential equations have been implemented on Comsol Multiphysics. The geometrical parameters impact on the JCA parameters can be thus investigated [174, 104].

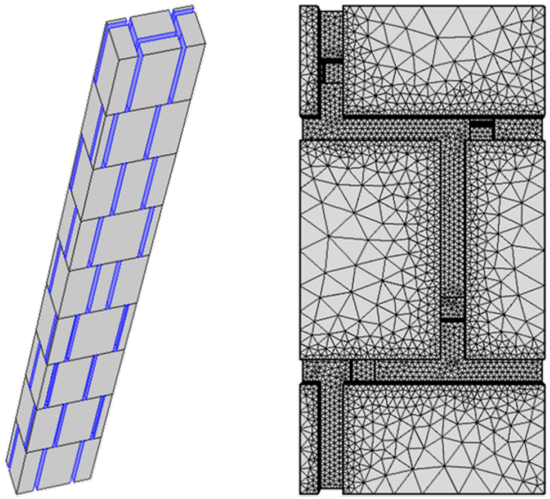

(a) (b)

Figure 5.3: FEM made with Comsol Multiphysics.

5.3 Meso-scale unit cells

In the section presented here, the study has been focused on two meso-scale unit cells combined with a MPP. They have been made using the parametric model Fig. 5.1 and modifying the parameters a_1, a_2 and a_3 allowing to keep the mass of the structure constant. All structures are made of ABS. Calculations have been performed for the frequency range [100, 6500] Hz.

This study is focused on the STL and the SAC of a MLRCS with a unit cell size large enough to not involve energy dissipation within the core and thus, to model the acoustic cavity using the Pressure Acoustics module. The size of the unit cell is defined by $L_x = 10$ mm and $L_y = 10$ mm. The thickness of the core is 0.3 mm while the thickness of the skins is 1 mm. The thickness of each layer is 2 mm. The perforation diameter is

1 mm. The configuration of each layer for the MLRCS is given by:

Table 5.2: Geometrical parameters of the meso-scale unit cell.

Layer	1	2	3	4	5	6	7	8	9
a_1	$3L_y/8$			$L_y/4$			$L_y/8$		
a_1	$L_y/8$			$L_y/4$			$3L_y/8$		

with $a_3 = L_x/4$ for all layers. In addition to the model made in Comsol Multiphysics, both structures (Fig. 5.4a and Fig. 5.4b) have been modelled using the extended method developed in Section 2.3.3 when there is no perforations on the upper skin. Results are shown in Fig. 5.5. As expected, only the mass law is obtained when the perforation is missing, and the SAC is null in all the frequency range of interest. In addition, the standard structure provides a higher STL at high frequencies compared to the MLRCS. Besides, when the MPP is used, the resonance frequency for both structures does not occur at the same frequency since it is at 1100 Hz for the standard structure whereas it is at 800 Hz for the MLRCS. The resonance frequency is observed at the same frequency for both the STL and the SAC. The peak is related to the combination of the MPP with the backed acoustic cavity. The expression of the resonance frequency is then given by:

$$f_0 = \frac{c_0}{2\pi}\sqrt{\frac{\sigma}{H(t_s + \delta_{tot})}}. \tag{5.7}$$

where $\delta_{tot} \simeq 8d/3\pi$, H is the height between of the core and σ is the perforation ratio with $\sigma = S/A$ in which A is the cross section of the acoustic cavity and S is the perforation surface. When this expression is applied for the standard structure, the calculation gives 1186 Hz and the resonance frequency is well predicted. In this case, the calculation of A is made on the surface depicted in Fig. 5.6a. Indeed, the fluid is travelling in the air volume corresponding to the acoustic cavity facing the perforation. On the opposite, in the case of the MLRCS, the resonance frequency is shifted at a lower frequency. This is explained by the expansion of the volume of the acoustic cavity (Fig. 5.6b). Therefore, the perforation ratio is reduced due to a higher area A and leads to a lower resonance frequency. The calculated resonance frequency for the MLRCS is thus 838 Hz which is near to the resonance frequency obtained with the FEM. Finally, a slight improvement of the MLRCS combined with the MPP is obtained at high frequencies compared to the same structures without perforations. Consequently, without altering the mass of the structure, it has been possible to shift the resonance at a lower frequency and thus, improve the acoustic efficiency at low frequencies.

In the case of perforations facing all the pores as illustrated in Fig. 5.1d, the same behavior for both structures is expected since the whole acoustic cavity created by the core geometry

will be filled by the acoustic fluid. Therefore, the advantage of MLRCS is missed, and it is not possible to shift the resonance frequency at low frequencies.

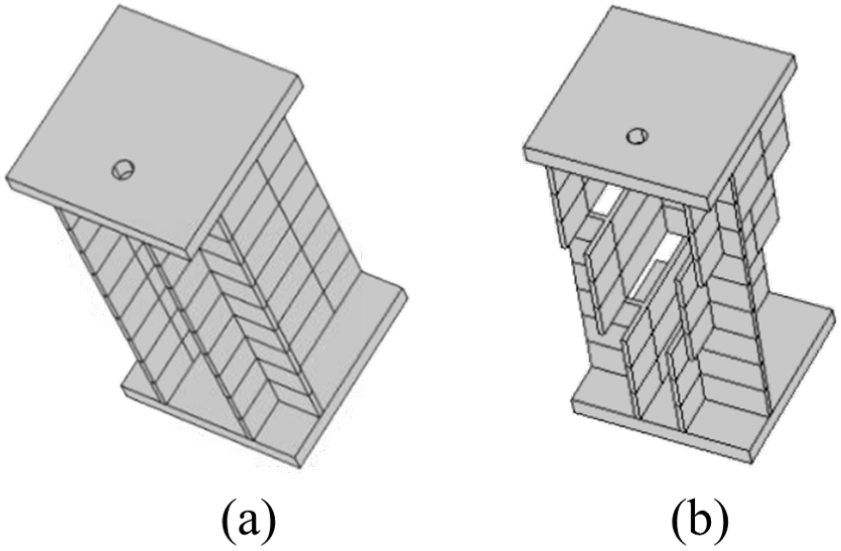

Figure 5.4: Meso-scale unit cells (a) standard (b) MLRCS.

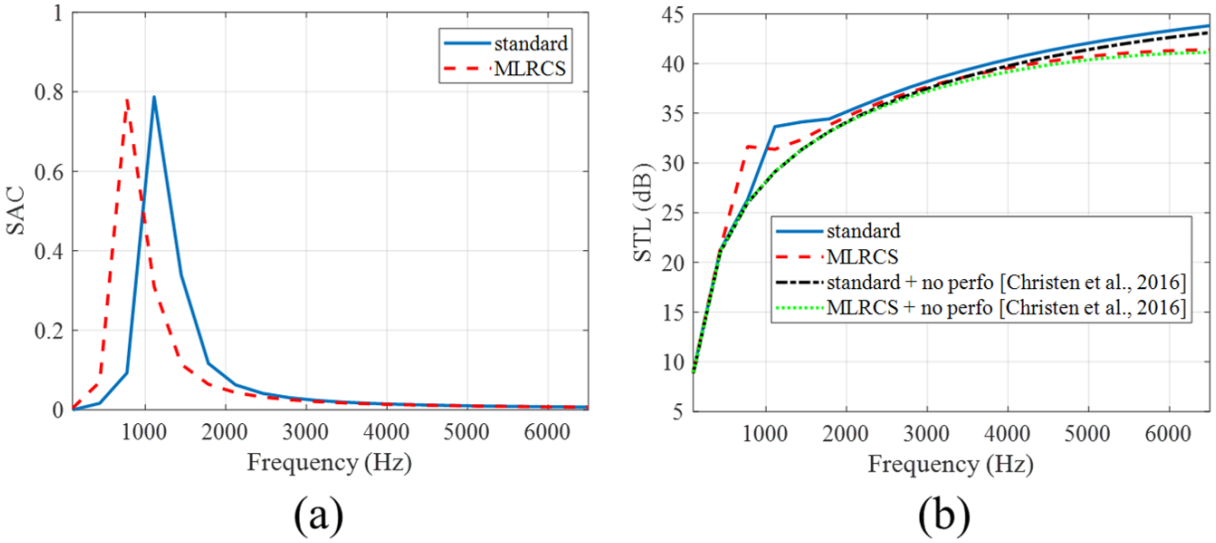

Figure 5.5: Comparison between the standard and the MLRCS with a meso-scale unit cell (a) SAC (b) STL.

5.4 Micro-scale unit cells

In this second study, the perforated skin configuration is illustrated in Fig. 5.1c. The size of the unit cell is $L_x = 2$ mm and $L_y = 4$ mm. The thickness of the core and the skins is 0.204 mm and 0.5 mm respectively. Each layer is 5 mm leading to a total of 45 mm for

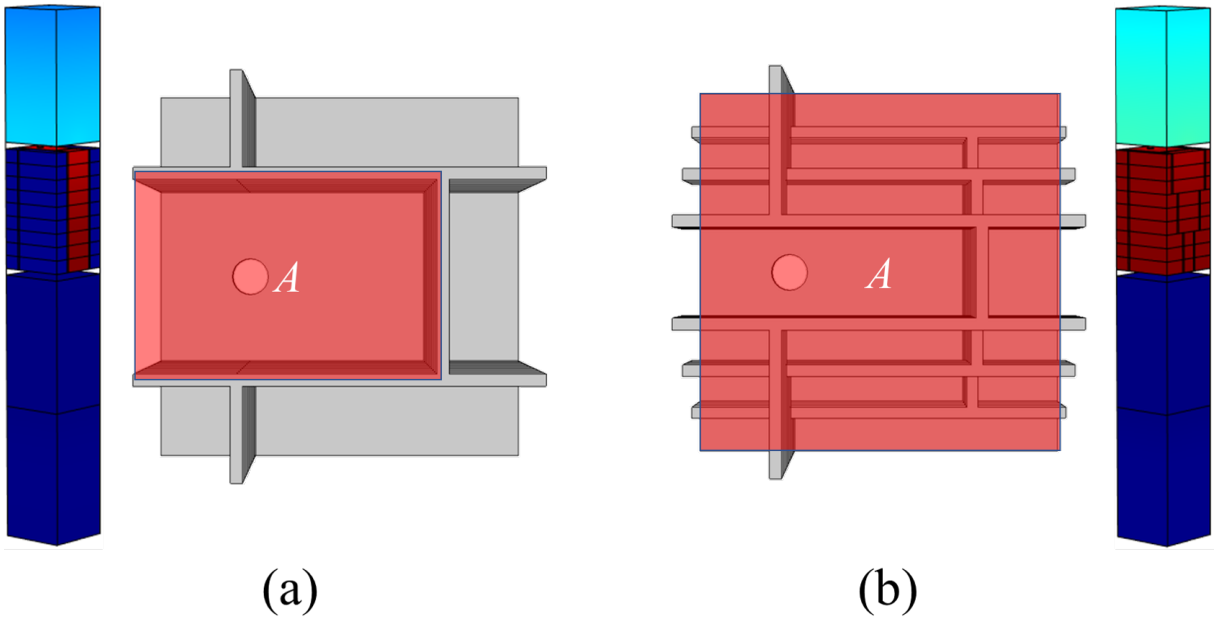

Figure 5.6: Acoustic cavity comparison between the (a) standard and (b) the MLRCS.

the height of the core. The perforation diameter is equal to 0.5 mm. The standard core is still defined by $a_1 = L_y/4$, $a_2 = L_y/4$ and $a_3 = L_x/4$.

5.4.1 MPP with 1 perforation

Two structures (Fig. 5.7) are investigated and compared to the standard case. The unit cell model has been implemented in Comsol Multiphysics using the Thermal-Acoustics module to model the fluid flow within the core as well as the perforation. The calculation has been performed for the SAC and the STL and are illustrated in Fig. 5.8.
A strong modification of the acoustic behavior is noticed between all configurations. The first peak of the SAC occurs at a lower frequency for both MLRCS. This later is mainly related to the perforation. However, the backed acoustic cavity interacts with the perforation leading to two different peaks for both MLRCS. Therefore, after 2500 Hz, it leads to two SAC peaks related to the backed acoustic cavity compared to the standard core in which only one peak is observed at 4500 Hz. MLRCS have the advantage to shift the absorption behavior at low frequencies. In addition, it is possible to obtain new SAC peaks at higher frequencies.
For the STL (Fig. 5.8b), the first peak is observed at a different frequency compared to the one of the SAC but leading to an improvement of the STL at low frequencies compared to the standard panel without perforation. Indeed, the first peak is slightly shifted at a lower frequency for the STL. This can be explained by the interaction of the acoustic cavity with the MPP and the solid part of the MLRCS. Moreover, after 2500 Hz, resonances are obtained allowing to strongly enhance the STL compared to the standard

panel without perforations modelled using the extended method described Section 2.3.3. Again, resonances do not correspond to the same frequency for the SAC and the STL. Both resonances are observed in the real and the imaginary part of the impedance surfaces of the MLRCS (Fig. 5.9). However, frequencies are still different to the ones obtained in the SAC and STL.
Finally, the SAC is improved at low frequencies for both MLRCS by adding one more resonance frequency. For the STL, acoustic performances are shifted at low frequencies for MLRCS and the STL is reduced for the 2^{nd} configuration compared to the standard case.

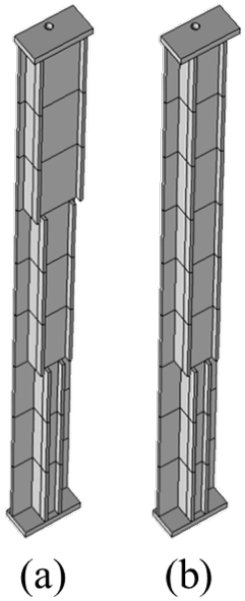

Figure 5.7: (a) Configuration 1 (b) Configuration 2.

5.4.2 Removed upper-skin and MPP of 2 perforations

In this last study, MLRCS are investigated considering two configurations: without the upper skin (WOUS) and with the MPP illustrated in Fig. 5.1d instead of an upper skin without perforations. For both structures all the backed acoustic cavity is crossed by the acoustic fluid. Three designs are used and depicted in Fig. 5.10. Two MLRCS are compared with the standard case (Fig. 5.10a). The value of the geometrical parameters a_1, a_2 and a_3 are given in Table 5.3. Concerning the third design (Fig. 5.10c), the second, fourth, sixth and eighth layer have been rotated with an angle of 180°. The main purpose is to modify the fluid flow within the core to increase the energy dissipation and thus, to improve the SAC.
By using the FEM of the unit cell for each configuration and solving the equations given in Section 1.5.3, the JCA parameters are retrieved and given as follows:

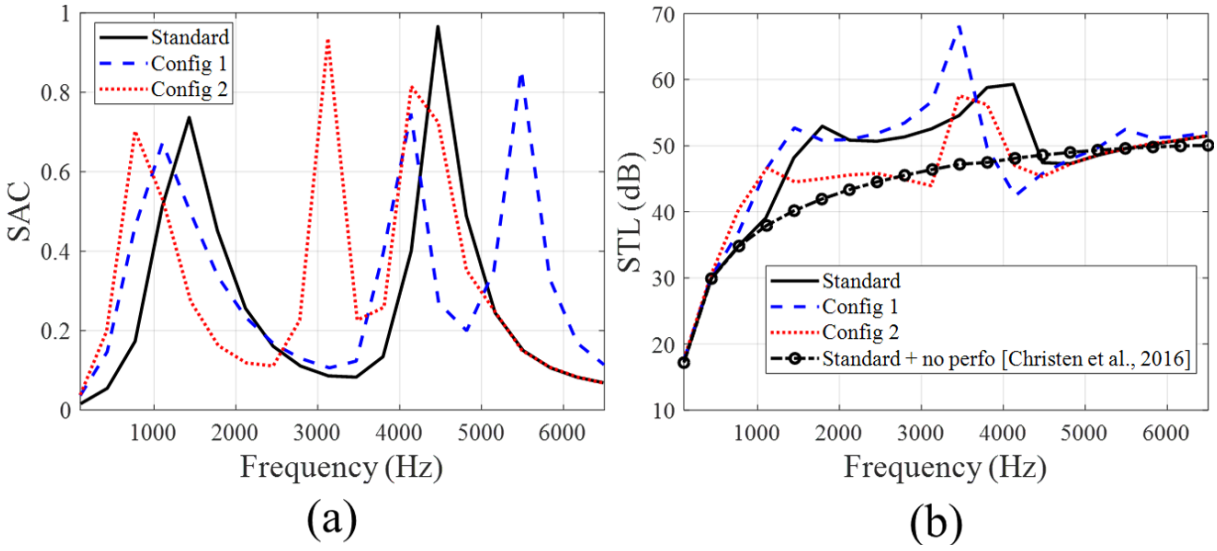

Figure 5.8: Comparison between the standard panel and both configurations for (a) the SAC and (b) the STL.

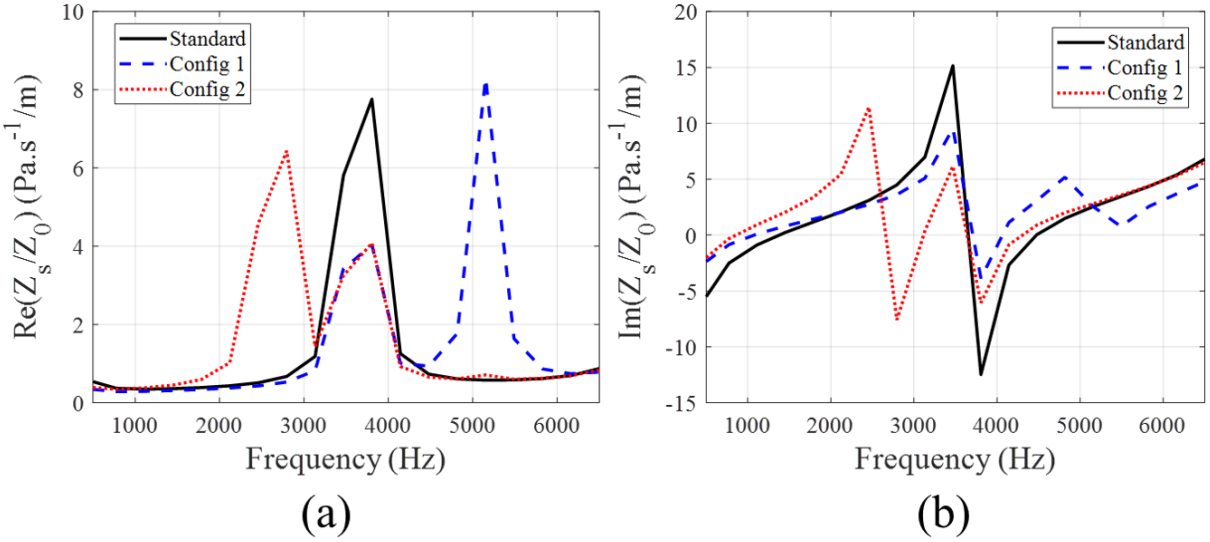

Figure 5.9: Comparison of the surfaces impedance between the standard panel and both configurations for (a) real part and (b) the imaginary part.

Table 5.3: Value of the geometrical parameters for the MLRCS.

Layer	1	2	3	4	5	6	7	8	9
a_1	$L_y/4$	$L_y/8$	$L_y/8$	$L_y/8$	$3L_y/8$	$L_y/8$	$3L_y/8$	$3L_y/8$	$L_y/4$
a_2	$L_y/4$	$L_y/8$	$L_y/8$	$L_y/4$	$L_y/8$	$L_y/4$	$3L_y/4$	$3L_y/8$	$L_y/4$
a_3	$L_x/4$	$L_x/8$	$3L_x/8$	$L_x/8$	$L_x/4$	$3L_x/8$	$3L_x/8$	$L_x/4$	$L_x/8$

The porosity is not modified since the volume of the solid and fluid domain are not altered. In addition, the tortuosity is the same for all configurations and remains equal to 1. However, all other parameters are changed. As expected, the fluid-solid surface

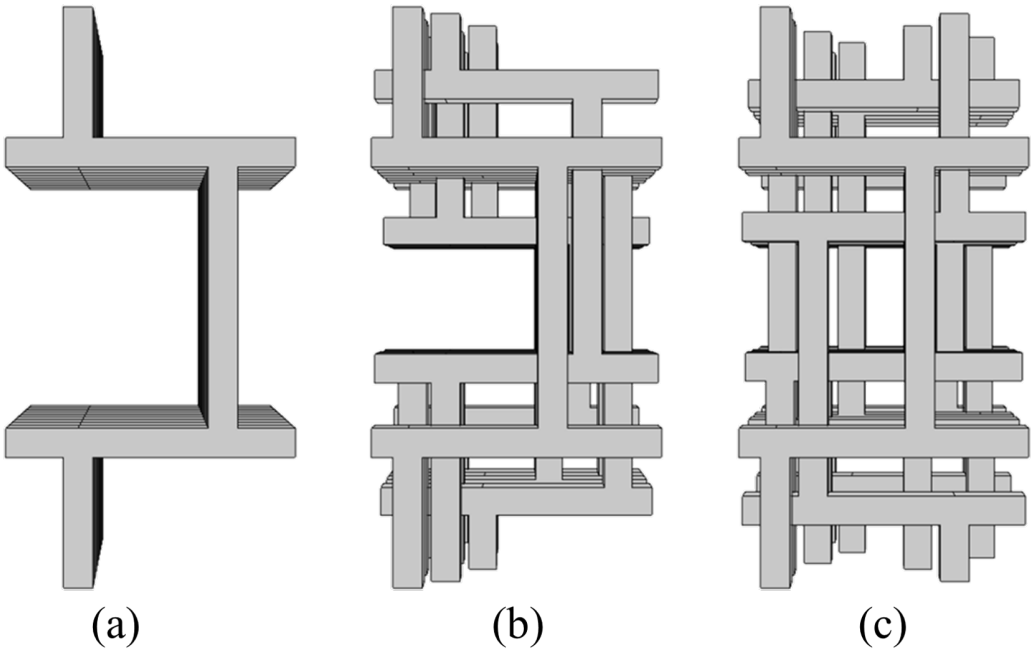

Figure 5.10: (a) Standard structure (b) MLRCS (c) MLRCS + rotations.

Table 5.4: Johnson-Champoux-Allard parameters in which permeabilities are expressed in $\cdot 10^{-8}$ m^2 and lengths in $\cdot 10^{-3}$ m.

JCA	φ	Λ_{therm}	Λ_{visc}	q_{therm}	q_{visc}	τ_∞
Standard	0.8064	898	898	9.141	9.021	1
MLRCS	0.8064	872.6	809.6	8.8315	7.071	1
Variations (%)	0	-2.8	-9.8	-3.4	-21.6	0
MLRCS+rot	0.8064	870	805.1	8.55	6.267	1
Variations (%)	0	-3.1	-10.3	-6.5	-30.5	0

is increased for the MLRCS, resulting in a decrease of the lengths and permeabilities. The viscous permeability is the most impacted parameter with a reduction reaching 30% when rotations are added. Therefore, the energy dissipation is expected to be higher for both configurations involving the MLRCS. The temperature (Fig. 5.11a)b)c)) and particle velocity (Fig. 5.11d)e)f)) for the standard structure does not include any distortion compared to the MLRCS and the fluid flow is not altered. In the case of MLRCS, different paths can be used by the acoustic fluid.

Finally, the SAC can be calculated using the JCA parameters (Fig. 5.12). The result for the standard structure is compared with the analytic formulation described by Allard et al. [20] modelling the acoustic cavity as a perforated panel with a square hole. A good agreement is obtained between both methods. However, such a model cannot be applied for MLRCS since the section area of the acoustic cavity is not constant. Besides, the MPP (Fig. 5.1d) has been added in the model using the formulations developed by Sgard

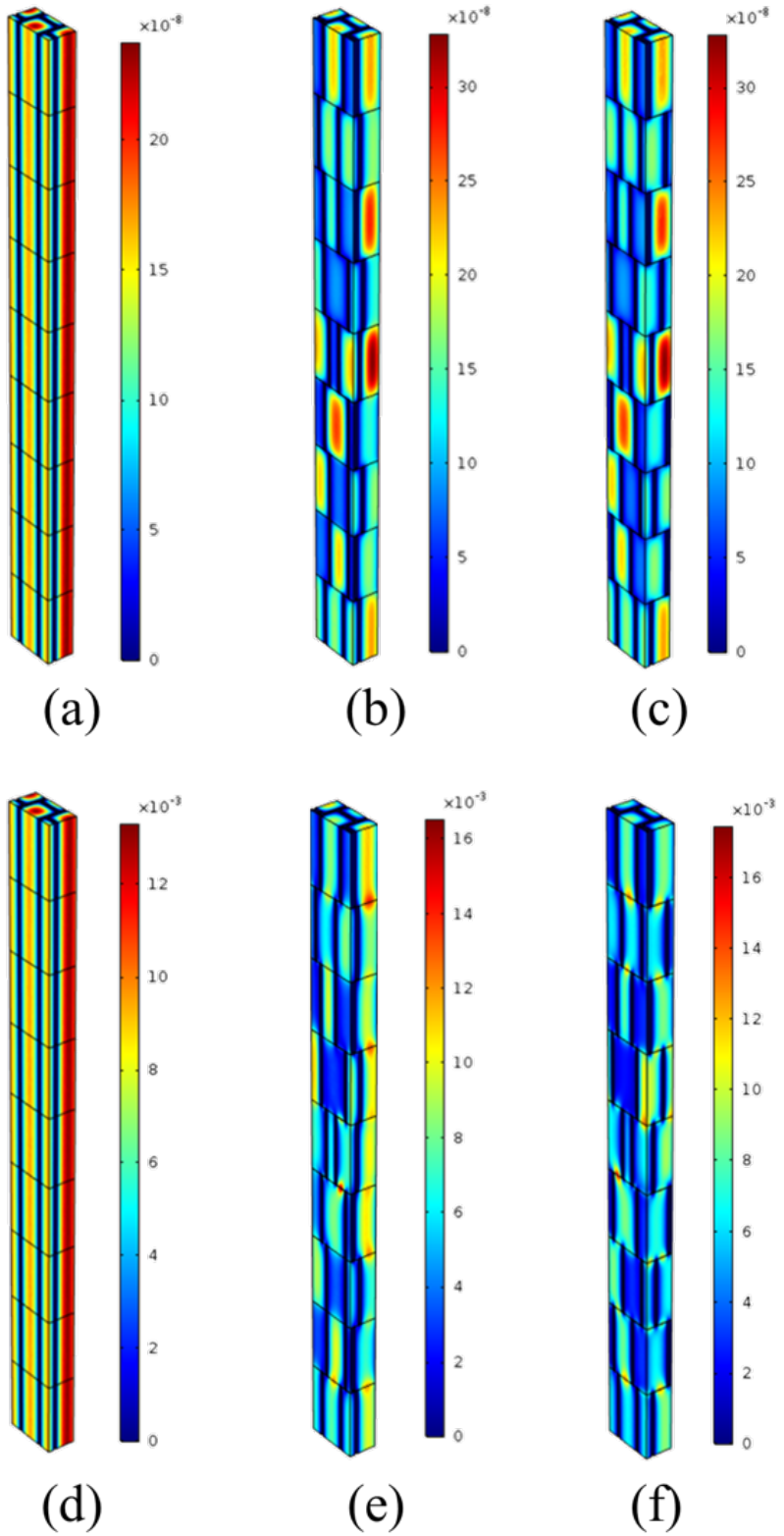

Figure 5.11: Comparison between all configurations concerning the temperature variation (a) Standard (b) MLRCS (c) MLRCS + rotations and the particle velocity (a) Standard (b) MLRCS (c) MLRCS + rotations.

et al. [155]. Indeed, it can be noticed that the MLRCS is governed by a porous media behavior in all the frequency range. Therefore, the JCA parameters lead to a dynamic tortuosity that can be used to calculate the SAC when it is front by a MPP.
A slight improvement of the SAC is obtained for both designs and configurations in all the frequency range of interest. In the case of the perforated upper skin, two resonance frequencies are observed.

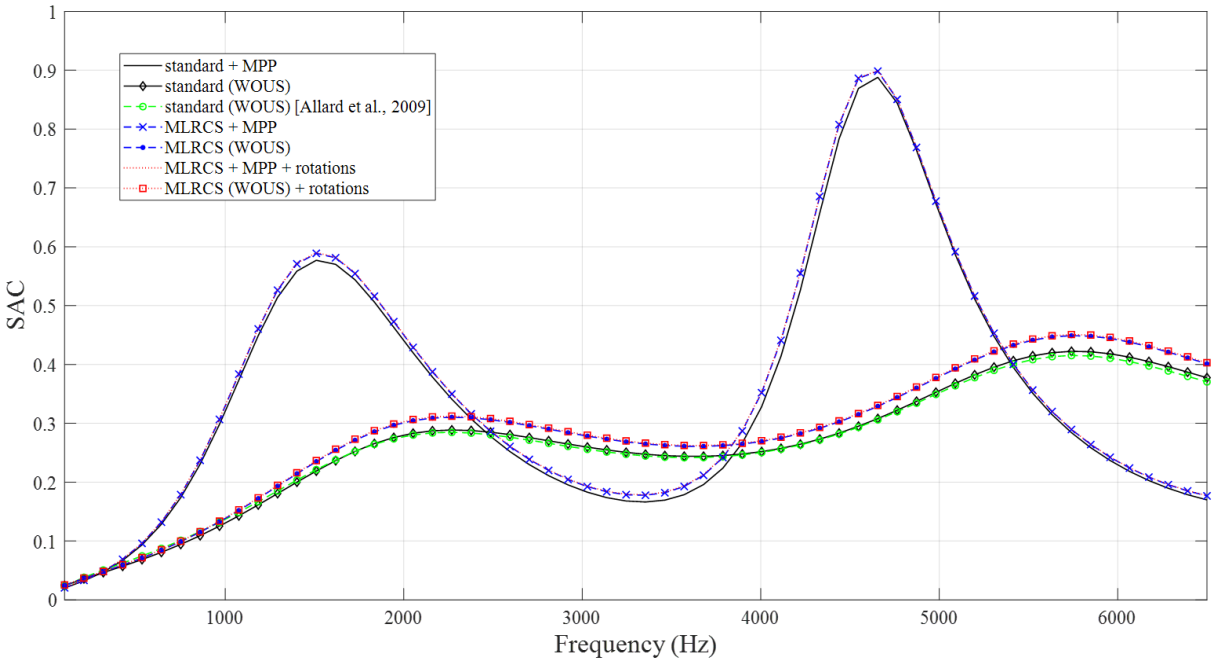

Figure 5.12: Comparison of the SAC between all configurations.

5.5 Conclusions

Most of the studies in the literature concerning honeycomb sandwich panels are focused on the STL without investigating the SAC. Therefore, this work could propose the analysis of both acoustic indicators at the same time, dealing with the solid and acoustic part, to show how MLRCS can be a great solution to improve the acoustic efficiency either at low or in a broadband frequency.
In this Chapter, MLRCS have been investigated in terms of SAC and STL. Three configurations have been studied considering structures with meso-scale and micro-scale unit cells, without upper skins or combined with a MPP with different perforation ratios.
The SAC and the STL have been improved using MLRCS. When meso-scale unit cells are used, the resonance frequency due to the MPP can be shifted at lower frequencies. Besides, micro-scale unit cells are considered and only 1 perforation is made on the upper skin, several resonance frequencies occur at high frequencies and the resonance frequency related to the perforation is still shifted at low frequencies. The SAC and the STL do

not behave in the same way since resonances do not occur at the same frequency. The MLRCS allows to improve the acoustic efficiency at low frequencies. When perforations are made in such a way that the fluid flow crosses all the core, MLRCS tend to behave as porous media, and by changing the core geometry, the JCA parameters can be modified and decreased to improve the SAC in a broadband frequency.
Finally, these results should be verified by experimental measurements using an impedance tube for medium and small samples. Moreover, a more complete parametric survey could be performed and an equivalent Helmholtz resonator model could be proposed to better explain the results when one perforation is made and combined with micro-scale unit cells.

Chapter 6

In-plane compression study of a multi-layer hexagonal core

Abstract

This work is focused on in-plane compression properties study of a multi-layer hexagonal core compared to a standard single hexagonal core. Structures are modelled considering plastic deformations. Obtained results are compared with an experimental measurement performed in the literature in which the structure was made using a 3D printer. The proposed design shows a great improvement of compression properties as well as a strong rigidity during the simulating compression test while the mass is maintained constant.

Contents

6.1 Introduction

Sandwich panels have been intensively studied in terms of mechanical and acoustic properties. They allow a high stiffness to weight ratio and are widely used for industrial applications. Advanced manufacturing processes such as 3D printing have led to wider design space possibilities and more proposed designs in the literature.
Out-of-plane compression properties have been improved by modifying the core geometry using regular hierarchical honeycombs [176] or a hybrid core combining a hexagonal and a corrugated core [177]. Besides, the in-plane compression of honeycomb panels is studied under dynamic loading [178] or investigating the effect of cell angles [179]. A similar numerical work has been carried out on auxetic honeycombs under dynamic crushing [180]. Different core geometries using Hex-Aux core shapes have been studied by Ingrole et al. [118] showing a high improvement of the rigidity under quasi-static compression taking the plastic deformation into account. This later paper is used to compare our results with their experimental measurements.
Multi-layer core systems have been investigated using their energy absorption capabilities under compression in the out-of-plane direction [165]. The impact of the number of layers to improve the energy absorption is investigated by Hou et al. [164] when the structure is under a blast loading. Besides, multi-layered corrugated cores separated by skins are modelled analytically for multiple mechanical properties using the Hamilton's principle [158, 160, 159]. Finally, multi-layer corrugated core systems without inner skins are modelled by finite element and compared with experimental measurements by Paczos et al. [161].
However, in-plane compression properties using multi-layer core topology systems haven't been studied yet. The main purpose of this Chapter is to compare a standard hexagonal core with a multi-layer hexagonal core under quasi-static compression loading. The plastic deformation is considered and both structures are modelled using a FEM with Ansys Workbench. Results are compared to an experimental measurement performed by Ingrole et al. [118] in which 3D printing is used to make the structure with ABS material. The values for the ABS are obtained by Dynamic Mechanical Analysis (DMA). Section 6.2 is focused on the description of the unit cells designs. Besides, Section 6.3 describes the FEM and the simulating test while Section 6.4 discusses about the obtained results. The work is concluded in Section 6.5.

6.2 Unit cells designs

The same standard hexagonal core proposed by Ingrol et al. [118] is used in this study and all geometrical parameters are given in the paper. Besides, a multi-layer hexagonal core is proposed in this thesis, by shifting a third of the core size in the direction x. Since

the thickness of the standard core is 60 mm, each layer of the proposed design is 20 mm. In addition, the shifting of the middle core is fixed at 4.5 mm. The unit cells designs as well as the used meshing are depicted in Fig. 6.1. Each layer of the proposed model are connected by contact areas. Contrary to the paper of Ingrole et al. [118], skins are modelled with a thickness of 1 mm. The shifting process allows to keep the mass constant.

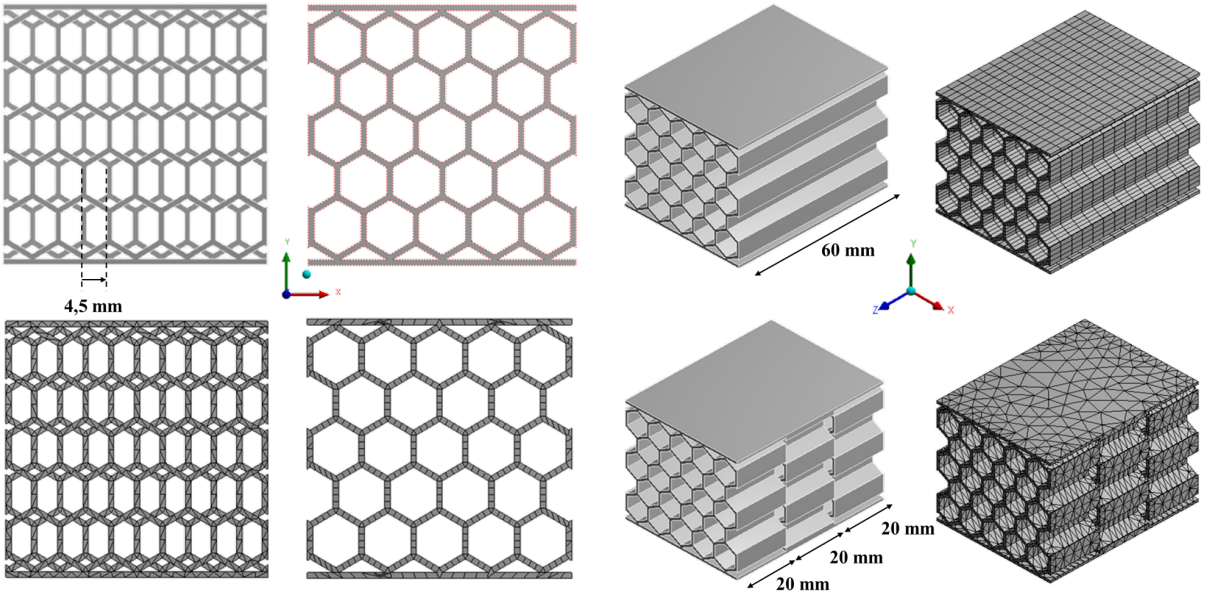

Figure 6.1: Unit cells designs and meshing.

6.3 Finite Element Model

The Finite Element Model (FEM) has been performed using Ansys Workbench. The ABS is used as the material of the structure and the material properties are listed in the following table:

Table 6.1: Material properties of the ABS.

Young Modulus	Density	Poisson's ratio	Yield Stress	Tangent Modulus
1.8 GPa	985 kg/m^3	0.35	31 MPa	36.84 MPa

The Tangent Modulus is calculated using the average value of the Elongation at Yield proposed in the following website (www.matweb.com). The bilinear isotropic hardening law is used to simulate the compression behavior of the structures. Therefore, the plastic deformation during the compression is taken into account.
Structures' meshing are given by the software leading to cubic solid elements for the standard structure while the proposed design is meshed using tetrahedral solid elements. All dofs of the bottom area of the bottom skin are blocked. The top area of the top skin

is fixed in the direction x and z but loaded by a quasi-static compression at the speed of 2 mm/min. The simulation is made for 370 steps between 0 and 900 s.

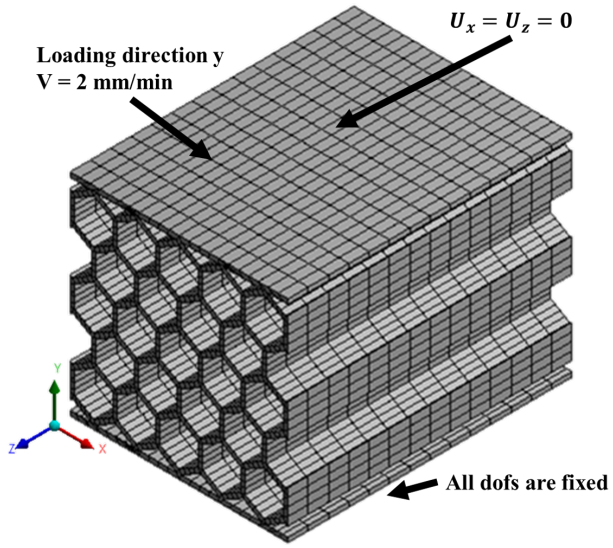

Figure 6.2: Simulated compression test using the FEM.

6.4 Results

Results are obtained in terms of strain-stress law (Fig. 6.3) and deformed shapes of both structures are illustrated at the 260^{th} s of the simulated test (Fig. 6.4). The absorbed energy is calculated using the Eq. (6.1) and the Young Modulus, the compression strength as well as the calculated total absorbed energy are given in Table 6.2.

$$W = \int_0^{\epsilon} \sigma(\epsilon) d\epsilon. \tag{6.1}$$

The compression behavior obtained for the standard hexagonal core and using the proposed FEM with the material properties retrieved by DMA shows a better agreement with the experimental measurement performed by Ingrole et al. [118]. The compression behavior begins with a linear part of the stress-strain region followed by a drop due to the collapse of the third hexagonal core line (Fig. 6.4) which then leads to a second increase related to the densification of the structure. The second drop is obtained when all hexagonal cells except the top and bottom line are collapsed with a second densification and another increase of the nominal stress. The same kind of behavior is obtained for the standard hexagonal core modelled by FEM but occurring when the strain reaches 0.3. Moreover, similar values of the Young Modulus are obtained between the FEM and the experimental measurement (42.1 MPa). This later is slightly changed compared to the paper [118] since the small shift occurring at the beginning of the measurement is taken

into account in this case.

Besides, the proposed multi-layer hexagonal core shows a strong improvement of the compression behavior. The Young Modulus calculated in the linear part of the strain-stress region is drastically enhanced as well as the compression strength. Besides, the proposed design allows a better absorption of the compression loading. The collapse behavior is not observed and a stagnation of the stress occurs after the linear stress-strain region. The proposed design leads to a better stability of the core (Fig. 6.4). Indeed, the middle layer maintains the deformation of both other layers thanks to the contact areas between them. Such improvements have been obtained without added mass.

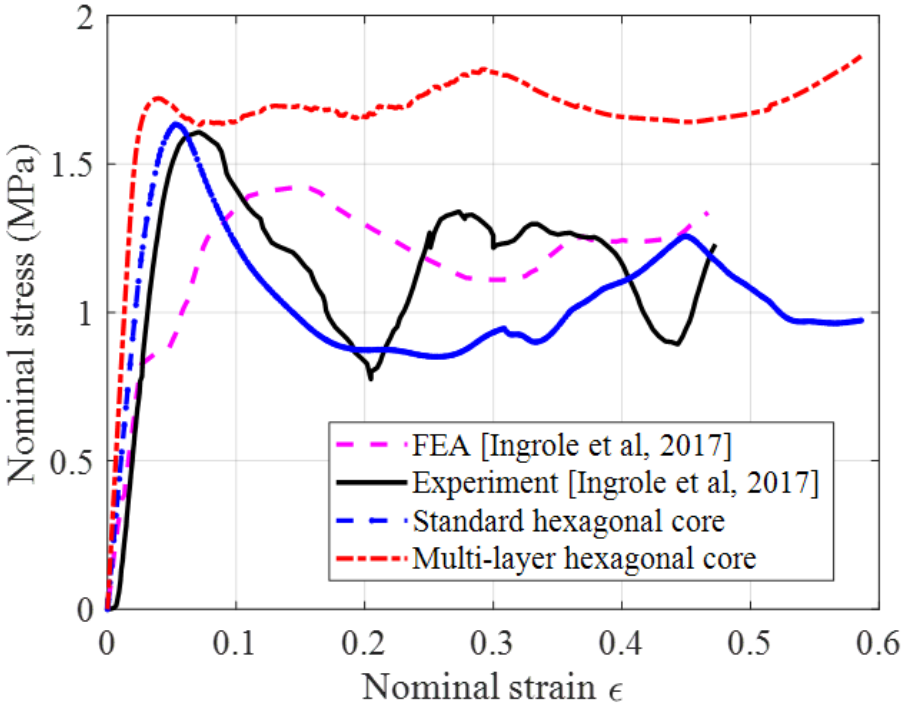

Figure 6.3: Stress-Strain results.

Table 6.2: Comparison of the in-plane properties between the standard and the multi-layer core structure.

	Young Modulus (MPa)	Compression Strength (MPa)	Energy absorbed (J)
Standard	45.9	1.6	$6{\cdot}10^5$
Multi-layer	75.5	1.9	$10{\cdot}10^5$

6.5 Conclusions

The main purpose of this Chapter is to study the in-plane compression properties of a multi-layer hexagonal core compared to a standard single hexagonal core when plastic

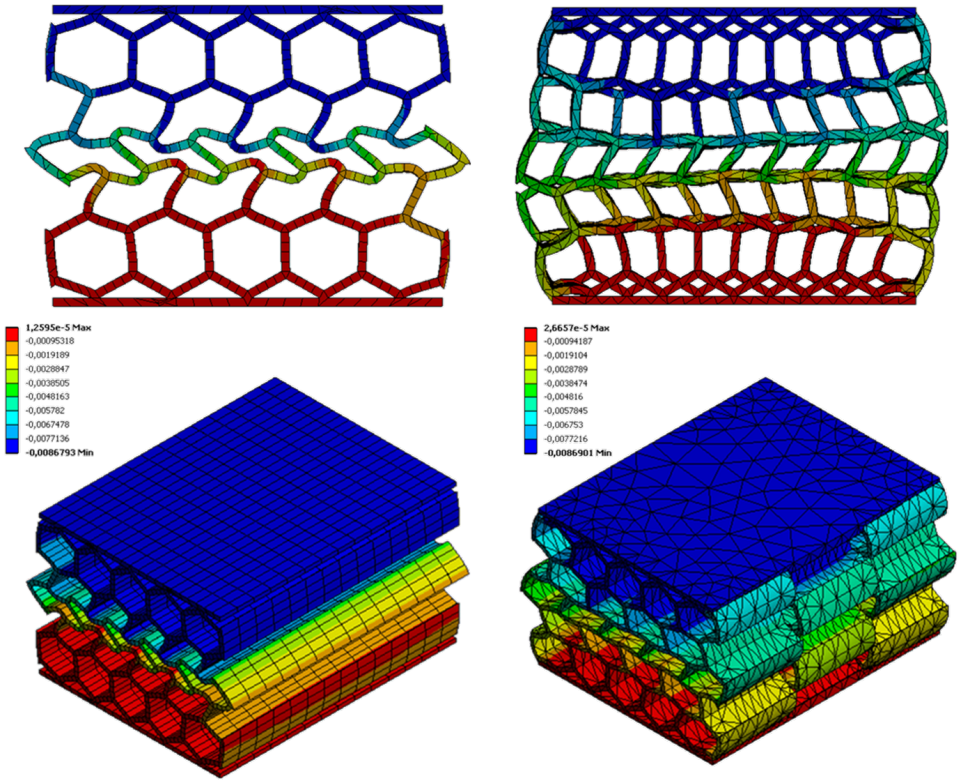

Figure 6.4: Unit cells deformations at 260 s under in-plane compression.

deformations are considered. Both structures have been modelled by FEM using Ansys Workbench. Results have been compared to an experimental measurement performed by Ingrole et al. [118]. Different material properties are used for the ABS compared to the ones used by Ingrole et al.

A good agreement of the FEM and the experimental measurement is obtained. The multi-layer hexagonal core exhibits a strong improvement of the compression properties while the mass is maintained constant. It remains stable and no collapses are observed. After the linear strain-stress region, the stress is slightly altered but remains globally constant. Although, the out-of-plane compression properties are reduced, such structures open new perspectives for obtaining high mechanical performances especially under in-plane compression loading. 3D printing can be used to make those structures and the geometrical parameters can be modified to investigate their impacts on the compression properties.

Chapter 7

Conclusions and Perspectives

7.1 Conclusions

The main purpose of this thesis work is to investigate the multi-scale vibroacoustic behavior of MLCTS in a broadband frequency using the PST and by performing a design space study while the mass is kept constant.

- A introduction to MLCTS has been proposed to describe the main issues related to the core geometry to apply the PST and the WFEM since new geometrical parameters are involved. In addition, MLCTS offer the possibility to compare a large number of configurations keeping the mass constant.

- Two models have been applied to calculate the STL. The first was described in the literature and combines the WFEM and the TMM to drastically reduce the computational cost. The second uses the principle of nodal surfaces calculations and has been extended in this thesis to be applied on more complex structures. The CMS applied to sound transmission problems has been used to reduce the computational cost of both models. The extended method has been experimentally validated on standard structures made of a single core and manufactured using a 3D printer.

- Several parametric surveys on MLRCS allowed to show their ability to modify the vibroacoustic behavior such as the transition frequencies and the STL. The critical frequency has been shifted to a higher frequency allowing to strongly enhance the STL in a broadband frequency. This is due to a lower dynamic rigidity since flexural wavenumbers of MLRCS are higher than standard structures. Besides, transition frequencies have been shifted to lower frequencies. However, it is possible to control the transition frequency regions corresponding to the trigger of different dynamic behaviors (shear, bending, ...) by modifying the core geometry. In the aerospace

industry, it is preferable to shift the first transition frequency at higher frequencies. Therefore, it has been possible to limit the decrease of the first transition frequency compared to the standard structure while having a high improvement of the STL when the shift is performed in the direction y. The enhancement could be provided while the mass has been maintained constant.

- Internal resonances as well as the veering effect which couples the shear and flexural waves have been obtained for MLRCS, when the skins and the core are made of the same material. The veering effect allows to strongly improve the STL in the critical frequency region. Its impact on the STL can be compared to add-on resonators without their drawbacks since the STL peak is not followed or precede on a drop and no mass is added on the structure. This dynamic behavior is mainly related to the conversion of flexural waves into shear waves of the skins with the internal resonance of both middle layers. The parametric analysis shows that the frequency in which the veering effect occurs can be modified depending on the core geometry and a stronger or weaker coupling can be obtained.

- An optimisation allowed to obtain the best core design for the middle layer when the MLRCS is made of 3 honeycomb cores layers. In addition, the design space has been explored to study the influence of the geometrical parameters on the STL as well as the static compression and shear modulus. An algorithm has been developed to compare a huge amount of designs having the same mass. A high improvement of the STL is still obtained for both optimized structures but leading to lower mechanical properties mainly due to the nature of the interfaces between layers made by contact areas.

- A model made using Comsol Multiphysiscs and considering the thermal-viscous effect as well as an equivalent fluid model using the JCA parameters are used to show the acoustic efficiency of MLRCS for both, the STL and the SAC, at low and in a broadband frequency. This study is performed for normal incidence acoustic waves. It is possible to modify the core geometry to target some specific frequencies in which the SAC and the STL can be improved. For micro-scale unit cells, resonance frequencies observed for the SAC and the STL are not the same. The core geometry turns out the possibility to alter the JCA parameters to explain the acoustic behavior of MLRCS. In this case, most of the parameters are reduced compared to the standard case since the solid-fluid interface is increased for MLRCS.

- Finally, high improvements of the in-plane compression properties using multi-layer core designs are obtained compared to standard single core structures while keeping the mass constant.

7.2 Perspectives

Based on the thesis work and the conclusions, future works can be carried out to enhance the vibroacoustic investigation of MLCTS:

- This thesis work is based on a parametric model that could be modified to explore other design spaces and thus, other geometrical parameters. Moreover, rotations between layers need to be investigated in depth, however, the structure should be modelled entirely by FEM and then leads to high computational cost.
- In the case of MLCTS involving high rigid skins compared to the core (ex: Aluminium + ABS), it is interesting to study the analytic solution of the 6^{th} order of the equation of motion to retrieve the flexural wavenumbers for the first and second transition frequency region and thus, simplify the identification of the dynamic behaviors occurring in MLCTS.
- The impact of the veering on the structural damping of MLRCS can be investigated. Besides, the optimisation can be performed with less constrains in the proposed parametric model to study a wider design space. In addition, since a large number of configurations needs to be explored, data mining can be used to analyse all the data to find a simplified model between the geometrical parameters and the output results (STL, compression and shear modulus).
- In Chapter 5, the study can be extended to oblique incidence acoustic waves and diffuse acoustic fields.
- Experimental measurements using the Beta Cabin should be performed on MLCTS which can be made using a 3D printer to verify the improvement in terms of STL and the appearance of the veering effect compared to standard structures made of a single core. The parametric survey and the optimisation could be thus validated. In the same way, measurements can be performed for the STL and the SAC under normal incidence acoustic waves using a medium and small impedance tube.
- The influence of the geometrical parameters on the in-plane compression properties can be studied and experimental validations can be conducted.

Publications

International Journals

F. Errico, G. Tufano, O. Robin, **N. Guenfoud**, M. Ichchou, N. Atalla, Simulating the sound transmission loss of complex curved panels with attached noise control materials using periodic cell wavemodes, Applied Acoustics 156 (2019),pp 21–28. (2019). 10.1016/j.apacoust.2019.06.027.

Accepted paper:

N. Guenfoud, C. Droz, M.N. Ichchou, O. Bareille, E. Deckers, W. Desmet, On the multi-scale vibroacoustic behavior of multi-layer rectangular core topology systems, Mechanical Systems and Signal Processing.

International Conferences:

N. Guenfoud, M. Ichchou, O. Bareille, W. Desmet, B. Pluymers, Multi-layer core topology systems. Proceeding of MEDYNA 2017: 2nd Euro-Mediterranean Conference on Structural Dynamics and Vibroacoustics (2017). https://medyna2017.sciencesconf.org/data/Medyna_2017_Proceedings.pdf

N. Guenfoud, M. Ichchou, O. Bareille, W. Desmet, B. Pluymers, Modeling and experimental measurements of the sound transmission loss for multi-layer core topology systems. Proceedings of ISMA 2018 - International Conference on Noise and Vibration Engineering, (2018) 4653-4662. http://past.isma-isaac.be/downloads/isma2018/proceedings/Proceedings_ISMA-USD2018.pdf

N. Guenfoud, M. Ichchou, O. Bareille, E. Deckers, W. Desmet, Parametric analysis of a triple core periodic unit cell including a middle random core. Proceeding of the 9th Eccomas Thematic Conference on Smart Structures and Materials (2019). https://congress.cimne.com/smart2019/frontal/doc/EbookSMART2019.pdf

Bibliography

[1] T. Münzel, F. P. Schmidt, S. Steven, J. Herzog, A. Daiber, M. Sørensen, Environmental noise and the cardiovascular system, Journal of the American College of Cardiology 71 (6) (2018) 688–697 (2018). doi:10.1016/j.jacc.2017.12.015.

[2] J.-M. Berthelot, Composite materials. Mechanical behavior and structural analysis, New-York: Springer, 1999 (1999).

[3] S. B. Dong, F. K. W. Tso, On a Laminated Orthotropic Shell Theory Including Transverse Shear Deformation, Journal of Applied Mechanics 39 (4) (1972) 1091–1097 (1972). doi:10.1115/1.3422834.

[4] L. Guillaumie, Vibroacoustic flexural properties of symmetric honeycomb sandwich panels with composite faces, Journal of Sound and Vibration 343 (2015) 71–103 (2015). doi:10.1016/j.jsv.2014.12.026.

[5] R. Pendleton, M. Tuttle, Manual on experimental methods for mechanical testing of composites, Springer Science & Business Media, 2012 (2012).

[6] C. Casavola, A. Cazzato, V. Moramarco, C. Pappalettere, Orthotropic mechanical properties of fused deposition modelling parts described by classical laminate theory, Materials & Design 90 (2016) 453–458 (2016). doi:10.1016/j.matdes.2015.11.009.

[7] M. Somireddy, A. Czekanski, Mechanical characterization of additively manufactured parts by fe modeling of mesostructure, Journal of Manufacturing and Materials Processing 1 (2) (2017) 18 (2017). doi:10.3390/jmmp1020018.

[8] M. Somireddy, A. Czekanski, C. V. Singh, Development of constitutive material model of 3d printed structure via fdm, Materials Today Communications 15 (2018) 143–152 (2018). doi:10.1016/j.mtcomm.2018.03.004.

[9] C. Roque, P. Martins, Maximization of fundamental frequency of layered composites using differential evolution optimization, Composite Structures 183 (2018) 77–83 (2018). doi:10.1016/j.compstruct.2017.01.037.

[10] J. N. Reddy, Mechanics of laminated composite plates and shells: theory and analysis, CRC press, 2004 (2004).

[11] R. Ganguli, Optimal design of composite structures: a historical review, Journal of the Indian Institute of Science 93 (4) (2013) 557–570 (2013).

[12] R. F. Gibson, A review of recent research on mechanics of multifunctional composite materials and structures, Composite Structures 92 (12) (2010) 2793–2810 (2010). doi:10.1016/j.compstruct.2010.05.003.

[13] A. Mouritz, E. Gellert, P. Burchill, K. Challis, Review of advanced composite structures for naval ships and submarines, Composite Structures 53 (1) (2001) 21–42 (2001). doi:10.1016/S0263-8223(00)00175-6.

[14] X. Huang, Y. Zhao, H. Wang, H. Qin, D. Wen, W. Zhou, Investigation of transport property of fibrous media: 3d virtual modeling and permeability calculation, Engineering with Computers 33 (4) (2017) 997–1005 (2017). doi:10.1007/s00366-017-0511-4.

[15] M. Swift, P. Bris, K. Horoshenkov, Acoustic absorption in re-cycled rubber granulate, Applied Acoustics 57 (3) (1999) 203–212 (1999). doi:10.1016/S0003-682X(98)00061-9.

[16] F. Han, G. Seiffert, Y. Zhao, B. Gibbs, Acoustic absorption behaviour of an open-celled aluminium foam, Journal of Physics D: Applied Physics 36 (3) (2003) 294–302 (2003). doi:10.1088/0022-3727/36/3/312.

[17] M. A. Biot, Theory of propagation of elastic waves in a fluid-saturated porous solid. i. low-frequency range, The Journal of the Acoustical Society of America 28 (2) (1956) 168–178 (1956). doi:10.1121/1.1908239.

[18] M. A. Biot, Theory of propagation of elastic waves in a fluid-saturated porous solid. ii. higher frequency range, The Journal of the Acoustical Society of America 28 (2) (1956) 179–191 (1956). doi:10.1121/1.1908241.

[19] K. Attenborough, Acoustical characteristics of porous materials, Physics Reports 82 (3) (1982) 179–227 (1982). doi:10.1016/0370-1573(82)90131-4.

[20] J. Allard, N. Atalla, Propagation of sound in porous media: modelling sound absorbing materials 2e, John Wiley & Sons, 2009 (2009).

[21] B. Brouard, D. Lafarge, J.-F. Allard, A general method of modelling sound propagation in layered media, Journal of Sound and Vibration 183 (1) (1995) 129–142 (1995). doi:10.1006/jsvi.1995.0243.

[22] Q. Serra, M. Ichchou, J.-F. Deü, Wave properties in poroelastic media using a wave finite element method, Journal of Sound and Vibration 335 (2015) 125–146 (2015). doi:10.1016/j.jsv.2014.09.022.

[23] Q. Serra, M. N. Ichchou, J.-F. Deü, On the use of transfer approaches to predict the vibroacoustic response of poroelastic media, Journal of Computational Acoustics 24 (02) (2016) 1550020 (2016). doi:10.1142/S0218396X15500204.

[24] M. Delany, E. Bazley, Acoustical properties of fibrous absorbent materials, Applied Acoustics 3 (2) (1970) 105–116 (1970). doi:10.1016/0003-682X(70)90031-9.

[25] Y. Miki, Acoustical properties of porous materials-generalizations of empirical models-, Journal of the Acoustical Society of Japan (E) 11 (1) (1990) 25–28 (1990). doi:10.1250/ast.11.25.

[26] Y. Miki, Acoustical properties of porous materials-modifications of delany-bazley models-, Journal of the Acoustical Society of Japan (E) 11 (1) (1990) 19–24 (1990). doi:10.1250/ast.11.19.

[27] R. Panneton, X. Olny, Acoustical determination of the parameters governing viscous dissipation in porous media, The Journal of the Acoustical Society of America 119 (4) (2006) 2027–2040 (2006). doi:10.1121/1.2169923.

[28] E. Gros, R. Panneton, A missing mass method to measure the open porosity of porous solids, Canadian Acoustics 32 (3) (2004) 20–21 (2004).

[29] O. Doutres, Y. Salissou, N. Atalla, R. Panneton, Evaluation of the acoustic and non-acoustic properties of sound absorbing materials using a three-microphone impedance tube, Applied Acoustics 71 (6) (2010) 506–509 (2010). doi:10.1016/j.apacoust.2010.01.007.

[30] Y. Atalla, R. Panneton, Inverse acoustical characterization of open cell porous media using impedance tube measurements, Canadian Acoustics 33 (1) (2005) 11–24 (2005).

[31] C.-N. Wang, J.-H. Torng, Experimental study of the absorption characteristics of some porous fibrous materials, Applied Acoustics 62 (4) (2001) 447–459 (2001). doi:10.1016/S0003-682X(00)00043-8.

[32] F. Sgard, X. Olny, N. Atalla, F. Castel, On the use of perforations to improve the sound absorption of porous materials, Applied Acoustics 66 (6) (2005) 625–651, innovative Applications of Materials for Acoustic Purposes (2005). doi:10.1016/j.apacoust.2004.09.008.

[33] N. Atalla, R. Panneton, F. Sgard, X. Olny, Acoustic absorption of macro-perforated porous materials, Journal of Sound and Vibration 243 (4) (2001) 659–678 (2001). doi:10.1006/jsvi.2000.3435.

[34] T. Weisser, J.-P. Groby, O. Dazel, F. Gaultier, E. Deckers, S. Futatsugi, L. Monteiro, Acoustic behavior of a rigidly backed poroelastic layer with periodic resonant inclusions by a multiple scattering approach, The Journal of the Acoustical Society of America 139 (2) (2016) 617–629 (2016). doi:10.1121/1.4940669.

[35] M. H. Fouladi, M. J. M. Nor, M. Ayub, Z. A. Leman, Utilization of coir fiber in multilayer acoustic absorption panel, Applied Acoustics 71 (3) (2010) 241–249 (2010). doi:10.1016/j.apacoust.2009.09.003.

[36] O. Doutres, N. Atalla, Experimental estimation of the transmission loss contributions of a sound package placed in a double wall structure, Applied Acoustics 72 (6) (2011) 372–379 (2011). doi:10.1016/j.apacoust.2010.12.011.

[37] O. Doutres, N. Atalla, Acoustic contributions of a sound absorbing blanket placed in a double panel structure: Absorption versus transmission, The Journal of the Acoustical Society of America 128 (2) (2010) 664–671 (2010). doi:10.1121/1.3458845.

[38] O. T. Thomsen, E. Bozhevolnaya, A. Lyckegaard, Sandwich Structures 7: Advancing with Sandwich Structures and Materials: Proceedings of the 7th International Conference on Sandwich Structures, Springer Science & Business Media, 2006 (2006).

[39] Q. Kepeng, Analysis and optimal design of lightweight sandwich structures and materials, Ph.D. thesis, Université de Franche-Comté (2008).

[40] M. Arunkumar, J. Pitchaimani, K. Gangadharan, M. L. Babu, Influence of nature of core on vibro acoustic behavior of sandwich aerospace structures, Aerospace Science and Technology 56 (2016) 155–167 (2016). doi:10.1016/j.ast.2016.07.009.

[41] C. Barton, J. Mixson, Noise transmission and control for a light twin-engine aircraft, Journal of Aircraft 18 (7) (1981) 570–575 (1981). doi:10.2514/3.57528.

[42] F. W. Grosveld, J. S. Mixson, Noise transmission through an acoustically treated and honeycomb-stiffened aircraft sidewall, Journal of Aircraft 22 (5) (1985) 434–440 (1985). doi:10.2514/3.45143.

[43] C. L. Dym, M. A. Lang, Transmission of sound through sandwich panels, The Journal of the Acoustical Society of America 56 (5) (1974) 1523–1532 (1974). doi:10.1121/1.1903474.

[44] C. L. Dym, C. S. Ventres, M. A. Lang, Transmission of sound through sandwich panels: A reconsideration, The Journal of the Acoustical Society of America 59 (2) (1976) 364–367 (1976). doi:10.1121/1.380871.

[45] M. A. Lang, C. L. Dym, Optimal acoustic design of sandwich panels, The Journal of the Acoustical Society of America 57 (6) (1975) 1481–1487 (1975). doi:10.1121/1.380588.

[46] J. A. Moore, R. H. Lyon, Sound transmission loss characteristics of sandwich panel constructions, The Journal of the Acoustical Society of America 89 (2) (1991) 777–791 (1991). doi:10.1121/1.1894638.

[47] N. Buannic, P. Cartraud, T. Quesnel, Homogenization of corrugated core sandwich panels, Composite Structures 59 (3) (2003) 299–312 (2003). doi:10.1016/S0263-8223(02)00246-5.

[48] A. Catapano, M. Montemurro, A multi-scale approach for the optimum design of sandwich plates with honeycomb core. part i: homogenisation of core properties, Composite Structures 118 (2014) 664–676 (2014). doi:10.1016/j.compstruct.2014.07.057.

[49] A. Catapano, M. Montemurro, A multi-scale approach for the optimum design of sandwich plates with honeycomb core. part ii: the optimisation strategy, Composite Structures 118 (2014) 677–690 (2014). doi:10.1016/j.compstruct.2014.07.058.

[50] S. Malek, L. Gibson, Effective elastic properties of periodic hexagonal honeycombs, Mechanics of Materials 91 (2015) 226–240 (2015). doi:10.1016/j.mechmat.2015.07.008.

[51] A. Wada, T. Kawasaki, Y. Minoda, A. Kataoka, S. Tashiro, H. Fukuda, A method to measure shearing modulus of the foamed core for sandwich plates, Composite Structures 60 (4) (2003) 385–390 (2003). doi:10.1016/S0263-8223(03)00041-2.

[52] A. Abbadi, Y. Koutsawa, A. Carmasol, S. Belouettar, Z. Azari, Experimental and numerical characterization of honeycomb sandwich composite panels, Simulation Modelling Practice and Theory 17 (10) (2009) 1533–1547 (2009). doi:10.1016/j.simpat.2009.05.008.

[53] D. Chen, Bending deformation of honeycomb consisting of regular hexagonal cells, Composite Structures 93 (2) (2011) 736–746 (2011). doi:10.1016/j.compstruct.2010.08.006.

[54] E. Nilsson, A. Nilsson, Prediction and measurement of some dynamic properties of sandwich structures with honeycomb and foam cores, Journal of Sound and Vibration 251 (3) (2002) 409–430 (2002). doi:10.1006/jsvi.2001.4007.

[55] L. Liu, K. Bhattacharya, Wave propagation in a sandwich structure, International Journal of Solids and Structures 46 (17) (2009) 3290–3300 (2009). doi:10.1016/j.ijsolstr.2009.04.023.

[56] M. I. Hussein, M. J. Leamy, M. Ruzzene, Dynamics of Phononic Materials and Structures: Historical Origins, Recent Progress, and Future Outlook, Applied Mechanics Reviews 66 (4) (2014). doi:10.1115/1.4026911.

[57] D. Mead, A general theory of harmonic wave propagation in linear periodic systems with multiple coupling, Journal of Sound and Vibration 27 (2) (1973) 235–260 (1973). doi:10.1016/0022-460X(73)90064-3.

[58] L. Brillouin, Wave propagation in periodic structures, Dover Publications Inc., 1946 (1946).

[59] B. R. Mace, D. Duhamel, M. J. Brennan, L. Hinke, Finite element prediction of wave motion in structural waveguides, The Journal of the Acoustical Society of America 117 (5) (2005) 2835–2843 (2005). doi:10.1121/1.1887126.

[60] D. Duhamel, B. Mace, M. Brennan, Finite element analysis of the vibrations of waveguides and periodic structures, Journal of Sound and Vibration 294 (1) (2006) 205–220 (2006). doi:10.1016/j.jsv.2005.11.014.

[61] R. Hintz, Analytical methods in component modal synthesis, AIAA Journal 13 (8) (1975) 1007–1016 (1975). doi:10.2514/3.60498.

[62] J. Young, W. Haile, Primer on the Craig-Bampton method, Finite Element Modeling Continuous Improvement, NASA, 2000 (2000).

[63] C. Droz, C. Zhou, M. Ichchou, J.-P. Lainé, A hybrid wave-mode formulation for the vibro-acoustic analysis of 2d periodic structures, Journal of Sound and Vibration 363 (2016) 285–302 (2016). doi:10.1016/j.jsv.2015.11.003.

[64] C. Droz, J.-P. Lainé, M. Ichchou, G. Inquiété, A reduced formulation for the free-wave propagation analysis in composite structures, Composite Structures 113 (2014) 134–144 (2014). doi:10.1016/j.compstruct.2014.03.017.

[65] R. F. Boukadia, C. Droz, M. N. Ichchou, W. Desmet, A bloch wave reduction scheme for ultrafast band diagram and dynamic response computation in periodic

structures, Finite Elements in Analysis and Design 148 (2018) 1–12 (2018). doi:10.1016/j.finel.2018.05.007.

[66] Z. Zergoune, M. Ichchou, O. Bareille, B. Harras, R. Benamar, B. Troclet, Assessments of shear core effects on sound transmission loss through sandwich panels using a two-scale approach, Computers & Structures 182 (2017) 227–237 (2017). doi:10.1016/j.compstruc.2016.11.017.

[67] R. Orris, M. Petyt, A finite element study of harmonic wave propagation in periodic structures, Journal of Sound and Vibration 33 (2) (1974) 223–236 (1974). doi:10.1016/S0022-460X(74)80108-2.

[68] F. Errico, M. Ichchou, S. D. Rosa, O. Bareille, F. Franco, The modelling of the flow-induced vibrations of periodic flat and axial-symmetric structures with a wave-based method, Journal of Sound and Vibration 424 (2018) 32–47 (2018). doi:10.1016/j.jsv.2018.03.012.

[69] C. Droz, O. Bareille, M. Ichchou, A new procedure for the determination of structural characteristics of sandwich plates in medium frequencies, Composites Part B: Engineering 112 (2017) 103–111 (2017). doi:10.1016/j.compositesb.2016.12.023.

[70] F. Fahy, P. Gardonio, Sound and structural vibration: radiation, transmission and response, Elsevier, 2007 (2007).

[71] O. Baho, Z. Zergoune, M. Ichchou, B. Harras, R. Benamar, B. Troclet, On global bending–shear core transition effects for the vibroacoustic of sandwich structures: Analytical and numerical investigations, Composite Structures 154 (2016) 453–463 (2016). doi:10.1016/j.compstruct.2016.07.062.

[72] L. Beranekand, I. Ver, Noise and vibration control engineering-principles and applications, Noise and vibration control engineering-Principles and applications John Wiley & Sons, Inc., 814 p., 1992 (1992).

[73] K. De Langhe, C. Moser, R. Boeykens, K. Kucukcoskun, Sound transmission loss predictions of aircraft panels: an update on recent technology evolutions, in: Inter-Noise and Noise-CON Congress and Conference Proceedings, Vol. 253-5, Institute of Noise Control Engineering, 2016, pp. 3354–3365 (2016).

[74] A. Parrinello, G. Ghiringhelli, Transfer matrix representation for periodic planar media, Journal of Sound and Vibration 371 (2016) 196–209 (2016). doi:10.1016/j.jsv.2016.02.005.

[75] S. Narayanan, R. Shanbhag, Sound transmission through a damped sandwich panel, Journal of Sound and Vibration 80 (3) (1982) 315–327 (1982). doi:10.1016/0022-460X(82)90273-5.

[76] G. Kurtze, B. G. Watters, New wall design for high transmission loss or high damping, The Journal of the Acoustical Society of America 31 (6) (1959) 739–748 (1959). doi:10.1121/1.1907780.

[77] M. Villot, C. Guigou, L. Gagliardini, Predicting the acoustical radiation of finite size multi-layered structures by applying spatial windowing on infinite structures, Journal of Sound and Vibration 245 (3) (2001) 433–455 (2001). doi:10.1006/jsvi.2001.3592.

[78] K. Renji, Sound transmission loss of unbounded panels in bending vibration considering transverse shear deformation, Journal of Sound Vibration 283 (2005) 478–486 (2005).

[79] C. Shen, F. Xin, T. Lu, Theoretical model for sound transmission through finite sandwich structures with corrugated core, International Journal of Non-Linear Mechanics 47 (10) (2012) 1066–1072 (2012). doi:10.1016/j.ijnonlinmec.2011.09.014.

[80] S. Kumar, L. Feng, U. Orrenius, Predicting the sound transmission loss of honeycomb panels using the wave propagation approach, Acta Acustica united with Acustica 97 (5) (2011) 869–876 (2011). doi:10.3813/AAA.918466.

[81] W. Lauriks, P. Mees, J. Allard, The acoustic transmission through layered systems, Journal of Sound and Vibration 155 (1) (1992) 125–132 (1992). doi:10.1016/0022-460X(92)90650-M.

[82] S. Ghinet, N. Atalla, Sound transmission loss of insulating complex structures, Canadian Acoustics 29 (3) (2001) 26–27 (2001).

[83] D. Rhazi, N. Atalla, Transfer matrix modeling of the vibroacoustic response of multimaterials structures under mechanical excitation, Journal of Sound and Vibration 329 (13) (2010) 2532–2546 (2010). doi:10.1016/j.jsv.2010.01.013.

[84] N. Atalla, Modeling the sound transmission through complex structures with attached noise control materials, Wave Motion 51 (4) (2014) 650–663 (2014). doi:10.1016/j.wavemoti.2013.11.001.

[85] R. Vaicaitis, Y. Lin, Response of finite periodic beam to turbulent boundary-layer pressure excitation, AIAA Journal 10 (8) (1972) 1020–1024 (1972). doi:10.2514/3.50288.

[86] A. Dijckmans, G. Vermeir, Development of a hybrid wave based–transfer matrix model for sound transmission analysis, The Journal of the Acoustical Society of America 133 (4) (2013) 2157–2168 (2013). doi:10.1121/1.4794364.

[87] R. Panneton, N. Atalla, Numerical prediction of sound transmission through finite multilayer systems with poroelastic materials, The Journal of the Acoustical Society of America 100 (1) (1996) 346–354 (1996). doi:10.1121/1.415956.

[88] U. Orrenius, H. Liu, A. Wareing, S. Finnveden, V. Cotoni, Wave modelling in predictive vibro-acoustics: Applications to rail vehicles and aircraft, Wave Motion 51 (4) (2014) 635–649 (2014). doi:10.1016/j.wavemoti.2013.11.007.

[89] M. A. Ben Souf, D. Chronopoulos, M. Ichchou, O. Bareille, M. Haddar, On the variability of the sound transmission loss of composite panels through a parametric probabilistic approach, Journal of Computational Acoustics 24 (01) (2016) 1550018 (2016). doi:10.1142/S0218396X15500186.

[90] S. D. Rosa, M. Capobianco, G. Nappo, G. Pagnozzi, Models and comparisons for the evaluation of the sound transmission loss of panels, Proceedings of the Institution of Mechanical Engineers, Part C: Journal of Mechanical Engineering Science 228 (18) (2014) 3343–3355 (2014). doi:10.1177/0954406214530597.

[91] S. Ghinet, N. Atalla, H. Osman, The transmission loss of curved laminates and sandwich composite panels, The Journal of the Acoustical Society of America 118 (2) (2005) 774–790 (2005). doi:10.1121/1.1932212.

[92] L. Koval, On sound transmission into an orthotropic shell, Journal of Sound and Vibration 63 (1) (1979) 51–59 (1979). doi:10.1016/0022-460X(79)90376-6.

[93] S. Ghinet, N. Atalla, H. Osman, Diffuse field transmission into infinite sandwich composite and laminate composite cylinders, Journal of Sound and Vibration 289 (4) (2006) 745–778 (2006). doi:10.1016/j.jsv.2005.02.028.

[94] F. Errico, M. Ichchou, F. Franco, S. D. Rosa, O. Bareille, C. Droz, Schemes for the sound transmission of flat, curved and axisymmetric structures excited by aerodynamic and acoustic sources, Journal of Sound and Vibration 456 (2019) 221–238 (2019). doi:10.1016/j.jsv.2019.05.041.

[95] F. Errico, G. Tufano, O. Robin, N. Guenfoud, M. Ichchou, N. Atalla, Simulating the sound transmission loss of complex curved panels with attached noise control materials using periodic cell wavemodes, Applied Acoustics 156 (2019) 21 –28 (2019). doi:10.1016/j.apacoust.2019.06.027.

[96] J. Christen, M. Ichchou, A. Zine, B. Troclet, Wave finite element formulation of the acoustic transmission through complex infinite plates, Acta Acustica united with Acustica 102 (6) (2016) 984–991 (2016). doi:10.3813/AAA.919013.

[97] Y. Yang, B. Mace, M. Kingan, Wave and finite element method for predicting sound transmission through finite multi-layered structures with fluid layers, Computers & Structures 204 (2018) 20–30 (2018). doi:10.1016/j.compstruc.2018.04.003.

[98] E. Deckers, S. Jonckheere, L. Van Belle, C. Claeys, W. Desmet, Prediction of transmission, reflection and absorption coefficients of periodic structures using a hybrid wave based – finite element unit cell method, Journal of Computational Physics 356 (2018) 282–302 (2018). doi:10.1016/j.jcp.2017.12.001.

[99] D.-Y. Maa, Theory and design of microperforated panel sound-absorbing constructions, Scientia Sinica 18 (1) (1975) 55–71 (1975). doi:10.1360/ya1975-18-1-55.

[100] D.-Y. Maa, Potential of microperforated panel absorber, The Journal of the Acoustical Society of America 104 (5) (1998) 2861–2866 (1998). doi:10.1121/1.423870.

[101] N. Atalla, F. Sgard, Modeling of perforated plates and screens using rigid frame porous models, Journal of Sound and Vibration 303 (1) (2007) 195–208 (2007). doi:10.1016/j.jsv.2007.01.012.

[102] N. Atalla, R. Panneton, F. Sgard, X. Olny, Acoustic absorption of macro-perforated porous materials, Journal of Sound and Vibration 243 (4) (2001) 659–678 (2001). doi:10.1006/jsvi.2000.3435.

[103] D. Lee, Y. Kwon, Estimation of the absorption performance of multiple layer perforated panel systems by transfer matrix method, Journal of Sound and Vibration 278 (4) (2004) 847–860 (2004). doi:10.1016/j.jsv.2003.10.017.

[104] T. G. Zieliński, F. Chevillotte, E. Deckers, Sound absorption of plates with micro-slits backed with air cavities: Analytical estimations, numerical calculations and experimental validations, Applied Acoustics 146 (2019) 261–279 (2019). doi:10.1016/j.apacoust.2018.11.026.

[105] C. Perrot, F. Chevillotte, M. Tan Hoang, G. Bonnet, F.-X. Bécot, L. Gautron, A. Duval, Microstructure, transport, and acoustic properties of open-cell foam samples: Experiments and three-dimensional numerical simulations, Journal of Applied Physics 111 (1) (2012) 014911 (2012). doi:10.1063/1.3673523.

[106] J. Boulvert, J. Costa-Baptista, T. Cavalieri, M. Perna, E. R. Fotsing, V. Romero-García, G. Gabard, A. Ross, J. Mardjono, J.-P. Groby, Acoustic modeling of micro-

lattices obtained by additive manufacturing (2019).
URL https://hal.archives-ouvertes.fr/hal-02178561

[107] H. Meng, M. Galland, M. Ichchou, O. Bareille, F. Xin, T. Lu, Small perforations in corrugated sandwich panel significantly enhance low frequency sound absorption and transmission loss, Composite Structures 182 (2017) 1–11 (2017). doi:10.1016/j.compstruct.2017.08.103.

[108] Y. Tang, S. Ren, H. Meng, F. Xin, L. Huang, T. Chen, C. Zhang, T. J. Lu, Hybrid acoustic metamaterial as super absorber for broadband low-frequency sound, Scientific Reports 7 (2017) 43340 (2017). doi:10.1038/srep43340.

[109] S. G. Johnson, Notes on perfectly matched layers (pmls), Lecture notes, Massachusetts Institute of Technology, Massachusetts 29 (2008).

[110] J. Rindel, Dispersion and absorption of structure-borne sound in acoustically thick plates, Applied Acoustics 41 (2) (1994) 97–111 (1994). doi:10.1016/0003-682X(94)90063-9.

[111] E. Davis, Designing honeycomb panels for noise control, 5th AIAA/CEAS Aeroacoustics Conference and Exhibit (1999) 1917 (1999). doi:10.2514/6.1999-1917.

[112] O. Baho, M. Ichchou, B. H. R. Benamar, Optimization of the vibro-acoustic indicators of honeycomb panels, Proceeding of the International Conference on Dynamics of Composite Structures (2015) 205–210 (2015).

[113] C. Droz, Z. Zergoune, R. Boukadia, O. Bareille, M. Ichchou, Vibro-acoustic optimisation of sandwich panels using the wave/finite element method, Composite Structures 156 (2016) 108–114 (2016). doi:10.1016/j.compstruct.2016.01.025.

[114] D. Griese, J. Summers, L. Thompson, The effect of honeycomb core geometry on the sound transmission performance of sandwich panels, Journal of Vibration and Acoustics 137 (021011) (2015) 1–11 (2015). doi:10.1115/1.4029043.

[115] R. Galgalikar, L. Thompson, Design optimization of honeycomb core sandwich panels for maximum sound transmission loss, Journal of Vibration and Acoustics 138 (5) (2016) 1–13 (2016). doi:10.1115/1.4033459.

[116] M. Mazloomi, M. Ranjbar, L. Boldrin, F. Scarpa, S. Patsias, N. Ozada, Vibroacoustics of 2d gradient auxetic hexagonal honeycomb sandwich panels, Composite Structures 187 (2018) 593–603 (2018). doi:10.1016/j.compstruct.2017.10.077.

[117] F. Franco, K. A. Cunefare, M. Ruzzene, Structural-Acoustic Optimization of Sandwich Panels, Journal of Vibration and Acoustics 129 (3) (2006) 330–340 (2006). doi:10.1115/1.2731410.

[118] A. Ingrole, A. Hao, R. Liang, Design and modeling of auxetic and hybrid honeycomb structures for in-plane property enhancement, Materials & Design 117 (2017) 72–83 (2017). doi:10.1016/j.matdes.2016.12.067.

[119] S. D. Broccolo, S. Laurenzi, F. Scarpa, Auxhex – a kirigami inspired zero poisson's ratio cellular structure, Composite Structures 176 (2017) 433–441 (2017). doi:10.1016/j.compstruct.2017.05.050.

[120] M. Ranjbar, L. Boldrin, F. Scarpa, S. Neild, S. Patsias, Vibroacoustic optimization of anti-tetrachiral and auxetic hexagonal sandwich panels with gradient geometry, Smart Materials and Structures 25 (5) (2016) 054012 (2016). doi:10.1088/0964-1726/25/5/054012.

[121] Z. Hou, X. Tian, J. Zhang, D. Li, Design and manufacturing of lightweight composite structures based on continuous fiber reinforced composites 3d printing, ICCM International Conferences on Composite Materials August (2017).

[122] H. Yang, H. Li, H. Zheng, A structural-acoustic optimization of two-dimensional sandwich plates with corrugated cores, Journal of Vibration and Control 23 (18) (2017) 3007–3022 (2017). doi:10.1177/1077546315625558.

[123] B. Du, L. Chen, J. Tan, H. Zhou, Y. Zhao, W. Wu, W. Li, D. Fang, L. Chen, Fabrication and bending behavior of thermoplastic composite curved corrugated sandwich beam with interface enhancement, International Journal of Mechanical Sciences 149 (2018) 101–111 (2018). doi:10.1016/j.ijmecsci.2018.09.049.

[124] T. Karttunen, J. Reddy, J. Romanoff, Two-scale constitutive modeling of a lattice core sandwich beam, Composites Part B: Engineering 160 (2019) 66–75 (2019). doi:10.1016/j.compositesb.2018.09.098.

[125] K. Qiu, W. Zhang, M. Domaszewski, D. Chamoret, Topology optimization of periodic cellular solids based on a superelement method, Engineering Optimization 41 (3) (2009) 225–239 (2009). doi:10.1080/03052150802414718.

[126] X. Huang, Y. M. Xie, Optimal design of periodic structures using evolutionary topology optimization, Structural and Multidisciplinary Optimization 36 (6) (2008) 597–606 (2008). doi:10.1007/s00158-007-0196-1.

[127] Y. Chen, S. Zhou, Q. Li, Multiobjective topology optimization for finite periodic structures, Computers and Structures 88 (11-12) (2010) 806–811 (6 2010). doi:10.1016/j.compstruc.2009.10.003.

[128] Z. Zuo, Topology optimization of periodic structures, Ph.D. thesis, RMIT University (2009).

[129] K. Qiu, Analysis and optimal design of lightweight sandwich structures and materials, Ph.D. thesis, Université de Franche-Comté (2008).

[130] J. Chen, C. Sun, Dynamic behavior of a sandwich beam with internal resonators, Journal of Sandwich Structures & Materials 13 (4) (2011) 391–408 (2011). doi:10.1177/1099636210391124.

[131] J. Chen, C. Sun, Wave propagation in sandwich structures with resonators and periodic cores, Journal of Sandwich Structures & Materials 15 (3) (2013) 359–374 (2013). doi:10.1177/1099636212468738.

[132] N. de Melo Filho, L. Van Belle, C. Claeys, E. Deckers, W. Desmet, Dynamic mass based sound transmission loss prediction of vibro-acoustic metamaterial double panels applied to the mass-air-mass resonance, Journal of Sound and Vibration 442 (2019) 28–44 (2019). doi:10.1016/j.jsv.2018.10.047.

[133] C. Claeys, N. de Melo Filho, L. Van Belle, E. Deckers, W. Desmet, Design and validation of metamaterials for multiple structural stop bands in waveguides, Extreme Mechanics Letters 12 (2017) 7–22 (2017). doi:10.1016/j.eml.2016.08.005.

[134] C. Claeys, K. Vergote, P. Sas, W. Desmet, On the potential of tuned resonators to obtain low-frequency vibrational stop bands in periodic panels, Journal of Sound and Vibration 332 (6) (2013) 1418–1436 (2013). doi:10.1016/j.jsv.2012.09.047.

[135] L. Van Belle, C. Claeys, E. Deckers, W. Desmet, On the impact of damping on the dispersion curves of a locally resonant metamaterial: Modelling and experimental validation, Journal of Sound and Vibration 409 (2017) 1–23 (2017). doi:10.1016/j.jsv.2017.07.045.

[136] C. Droz, O. Robin, M. Ichchou, N. Atalla, Improving sound transmission loss at ring frequency of a curved panel using tunable 3d-printed small-scale resonators, The Journal of the Acoustical Society of America 145 (1) (2019) 72–78 (2019). doi:10.1121/1.5088036.

[137] G. Tufano, F. Errico, O. Robin, C. Droz, M. Ichchou, B. Pluymers, W. Desmet, N. Atalla, K-space analysis of complex large-scale meta-structures using the inho-

mogeneous wave correlation method, Mechanical Systems and Signal Processing 135 (2020) 106407 (2020). doi:10.1016/j.ymssp.2019.106407.

[138] L. Van Belle, C. Claeys, E. Deckers, W. Desmet, The impact of damping on the sound transmission loss of locally resonant metamaterial plates, Journal of Sound and Vibration 461 (2019) 114909 (2019). doi:10.1016/j.jsv.2019.114909.

[139] L. Van Belle, C. Claeys, E. Deckers, W. Desmet, On the impact of damping on the dispersion curves of a locally resonant metamaterial: Modelling and experimental validation, Journal of Sound and Vibration 409 (2017) 1 – 23 (2017). doi:10.1016/j.jsv.2017.07.045.

[140] J.-P. Groby, A. Wirgin, E. Ogam, Acoustic response of a periodic distribution of macroscopic inclusions within a rigid frame porous plate, Waves in Random and Complex Media 18 (3) (2008) 409–433 (2008). doi:10.1080/17455030802061300.

[141] J.-P. Groby, A. Wirgin, L. De Ryck, W. Lauriks, R. P. Gilbert, Y. S. Xu, Acoustic response of a rigid-frame porous medium plate with a periodic set of inclusions, The Journal of the Acoustical Society of America 126 (2) (2009) 685–693 (2009). doi:10.1121/1.3158936.

[142] V. Burlayenko, T. Sadowski, Analysis of structural performance of sandwich plates with foam-filled aluminum hexagonal honeycomb core, Computational Materials Science 45 (3) (2009) 658–662, proceedings of the 17th International Workshop on Computational Mechanics of Materials (2009). doi:10.1016/j.commatsci.2008.08.018.

[143] L. Yan, B. Yu, B. Han, C. Chen, Q. Zhang, T. Lu, Compressive strength and energy absorption of sandwich panels with aluminum foam-filled corrugated cores, Composites Science and Technology 86 (2013) 142–148 (2013). doi:10.1016/j.compscitech.2013.07.011.

[144] L. Yan, B. Han, B. Yu, C. Chen, Q. Zhang, T. Lu, Three-point bending of sandwich beams with aluminum foam-filled corrugated cores, Materials & Design 60 (2014) 510–519 (2014). doi:10.1016/j.matdes.2014.04.014.

[145] A. Marasco, D. Cartié, I. Partridge, A. Rezai, Mechanical properties balance in novel z-pinned sandwich panels: Out-of-plane properties, Composites Part A: Applied Science and Manufacturing 37 (2) (2006) 295–302 (2006). doi:10.1016/j.compositesa.2005.03.029.

[146] G. Zhang, B. Wang, L. Ma, L. Wu, S. Pan, J. Yang, Energy absorption and low velocity impact response of polyurethane foam filled pyramidal lattice core sand-

wich panels, Composite Structures 108 (2014) 304–310 (2014). doi:10.1016/j.compstruct.2013.09.040.

[147] T. Fu, Z. Chen, H. Yu, Z. Wang, X. Liu, An analytical study of sound transmission through corrugated core fgm sandwich plates filled with porous material, Composites Part B: Engineering 151 (2018) 161–172 (2018). doi:10.1016/j.compositesb.2018.06.010.

[148] M. Arunkumar, J. Pitchaimani, K. Gangadharan, M. Leninbabu, Vibro-acoustic response and sound transmission loss characteristics of truss core sandwich panel filled with foam, Aerospace Science and Technology 78 (2018) 1–11 (2018). doi:10.1016/j.ast.2018.03.029.

[149] F. Han, G. Seiffert, Y. Zhao, B. Gibbs, Acoustic absorption behaviour of an open-celled aluminium foam, Journal of Physics D: Applied Physics 36 (3) (2003) 294–302 (2003). doi:10.1088/0022-3727/36/3/312.

[150] C.-N. Wang, J.-H. Torng, Experimental study of the absorption characteristics of some porous fibrous materials, Applied Acoustics 62 (2001) 447–459 (2001). doi:10.1016/S0003-682X(00)00043-8.

[151] M. Swift, P. Bris, K. Horoshenkov, Acoustic absorption in re-cycled rubber granulate, Applied Acoustics 57 (3) (1999) 203–212 (1999). doi:10.1016/S0003-682X(98)00061-9.

[152] M. H. Fouladi, M. J. M. Nor, M. Ayub, Z. A. Leman, Utilization of coir fiber in multilayer acoustic absorption panel, Applied Acoustics 71 (3) (2010) 241–249 (2010). doi:10.1016/j.apacoust.2009.09.003.

[153] F. Bucciarelli, G. M. Fierro, M. Meo, A multilayer microperforated panel prototype for broadband sound absorption at low frequencies, Applied Acoustics 146 (2019) 134–144 (2019). doi:10.1016/j.apacoust.2018.11.014.

[154] C. Wang, L. Huang, On the acoustic properties of parallel arrangement of multiple micro-perforated panel absorbers with different cavity depths, The Journal of the Acoustical Society of America 130 (1) (2011) 208–218 (2011). doi:10.1121/1.3596459.

[155] F. Sgard, X. Olny, N. Atalla, F. Castel, On the use of perforations to improve the sound absorption of porous materials, Applied Acoustics 66 (6) (2005) 625–651 (2005). doi:10.1016/j.apacoust.2004.09.008.

[156] O. Doutres, N. Atalla, Acoustic contributions of a sound absorbing blanket placed in a double panel structure: Absorption versus transmission, The Journal of the Acoustical Society of America 128 (2) (2010) 664–671 (2010). doi:10.1121/1.3458845.

[157] H. Meng, M. Galland, M. Ichchou, F. Xin, T. Lu, On the low frequency acoustic properties of novel multifunctional honeycomb sandwich panels with micro-perforated faceplates, Applied Acoustics 152 (2019) 31–40 (2019). doi:10.1016/j.apacoust.2019.02.028.

[158] E. Magnucka-Blandzi, Z. Walczak, L. Wittenbeck, M. Rodak, Strength of a metal seven-layer rectangular plate with trapezoidal corrugated cores, Journal of Theoretical and Applied Mechanics 55 (2) (2017) 433–446 (2017). doi:10.15632/jtam-pl.55.2.433.

[159] E. Magnucka-Blandzi, Z. Walczak, L. Wittenbeck, P. Jasion, M. Rodak, W. Szyc, J. Lewiński, Stability and vibrations of a metal seven-layer rectangular plate with trapezoidal corrugated cores, Thin-Walled Structures 114 (2017) 154–163 (2017). doi:10.1016/j.tws.2016.11.025.

[160] J. Lewiński, E. Magnucka-Blandzi, W. Szyc, Shear modulus of elasticity for thin-walled trapezoidal corrugated cores of seven-layer sandwich plates, Engineering Transactions 63 (4) (2015) 421–438 (2015).

[161] P. Paczos, P. Wasilewicz, E. Magnucka-Blandzi, Experimental and numerical investigations of five-layered trapezoidal beams, Composite Structures 145 (2016) 129–141 (2016). doi:10.1016/j.compstruct.2016.02.079.

[162] A. Pydah, R. Batra, Analytical solution for cylindrical bending of two-layered corrugated and webcore sandwich panels, Thin-Walled Structures 123 (2018) 509–519 (2018). doi:10.1016/j.tws.2017.11.023.

[163] A. Pydah, R. Batra, Blast loading of bumper shielded hybrid two-core miura-ori/honeycomb core sandwich plates, Thin-Walled Structures 129 (2018) 45–57 (2018). doi:10.1016/j.tws.2018.03.020.

[164] S. Hou, C. Shu, S. Zhao, T. Liu, X. Han, Q. Li, Experimental and numerical studies on multi-layered corrugated sandwich panels under crushing loading, Composite Structures 126 (2015) 371–385 (2015). doi:10.1016/j.compstruct.2015.02.039.

[165] C. Shu, S. Zhao, S. Hou, Crashworthiness analysis of two-layered corrugated sandwich panels under crushing loading, Thin-Walled Structures 133 (2018) 42–51 (2018). doi:10.1016/j.tws.2018.09.008.

[166] H. Wen-chao, N. Chung-fai, Sound insulation improvement using honeycomb sandwich panels, Applied Acoustics 53 (1) (1998) 163–177 (1998). doi:10.1016/S0003-682X(97)00033-9.

[167] N. Sui, X. Yan, T.-Y. Huang, J. Xu, F.-G. Yuan, Y. Jing, A lightweight yet soundproof honeycomb acoustic metamaterial, Applied Physics Letters 106 (17) (2015) 171905 (2015). doi:10.1063/1.4919235.

[168] N. Guenfoud, C. Droz, M. Ichchou, O. Bareille, W. Desmet, B. Pluymers, Modeling and experimental measurements of the sound transmission loss for multi-layer core topology systems, Proceedings of ISMA 2018 - International Conference on Noise and Vibration Engineering (2018) 4653–4662. http://past.isma-isaac.be/downloads/isma2018/proceedings/Proceedings_ISMA-USD2018.pdf (2018).

[169] N. Guenfoud, M. Ichchou, O. Bareille, W. Desmet, B. Pluymers, Multi-layer core topology systems, Proceeding of MEDYNA 2017: 2nd Euro-Mediterranean Conference on Structural Dynamics and Vibroacoustics (2017) 156–159. https://medyna2017.sciencesconf.org/data/Medyna_2017_Proceedings.pdf (2017).

[170] F. Errico, M. Ichchou, S. D. Rosa, F. Franco, O. Bareille, Investigations about periodic design for broadband increased sound transmission loss of sandwich panels using 3d-printed models, Mechanical Systems and Signal Processing (2019) 106432 (2019). doi:10.1016/j.ymssp.2019.106432.

[171] B. R. Mace, E. Manconi, Wave motion and dispersion phenomena: Veering, locking and strong coupling effects, The Journal of the Acoustical Society of America 131 (2) (2012) 1015–1028 (2012). doi:10.1121/1.3672647.

[172] E. Manconi, B. Mace, Veering and Strong Coupling Effects in Structural Dynamics, Journal of Vibration and Acoustics 139 (2) (2017). doi:10.1115/1.4035109.

[173] N. Guenfoud, C. Droz, M. Ichchou, O. Bareille, E. Deckers, W. Desmet, Parametric analysis of a triple core periodic unit cell including a middle random core, Proceeding of the 9th Eccomas Thematic Conference on Smart Structures and Materials (2019) 1157–1168. https://congress.cimne.com/smart2019/frontal/doc/EbookSMART2019.pdf (2019).

[174] J. Boulvert, T. Cavalieri, J. Costa-Baptista, L. Schwan, V. Romero-García, G. Gabard, E. R. Fotsing, A. Ross, J. Mardjono, J.-P. Groby, Optimally graded porous material for broadband perfect absorption of sound, Journal of Applied Physics 126 (17) (2019) 175101 (2019). doi:10.1063/1.5119715.

[175] M. Ottink, J. Brunskog, C.-H. Jeong, E. Fernandez-Grande, P. Trojgaard, E. Tiana-Roig, In situ measurements of the oblique incidence sound absorption coefficient for finite sized absorbers, The Journal of the Acoustical Society of America 139 (1) (2016) 41–52 (2016). doi:10.1121/1.4938225.

[176] Y. Zhang, M. Lu, C. H. Wang, G. Sun, G. Li, Out-of-plane crashworthiness of bio-inspired self-similar regular hierarchical honeycombs, Composite Structures 144 (2016) 1–13 (2016). doi:10.1016/j.compstruct.2016.02.014.

[177] B. Han, K. Qin, B. Yu, B. Wang, Q. Zhang, T. J. Lu, Honeycomb–corrugation hybrid as a novel sandwich core for significantly enhanced compressive performance, Materials & Design 93 (2016) 271–282 (2016). doi:10.1016/j.matdes.2015.12.158.

[178] Y. Liu, X.-C. Zhang, The influence of cell micro-topology on the in-plane dynamic crushing of honeycombs, International Journal of Impact Engineering 36 (1) (2009) 98–109 (2009). doi:10.1016/j.ijimpeng.2008.03.001.

[179] B. Atli-Veltin, F. Gandhi, Effect of cell geometry on the energy absorption of honeycombs under in-plane compression, AIAA Journal 48 (2) (2010) 466–478 (2010). doi:10.2514/1.45021.

[180] X. chun Zhang, H. min Ding, L. qiang An, X. lei Wang, Numerical investigation on dynamic crushing behavior of auxetic honeycombs with various cell-wall angles, Advances in Mechanical Engineering 7 (2) (2015) 679678 (2015). doi:10.1155/2014/679678.